

Technische Universität München  
Institut für Energietechnik

Lehrstuhl für Thermodynamik

# **Development, implementation and validation of LES models for inhomogeneously premixed turbulent combustion**

**Ludovic Durand**

Vollständiger Abdruck der von der Fakultät für Maschinenwesen der Technischen  
Universität München zur Erlangung des akademischen Grades eines

DOKTOR – INGENIEURS

genehmigten Dissertation.

Vorsitzender:

Univ.-Prof. Dr.-Ing. W. A. Wall

Prüfer der Dissertation:

1. Univ.-Prof. W. H. Polike, Ph.D. (CCNY)

2. Univ.-Prof. Dr. rer. nat. F. Dinkelacker,  
Universität Siegen

Die Dissertation wurde am 27.06.2007 bei der Technischen Universität München eingereicht und  
durch die Fakultät für Maschinenwesen am 18.10.2007 angenommen.



Personne ne sait répondre à ces questions! On ne nous apprend même pas à nous les poser.

*S. Balibar, [Bal05]*

## **Danksage, Remerciements**

Diese Arbeit entstand am Lehrstuhl für Thermodynamik der Technischen Universität München und wurde von der bayrischen Forschungsgemeinschaft **FortVer** gefördert.

Mein erster und besonderer Dank gilt meinem Doktorvater, Herrn Professor Wolfgang Polifke, für seine fachliche Betreuung und sein in mich gesetztes Vertrauen. Seine Begeisterung für die Modellierung der turbulenten vorgemischten Verbrennung hat zu intensiven und anregenden Diskussionen geführt, in denen er stets reges Interesse am Fortgang meiner Arbeit zeigte. Gleichzeitig gab er mir die Möglichkeit, selbständig zu arbeiten und eigene Lösungsansätze zu entwickeln.

Ich freue mich, dass Herr Professor Friedrich Dinkelacker das Koreferat übernommen hat. Als Projektpartner hat er unsere Arbeit mit Interesse verfolgt, relevante Kommentare und Verbesserungen eingebracht. Herrn Professor Wolfgang Wall vom Lehrstuhl für numerische Mechanik danke ich für die freundliche Übernahme des Vorsitzes bei der mündlichen Prüfung.

Mein Dank gilt auch meinen Kolleginnen und Kollegen, für die fachliche Unterstützung, die freundschaftliche Atmosphäre, und die "Freude am Forschen" am Lehrstuhl. Mein besonderer Dank gilt meinem dreijährigen Bürokollegen Andreas Huber, für seine tägliche gute Laune, unsere gemeinsamen Überlegungen und wertvolle Diskussionen. Weiterhin danke ich "meinen" Studenten und wissenschaftlichen Hilfskräften für ihren Einsatz, ihre tatkräftige Unterstützung, und auch ihre Fragen, die mich zu neuen Überlegungen geführt haben.

Puisque cette thèse marque aussi la fin de mon parcours scolaire et universitaire, je souhaite remercier les instituteurs, professeurs et responsables de stages qui ont toujours entretenu ma curiosité, et mon envie de savoir et comprendre.

Un très grand merci aussi à tous mes amis pour leur disponibilité, et qui de près ou de loin, m'ont soutenu, conseillé et encouragé pendant ces quatre années. Tout m'aurait paru plus difficile sans ces coups de téléphone, ces heures de sport, et autres bons moments passés ensemble.

Enfin, j'adresse mes plus profonds remerciements à ma famille, ma soeur, ma grand-mère et mes parents, pour leur soutien et leur confiance, et grâce à qui j'ai la chance de pouvoir écrire ce travail aujourd'hui.

# Abstract - Zusammenfassung

More and more engine systems are designed with lean premixed turbulent flames, for ecological reasons and pollutant emission restrictions. Unfortunately, these combustion systems are prone to flame instabilities, since the heat release is very sensitive to air-fuel ratio variations for lean mixture. In the present work, three Large Eddy Simulation (LES) combustion models for lean inhomogeneously premixed turbulent combustion are compared, implemented and validated using an unstructured commercial solver against experimental results: Thickened Flame (TF), Turbulent Flame speed Closure (TFC-LES) and Subgrid Flame Closure (SFC) models. The derivation of the new SFC model is detailed in this thesis. The validation is based on velocity profiles, as well as flame position measurements for three burners: The Volvo test-rig, the Paul Scherrer Institut (PSI) burner, and our TD1 burner. The SFC and TF' models have given similar and accurate results compared to the experimental measurements. The TFC-LES model requires the adaptation of its model constant.

Aus Umweltgründen werden Verbrennungssysteme zunehmend mit mageren Vormischflammen betrieben. Verbrennungsinstabilitäten treten damit häufiger auf, da die Wärme-freisetzung sehr stark auf Schwankungen des Mischungsverhältnisses reagiert. In der vorliegenden Arbeit, werden drei Large Eddy Simulation (LES) Verbrennungsmodelle für die inhomogene magere Verbrennung verglichen, in einem kommerziellen Strömungslöser implementiert, und anhand experimenteller Ergebnisse validiert: das Thickened Flame, das Turbulent Flame speed Closure (TFC-LES) und das Subgrid Flame Closure (SFC) Modell. Die Herleitung des neuen SFC Modells wird in dieser Arbeit ausführlich beschrieben. Ergebnisse werden anhand experimenteller Geschwindigkeitsprofile und Messungen der Flammenposition mit drei Versuchsaufbauten untersucht: der Volvo Anlage, dem Brenner des Paul Scherer Instituts, und unserem Brenner. Das SFC und TF Modell weisen ähnlich gute Ergebnisse im Vergleich zu den Experimenten auf. Ergebnisse zeigen dass die Konstante des TFC Modells keinen universellen Charakter besitzt.

# Contents

<b>1</b>	<b>Introduction</b>	<b>1</b>
1.1	Industrial background: Turbulent premixed combustion . . . . .	1
1.1.1	Turbulent reactive flows in industrial processes . . . . .	1
1.1.2	CFD simulations as industrial development tools . . . . .	2
1.1.3	Turbulence modeling: RANS and LES . . . . .	2
1.1.4	Inhomogeneously premixed combustion . . . . .	3
1.2	Layout of the thesis . . . . .	4
<b>2</b>	<b>Turbulence and combustion theory</b>	<b>7</b>
2.1	Description of reacting flows . . . . .	7
2.1.1	Continuity, momentum and energy transport equations . . . . .	7
2.1.2	Need for additional laws . . . . .	9
2.1.3	Mixture and thermo-chemistry description . . . . .	10
2.2	Turbulence theory . . . . .	14
2.2.1	Phenomenology . . . . .	14
2.2.2	Effect on the flow - Reynolds number . . . . .	17
2.2.3	Mathematical representation - Kolmogorov Spectra . . . . .	17
2.3	Combustion theory . . . . .	20
2.3.1	Premixed and diffusion flames . . . . .	20
2.3.2	Non-perfectly, inhomogeneously and partially premixed combustion	23
2.3.3	Laminar premixed flames . . . . .	24
2.3.4	Stretched laminar premixed flames . . . . .	29
2.4	Premixed turbulent combustion . . . . .	33
2.4.1	Interaction flame-turbulence . . . . .	33
2.4.2	Definition of dimensionless numbers . . . . .	34
2.4.3	Combustion Regimes . . . . .	37
2.4.4	Diagrams for turbulent premixed combustion . . . . .	39
<b>3</b>	<b>Modeling of turbulent reactive flows</b>	<b>41</b>
3.1	DNS . . . . .	42
3.1.1	Cold flows . . . . .	42
3.1.2	Reactive flows . . . . .	43
3.2	RANS modeling . . . . .	44
3.2.1	Reynolds and Favre averaging . . . . .	44
3.2.2	Turbulent variables and non-reactive models . . . . .	46

3.2.3	RANS combustion modeling . . . . .	47
3.3	LES modeling . . . . .	47
3.3.1	Filters and cut-off scales . . . . .	47
3.3.2	LES Models . . . . .	49
3.4	LES premixed combustion models . . . . .	50
3.4.1	Modeling approach and closure strategies . . . . .	50
3.4.2	Models based on species mass fractions . . . . .	52
3.4.3	Models based on the progress variable . . . . .	55
3.4.4	Progress variable and Flame Surface Density models . . . . .	56
3.4.5	Level-set approach: $G$ -equation . . . . .	58
3.5	Choice of the Thickened Flame (TF), Turbulent Flame speed Closure (TFC-LES) and Subgrid Flame	
<b>4</b>	<b>Thickened Flame model</b>	<b>61</b>
4.1	Principle of the TF model . . . . .	61
4.1.1	Artificial thickening of the flame . . . . .	62
4.1.2	The efficiency function . . . . .	63
4.1.3	Velocity fluctuation at the test-filter . . . . .	65
4.2	Finite-volume based evaluation of test filter velocity: TF' model . . . . .	66
4.3	Conclusion . . . . .	68
<b>5</b>	<b>Progress variable approach</b>	<b>69</b>
5.1	Definitions . . . . .	69
5.1.1	Progress variable transport equation . . . . .	69
5.1.2	Reference case: adiabatic and perfectly premixed combustion . . . . .	70
5.2	Inhomogeneously premixed combustion . . . . .	71
5.2.1	Extended transport equation for the progress variable . . . . .	71
5.2.2	Case of the lean inhomogeneously premixed combustion . . . . .	74
5.2.3	Influence on the laminar flame speed . . . . .	76
5.3	Non-adiabatic combustion . . . . .	81
5.3.1	Enthalpy loss term . . . . .	82
5.3.2	Enthalpy index . . . . .	82
5.3.3	Feedback enthalpy-progress variable . . . . .	84
5.4	Conclusion . . . . .	86
<b>6</b>	<b>Turbulent Flame speed Closure model</b>	<b>87</b>
6.1	Original model with RANS turbulence modeling . . . . .	87
6.1.1	Gradient formulation of the source term . . . . .	87
6.1.2	Turbulent flame velocity $S_t$ . . . . .	89
6.1.3	Counter-gradient diffusion . . . . .	93
6.2	Closure LES-TFC . . . . .	94
6.2.1	LES-TFC model closure . . . . .	94
6.2.2	LES-TFC with turbulent kinetic energy . . . . .	95
6.2.3	Bending effect and stretch factor . . . . .	96
6.2.4	LES-TFC closure drawbacks . . . . .	97
<b>7</b>	<b>Subgrid Flame Closure model</b>	<b>99</b>

7.1	Model concept: subgrid flame closure . . . . .	99
7.1.1	Paradoxical difficulty in LES modeling . . . . .	99
7.1.2	Comparison of subgrid and integral length scales . . . . .	101
7.2	Closure for the thickened flame regime . . . . .	104
7.2.1	Flamelet velocity . . . . .	105
7.2.2	Resolved burning velocity . . . . .	109
7.3	Closure for the corrugated flame regime . . . . .	111
7.3.1	Resolved burning velocity . . . . .	111
7.3.2	Fractal dimension . . . . .	113
7.4	Modeling bending effect and quenching with CFD . . . . .	114
7.4.1	Strain, stretch, bending effect and quenching . . . . .	114
7.4.2	Causes for stretch and contributions to stretch . . . . .	115
7.4.3	Turbulence to stretch . . . . .	117
7.4.4	Stretch to quenching . . . . .	120
7.4.5	Strategy for developing a bending effect sub-model with the SFC model	121
7.5	A bending effect and quenching sub-model for the SFC model . . . . .	123
7.5.1	Chemical time approach . . . . .	124
7.5.2	Generalized Karlovitz number . . . . .	125
7.5.3	Sub-model for the bending effect . . . . .	131
7.6	SFC model formulation . . . . .	133
7.6.1	Blend function and model formulation . . . . .	133
7.6.2	Comparison with the TFC model . . . . .	134
<b>8</b>	<b>Results and discussions</b>	<b>139</b>
8.1	Volvo test-rig . . . . .	139
8.1.1	Experiments and geometry . . . . .	139
8.1.2	Modeling and boundary conditions . . . . .	141
8.1.3	Validation of the TF model . . . . .	144
8.1.4	Comparison of the TFC-LES, TF' and SFC models . . . . .	145
8.1.5	Comparison with previous works . . . . .	150
8.2	Paul Scherrer Institute burner . . . . .	156
8.2.1	Experiments and geometry . . . . .	156
8.2.2	Modeling and boundary conditions . . . . .	158
8.2.3	Comparison of the TFC-LES, TF' and SFC models . . . . .	160
8.2.4	Comparison with other LES simulations . . . . .	165
8.2.5	Comparison with other experimental results . . . . .	165
8.3	TD1 burner . . . . .	173
8.3.1	Experiments and geometry . . . . .	173
8.3.2	Modeling and boundary conditions . . . . .	174
8.3.3	Discussion . . . . .	175
8.4	Computer requirement . . . . .	182
8.4.1	Mesh refinement . . . . .	182
8.4.2	Modeling . . . . .	182
<b>9</b>	<b>Conclusion</b>	<b>185</b>

<b>A Annexes</b>	<b>205</b>
A.1 Fractal theory . . . . .	205
A.2 TF and TF' models: Thermo-chemical properties . . . . .	206
A.2.1 Reduced reaction mechanisms . . . . .	206
A.2.2 Reaction rates . . . . .	207
A.2.3 DTF-LES Model . . . . .	210
A.3 TF and TF' models: Implementation in <i>Fluent</i> . . . . .	212
A.3.1 Cartesian mesh: original TF Model . . . . .	212
A.3.2 Modification for unstructured meshes: TF' version . . . . .	215
A.3.3 TF' model with MSM turbulence model . . . . .	217
A.3.4 Evaluation of the similarity constant for TF'-MSM . . . . .	219
A.4 Progress variable approach: Evaluation of $\bar{S}_l(\tilde{Z}, \widetilde{Z''^2})$ . . . . .	221
A.5 SFC model: Mesh refinement and resolved turbulent energy . . . . .	222
A.6 Post-processing achieved with <i>Tecplot</i> and <i>Matlab</i> . . . . .	225
A.6.1 Computation . . . . .	225
A.6.2 Exporting to <i>Tecplot</i> . . . . .	225
A.6.3 Treatment in <i>Matlab</i> . . . . .	226
A.7 SFC model: Synopsis . . . . .	226

# Nomenclature

## Latin Characters

$a$	$\text{m}^2/\text{s}$	thermal diffusivity
$b_{nt}$	$\text{m}$	thickened flame thickness (thickened flame regime)
$C_i$	$\text{mol}/\text{m}^3$	molar concentration (species $i$ )
$c_p$	$\text{J}/(\text{kg K})$	specific calorific coefficient
$e$	$\text{J}/\text{kg}$	specific internal energy
$D, D_t$	$\text{m}^2/\text{s}$	molecular, turbulent scalar diffusion coefficient
$\mathcal{D}$	-	fractal dimension
$\mathbf{f}$	$\text{m}/\text{s}^2$	volume forces
$h$	$\text{J}/\text{kg}$	specific enthalpy
$\mathcal{I}_h$	-	enthalpy index
$\mathbf{j}_k$	$\text{kg}/(\text{m}^2 \text{ s})$	diffusion flux
$k$	$\text{m}^2/\text{s}^2$	turbulent kinetic energy
$l_t$	$\text{m}$	turbulent integral length scale
MR	-	mesh refinement
$m$	$\text{kg}$	mass
$q^2$	$\text{m}^2/\text{s}^2$	turbulent kinetic energy included in a band of wave number
$p$	$\text{Pa}$	pressure
$\mathbf{q}$	$\text{W}/(\text{m}^2 \text{ s})$	heat flux
$R$	$\text{J}/(\text{kg K})$	gas constant
RTE	-	resolved turbulent energy
$S_l$	$\text{m}/\text{s}$	laminar flame speed
$S_{t\Delta}$	$\text{m}/\text{s}$	subgrid turbulent flame speed
$t_c$	$\text{s}$	chemical time scale
$t_t$	$\text{s}$	turbulent time scale
$\mathbf{u}$	$\text{m}/\text{s}$	velocity vector
$\mathbf{u}_k$	$\text{m}/\text{s}$	diffusion velocity vector
$u', u_{sgs}$	$\text{m}/\text{s}$	turbulent, subgrid-scale velocity
$u_{nt}$	$\text{m}/\text{s}$	thickened flame speed (thickened flame regime)
$\mathbf{v}_k$	$\text{m}/\text{s}$	species velocity vector
$t_{ij}$	$\text{Pa}$	viscosity tensor

$T$	K	temperature
$T_{ad}, T_i$	K	adiabatic, inner-layer flame temperature
$T_u, T_b$	K	unburnt, burnt temperature
TI	-	turbulence intensity
vol	$m^3$	cell volume
$y_i$	-	mass fraction (species i)
$\mathbf{w}$	m/s	vorticity vector

### Greek Characters

$\delta_l$	m	laminar flame thickness
$\delta_r$	m	reactive zone thickness
$\delta = 1/Ze$	-	ratio reactive zone to laminar flame thickness
$\Delta$	m	mesh size
$\varepsilon$	$m^2/s^3$	turbulent dissipation
$\epsilon$	m	oxidation layer thickness
$\kappa$	1/m	wave number
$\phi = \frac{AFR_{st}}{AFR}$	-	equivalence ratio
$\mu, \mu_t$	kg/(m s)	molecular, turbulent dynamic viscosity
$\nu, \nu_t$	$m^2/s$	molecular, turbulent kinematic viscosity
$\rho$	$kg/m^3$	density
$\xi$	m	fractal measurement scale

### Superscripts

$\Delta$	subgrid-scale
"	fluctuation (corresponding to Reynolds averaging/filtering)
'	mass-weighted fluctuation (corresponding to Favre averaging/filtering)
$\bar{x}$	Reynolds averaging/filtering
$\tilde{x}$	Favre averaging/filtering
$\hat{x}$	LES test-filter
$\langle x \rangle$	ensemble averaging

### Indices

b	burnt
l	laminar
nt	turbulent flamelet (thickened flame regime)
sgs	subgrid-scale
st	stoichiometric
t	turbulent
u	unburnt

**Non-dimensional Numbers**

Re	=	$U L/\nu$	Reynolds number
Re <sub>t</sub>	=	$u' l_t/\nu$	Turbulent Reynolds number
Re <sub>Δ</sub>	=	$u_{sgs} \Delta/\nu$	Subgrid Reynolds number
Da	=	$t_t/t_c$	Damköhler number
Da <sub>Δ</sub>	=	$t_{\Delta}/t_c$	Subgrid Damköhler number
Ka	=	$K t_c$	Karlovitz number
Ka <sub>t</sub>	=	$t_c/t_{\eta}$	Turbulent Karlovitz number
Ka <sub>δ</sub>	=	$\delta^{-2} t_c/t_{\eta}$	Second turbulent Karlovitz number
Le	=	$a/D$	Lewis number
Sc	=	$\nu/D$	Schmidt number
Pr	=	$\nu/a$	Prandtl number
Ze	=	$\delta_l/\delta_r$	Zeldovitch number

**Universal Constants**

$p^0$	=	101325 Pa	reference pressure
$\mathcal{R}$	=	8.31451 J/(mol K)	universal molar gas constant
$T^0$	=	298.15 K	reference temperature

**Abbreviations**

AFR	Air-Fuel-Ratio
CFD	Computational Fluid Dynamics
DNS	Direct Numerical Simulation
LES	Large Eddy Simulation
l.h.s.	left hand side
RANS	Reynolds-Averaged Navier-Stokes
r.h.s.	right hand side
SFC	Subgrid Flame Closure
TFC	Turbulent Flame speed Closure
TF	Thickened Flame
tke	turbulent kinetic energy

**Scalars - vectors - tensors - operators**

$p$	scalar
$\mathbf{u}$	vector
$u_i$	component i of the vector $\mathbf{u}$

$u_{i,j}$	derivate in the j direction for the component i of the vector $\mathbf{u}$
$\bar{\mathbf{T}}$	tensor
$T_{ij}$	element (i,j) of the tensor $\bar{\mathbf{T}}$
$T_{ij,k}$	derivate in the k direction for $T_{ij}$
$\vec{x}_i$	coordinate vectors
$\delta_{ij}$	Kroenecker's symbol
$\cdot$	scalar product
$\times$	vector product
$:$	tensor reduction
$\vec{\nabla}$	Nabla operator
$\vec{\nabla} p = \overrightarrow{\text{grad}} p = p_{,i} \vec{x}_i$	gradient of the scalar $p$
$\vec{\nabla} \cdot \mathbf{u} = \text{div } \mathbf{u} = u_{i,i}$	divergence of the vector $\mathbf{u}$
$\vec{\nabla} \times \mathbf{u} = \overrightarrow{\text{rot}} \mathbf{u} = \epsilon_{ijk} u_{i,j} \vec{x}_k$	rotational of the vector $\mathbf{u}$

### Comparison - equality symbols

$\equiv$	definition
$=$	equal
$\approx$	about equal
$\sim$	scales with
$\neq$	not equal

Except specific indications, Einstein Summation is implicitly employed. Compact notation (for example:  $u_{i,j} \equiv \frac{\partial u_i}{\partial x_j}$ ) for derivative operators is employed in text.

Except in chapter 3, where these notions are defined,

- only LES equations are employed. The same notation  $\bar{f}$  and  $\tilde{f}$  as for the RANS equations have been used to avoid introduction of multiple notations.
- only the Favre filtering is employed. For this reason, a simple ' is used for its notation, in order to simplify notations.

# 1 Introduction

The financial support for this thesis has been provided by the project **FortVer** [BAY] from **abayfor** [Arb] thanks to the Bavarian research ministry. The aim of the project **FortVer** was to carry out experimental investigations as well as numerical modeling of turbulent combustion in collaboration with several universities in Bavaria. Our specific goals were to compare existing LES models for inhomogeneously premixed turbulent combustion, and eventually develop a new LES combustion model.

The first section of this introduction defines the notion of *turbulence*, and describes how the turbulent combustion is used, and why it has to be used, for industrial applications. The expressions Computational Fluid Dynamics (CFD) and *Large Eddy Simulations (LES)* are also explained, in order to show how turbulent reactive flows can be simulated. Then, *lean inhomogeneously premixed combustion* and its consequences are presented. The second section details the structure of this thesis organized in three parts: Theory and modeling, presentation of the three investigated LES models, and validation on three different test-rigs.

## 1.1 Industrial background: Turbulent premixed combustion

This thesis deals with combustion modeling. It focuses on the development of new computational methods for industrial applications, rather than on amelioration of existing process and design of new products. These computational methods are commonly called *Computational Fluid Dynamics (CFD)* simulations, and aim to predict the behavior of complex (3-dimensional, unsteady, turbulent) and eventually reactive flows. Presently, so-called *Large Eddy Simulations (LES)* combustion models are investigated for turbulent reactive flows.

### 1.1.1 Turbulent reactive flows in industrial processes

Reactive flows in industrial applications (engine, turbomachines, burners, ...) are turbulent. Turbulence describes a regime where the flow is agitated by physical fluctuations (velocity, pressure, temperature). These fluctuations have a large impact on flame properties in the flow. The flame reacts to fluctuations, and its behavior and stabilization are likely to be influenced. The presence of turbulence also allows to increase the burning rate, since velocity fluctuations tend to increase the turbulent burning velocity. This is crucial for industrial applications, as the released power density proportionally scales with the burning rate. Too much turbulence intensity can also lead to instabilities or flame quenching.

The aim for industrial designers is then to use in the best way the turbulent properties of reactive flows, and to achieve the best performance with burners.

Nowadays, the notion of performance must be also understood in terms of efficiency and pollutant emissions, and not only in terms of released power. The global performance of a system is a compromise between these three main elements. The notions of “peak oil” and “depletion”<sup>1</sup> have encouraged industries to develop more efficient systems, in order to spare remaining fossil combustible. In parallel, more and more strict regulations on pollutant emissions dictate industries to develop more efficient systems delivering a given power using less combustible, and reducing formation of pollutant. For instance, one of the main challenge for automotive industry today is to reduce CO<sub>2</sub> and NO<sub>x</sub> production. This means more research for a better understanding of turbulent combustion, where both experimental investigations and numerical simulations are helpful.

### **1.1.2 CFD simulations as industrial development tools**

CFD simulations are more and more used in industrial design processes for two main reasons. First of all, apart from being in many cases cheaper to conduct than equivalent experimental studies, CFD simulations are easier to handle. It is mostly more convenient to change one parameter (inlet velocity or temperature) in a computer program, than during an experimental process. If a geometric change is required, it is still easier and faster to re-design the geometry for simulations than to have to produce it again for experiments. This relative flexibility has enabled the development of so-called automatic optimization methods.

Secondly, the ever increasing development of CPU's speed and memory capacity contributes to the generalization of CFD simulations. Simulations are becoming faster and more variables are considered in simulations. For example, computations for turbomachines were only possible stage by stage, or using axi-symmetrical simplifications. A few years ago, simulations were then executed for compressor, combustor and turbines separately. Design of turbomachine can be made now by simulating complete three-dimensional engine structures. This last step is crucial, since the different turbomachine parts interact.

### **1.1.3 Turbulence modeling: RANS and LES**

The detailed simulation of turbulent flows may remain time-consuming. The description of turbulent eddies requires dividing the computational domain into very small volumes (“computational cells”), in which equations of flow must be solved: The smaller scale of turbulence is investigated, the more cells are required. In order to resolve all these equations, the influence of turbulence has been modeled using averaged equations (Reynolds Averaged Navier-Stokes or RANS equations). The main advantage of this method is that

---

<sup>1</sup>“The term Peak Oil refers the maximum rate of the production of oil in any area under consideration, recognizing that it is a finite natural resource, subject to depletion.” (C. Campbell [Cam])

the mesh is designed according to the geometrical configuration, rather than on the turbulence properties. This enables the reduction of required cells.

Due to the increasing performance of computers, new models for turbulence have appeared. With *Large Eddy Simulation* (LES), rather than averaging the effect of turbulence, the equations are filtered. A part of the turbulent eddies (the largest) are explicitly resolved and computed, and the smallest ones are modeled as with RANS modeling. LES costs more CPU-time and memory capacities than RANS, because of finer resolved scales and meshes.

LES methods are expected to bring much better numerical predictions than RANS methods, because the effect of turbulence is considered more accurately. The largest eddies, which are explicitly computed, have more influence on the flow, and are more dependent on the geometry than the smallest one. The hypothesis of isotropy is much less problematic than with RANS modeling, since it is just applied in order to model the effect of the smallest eddies, and not the effect of the largest ones. For combustion, the passage of successive eddies, which modify the velocity distribution, and consequently the flame position, is also computed by LES. Phenomena, such as Von Karman vortex street in wake of bluff-bodies, which lead to flame intermittency and flapping can be partially resolved and thus predicted.

### 1.1.4 Inhomogeneously premixed combustion

Beside turbulence, as previously suggested, mixture fluctuations have also to be considered for industrial configurations, since obtaining a perfectly homogeneous mixture from fuel and oxidant would impose complex constraints. A better modeling of inhomogeneously premixed lean combustion is also required, since mixture inhomogeneities influence the flame stability. For illustration, mechanisms of thermo-acoustic flame instabilities are depicted in Figure 1.1 (p.4), where the gray zone delimits our zone of interest. As turbulence, mixture fluctuations must be correctly predicted, in order to evaluate correctly local and instantaneous chemical reaction rates.

Usually, three types of incompletely premixed combustion are distinguished: non-perfectly premixed, inhomogeneously premixed and partially premixed combustion. The non-perfectly premixed combustion refers to a time-averaged uniform lean mixture. The averaged mixture is locally uniform, but with temporal fluctuations. The inhomogeneously premixed combustion refers to a non-uniform lean mixture, with spatial and time fluctuations. The partially premixed combustion also refers to a non-uniform mixture, but which displays both lean and rich zones. In this thesis, the modeling of the inhomogeneously premixed lean turbulent combustion is detailed.

## 1.2 Layout of the thesis

This dissertation is divided into three parts: presentation of turbulent combustion theory and modeling, detailed description of three LES combustion models and validation of these models.

To begin with, Chapter 2 presents theoretical requirements for investigating reactive flows: Navier-Stokes, energy and species transport equations. Notion of turbulence is introduced, before describing turbulence-combustion interaction for premixed flames. Chapter 3 details modeling strategies for turbulence, as well as for turbulent combustion. Differences between RANS, LES and DNS (Direct Numerical Simulations) computations are explained. A larger part is then dedicated to LES modeling, with a review of existing LES combustion models for turbulent premixed flames.

Secondly, Chapters 4, 5, 6 and 7 respectively present the Thickened Flame (TF) model (derived by Colin et al. [CDVP00]), the progress variable approach, the Turbulent Flame speed Closure model (TFC-LES) (derived by Zimont [Zim79] for RANS, and applied for LES by Flohr and Pitsch [FP00]), and the Subgrid Flame Closure (SFC) model. These models seem to be the mostly relevant for industrial applications, due to their robustness, precision and moderate CPU-costs. The TF model is based on species transport equation and brings the advantage of being usable with different chemical mechanisms. Its main drawback is due to its model formulation based on a high order derivative operator, which makes its implementation in commercial solvers difficult, where the code source is not available. The progress variable approach, detailed in chapter 5, has the advantage to reduce the combustion modeling to a unique additional variable. This variable indicates whether the mixture is locally burnt or unburnt. For the case of the non-perfectly premixed combustion, the formulation must be adapted: A second additional variable is required and the progress variable transport equation is modified. In the chapter 6, the TFC-LES model is described. This model closure has largely been used with RANS modeling for industri-

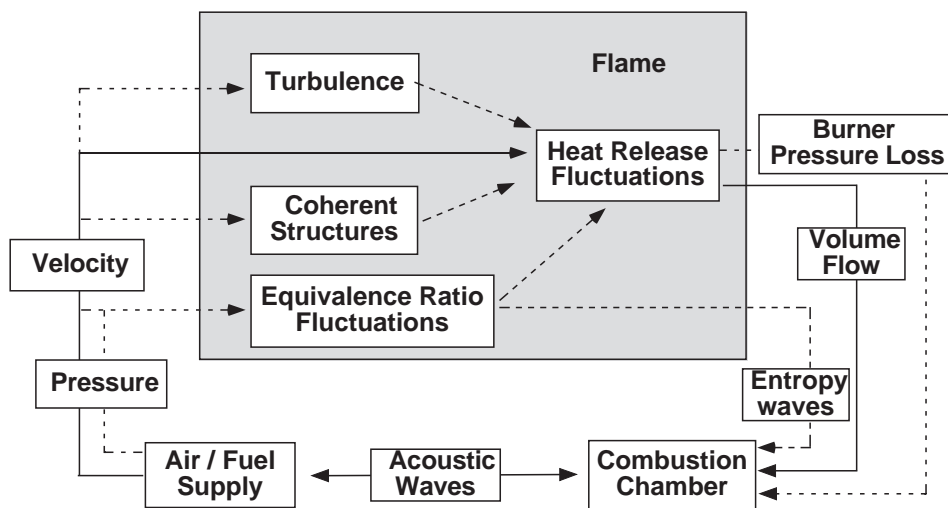


**Fig. 1.1:** Flame instabilities, according to Polifke [Pol04] (p. 3)

al applications, and it is the default model for perfectly premixed turbulent combustion with RANS modeling in *Fluent*. Up to now, the LES formulation has not yet been largely used, probably because of the non-universality of its model constant. In the chapter 7, a new model is derived. It is also based on the progress variable approach, and similar to the TFC-LES model. But, compared to the TFC-LES model, it brings the advantage of a wider range of applications, and should avoid the adaptation of a model constant.

Finally, Chapter 8, validates the three models on three different burner configurations: The Volvo test-rig, the Paul Scherrer Institut (PSI) burner, and the TD1 burner, developed at Lehrstuhl für Thermodynamik at the TU München.



## 2 Turbulence and combustion theory

The aim of this chapter is to present concepts which are intensively employed in this thesis. Turbulent combustion is described, before focusing on the specific subject *LES simulation of inhomogeneous premixed turbulent combustion*. The conservation and Navier-Stokes equations are described in the first section 2.1 (p.7). In the second section 2.2 (p.14), the concept of turbulence is presented. Combustion theory with different flame configurations and relevant variables is then described, neglecting for a while the interaction with a moving flow. The last section 2.4 (p.33) gives an overview on premixed turbulent combustion.

### 2.1 Description of reacting flows

In this thesis, a continuum one-phase gas mixture is employed. In this first section, a set of equations required to describe a reactive gas flow are presented.

#### 2.1.1 Continuity, momentum and energy transport equations

##### Mass conservation equation

In a *control volume*, the mass conservation law is valid for any fluid. It describes the local change of the density  $\rho$  because of density fluxes through the surfaces of the volume control:

$$\frac{\partial \rho}{\partial t} + \frac{\partial \rho u_i}{\partial x_i} = 0. \quad (2.1)$$

This *conservative form* of the equation corresponds to the so-called *Euler description* of the flow, based on a control volume observation. An integral result can be deduced employing Ostrogradsky's theorem. This theorem expresses the rate of change of a variable in a volume by evaluating its flux through the surrounding surface.

A second description, the so-called *Lagrange form*, consists in tracking particles or volumes of the fluid along their movement (*convective form*). Using the *particle derivation*:

$$\frac{d}{dt} = \frac{\partial}{\partial t} + u_i \frac{\partial}{\partial x_i}, \quad (2.2)$$

the conservation equation can be written:

$$\frac{d\rho}{dt} + \rho \frac{\partial u_i}{\partial x_i} = 0. \quad (2.3)$$

In this thesis the Euler description is mostly used, since it corresponds to the CFD solver description. This is also the description which is implicitly obtained from experiments: measurements are always carried out along fixed planes of the space, as stressed by Mathieu [Mat73](p. 15).

A property concerning the *compressibility* of the fluid *or* of the flow is derived from mass conservation equation. A fluid is incompressible if its density is constant. Generally, gas are considered as compressible fluids, whereas liquids can be mostly (in case of usual pressure and temperature conditions) considered as incompressible fluids. This definition is generalized for a flow. A flow is said to be incompressible if each particle of fluids has a constant density. In terms of the Lagrangian description, it reads according to Sini [Sin00](p. 59):

$$\frac{d\rho}{dt} = 0 \Rightarrow \frac{\partial u_i}{\partial x_i} = 0. \quad (2.4)$$

Consequences of this definition are more detailed with Eq. (2.13) in section 2.1.2 (p.9).

### Momentum conservation equations

Newton's second law of motion can be applied to any volume of fluid taken in its movement i.e. using the Lagrangian description as demonstrated by Piquet [Piq02](p. 6). Momentum change can be due to volume forces  $\mathbf{f}$  (typically the gravity effect), or surface forces  $\bar{\mathbf{T}}$  (typically pressure and viscosity effects):

$$\rho \frac{du_i}{dt} = \rho \left( \frac{\partial u_i}{\partial t} + u_j \frac{\partial u_i}{\partial x_j} \right) = \frac{\partial T_{ij}}{\partial x_j} + \rho f_i. \quad (2.5)$$

The tensor  $\bar{\mathbf{T}}$  groups the effect of the pressure  $p$ , which acts perpendicularly to the surface of the fluid volume, and the effect of the viscosity tensor  $\bar{\mathbf{t}}$ :

$$T_{ij} = -p\delta_{ij} + t_{ij}. \quad (2.6)$$

This equation can be written in its equivalent conservative form. Only the l.h.s. is modified and expanded with the conservation equation Eq. (2.1):

$$\rho \frac{du_i}{dt} = \frac{\partial \rho u_i}{\partial t} + \frac{\partial \rho u_i u_j}{\partial x_j}. \quad (2.7)$$

The momentum transport equation under the conservative form yields:

$$\frac{\partial \rho u_i}{\partial t} + \frac{\partial \rho u_i u_j}{\partial x_j} = -\frac{\partial p}{\partial x_i} + \frac{\partial t_{ij}}{\partial x_j} + \rho f_i, \quad \forall i \in [1, 2, 3]. \quad (2.8)$$

Compared to the convective form, the only but important difference is the presence of the density in the derivation operators. Practical consequences for the averaging procedures in CFD solvers are explained in section 3.2.1 (p.44).

### Energy and enthalpy conservation equations

A balance equation for the energy is required, since reactive flows are considered with exo/endo-thermal chemical reactions in vicinity of cooled walls. Writing the first law of Thermodynamics for the specific total energy  $e + \mathbf{u}^2/2$  and considering chemical reactions, radiation  $r$  (in this thesis the radiation is not taken into consideration:  $r = 0$  in the following) and heat fluxes  $\mathbf{q}$  through the surface of the control volume, one obtains:

$$\frac{\partial}{\partial t} \left( \rho \left( e + \frac{\mathbf{u}^2}{2} \right) \right) + \frac{\partial}{\partial x_i} \left( \rho \left( e + \frac{\mathbf{u}^2}{2} \right) u_i \right) = \frac{\partial T_{ij} u_j}{\partial x_i} + \rho g_i u_i - \frac{\partial q_i}{\partial x_i} + r. \quad (2.9)$$

The specific internal energy  $e$  has been introduced.

For industrial opened systems with mass flows, the thermodynamical system cannot be anymore described as fluid contained in a closed volume, but as fluid tracked in its movement. In such cases, the specific enthalpy  $h$  is more appropriate than the specific internal energy  $e$ :

$$h = e + p/\rho. \quad (2.10)$$

The conservation equation for the total enthalpy  $h + \mathbf{u}^2/2$  is expressed by replacing  $e$  by  $(h - p/\rho)$  in Eq. (2.9). In the l.h.s. two new terms  $-\frac{\partial p}{\partial t}$  and  $-u_i p_{,i}$  appear. In the r.h.s. the pressure part of the viscous term can be expanded:

$$\frac{\partial T_{ij} u_j}{\partial x_i} = -u_i \frac{\partial p}{\partial x_i} - p \frac{\partial u_i}{\partial x_i} + \frac{\partial t_{ij} u_j}{\partial x_i}. \quad (2.11)$$

The first term  $p_{,i} u_i$  cancels, and the second term  $p u_{i,i}$  cancels for incompressible flows. For generality, it is kept in the following total enthalpy conservation equation:

$$\frac{\partial}{\partial t} \left( \rho \left( h + \frac{\mathbf{u}^2}{2} \right) \right) + \frac{\partial}{\partial x_i} \left( \rho \left( h + \frac{\mathbf{u}^2}{2} \right) u_i \right) = \frac{\partial p}{\partial t} - p \frac{\partial u_i}{\partial x_i} + \frac{\partial T_{ij} u_j}{\partial x_i} + \rho g_i u_i - \frac{\partial q_i}{\partial x_i} + r. \quad (2.12)$$

Compared to the energy equation, the enthalpy equation differs by the explicit action of the pressure in terms of rate of change  $\frac{\partial p}{\partial t}$  and compressibility force  $p \vec{\nabla} \cdot \mathbf{u} = p u_{i,i}$ .

#### 2.1.2 Need for additional laws

Extra conditions are required to close and resolve the system, since there are 12 unknowns ( $\rho, \mathbf{u}, p, e, T_{ij}$ ) for 5 equations. The condition of pressure ( $p \approx p^0$ ) and temperature ( $T \in [270 - 2500]$  K) considered for this work makes the approximation of the *ideal gas law* possible:

$$p = \rho RT. \quad (2.13)$$

$R = \mathcal{R}/M$  ( $R \approx 287$  [J/(kg K)] for air at atmospheric conditions) is the gas constant, ratio of the universal molar gas constant  $\mathcal{R} = 8.314$  [J/(mol K)] with the gas molar mass  $M$  [kg/mol]. For an incompressible flow, the variation of density is not depending on the pressure, so that a constant pressure  $p = p_0$  can be considered. In this work, the density is thus

changing only because of the temperature, what is sometimes named *semi-compressible* flow. Adding this equation to the current system, the lack of equations is obviously due to the six unknown terms of the strain tensor  $t_{ij}$ , which symmetry can be demonstrated by deriving the momentum equations as mentioned by Piquet [Piq02](p. 8). Six additional laws between the fluid deformation and its viscous constraint have to be introduced. Newton introduced such a law based on a linear and isotropic response of the fluid to the constraints:

$$t_{ij} = \lambda \frac{\partial u_i}{\partial x_i} + 2\mu D_{ij}. \quad (2.14)$$

This law is employed in the following, since it is perfectly adapted to characterize mixture of hydrocarbons (methane, propane) with air. It should be inadequate for flows which viscosity depends on history effects, on distant action or for non-isotrop fluid (e.g. fluids with fibers), as stressed by Piquet [Piq99](p. 9). The tensor  $D_{ij}$  is defined as the symmetric part of the velocity gradient tensor:

$$D_{ij} \equiv \frac{1}{2} \left( \frac{\partial u_i}{\partial x_j} + \frac{\partial u_j}{\partial x_i} \right). \quad (2.15)$$

Its diagonal elements  $D_{11}, D_{22}, D_{33}$  are interpreted as stretching rates in the direction  $x$ ,  $y$  and  $z$ . Its non-diagonal elements  $D_{ij}$ ,  $i \neq j$  are interpreted as strain rate in the normal directions  $i$  and  $j$ . Its trace  $D_{ii} = D_{11} + D_{22} + D_{33} = \vec{\nabla} \cdot \mathbf{u}$  is the volume dilatation rate of a fluid element. The two *phenomenological coefficients*  $\lambda$  and  $\mu$  are named as Lamé dynamic viscous coefficients, and as illustrated by Piquet [Piq99](p. 10) should fulfill the two relations:

$$3K = 3\lambda + 2\mu \geq 0, \quad (2.16)$$

$$\mu \geq 0. \quad (2.17)$$

In the following, the Stokes condition is used (see Chassaing [Cha00](p. 115-117)), which imposes:

$$K = 0, \quad (2.18)$$

$$\text{and therefore: } \lambda = -\frac{2}{3}\mu. \quad (2.19)$$

It implies that a uniform compression in all directions does not act as an irreversible phenomenon but as a pressure force.

### 2.1.3 Mixture and thermo-chemistry description

Balance equations for one gas have been presented. Since this work aims at describing the combustion process in gaseous phase, the equations describing a gas mixture are explained in this section.

### Mass and molar fractions

The first requirement to characterize a mixture is to evaluate its composition i.e. the quantity of each species contained in this mixture. The *mass fraction*  $y_k$  is defined as the ratio of the mass of the species  $m_k$  to the mixture mass  $m = \rho d\nu$  in the control volume  $d\nu$  with its local mixture density  $\rho$ :

$$y_k \equiv \frac{m_k}{m}. \quad (2.20)$$

$y_k$  is a local dimensionless quantity and can be evaluated for any control volume  $d\nu$ . Its main property is that the sum of the mass fractions in the mixture always equals one:

$$\sum_{k=1}^n y_k = \sum_{k=1}^n \frac{m_k}{m} = 1. \quad (2.21)$$

The same type of quantification based on the mole numbers is also often used. The *molar concentration*  $C_k$  must be first defined:

$$C_k \equiv \frac{n_k}{d\nu}, \quad (2.22)$$

where  $n_k$  is the number of moles of the species  $i$ , and  $C_k$  has the dimension [mol/m<sup>3</sup>]. The total number of moles  $n$  in the control volume is:

$$n = \sum_{k=1}^n n_k, \text{ so that: } C = \frac{n}{d\nu} = \sum_{k=1}^n C_k. \quad (2.23)$$

Beside the mass fraction, a dimensionless *molar fraction*  $X_k$  is defined using the concentration:

$$X_k \equiv \frac{C_k}{C}. \quad (2.24)$$

It also fulfills the normalization property:

$$\sum_{k=1}^n X_k = \sum_{k=1}^n \frac{C_k}{C} = 1. \quad (2.25)$$

The mass fraction  $y_k$  is mostly used in this thesis, but useful relations are derived to convert mass fraction into molar fraction and into concentration. The concentration is namely required to evaluate the Arrhenius reaction rates in section A.2 (p.206). For this topic it is useful to define the *partial density*  $\rho_k = y_k \rho$ . This quantity refers to the relative density of the species  $i$  in the mixture, and is simply given as:

$$\rho_k = M_k C_k. \quad (2.26)$$

$M_k$  is the species molar mass [kg/mole], so that with  $m = \rho d\nu$ , the mixture mass in the control volume  $d\nu$ , one obtains:

$$y_k = \frac{\rho_k}{\rho} = \frac{M_k C_k}{\rho} \quad (2.27)$$

$$\text{and } y_k = \frac{M_k X_k}{m}. \quad (2.28)$$

### Species mass conservation

The aim of thermo-chemistry consists in describing:

- How the flow changes with combustion
- How the different species react or move within the flow.

Species behavior at each position and time in the flow can be estimated by solving a transport equation for the species mass fractions. The transport equation for a mass fraction is similar to the previous balance equations. The l.h.s. describes how the quantity is changing in the control volume, while the r.h.s. describes the reasons for this change (diffusion, source term, ...), as illustrated by Couombeau [Cou99]. Nevertheless each species moves in the flow with its own velocity  $\mathbf{v}_k$  which can be different from the flow velocity  $\mathbf{u}$ . So that each species is drifting or diffusing comparing to the flow with the so-called *diffusion velocity*:

$$\mathbf{u}_k = \mathbf{v}_k - \mathbf{u}. \quad (2.29)$$

A conservation equation for the mass of each species is valid using its own velocity components  $v_{k_i}$  and defining a source term  $w_k$  [kg/(m<sup>3</sup> s)]:

$$\frac{\partial \rho y_k}{\partial t} + \frac{\partial \rho y_k v_{k_i}}{\partial x_i} = w_k. \quad (2.30)$$

The evaluation of the source term  $w_k$  is the main problem in this work. It will be studied, detailed and modeled in the next chapters. Within this chapter, the focus is placed on the other terms. In order to write the species mass fraction conservation equation in a very similar way to the previous balance equations, the l.h.s. is written with the flow velocity  $\mathbf{u}$ :

$$\frac{\partial \rho y_k}{\partial t} + \frac{\partial \rho y_k u_i}{\partial x_i} = - \frac{\partial \rho y_k u_{k_i}}{\partial x_i} + w_k. \quad (2.31)$$

Fick's law (similar to Fourier's law for energy) is an empirical law which evaluates the diffusion flux  $\mathbf{j}_k$ . Its isotropy hypothesis makes concentration gradients the only cause for diffusion fluxes:

$$\mathbf{j}_k \equiv \rho y_k \mathbf{u}_k = -\rho D_{kl} \vec{\nabla} y_k. \quad (2.32)$$

The diffusion coefficient  $D_{kl}$  [m<sup>2</sup>/s] is normally defined for a *binary mixture*. In a mixture all the binary diffusions should be taken into consideration. This is very complex in terms of formalism and computation effort. The mixtures considered in this work always contain a large and constant mass quantity of non-reactive nitrogen N<sub>2</sub> ( $y_{N_2} \approx 0.73$  in air). This gas is thus considered as a solvent for the mixture, so that only the binary diffusion in nitrogen N<sub>2</sub> is considered:

$$D_k \equiv D_{kl} \approx D_{kN_2}. \quad (2.33)$$

The species mass fraction conservation equations are often written introducing the Schmidt number  $Sc_k = \nu/D_k$ , which characterizes the diffusion of the species  $k$  compared

to the kinematic diffusion  $\nu$ . The Schmidt number is considered as constant in the given range of temperature:

$$\frac{\partial \rho y_k}{\partial t} + \frac{\partial \rho y_k u_i}{\partial x_i} = \frac{\partial}{\partial x_i} \left( \rho \frac{\nu}{Sc_k} \frac{\partial y_k}{\partial x_i} \right) + w_k. \quad (2.34)$$

### Mixture properties

The use of mass fractions is relevant and convenient to express the extensive variables as the weighted sum of the specific values. As example the specific enthalpy of the mixture reads:

$$h(T) = \sum_i y_i h_i(T). \quad (2.35)$$

The specific calorific coefficient of the mixture  $c_p$  is similarly defined:

$$c_p(T) = \sum_i y_i c_{p_i}(T), \quad (2.36)$$

and makes the evaluation of the temperature from the enthalpy possible, according to the relation:

$$dh = c_p dT. \quad (2.37)$$

In the following, the value of the calorific coefficient  $c_p(T)$  has been simplified to the temperature dependence. The mixture is namely only changing with the combustion. Lean premixed combustion of methane or propane have been studied, for which the mass fraction of nitrogen is always the largest:  $y_{N_2} \approx 0.73$ . Consequently, the influence of species mass fraction changes on the coefficient is negligible compared to the temperature influence. Coefficients for the different species  $k$  have been taken from the *Fluent*-database based on the NIST coefficients [FLU05, Nat]. They are given separately for ranges [300–1000] and [1000–5000] K, so that they have been extrapolated with the same order polynomial in the range of interest [300–2400] K:

$$c_{p,k}(T) = a_{0,k} + a_{1,k}T + a_{2,k}T^2 + a_{3,k}T^3 + a_{4,k}T^4. \quad (2.38)$$

These last coefficients have been used during this thesis, and are listed in Table 2.1 (p.14). For each fuel mixture, with methane and propane, a polynomial function describing the specific heat of the mixture has been defined, and evaluated as function of the temperature. For a given equivalence ratio, the maximum discrepancy for the mixture coefficient  $c_p$  does not exceed 3% between a burnt and an unburnt mixture. The discrepancy between two lean mixtures,  $\phi = 0.5$  and  $\phi = 0.8$  for example, is also small. The values for the methane- and propane-mixtures, given in Table 2.1 (p.14), are calculated respectively with the equivalence ratio  $\phi = 0.6$  and  $\phi = 0.65$ .

Some other variables may also depend on the mixture composition. Typically, the gas constant  $R$ , introduced in the perfect gas law  $p = \rho RT$ , depends on the composition through the molar mass  $M$ , but its dependence is mostly neglected:

$$R \equiv \frac{\mathcal{R}}{M} = \mathcal{R} \sum_i \frac{1}{y_i M_i}. \quad (2.39)$$

gas	$a_0$	$a_1$	$a_2$	$a_3$	$a_4$
CH <sub>4</sub>	9.588716 10 <sup>2</sup>	4.165085	-1.653264 10 <sup>-4</sup>	-6.673179 10 <sup>-7</sup>	1.617894 10 <sup>-10</sup>
C <sub>3</sub> H <sub>8</sub>	-2.204357 10 <sup>2</sup>	7.579325	-4.759486 10 <sup>-3</sup>	1.546867 10 <sup>-6</sup>	-2.021633 10 <sup>-10</sup>
O <sub>2</sub>	7.7522549 10 <sup>2</sup>	5.326955 10 <sup>-1</sup>	-2.894624 10 <sup>-4</sup>	7.429044 10 <sup>-8</sup>	-6.106591 10 <sup>-12</sup>
N <sub>2</sub>	1.038146 10 <sup>3</sup>	-1.349672 10 <sup>-1</sup>	4.879364 10 <sup>-4</sup>	-2.762596 10 <sup>-7</sup>	4.830123 10 <sup>-11</sup>
H <sub>2</sub> O	1.831966 10 <sup>3</sup>	-1.823495 10 <sup>-01</sup>	1.120206 10 <sup>-03</sup>	-5.680589 10 <sup>-07</sup>	8.967130 10 <sup>-11</sup>
CO <sub>2</sub>	4.726495 10 <sup>2</sup>	1.563518	-1.163937 10 <sup>-03</sup>	4.218476 10 <sup>-07</sup>	-5.906816 10 <sup>-11</sup>
mixture CH <sub>4</sub>	9.762794 10 <sup>2</sup>	1.565244 10 <sup>-1</sup>	2.912254 10 <sup>-4</sup>	-2.100258 10 <sup>-7</sup>	3.975093 10 <sup>-11</sup>
mixture C <sub>3</sub> H <sub>8</sub>	9.288992 10 <sup>2</sup>	3.235492 10 <sup>-1</sup>	1.037387 10 <sup>-4</sup>	-1.247782 10 <sup>-7</sup>	2.609245 10 <sup>-11</sup>

**Tab. 2.1:** Calorific coefficients  $c_p(T)$  [J/(kg K)]

## 2.2 Turbulence theory

In this part, the phenomenon of turbulence is presented with its manifestations and consequences. Mathematical notions and representations of turbulence, which are required for the next chapters are detailed. Its modeling within CFD software is described in the next chapter.

### 2.2.1 Phenomenology

Simplest occurrence of turbulence is water flowing from a stop cock. When the water is flowing slowly, the water displays a regular and constant tube. When the water flow overcomes a certain mass flow rate, the flow is becoming irregular and fluctuating: the flow is turbulent. This phenomenon can be experimentally investigated by injecting some colorant in a water flow with different inlet velocities. Exceeding a certain inlet velocity, the colorant flow is turbulent and diffuses rapidly in the water, as depicted Figure 2.1 (p.15).

#### Fluctuation scales

The occurrence of turbulence is simple to recognize, but a precise and absolute definition of turbulence is difficult to formulate. Turbulence describes the nature of a flow which velocity field (and other relevant variable) is changing in a complex way both in time and space, because a continuous repartition of fluctuation scales is involved. In Figure 2.2 (p.15), two photographs of a similar flow structure are depicted. On the left, the gas flow structure generated by a nuclear bomb explosion can be seen. On the right, the flow generated by a water drop falling on a stagnant surface is depicted (rotated figure). The macro-structure are the same, but only the nuclear explosion exhibits a continuous range of structures from small up to large scales. The nuclear explosion is of turbulent nature, while the water drop generates a complex but laminar flow structure. An analogy may be given by the comparison of two complex acoustic signals, one representing white noise (containing all the frequencies of the spectrum) and a second one appearing very *noisy*, but composed only of discrete frequencies.

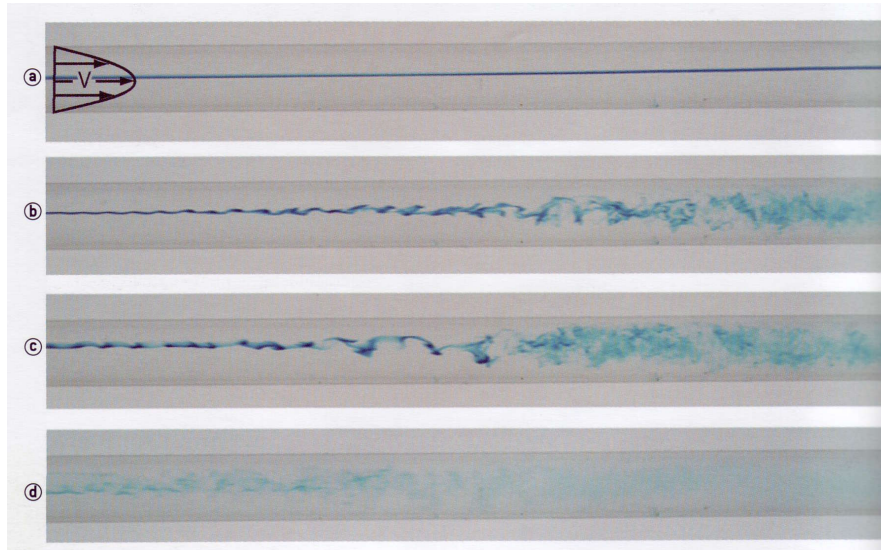


**Fig. 2.1:** Turbulence in a canal, with courtesy of O. Cadot (illustration found in Guyon and al. [GHP05](p. 10))

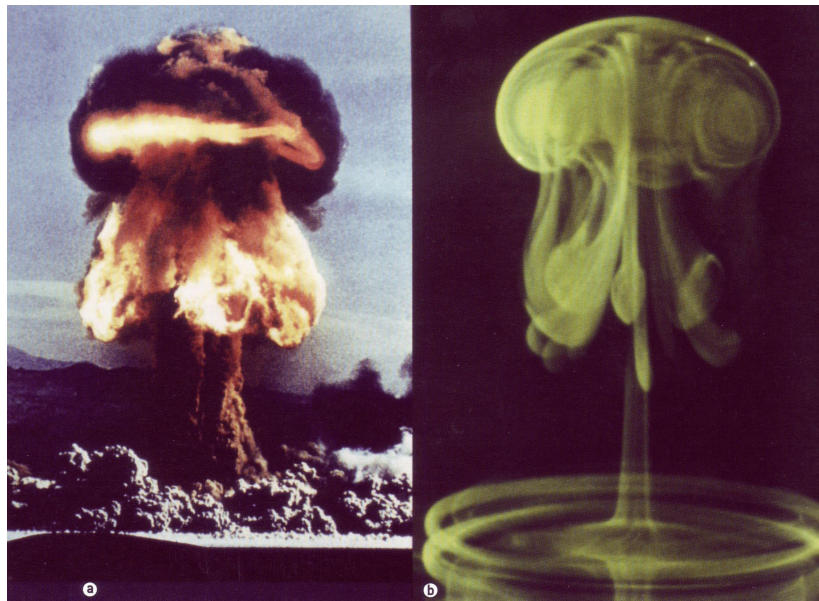


**Fig. 2.2:** Turbulent and complex laminar flow structures, original comparison by L.W. Sigurdson [Sig97, PS94] (illustration found in Guyon and al. [GHP05](p. 94))

### Vorticity

A fundamental property of turbulent flows is their non-vanishing vorticity, defined by:

$$\mathbf{w} \equiv \vec{\nabla} \times \mathbf{u}, \quad (2.40)$$

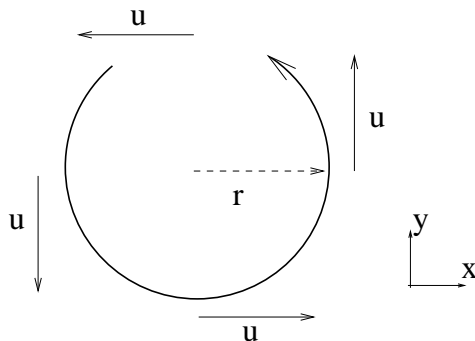


**Fig. 2.3:** Eddy vorticity

as explained for instance by Friedrich [Fri04]. The transport equation for the vorticity can be derived applying the rotational operator to the Navier-Stokes equations Eq. (2.8) and using the assumption of incompressibility:

$$\frac{\partial w_i}{\partial t} + u_j \frac{\partial w_i}{\partial x_j} = w_j \frac{\partial u_i}{\partial x_j} + \nu \frac{\partial^2 w_i}{\partial^2 x_j}, \quad \forall i \in [1,3]. \quad (2.41)$$

The pressure gradient is eliminated by applying the rotational operator. The density has no more explicit influence on this equation, except that the dynamic viscosity is replaced by the kinematic viscosity  $\nu = \mu/\rho$ .

The velocity and vorticity are very dependent: A non-linear term  $(\mathbf{w} \cdot \vec{\nabla})\mathbf{u} = w_j u_{i,j}$  equivalent to a source term appears in the r.h.s. of the equation. This term is responsible for the interaction between the vorticity and the velocity gradient and is crucial for turbulence. If the flow is two-dimensional in a plane  $(\vec{x}, \vec{y})$ , only  $w_3$  can be non zero but  $u_{1,3} = u_{2,3} = 0$ , so that the source term for the vorticity requires a *three-dimensional flow structure* to act. Therefore, a turbulent flow can only be three-dimensional, and exhibits a complex vorticity field because of the non-linear source term  $(\mathbf{w} \cdot \vec{\nabla})\mathbf{u}$ , which is scale-dependent.

The vorticity stresses also the presence of eddies, and particularly of the smallest. Considering an eddy of size  $r$  and velocity  $u(r)$ , its vorticity reads (see Figure 2.3 (p.16)):

$$\omega(r) \approx 2 \frac{u(r)}{r}. \quad (2.42)$$

This expression suggests that the eddy size has an important influence. This can be demonstrated anticipating the two main properties of the turbulence spectrum theory by Kolmogorov [Kol41, Kol62], and presented Eq. (2.51). The turbulent dissipation is constant in the inertial range:

$$\varepsilon \sim \frac{u'(r)^3}{r} \sim u'(r)^2 \omega(r) = \text{constant}.$$

The turbulent kinetic energy  $u'(r)^2$  scales with  $r^{5/3}$  in the inertial range, it implies that the vorticity of eddies scales according to:

$$\omega(r) \sim r^{-5/3}. \quad (2.43)$$

The vorticity is thus larger for the smallest turbulent eddies. The smallest eddies generate a larger velocity gradient than the large eddies, as the vorticity is based on the velocity gradient.

### 2.2.2 Effect on the flow - Reynolds number

The Reynolds number  $Re$  is the indicator of the turbulent nature of the flow. Considering a cylinder of diameter  $D$  placed in a fluid of kinematic viscosity  $\nu$  with the velocity  $U$ , it is possible to express two characteristic times:

- The convection time  $t_{conv} \sim D/U$ , which evaluates the time needed for a particle to be transported from one side of the cylinder to the other
- The diffusion time  $t_{diff} \sim D^2/\nu$ , which evaluates the time needed for the diffusion process.

The ratio of these two scales is the Reynolds number [Rey83]:

$$Re = \frac{t_{diff}}{t_{conv}} \sim \frac{DU}{\nu}. \quad (2.44)$$

It informs for a flow which phenomenon between diffusion and convection is dominant.

Historically, Reynolds [Rey83] pointed out the importance of this dimensionless number considering the water flow around a cylinder. He related the force applied to the cylinder as a function of the flow velocity. He discovered that for larger velocities, the force does not scale anymore linearly with the flow velocity because of turbulence.

The definition has been extended to the turbulent Reynolds number  $Re_t$ , which compares the convection due to the turbulent eddies to the diffusion, as detailed in section 2.4.2 (p.34).

### 2.2.3 Mathematical representation - Kolmogorov Spectra

A turbulent flow has the particularity to display chaotic fluctuations around mean values. The local and instantaneous value of a variable is written as the superposition of the mean value with the fluctuating value (component of the velocity field for example):

$$u_i(\vec{x}, t) = \overline{u_i}(\vec{x}) + u'_i(\vec{x}, t), \quad (2.45)$$

$$\overline{u'_i}(\vec{x}, t) = 0. \quad (2.46)$$

The mean velocity  $\overline{u_i}(\vec{x})$  depends on the position only, and the fluctuations mean value cancels out.

Although the fluctuations mean value is zero, they are of much importance for the flow since the Navier-Stokes equations contain non-linear terms  $u_i u_j$  in Eq. (2.8), which fluctuating part is non zero:

$$\overline{u'_i u'_j} \neq 0. \quad (2.47)$$

This is actually the main difficulty for modeling, and is derived in section 3.2.1 (p.44) The mean value of the square of the velocity fluctuations is named the *turbulent kinetic energy*:

$$k \equiv \frac{1}{2} \overline{u'_i u'_i} = \frac{1}{2} \left( \overline{u'^2_x} + \overline{u'^2_y} + \overline{u'^2_z} \right). \quad (2.48)$$

From the turbulent kinetic energy, a mean fluctuation  $u'$  in terms of velocity fluctuation is also defined, as well as a so-called *turbulence intensity* TI, which compares the velocity of the mean flow to the velocity perturbations:

$$u' \equiv \sqrt{\frac{2}{3} k}, \quad (2.49)$$

$$\text{TI} \equiv \frac{u'}{|\bar{\mathbf{u}}|}. \quad (2.50)$$

Going further in the statistical description of turbulent fluctuations, Kolmogorov has depicted the turbulent kinetic energy in terms of an energy spectrum based on the eddy length scale, as reported by Batchelor, and Tennekes and Lumley [Bat53, TL87]. Since a turbulent flow is a superposition of various size eddies, Kolmogorov has evaluated the energy  $E(\kappa)$  for each eddy size class. While  $k$  is the whole turbulent kinetic energy,  $E(\kappa)$  states for the spectral density energy [ $\text{m}^3/\text{s}^2$ ] at the wave number  $\kappa = \pi/r$  [ $1/\text{m}$ ], where  $r$  is the size of an eddy.

Under the hypothesis of homogeneous and isotropic turbulence, and assuming that the rate of production and dissipation of the turbulent kinetic energy are in balance, Kolmogorov [Kol41, Kol62] has demonstrated that turbulence follows an *energy cascade* from the largest to the smallest eddies. This result has been supported by numerous experimental results. What is particularly interesting in terms of statistic and of Fourier's transforms is that the spectrum is a continuous function of the eddy length scale rather than a finite superposition of discrete values, as shown in section 2.2.1 (p.14). Therefore, the effect of turbulence cannot be reduced to the effect of one eddy size, but must be always considered in terms of an energy spectrum. Four length scales are nevertheless very convenient to characterize the spectrum. They are presented in the following. The turbulent energy spectrum display three domains according to Pope [Pop00](p. 231), and Tennekes and Lumley [TL87](p. 262-267) from the left to the right in Figure 2.4 (p.19):

- The *large-scale spectrum* contains the small wave number eddies which assure the transfer of energy from the mean flow to turbulence. This domain of the turbulence spectrum is dominated by the mean flow characteristics like the mean strain rate, and therefore depending on the geometry.
- The *inertial range* or *equilibrium range* is the most important domain of the spectrum, and valid for large Reynolds number. The turbulent kinetic energy is transferred

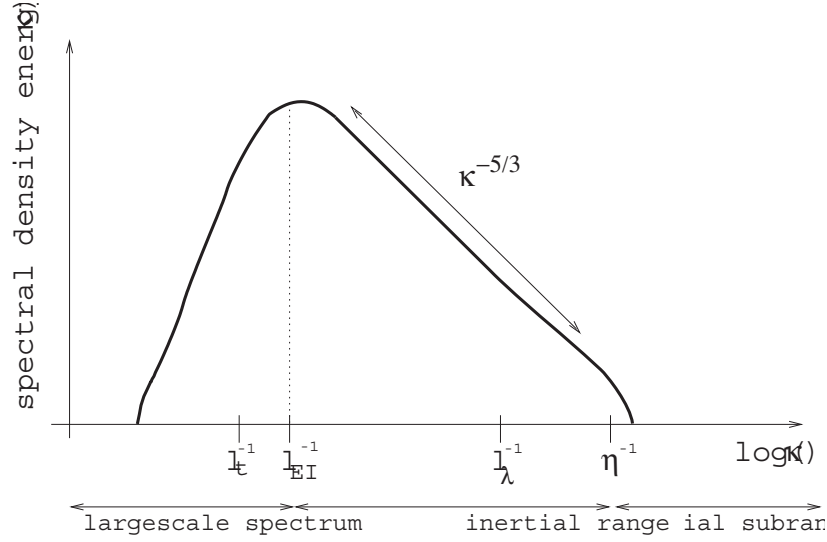


**Fig. 2.4:** Energy cascade

from the largest  $l_t$  to the smallest  $\eta$  length scales. The energy transfer scales with the *dissipation rate*, expressed with the eddy velocity  $u(r)$  and length  $r$  scales:

$$\varepsilon \sim \frac{u(r)^3}{r} \sim \frac{u(\eta)^3}{\eta}, \quad (2.51)$$

which is constant in this domain, leading to:

$$E(\kappa) \sim C\kappa^{-5/3}\varepsilon^{2/3}. \quad (2.52)$$

- The *inertial subrange* or *dissipation range* corresponds to the domain where the turbulent kinetic energy is transferred to the mean flow by viscous effects.

The separation of these domains points out two important length scales, and two other typical length scales for the spectrum:

- The *inertial length scale*  $l_{EI}$  for which the turbulent energy is maximum and which delimits the large-scale spectrum from the inertial range.
- The *Kolmogorov length scale*  $\eta$  defines the smallest eddies, and delimits the inertial range from the inertial subrange. The Reynolds number based on this scale

$$\text{Re}_\eta = \frac{u(\eta)\eta}{\nu} = 1 \quad (2.53)$$

shows that turbulent diffusion and molecular dissipation are of the same order at this scale.

- The so-called *integral length scale*  $l_t$  defined as the mean size weighted by the energy of the eddies:

$$l_t \equiv \frac{\int_0^\infty \frac{1}{\kappa} E(\kappa) d\kappa}{\int_0^\infty E(\kappa) d\kappa} \quad (2.54)$$

and which corresponds about to  $l_{EI} \approx 1/6 l_t$  (see again Pope [Pop00] (p. 187 and 231)). This scale is the most relevant scale for turbulence, and actually for LES modeling. The Reynolds number based on this scale:

$$\text{Re}_t = \frac{u' l_t}{\nu} \quad (2.55)$$

is mostly employed, since it measures the ratio between the diffusion due to turbulence to molecular diffusion.

- The *Taylor length scale* [Tay35] [Sie06] (p. 10 and 12) defined as:

$$l_\lambda \equiv \sqrt{\frac{u'}{\frac{\partial u}{\partial x}}}, \quad (2.56)$$

which physical signification is not obvious. It has the advantage of relating the turbulence velocity to the mean strain rate. The Taylor scale  $l_\lambda$  is in the range delimited by the Kolmogorov scale  $\eta$  and the integral length  $l_t$ . It scales with the latter according to the turbulent Reynolds number:

$$l_\lambda = \text{Re}_t^{-1/2} l_t. \quad (2.57)$$

## 2.3 Combustion theory

This part presents the notion of premixed flames and of diffusion flames, before detailing the characteristics of laminar premixed flames. The last section 2.3.4 (p.29) focuses on the effect of strain on laminar premixed flame. This effect is of high importance for the development of models for the turbulent combustion in section 7.4 (p.114).

### 2.3.1 Premixed and diffusion flames

#### Definitions

There are two flame configurations independent of whether the flow is turbulent or not: *Premixed flames* and *diffusion flames*. The distinction between these two types lays on whether the fuel and the oxidant are mixed before combustion occurs, as illustrated in Figure 2.5 (p.21). If fuel and oxidizer are injected from two different ducts and burning together by mixing, they form a diffusion flame. The process of mixing is mainly controlling the flame position, i.e. the spatial distribution of heat release. The fuel must be brought in the reaction zone fast enough to maintain the flame burning. If on the contrary, fuel and oxidant are premixed in a chamber or vessel before being ignited, a premixed flame is then displayed. The chemical aspect is dominant. The type of combustion is essentially imposed by the geometry of the burner.

Each of them presents advantages, so that in industrial applications, both are employed. They are sometimes used simultaneously to combine their respective advantages. For



the system. This phenomenon called *flashback* is a major disadvantage of premixed flames. One should naturally not conclude that a diffusion flame is not dangerous. For example the accident of Concorde in July 2000 was due to the formation of a diffusion flame in the wake of the plane as illustrated by Veynante et al. [VLED02].

The main disadvantage is that the burning efficiency is controlled and eventually reduced by the species mixing, as showed by Poinso and Veynante [PV01](p. 89). The speed of chemical reactions can be slowed down, because mixing does not bring fast enough the reactants into the reaction zone.

Premixed flames profit from these advantages:

- Combustion can be more efficient than for diffusion flames. The flame velocity scales with the thermal diffusion  $S_l \sim a/t_c$ . It does not depend *directly* on species mixing, since premixing has been first achieved. The flame velocity can be increased with the thermal diffusion  $a$  by increasing the unburnt temperature. The control of the flame speed is thus simpler with premixed flames than with diffusion flames.
- The flame temperature is directly controlled by the stoichiometry of the mixture. By this way, the production of  $\text{NO}_x$  can be controlled, since it largely depends on the flame temperature. The maximum diffusion flame temperature cannot be easily controlled, since the mixture is not controlled. This point is naturally quite important considering the newest regulations which aim to develop burners with lower pollutant emissions. This is the main reason for the more frequently use of premixed flames. One should nevertheless take care of flashback (as explained above), interaction flame-flow dynamics (thermo-acoustic) and sensibility to mixture variations (in particular for lean mixture, for which small variations have large effect on flame properties).

### Takeño flame index

In industrial burners, the combustor geometry may be designed, so that both flame configurations cohabit: Diffusion flame together with premixed flame. Going back to the example of the Bunsen burner in Figure 2.6 (p.21), a position of the air baffle delivering both premixed flame and diffusion flame may be simply selected.

The *Takeño index* [YST96] has been introduced to evaluate whether the combustion *locally* occurs with the premixed flame configuration or with the diffusion flame configuration:

$$G_{FO} \equiv \nabla y_F \cdot \nabla y_O. \quad (2.58)$$

For premixed flames, this index is positive since fuel and oxygen are consumed along the same spatial direction. Their mass fraction are maximum in the unburnt gas and minimal in the burnt gas. For diffusion flames, the fuel is mixing with the air, and the flame delimits the two regions. In this case gradients of mass fraction of fuel and oxygen are of opposite

sign (see Figure 2.5 (p.21)). The index is negative for a diffusion flame. The definition of the Takeno flame index has been extended to a normalized flame index:

$$\xi_p = \frac{1}{2} \left( 1 + \frac{G_{FO}}{|G_{FO}|} \right). \quad (2.59)$$

Such an index is convenient for modeling. One can simply weight the use or influence of a model for the premixed flame configuration or for the diffusion flame configuration. This index has been employed for numerical simulations of such burner configurations by Mizobuchi et al. [MTS<sup>+</sup>02], Domingo et al. [DVB02]<sub>(p. 535)</sub> [DVR05]<sub>(p. 178)</sub>, and Vervisch [Ver04]<sub>(p. 25-26)</sub>.

In this work the focus is placed on the premixed flame configuration, so that the use of this index is not required.

### 2.3.2 Non-perfectly, inhomogeneously and partially premixed combustion

#### Definitions

Considering the premixed flame regime, different cases of perturbations or discrepancies compared to the perfect premixed case may occur. Air and fuel must be mixed before burning. This operation of mixing is likely to be *incompletely* achieved, because of industrial production imperatives. In this case, the mixture equivalence ratio (normalized air-fuel ratio AFR), which entered the burner fluctuates in time and space around the mean value:

$$\phi(x, t) = \bar{\phi}(x) + \phi'(x, t). \quad (2.60)$$

Three cases for premixed flames are distinguished with respect to the mean value:

- *Non-perfectly (or imperfectly) premixed combustion:*  $\bar{\phi}(x) = \text{const}$  and  $\phi'(x, t) \neq 0$ .  
In this case the gas mixture is homogeneous in space, with a uniform spatial mean value, but time fluctuations occur.
- *Inhomogeneously premixed combustion:*  $\bar{\phi}(x) \neq \text{const}$  with  $\bar{\phi}(x) \leq 1$ , and possibly  $\phi'(x, t) \neq 0$ .  
In this case the gas mixture is not homogeneous in space: The spatial mean value is not uniform, and time fluctuations can also occur. The mean mixture is stoichiometric or lean, which prevents diffusion flame configuration from occurring.
- *Partially premixed combustion:*  $\bar{\phi}(x) \neq \text{const}$ , and possibly  $\phi'(x, t) \neq 0$ .  
In this case the gas mixture is like previously inhomogeneous in space. It also displays zone with rich mixture ( $\bar{\phi}(x) > 1$ ), which locally leads to formation of diffusion flame. This occurs for lean mixture burners with a rich pilot flame, which the injection is achieved with a larger fuel-air ratio than unity. For this type of flame, the Takeno index is required to distinguish the zone with premixed and diffusion flames.

In this work, three burners have been used for the validation detailed in section 8 (p.139). Two of them display a perfectly premixed flame. The third one is constituted by a lean mixture burner with an opened combustion chamber. Fresh air with  $\phi = 0$  is aspired from outside, so that the flame is inhomogeneously premixed. The partially premixed combustion is not considered in the following.

The main consequence of the inhomogeneity is that the laminar flame speed, which depends on the local AFR, is no more uniform in the burner, and naturally influences the combustion process. Discussion on the consequences for the modeling are precisely exposed in section 5.2 (p.71).

### Mixture fraction and local equivalence ratio

A variable must be introduced to describe the local value of the equivalence ratio. For the modeling of diffusion flames, a mixture fraction  $Z$  can be defined by:

$$Z \equiv y_f - \frac{y_{O_2}}{s} \quad (2.61)$$

where  $s$  describes the mass of oxygen required to burn the mass of fuel with stoichiometric conditions ( $s_{CH_4} = 4.00$  and  $s_{C_3H_8} = 3.63$ ). This scalar is passive, since its source term is zero. This property can be demonstrated by writing its transport equation as a linear function of the fuel and oxidant transport equation. Finally, this scalar describes the local mixture between the stream of oxidant and the stream of fuel.

In this work, this original definition is less practical, since premixed combustion is considered. Actually, the local equivalence ratio or the quantity of fuel in the mixture must be known. Rather than transporting the local equivalence ratio  $\phi$ , the mass fraction of fuel *independently of the reaction* is directly transported:

$$\frac{\partial \rho Z}{\partial t} + \frac{\partial \rho Z u_i}{\partial x_i} = \frac{\partial}{\partial x_i} \left( \rho \frac{\nu}{Sc_Z} \frac{\partial Z}{\partial x_i} \right). \quad (2.62)$$

By this way, this mixture fraction  $Z$  stands for the local mass fraction of fuel *without considering the reaction*. It belongs to the range  $[0; y_f^0]$ , where  $y_f^0$  is the maximum fuel mass fraction at the inlet.

A simple relation links it to the local equivalence ratio  $\phi$ :

$$Z = \frac{1}{1 + \frac{s}{\phi} \left( 1 + 3.76 \frac{M_{N_2}}{M_{O_2}} \right)} \approx \frac{1}{1 + 18.16 \frac{s}{\phi}}. \quad (2.63)$$

### 2.3.3 Laminar premixed flames

The main property of premixed flames is its flame front, which propagates (or may stagnate in the mean flow, if the flow and flame velocities are opposed). It separates unburnt gas from the burnt gas. Premixed flames can be described by their burning velocity, thickness and adiabatic temperature. These three characteristics depend on a few

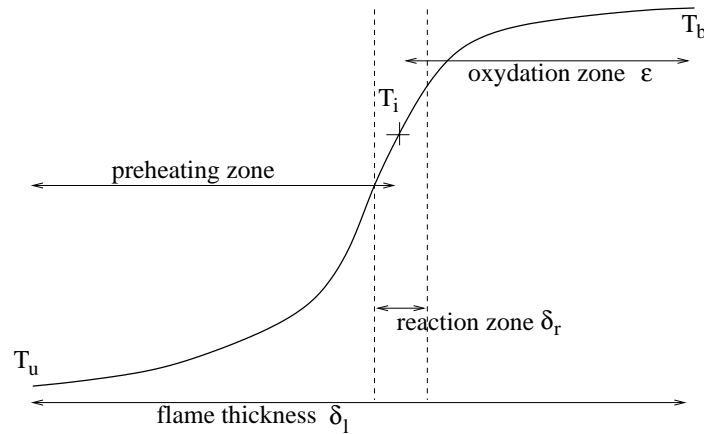


**Fig. 2.7:** Structure of the laminar premixed flame

parameters: Unburnt temperature, equivalence ratio mixture, pressure, fuel and oxidant. Laminar and unstretched flames depend only on thermo-chemical properties, and not on the flow structure. For this work the aim is to develop models for turbulent premixed flames, in which the burning velocity also depends on the flow. At the end of this section, the behavior of laminar premixed flames in presence of strain is described, since such laminar flows have also an influence of the propagation velocity of the flame.

### Structure of a laminar premixed flame front

First theoretical investigations on laminar flames have been carried out by Mallard and Le Chatelier in 1883 [MC83]. A two-zone structure for the premixed flame front is assumed as illustrated in Figure 2.7 (p.25):

- The preheating zone dominated by convection and heat diffusion
- The reaction zone plus oxidation zone dominated by heat diffusion and reaction.

In the preheating zone the mixture is warmed up and the first elementary reactions take place leading to the formations of radicals. In the reaction zone, the most exothermic reactions occur and the heat release is maximum. The propagation of the flame is therefore controlled by the conduction of heat from the reaction zone to the preheating zone. The thickness of the reaction zone  $\delta_r$  is generally thin: About 1/10 of the complete flame front thickness  $\delta_l$  for stoichiometric methane/air or propane/air mixtures, but can increase up to 1/3 for lean preheated premixed flames used in gas turbines.

### Adiabatic flame temperature

This characteristic of the laminar premixed flame is the easiest to define and to evaluate, since it can essentially be described by the first law of thermodynamics. With the hypo-

thesis that there is no loss of enthalpy (by heat exchange with outside) during combustion, the enthalpy of the thermodynamic system composed of the mixture fuel/air must remain the same before and after the combustion process. In other words, the heat released by the combustion of the reactants increases the temperature of the products:

$$h_u = h_b \quad (2.64)$$

$$\int_{T^0}^{T_u} c_{p,reactants} dT + h_{f,reactants}^0 = \int_{T^0}^{T_b} c_{p,products} dT + h_{f,products}^0. \quad (2.65)$$

The index 0 refers to the state at the reference temperature  $T^0 = 298.15$  K, and  $h_f$  is the specific formation enthalpy. If the specific calorific coefficients  $c_p$  and the chemical enthalpies  $h_f$  for the reactants as for the products are known, the burnt and adiabatic flame temperature can be evaluated. For example, assuming a constant specific calorific coefficient  $c_p$ , and noting  $\Delta h_f = h_{f,reactants}^0 - h_{f,products}^0$  the reaction enthalpy, an approximation of the flame temperature is obtained from Eq. (2.65):

$$T_b \approx T_u + \frac{\Delta h_f}{c_p}. \quad (2.66)$$

Writing the total enthalpy conservation, the dynamic enthalpy due to the mixture velocity has been neglected, since in most combustion applications the gas velocity is too small to compete with the sensible and chemical enthalpies.

Assuming a complete combustion, the influent parameters for the flame temperature are:

- The nature of the fuel, acting on the formation enthalpy and thus on the reaction enthalpy  $\Delta h_f$
- The air fuel ratio (AFR) of the mixture acting on the quantity of fuel to burn, and maybe also slightly on the calorific coefficient  $c_p$ , see Table 2.1 (p.14)
- The unburnt temperature  $T_u$ .

### Laminar Flame speed

Mallard and Le Chatelier [MC83] described the laminar flame speed, noted  $S_l$ , as the propagation velocity of the flame front (or reaction layer) into the stagnant flammable mixture and normal to the flame front surface. They derived the following expression for  $S_l$ :

$$S_l \sim \sqrt{\frac{a\dot{w}}{\rho}}, \quad (2.67)$$

where  $a$  is the thermal diffusivity,  $\rho$  the density and  $\dot{w}$  the reaction rate. The laminar flame speed depends therefore on parameters acting on the variables: fuel, mixture property, and indirectly temperature and pressure. Mallard and Le Chatelier's theory was later confirmed and extended by Zeldovitch, Frank-Kamanetskii and Semenov [ZBLM85]. They

postulated that most elementary reactions occur in the reaction zone above the *inner-layer temperature*  $T_i$  (close to the burnt temperature  $T_b$ ), and derived an explicit and more precise expression for the laminar flame speed  $S_l$ .

Other authors like Williams [Wil84], Echekki and Ferziger [EF89], Poinso and Veynante [PV01](p. 47) have developed analytical expressions for the reaction rate or the laminar flame speed. These formulations are not listed here, but a review has been carried out by Poinso and Veynante [PV01](p. 44-53).

The reaction rate  $\dot{w}$  is evaluated from the Arrhenius expression for a global reaction mechanism. The Arrhenius expression has been developed for elementary reactions, and then extended to detailed and reduced chemical mechanisms. This simplification to a global mechanism leads to the expression:

$$\dot{w} = A[F]^\alpha [Ox]^\beta \exp\left(-\frac{T_a}{T}\right), \quad (2.68)$$

where  $T_a$  is the *activation temperature* obtained from the *activation energy*:

$$T_a \equiv \frac{E_a}{\mathcal{R}}. \quad (2.69)$$

The global coefficients  $A$ ,  $E_a$ ,  $\alpha$  and  $\beta$  are mostly fitted from experiments (for example work by Westbrook and Dryer [WD81]).

Nowadays one-dimensional laminar flame solvers like *Chemkin* make the computation of laminar flames using detailed chemical mechanisms very precise. Elementary reactions are considered with Arrhenius expressions for each of them. Laminar flame speeds can be evaluated for different conditions in a few minutes. Tables extracted from computations or measurements are also available and deliver the flame speed with parameter variations (see Kuo [Kuo86], Turns [Tur00] and Williams [Wil84]). Correlations for propane and methane have been also fitted with analytical functions, taking into account the influence of the different parameters. They are expressed under the generic form by Poinso and Veynante [PV01](p. 55):

$$S_l(p, T_u) = S_l(p^0, T^0) \left(\frac{p}{p^0}\right)^{\alpha_p} \left(\frac{T_u}{T^0}\right)^{\alpha_T} \quad (2.70)$$

where  $T^0$  and  $p^0$  are the referenced temperature and pressure, and  $\alpha_p$  and  $\alpha_T$  the coefficients which should be fitted for the different conditions. Correlations have been carried out for methane by Gu et al. [GHLW00](p. 46-47). They are based on computations using the chemical reaction mechanism of GRI-Mech 1.2 describing the methane oxidation chemistry in terms of 177 elementary reactions of 32 species. A similar procedure has been carried out for propane after experimental measurements by Metghalchi and Keck [MK80]. These results are summarized in Table 2.2 (p.28) according to Poinso and Veynante [PV01](p. 55, Tab. 2.7). The equivalence ratio  $\phi$  is expressed as the ratio of fuel and oxidant masses compared to stoichiometric conditions:

$$\phi \equiv \left(\frac{y_f}{y_O}\right) / \left(\frac{y_f}{y_O}\right)_{st}. \quad (2.71)$$

Fuel	$S_l(p^0, T^0)$ [m/s]	$\alpha_T$ [-]	$\alpha_p$ [-]
CH <sub>4</sub> , $\phi = 0.8$	0.259	2.105	-0.504
CH <sub>4</sub> , $\phi = 1$	0.360	1.612	-0.374
C <sub>3</sub> H <sub>8</sub> , $\phi \in [0.8; 1.5]$	$0.34 - 1.38(\phi - 1.08)^2$	$2.18 - 0.8(\phi - 1)$	$-0.16 - 0.22(\phi - 1)$

**Tab. 2.2:** Correlations for the laminar flame speed [m/s]

It is smaller than unity for a mixture with excess of oxidant, as considered in this thesis. The air fuel ratio<sup>1</sup> (AFR) corresponds to an inverse definition:  $AFR = \frac{y_O}{y_f}$ . The validity of these correlations are claimed for  $T_u \in [300; 400]$  K and  $p \in [1; 10]$  bar for methane, and for  $T_u \in [300; 700]$  K and  $p \in [0.4; 50]$  bar for propane. In first approximation the laminar flame speed increases almost with the square of the temperature, whereas it decreases with about the square root of pressure:

$$S_l \sim T_u^2 p^{-1/2} \quad (2.72)$$

The influence of the AFR does not explicitly appear in the presented correlations, but the flame speed is maximum close to the stoichiometric mixture. It decreases for leaner as well as for richer mixtures up to extinction of the flame at the respective *lean blow-out* and *rich blow-out*. These two limits correspond to an excess respectively of air or fuel. The equilibrium between heat release and required preheating of the reactants must be maintained to reach the inner-layer temperature  $T_i$ , and to provoke the chain-break reactions.

Correlations using more parameters are valid in wider range of pressure, temperature and AFR. One possibility is employed and detailed in section 2.3.4 (p.31) for the evaluation of the Markstein number.

### Flame front thickness

The evaluation of the flame front thickness is more problematic, since its definition is already an issue. There are indeed at least four definitions which can be used:

- The *global thickness* defined by the distance from  $\Theta = 0.01$  to  $0.99$ , where  $\Theta$  is the reduced temperature based on the unburnt  $T_u$  and the burnt  $T_b$  temperatures.
- The *thermal thickness* defined with:

$$\delta_{l,T} \equiv \frac{T_b - T_u}{\max\left(\left|\frac{\partial T}{\partial x}\right|\right)} \quad (2.73)$$

Poinsot and Veynante [PV01](p. 57) recommend this value, because the term with the temperature gradient brings the most precise information for the choice of the mesh refinement.

<sup>1</sup>in Germany, the AFR is called *Luftzahl* and noted  $\lambda$

- The *diffusive thickness* defined with:

$$\delta_l \equiv \frac{a}{S_l}, \quad (2.74)$$

is used in this thesis, with  $a$  evaluated at the unburnt conditions. It permits to simply derive analytical relations.

- The *reaction thickness* defined with:

$$\delta_r \equiv \frac{\delta_l}{Ze}, \quad (2.75)$$

within  $Ze = \frac{E_a}{\mathcal{R}T_b^2}(T_b - T_u)$  is the Zeldovitch number. For a mixture of methane and air at atmospheric conditions  $Ze \approx 8 - 10$ . This is not properly a relevant measure of the flame front thickness, since it does not consider the thinnest part of the flame front. Nevertheless it yields crucial information when compared with the scales of turbulence as explained in section 2.4.3 (p.37).

#### 2.3.4 Stretched laminar premixed flames

Up to this part the flame properties have been developed and evaluated ignoring flow structures, or at least without considering its dynamic characteristics. The flame properties essentially depend on chemical parameters. Flame properties may also depend on the flow characteristics, such as shear stress or curvature.

*This section about the Markstein number definition and evaluation is much detailed, since this dimensionless number is required for the development of a part of the new Subgrid Flame Closure model in section 7.5 (p.123).*

##### Markstein length and Markstein number

Markstein [MGP64] was one of the first to propose a mathematical formalism to account for the deformation of the premixed flame front due to the flow structure. Considering that the actual laminar flame speed  $S_{l,s}$  should depend on the flame curvature, and according to a linearized analysis of the flame front, Markstein has demonstrated:

$$S_{l,s} = S_l \left( 1 + \frac{\mathcal{L}}{R_{flame}} \right). \quad (2.76)$$

The curvature of the flame  $R_{flame}$  is evaluated from:

$$R_{flame}^{-1} = -\nabla \mathbf{n} \quad (2.77)$$

where  $\mathbf{n}$  is the unit vector normal to the flame front. The length  $\mathcal{L}$ , which is of the order of magnitude of the flame front thickness, has been later named the *Markstein length*.

Simultaneously, the dimensionless Markstein number  $Ma$  has been defined as the ratio between the Markstein length and the flame front thickness [MGP64](p. 22):

$$\mathcal{L} \equiv Ma\delta_l. \quad (2.78)$$

Physically, the Markstein length  $\mathcal{L}$  measures the sensibility of flame dynamics to flow perturbations. When the flame is submitted to a curvature  $R_{flame}$ , the flame speed is all the more modified as the Markstein length  $\mathcal{L}$  becomes larger. The Markstein number represents the normalized sensibility of a flame to the deformations induced by the flow to the flame front. A flame with a small Markstein number  $Ma \approx 0$  is fairly insensitive to flow perturbations.

The relation Eq. (2.76) can be restated employing the flame stretch:

$$\begin{aligned} K = S_l \nabla \mathbf{n} &= -S_l / R_{flame} \\ \text{so that: } S_{l,s} &= S_l - \mathcal{L}K. \end{aligned} \quad (2.79)$$

The Karlovitz number  $Ka$  can be defined to estimate the flame stretch to the chemical time:

$$Ka \equiv K \frac{\delta_l}{S_l}, \quad (2.80)$$

this allows to write the following relation:

$$\frac{S_{l,s}}{S_l} = 1 - MaKa. \quad (2.81)$$

Some authors base the definition Eq. (2.80) on the *stretched laminar flame speed*  $S_{l,s}$  like Brutscher et al. [BZB02](p. 1825), Peters [Pet94](p. 21), and Hoffmann [Hof04](p. 59):

$$Ka \equiv K \frac{\delta_l}{S_{l,s}}, \quad (2.82)$$

$$\text{which leads to: } \frac{S_l}{S_{l,s}} = 1 + MaKa. \quad (2.83)$$

The relations Eqs. (2.81) and (2.83) are theoretically defined for small flame stretch, and are numerically equivalent for small values of the Karlovitz number  $Ka$ . The Karlovitz number is defined more precisely in section 2.4.2 (p.34).

### Various Markstein numbers

The flame front can be stretched as a result of a linear flow strain rate or of a flow curvature effect. The flame front is reacting in different ways for these two types of stretch. The notion of strain and stretch is just presented in this section, their evaluations are namely detailed in section 7.4 (p.114). Markstein numbers have been studied for strain rate and curvature separately as far as possible for numerical works by Bradley et al., Groot et al., and Poinot and Veynante [BGG96, GOdG<sup>+</sup>02, PV01], as well as for experimental works by

Gu et al., Karpov et al., Konle, and Weiss [GHLW00, K LW97, Kon05, Wei06]. The equation Eq. (2.83) is modified to point out the effect of strain and curvature:

$$\frac{S_l}{S_{l,s}} = 1 + \text{Ma}_{str} \text{Ka}_{str} + \text{Ma}_{cur} \text{Ka}_{cur}. \quad (2.84)$$

where the subscripts “str” and “cur” stand respectively for the strain and curvature components.

In the following and particularly for the turbulent combustion modeling, a global Markstein number is considered. In presence of turbulence, the individual effect of strain rate and curvature can no longer be identified, and the notion itself is disputable as stressed by Lipatnikov and Chomiak [LC04b].

### Estimations for the Markstein number

Theoretical works based on flame computations with detailed chemical mechanism have been achieved in order to evaluate the Markstein number. Historically Sivashinsky [Siv77] first gave an evaluation of the Markstein number without taking into account the thermal expansion. This expression is based on the fuel Lewis number  $\text{Le} = a/D$  and the Zeldovitch number  $\text{Ze} \equiv \delta_l/\delta_r = E_a/(RT_b^2)(T_b - T_u)$ :

$$\text{Ma} = \frac{\mathcal{L}}{\delta_l} = 1 + \text{Ze} \frac{1 - \text{Le}}{2 \text{Le}}. \quad (2.85)$$

This expression stresses the influence of the Lewis number. Fuels such as methane with  $\text{Le} \approx 0.9 < 1$  behave differently from fuel, such as propane, with  $\text{Le} > 1$ . The Markstein number is likely to be positive for Lewis numbers smaller than one.

According to asymptotic analysis, Clavin and Williams [CW82] derived another expression for the Markstein number where the gas expansion

$$\gamma \equiv \frac{T_b - T_u}{T_b} \quad (2.86)$$

plays an important role:

$$\text{Ma} = \frac{\mathcal{L}}{\delta_l} = \frac{1}{\gamma} \ln \frac{1}{1 - \gamma} + \text{Ze} \frac{\text{Le} - 1}{2} \left( \frac{1 - \gamma}{\gamma} \right) \int_0^{\frac{\gamma}{1 - \gamma}} \ln \frac{1 + x}{x} dx. \quad (2.87)$$

Numerically this expression is likely to deliver positive values of the Markstein number, and even strictly positive values when the gas expansion parameter is large enough:  $\gamma > 0.8$ , according to Clavin [Cla85](p. 24).

Peters [Pet94] derived a similar expression using detailed chemical mechanisms and achieved fairly exhaustive computations of Markstein numbers for different fuels (hydrogen, methane, methanol, ethane, ethanol, propane, n-heptane, iso-octane), unburnt temperature ( $T_u \in [300 - 800]$  K), equivalence ratio ( $\phi \in [0.5 - 1]$ ) and pressure ( $p \in [0.1 - 60]$

bar). Comparison of these numerical results against experimental measurements shows reasonable agreement. Nevertheless, uncertainties in experimental investigations and discrepancies between different authors prevent from concluding more precisely on the quality of the numerical approximation [PV05](p. 71). The expression employed has been first derived by Rogg and Peters [RP90] [Pet94](p. 22):

$$\text{Ma} = \frac{\mathcal{L}}{\delta_l} \approx \frac{1+\theta}{\theta} \left[ \ln(1+\theta) + 2 \frac{\text{Le}-1}{\epsilon} \int_0^\theta \frac{\ln 1+x}{x} dx \right]. \quad (2.88)$$

This expression is similar to Eq. (2.87), but some parameters are evaluated differently:

$$\theta = \frac{T_i - T_u}{T_u} \quad (2.89)$$

states for a dimensionless temperature parameter based on the inner-layer temperature  $T_i$ . Moreover, the parameter

$$\epsilon = \frac{T_b - T_i}{T_b - T_u} \quad (2.90)$$

scales with the oxidation layer thickness (see Figure 2.7 (p.25)). A few years later, Müller et al. [MBP97](p. 354) produced quasi identical results using the previous expression but including a classical evaluation of the Zeldovitch number  $\text{Ze} = E_a / (RT_b^2) (T_b - T_u)$  instead of the oxidation layer thickness  $\epsilon$ :

$$\text{Ma} = \frac{\mathcal{L}}{\delta_l} \approx \frac{1+\theta}{\theta} \left[ \ln(1+\theta) + \frac{\text{Ze} \text{Le} - 1}{2 \text{Le}} \int_0^\theta \frac{\ln 1+x}{x} dx \right]. \quad (2.91)$$

In the following this expression is employed to evaluate the relevant Markstein numbers for the burners considered, because of its large range of application in terms of unburnt temperature, AFR, pressure and fuels. The inner-layer temperature  $T_i$  is evaluated using the pressure and the activation energy:

$$T_i(p) = - \frac{E_a}{\ln\left(\frac{p}{B}\right)}. \quad (2.92)$$

The burnt temperature is obtained with a polynomial of the AFR valid for lean flames:

$$T_b = aT_u + b + c\phi + d\phi^2 + e\phi^3. \quad (2.93)$$

Conjointly, it is possible to evaluate the laminar flame speed  $S_l$ :

$$S_l = F y_f^m \exp\left(-\frac{G}{T_i}\right) \left(\frac{T_b - T_i}{T_b - T_u}\right)^n \frac{T_u}{T_i}. \quad (2.94)$$

The coefficients needed for the complete evaluation are just listed for the fuel of interest methane and propane in Table 2.3 (p.33) and Table 2.4 (p.33) according to Müller et al. [MBP97].

Fuel	$a$	$b$ [K]	$c$ [K]	$d$ [K]	$e$ [K]	Le
CH <sub>4</sub>	0.627	1270.15	-2449.0	6776	-3556	0.91
C <sub>3</sub> H <sub>8</sub>	0.53	1434.0	-2952.0	7518	-3856	1.63

**Tab. 2.3:** Coefficients for the adiabatic flame temperature and Lewis number [MBP97]

Fuel	$B$ [bar]	$E_a$ [K]	$F$ [m/s]	$G$ [K]	m	n
CH <sub>4</sub>	$3.1557 \times 10^8$	23873.0	$2.2176 \times 10^{-1}$	-6444.27	0.565175	2.5158
C <sub>3</sub> H <sub>8</sub>	$2.2501 \times 10^6$	17223.5	$1.27489 \times 10^1$	-1324.78	0.582214	2.3970

**Tab. 2.4:** Approximation constants for burning velocity [MBP97]

## 2.4 Premixed turbulent combustion

In this chapter, the concepts of fluid mechanics, of turbulence and of laminar flame have been successively presented and lead to this last section: premixed turbulent combustion, which is the main subject of this thesis. This subject is difficult, because it accumulates the comprehension and modeling difficulties of each of the three subparts. The modeling of flame with the Navier-Stokes equations has been achieved with the transport of species mass fraction (see section 2.1.3 (p.10)). But, the main issue remains the understanding of the reciprocal interaction between flame and turbulence, and principally the modification of the flame speed and reaction rate in presence of turbulence. In this part, the mechanisms of interaction between flame and turbulence is presented, before detailing the different flame structures depending on turbulent and chemical parameters.

### 2.4.1 Interaction flame-turbulence

This section deals with the mechanisms of interaction between flames and turbulence. The first paragraph briefly presents how the flame can act on the turbulence intensity, and on the turbulence production. The second paragraph illustrates how turbulent eddies act on the flame structure.

#### Effect of flame on turbulence

The flame can act on turbulence in two opposite ways. The first effect of flame on turbulence consists in a reduction of the turbulence intensity compared to the same cold configuration. This can be explicitly expressed with the Reynolds number  $Re = UD/\nu(T)$ . The kinematic viscosity  $\nu(T)$  is increasing with the temperature, so that a reactive flow exhibits a reduced Reynolds number compared to the cold flow, and therefore less turbulence. This can be illustrated physically. The increased molecular viscosity tends to homogenize the flow in a more efficient way. This tends to reduce the local magnitude of the velocity gradient. In turns this reduces the non-linear term  $(\mathbf{u} \cdot \nabla)\mathbf{u}$  in the momentum balance equations, and thus the energy transfer between the different turbulent scales. For mo-

deling, a so-called *counter-gradient diffusion* or *pressure-induced transport* term may be required, as mentioned by Lipatnikov and Chomiak [LC04a, LC04c], and discussed in section 6.1.3 (p.93). It describes the diffusion of species in the inverse direction to the Fick's law, because of density gradients between cold and burnt zones.

Nevertheless, the presence of the flame can produce turbulence due to its fluctuating surface. At a position where unburnt and burnt gas succeed, the intermittency may generate turbulence. This phenomenon should be implicitly included in the first term of the balance equation  $\partial\rho\mathbf{u}/\partial t$ , since the movement of the flame surface mainly acts in terms of flow dynamics as a change of the local density  $\rho$ . In CFD simulations, where variables are averaged or filtered as detailed in the next chapter, this effect should be modeled. Borghi [Bor88](p. 273) presented a model to evaluate the production of turbulent kinetic energy in presence of combustion.

### Effect of turbulence on flame

The propagation of the flame front in a moving flow is no more only due to the flame speed itself, but also on the flow velocity. Since the flow velocity is rarely uniform, the flame deforms and tends to follow local flow structures. In presence of turbulence, each eddy can locally act on the flame front and deformate it. In particular, very small eddies are likely to enter the flame front, up to the reaction zone and modify the intrinsic structure of the flame front. In short, the turbulence has two main effects on flame:

- Wrinkle the flame front with the largest eddies:  $r > \delta_l$
- Penetrate and modify the structure of the flame front with the smallest eddies:  $r < \delta_l$ .

The first effect tends to locally stretch the flame front, and section 2.3.4 (p.29), relative to the stretched laminar flames, is useful to understand the action of turbulence on flames. The effect of the eddies on the flame depends also of the velocity ratio as displayed in Figure 2.8 (p.35).

Because of the fact that turbulence contains a large spectrum of eddy size and velocity, dimensionless numbers have been defined to represent and qualify the effect of turbulence on the flame.

## 2.4.2 Definition of dimensionless numbers

### Turbulent Reynolds number

The Reynolds number  $Re$ , defined in Eq. (2.44), evaluates the convective force relative to the diffusion force [Rey83]. A *turbulent Reynolds number*  $Re_t$  is similarly defined using the turbulent scales:

$$Re_t \equiv \frac{u' l_t}{\nu}. \quad (2.95)$$

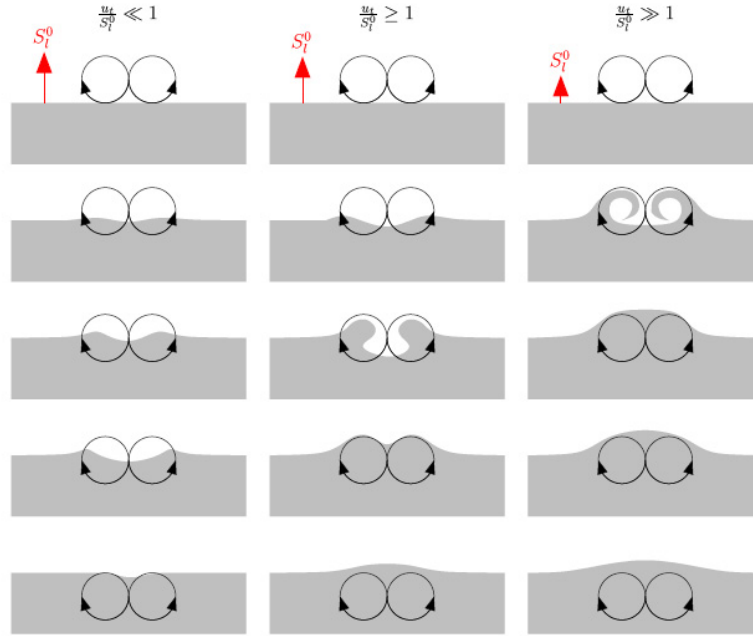


**Fig. 2.8:** Influence of the eddy velocity on the flame interaction, taken from Hoffmann [Hof04](p. 160)

This dimensionless number compares the kinematic diffusion due to turbulence to the molecular kinematic diffusion  $\nu$ . Compared to the original Reynolds number  $Re$ , the turbulent Reynolds number  $Re_t$  has a local meaning. The Reynolds number is namely based on global scale and a sole value is relevant for a geometry (which gives the reference scale  $L$ ), and for a *duty point* (which gives the reference velocity  $U$ ). The turbulent Reynolds number can be locally defined, since the integral length scale  $l_t$  and velocity fluctuations  $u'$  are likely to differ at different locations of the geometry considered. Besides it is directly expressed with turbulent variables and delivers a preciser evaluation of the actual and local turbulence property.

The turbulent Reynolds number also measures the ratio between the largest  $l_t$  and the smallest  $\eta$  turbulent scales. According to the equations Eq. (2.95) and  $\varepsilon = u'(r)^3/r = u(\eta)^3/\eta = u'^3/l_t$  (Eq. (2.51)), the scale ratio reads :

$$\frac{l_t}{\eta} = Re_t^{3/4}. \quad (2.96)$$

### Damköhler number

Contrary to the Reynolds number, based on ratio of force or diffusion, the (turbulent) Damköhler number [Dam40] is based on time scales. It compares the respective turbulent and chemical time scales:

$$Da \equiv \frac{t_t}{t_c}. \quad (2.97)$$

Where the turbulent time scale is evaluated from the integral length and velocity scales:

$$t_t \sim \frac{l_t}{u'}, \quad (2.98)$$

and the chemical time scale from the laminar heat diffusion and the laminar flame speed:

$$t_c \sim \frac{a}{S_l^2}. \quad (2.99)$$

A Damköhler number smaller than one  $Da < 1$  corresponds to a *slow chemistry*. The turbulent time scale is smaller than the chemical time scale, and therefore turbulence is faster than combustion. Reciprocally, a Damköhler number larger than one  $Da > 1$  indicates a *fast reaction process* which is most common for industrial burners.

### Turbulent Karlovitz number

Whereas the Damköhler number compares the chemical time  $t_c$  to the integral time scale  $t_t$ , the turbulent Karlovitz number [KJKW54] compares the chemical time to the smallest turbulent scales i.e. the Kolmogorov scales:

$$Ka_t \equiv \frac{t_c}{t_\eta} = \frac{\delta_l^2}{\eta^2} = \frac{u(\eta)^2}{S_l^2}. \quad (2.100)$$

The turbulent Karlovitz number indicates whether the smallest eddies have any influence on the flame front. It is naturally also related to the Karlovitz number  $Ka$ , already defined in Eqs. (2.80) and (2.82), for which the flame stretch  $K$  is based on the strain rate produced by the smallest eddies:

$$K \equiv \frac{1}{t_\eta}. \quad (2.101)$$

A second turbulent Karlovitz number based on the reactive layer on the flame front can be defined (see Peters [Pet00](p. 78)):

$$Ka_\delta \equiv \frac{\delta_r^2}{\eta^2} = \delta^2 Ka_t, \quad (2.102)$$

where  $\delta = Ze^{-1}$  states for the relative thickness of the reactive layer  $\delta_r$  in the flame front  $\delta_l$ . The second Karlovitz number indicates whether the smallest eddies are small enough to enter the reactive layer  $\delta_r$ .

### Relations between dimensionless numbers and relevant ratios

A relation between the turbulent Reynolds, Damköhler and Karlovitz numbers can be written. Using the Prandtl number

$$Pr \equiv \frac{\nu}{a} \quad (2.103)$$

which estimates the relative transfer of diffusion for momentum and heat. According to Eqs. (2.51) and (2.53)

$$\eta \sim \left( \frac{\nu^3}{\varepsilon} \right)^{1/4}, \quad (2.104)$$

one obtains:

$$\text{Pr Re}_t \sim \text{Da}^2 \text{Ka}_t^2. \quad (2.105)$$

Other dimensionless ratios can be expressed using dimensionless numbers. In the following, the ratio of the turbulent velocity  $u'$  to the laminar flame speed  $S_l$  is largely employed in order to establish combustion regime diagrams:

$$\frac{u'}{S_l} \sim \sqrt{\frac{\text{Pr Re}_t}{\text{Da}}}. \quad (2.106)$$

The ratio between the integral length scale  $l_t$  and the laminar flame thickness  $\delta_l$  can similarly be expressed:

$$\frac{l_t}{\delta_l} \sim \sqrt{\text{Pr Re}_t \text{Da}}. \quad (2.107)$$

### 2.4.3 Combustion Regimes

According to the ratio of size and velocity between the chemical and turbulent scales, different regimes of premixed turbulent combustion are distinguished.

#### Laminar flames

This regime is defined for small turbulent Reynolds number:

$$\text{Re}_t < 1. \quad (2.108)$$

This type of combustion has been described in section 2.3.3 (p.24). In the following, reference is made to this combustion regime to assure that turbulent model formulations recover the laminar flame speed in zones of low turbulence intensity.

#### Well stirred reactor

This regime is principally defined for reduced Damköhler number with a moderate turbulence intensity:

$$\text{Da} < 1 \text{ and } \text{Ka}_\delta < 1. \quad (2.109)$$

The turbulent time scale is smaller than the chemical time scale, but the smallest eddies are not fast enough to disrupt the inner layer of the flame front. The name of the regime is related to the action of turbulence: Turbulence can homogenize mixture before it starts burning. In this regime, the chemical mechanism is therefore more influent than turbulence, and the notion of *flame front* irrelevant. This regime is not studied in this work, since it is rarely relevant in industrial applications.

**Corrugated and wrinkled flame regime**

These two regimes are defined for large Damköhler numbers and moderate turbulence intensity. These two regimes are bounded from each other by the relative flame speed compared to the turbulent velocity, where turbulence is prevalent in the corrugated regime:

$$\text{wrinkled flame regime: } \quad Da > 1, Re_t > 1, Ka_t < 1 \text{ and } \frac{u'}{S_l} < 1, \quad (2.110)$$

$$\text{corrugated flame regime: } \quad Da > 1, Re_t > 1, Ka_t < 1 \text{ and } \frac{u'}{S_l} > 1. \quad (2.111)$$

The wrinkled flame regime corresponds to a flame placed in a weakly turbulent flow. In the corrugated flame regime, the flame front is more folded because the turbulent velocity is larger than the flame speed. For these two regimes, the flame front is considered as a continuous collection of flamelets. Each flamelet of the flame front behaves like a laminar flame. Flamelets move and behave differently because of the local action of eddies. Eddies cannot enter the flame front, and cannot modify the structure of the flame front. The flamelet has the same local characteristics than a laminar flame: flame thickness and velocity remain the same.

The corrugated flame regime is of interest for industrial applications, because industrial burners are likely to display some zones where the combustion occurs with this type of regime.

**Thickened flame regime**

In this regime and contrary to the corrugated flame regime, the smallest eddies can penetrate the flame front, or at least the preheated zone. Consequently, the turbulent Reynolds  $Re_t$  and Karlovitz  $Ka_t$  numbers are larger:

$$Da > 1, Re_t \gg 1 \text{ and } Ka_t > 1. \quad (2.112)$$

The Kolmogorov eddies increase the diffusion within the flame front, so that the flame front thickness is increased and lead to the formation of the so-called *thickened flamelets*. The thickened flamelet velocity is actually also modified and no more identical to the laminar flame speed. In this regime, turbulence and combustion cannot be dissociated. This regime cannot be considered as a juxtaposition of a flame and a turbulent flow: Chemical and turbulent characteristics become implicitly dependent. This regime, together with the corrugated flame regime, is of greatest importance for industrial applications. In the following, focus for turbulent combustion modeling is always placed on these two regimes.

### Broken zone regime

This regime occurs when turbulence is still more intensive than in the thickened flame regime. The smallest eddies are small enough to enter not only the flame front, but also the reactive layer  $\delta_r$ :

$$Da > 1, Re_t \gg 1 \text{ and } Ka_\delta > 1. \quad (2.113)$$

In the thickened flame regime, the flamelet velocity is becoming larger than the laminar flame speed, because of the increased diffusion in the preheated zone. In the broken zone region, the effect of eddies penetrating the inner-layer zone may tend to reduce the flamelet velocity, and may lead to local extinction, which is classically described as *quenching*. Consequence of this local quenching at the macro-scale may be the so-called *bending effect*, for which a model is proposed in section 7.4 (p.114). The limit between the thickened flame regime and the broken zone regime is difficult to define. This is very dependent on the instantaneous and local turbulent condition and also on the chemical properties of the mixture.

#### 2.4.4 Diagrams for turbulent premixed combustion

The disposition of the different combustion regimes is depicted in diagrams. Historically, Borghi [Bor85] presented the first turbulent combustion regime diagram with the axes  $u'/S_l$  and  $l_t/\delta_l$ , compiling his own work and different authors contributions on several regimes. Later, Peters [Pet86], Abdel-Gayed and Bradley [AB89], Poinot et al. [PVC90], and Hoffmann [Hof04] proposed similar diagrams with extended zone separations. The axis are still expressed in terms of the dimensionless length scale  $l_t/\delta_l$  and velocity scale  $u'/S_l$ . Williams [Wil00] proposed a diagram with the Damköhler and turbulent Reynolds numbers for the axis. Diagrams with sketches may be convenient to illustrate the flame front configuration as depicted by Kröner [Krö03](p. 30) or Siewert [Sie06](p. 22) for example. In this work, the diagram presented by Peters [Pet86](p. 1239) and later extended [Pet00](p. 79) is taken as reference. The different regimes of premixed turbulent combustion are well delimited. This diagram has nevertheless two drawbacks. The limit  $Da = 1$  does not appear, and the zone such as  $Re_t > 1$ ,  $Da < 1$  and  $Ka_\delta < 1$  belongs to the thin reaction regime. This zone is rather likely to be the well-stirred reactor regime. Therefore, a slightly modified Peter's diagram is employed for convenience in this thesis and presented in Figure 2.9 (p.40).

Pitsch [Pit05](p. 594) [Pit06](p. 468) has also presented an interesting diagram in the case of the LES modeling. The horizontal axis is based on the Karlovitz number, and the vertical axis on the ratio between flame thickness and grid scale.

Five dimensionless numbers have been defined and used:  $Re_t$ ,  $Da$ ,  $Ka_t$ ,  $Pr$  and  $\delta$  or  $Ze$ . This should theoretically give five degrees of freedom to construct combustion diagrams. The Prandtl  $Pr$  and Zeldovitch  $Ze$  numbers are implicitly imposed for a certain combustible mixture. The three remaining dimensionless numbers are reduced to two with the relation Eq. (2.105), which makes the use of a two-dimensional diagram possible. Changing the Zeldovich number would rotate the line  $Ka_\delta = 1$ , and modify the width of the thickened

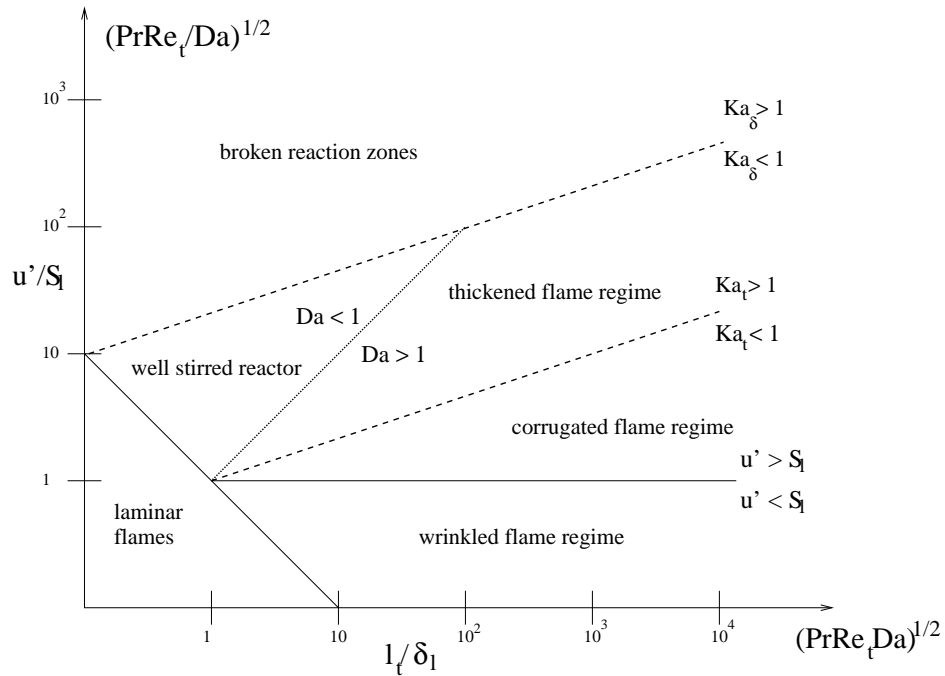


**Fig. 2.9:** Modified Borghi-Peters Diagram

flame regime. Changing the Prandtl number would scale the whole diagram and conserve the proportion, since both axes (Eq. (2.107) and Eq. (2.106)) scale in the same way with the Prandtl number.

### 3 Modeling of turbulent reactive flows

Modeling is required because solving the Navier-Stokes equations presented in the previous chapter is difficult. Finding an analytical solution to the non-linear and multi-dimensional differential equation system is generally impossible. Turbulence makes this resolution still more complex, since a wide range of scales must be considered, as well as reactive flows, since elementary chemical reactions with hundreds of species must be computed. Modeling is introduced in order to simplify the mathematical description of physical problems. In this chapter, three manners of modeling turbulent combustion are presented, depending on turbulence modeling. The difference consists in the level of details i.e. of turbulent structures, which are computed as depicted in Figure 3.1 (p.41).

In the so-called *Direct Numerical Simulation (DNS)*, the whole spectrum of turbulence is explicitly resolved. The mesh for the fluid geometry must be designed to enable the discretization of the smallest eddies. *Reynolds-Averaged Navier-Stokes (RANS)* models the macroscopic effect of turbulence, with a so-called turbulent diffusion, considering the averaged flow equations. With *Large Eddy Simulation (LES)*, theme of this thesis, the largest turbulent eddies are resolved, whereas the effect of the small eddies is modeled. In the following part, the three representations of turbulence are presented. The focus is placed on LES modeling. The consequence of turbulence modeling for combustion modeling are detailed. More details about DNS, RANS as well as LES modeling can be found in the following reference books: Ferziger and Peric, Lesieur, Mathieu and Scott, Oran and Boris,

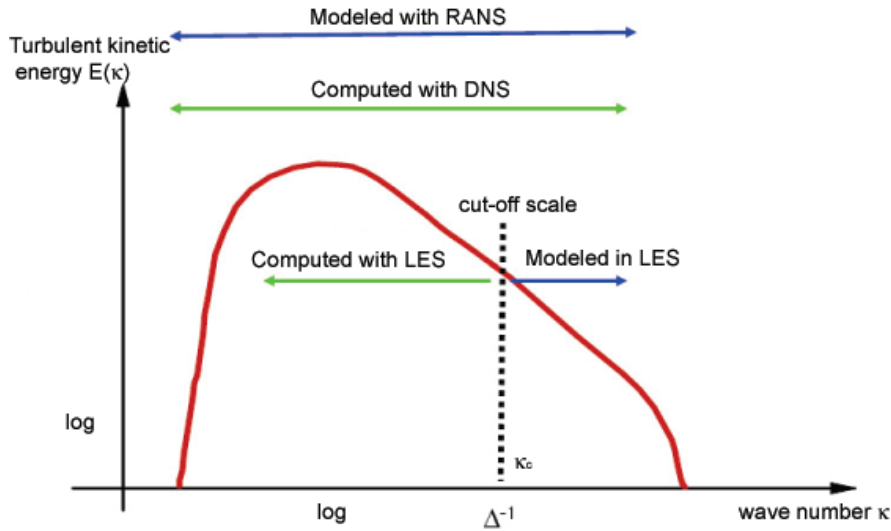


Fig. 3.1: Modeling and turbulent energy spectrum

Piquet, Poinso and Veynante and Pope [FP02, Les87, MS00, OB01, Piq99, PV05, Pop00].

### 3.1 DNS

The first section 3.1.1 (p.42) presents an overview of DNS of cold flows. The second section 3.1.2 (p.43) describes its adaptation in order to simulate reactive flows.

#### 3.1.1 Cold flows

As already displayed in Figure 3.1 (p.41), all scales of turbulence are resolved with DNS. The required mesh refinement is estimated by developing any flow variable in Fourier series:

$$u(x, t) = \sum_{\kappa=0}^{\infty} u_{\kappa}(x, t) e^{i\kappa x}. \quad (3.1)$$

$\kappa$  is the wavenumber and  $u_{\kappa}$  the velocity amplitude associated with the wavenumber  $\kappa$ . The grid must be fine enough, so that the grid cut-off  $\pi/\Delta$  enables the resolution of the Kolmogorov eddies of size  $\eta$ . The relation, mentioned by Ferziger and Peric [FP02](p. 270), expresses this condition in terms of the wavenumber  $\kappa_{\eta}$ :

$$\Delta < \frac{\pi}{\kappa_{\eta}}. \quad (3.2)$$

The computational domain must be also large enough to contain the largest scales of the flow. Selecting the integral length scale rather than any other larger geometrical length scale, and considering that the mesh counts  $n$  points in each direction, the condition reads:

$$n\Delta > l_t. \quad (3.3)$$

Combining the last two equations and the relation  $l_t/\eta = \text{Re}_t^{3/4}$  presented Eq. (2.96), the minimal number of points in *one direction* can be evaluated. This relation only depends on the turbulent Reynolds number, as shown by Poinso and Veynante [PV05](p. 159):

$$n^3 > \text{Re}_t^{9/4}. \quad (3.4)$$

Pragmatically, the equivalent relation is mostly used:

$$\text{Re}_t < n^{4/3}, \quad (3.5)$$

it fixes a limit for the flow turbulence intensity, which can be investigated with a type of computer. It also stresses that the simulation cost for a 3D turbulent flow increases faster than the square of the turbulent Reynolds number.

Moreover DNS is *intrinsically* a transient simulation, so that a relevant time-step size  $\Delta t$  must be selected. Not entering in the details of the time discretization, but simply considering an explicit scheme where the CFL (Courant-Friedrich-Levy) condition is relevant, the time-step size should fulfill:

$$\Delta t < CFL \frac{\Delta}{U}. \quad (3.6)$$

Obviously, finer grids and larger flow velocities, impose smaller time steps.

Actually, very largest 3D-DNS are carried out on  $512 \times 512 \times 512$  up to  $1024 \times 1024 \times 1024$ -meshes, which count between one hundred million and one billion cells. Such huge meshes allow the computation of flows with turbulent Reynolds number approaching ten thousand.

Jointly with the high CPU-cost, DNS are very demanding in terms of numerical scheme precision and thus discretization order. Unfortunately, this makes the convergence and numerical stability more difficult to obtain. Therefore, boundary conditions treatment becomes an issue in DNS. The order reduction for the discretization scheme near the boundary conditions is a problem, so that many simulations are carried out on cubes with periodical boundary conditions.

### 3.1.2 Reactive flows

For DNS of reactive flows<sup>1</sup>, the Kolmogorov scales as well as the chemical scales must be resolved. As suggested in section 2.4.3 (p.37) with the different combustion regimes, the flame front scale is likely to be smaller than the smallest turbulent eddies for industrial burners. The mesh must be refined to enable the computation of the flame front structure as illustrated by Durand et al. [DPR<sup>+</sup>04] for example. Besides, the direct simulation of the combustion requires the use of detailed reaction mechanisms with numerous species and thus numerous transport equations, to take into account *most* physical effects (such as multi-diffusion and not only binary diffusion effect, Soret- and Duffour-effects).

Therefore DNS of reactive flows still cost more than the cold flow simulations. As proposed by Poinso and Veynante [PV05](p. 160),  $p \approx 20$  points should be placed in the flame front:

$$p\Delta = \delta_l. \quad (3.7)$$

Considering Eq. (2.107), a relation between grid refinement parameters  $n$  and  $p$ , Damköhler and turbulent Reynolds numbers can be derived:

$$\text{Re}_t \text{Da} < \left(\frac{n}{p}\right)^2. \quad (3.8)$$

The relation Eq. (3.4) imposes the maximal turbulent Reynolds number according to the mesh refinement due to the turbulence. The last inequality Eq. (3.8) is imposing the maximum Damköhler number considering a fine resolution of the flame front. A finer resolution of the flame front reduces drastically the possible range of Damköhler number which can be investigated. This also implies that simulations with complex chemical mechanisms impose smaller Damköhler numbers. Correct predictions of intermediate species concentrations require a finer resolution in the flame front:  $p > 20$ . This explains that DNS with simplified chemical mechanisms (and diffusion effect considerations) are also investigated.

---

<sup>1</sup>Actually, DNS of reactive flows is not a proper term: Detailed reaction mechanism is the most precise modeling for combustion, but it remains a representation how combustion occurs. It does not offer a *direct* simulation of reaction mechanisms, as it does for turbulence.

## 3.2 RANS modeling

Obviously, DNS cannot be employed for industrial applications. RANS enables simulations of complex flows by approximating turbulence. Engineers are mostly interested in the mean flow and its fluctuation intensity. They rarely focus on instantaneous and local effects of turbulent eddies. A mathematical formalism has been developed to take into account the overall effect of turbulence in the Navier-Stokes equations. This way, simulations and meshes can be designed according to global geometrical scales, and not to turbulent scales. It allows the use of coarser meshes, which enable computations in a relative short time.

### 3.2.1 Reynolds and Favre averaging

RANS modeling considers the mean effect of turbulence, so that the Navier-Stokes equations presented in Eq. (2.8) must be averaged. Two different averaging are possible.

#### Reynolds averaging

Writing each variable as sum of its mean value with a fluctuation:

$$f = \bar{f} + f'' \text{ such as } \bar{f}'' = 0 \quad (3.9)$$

may permit the development of the Navier-Stokes equations with the Reynolds averaging. The Reynolds-averaged mass conservation equation in the conservative form Eq. (2.1) becomes:

$$\begin{aligned} \frac{\partial \bar{\rho}}{\partial t} + \frac{\partial \bar{\rho} \bar{u}_i}{\partial x_i} &= 0 \\ \Leftrightarrow \frac{\partial \bar{\rho}}{\partial t} + \frac{\partial \bar{\rho} \bar{u}_i}{\partial x_i} &= - \frac{\partial \overline{\rho'' u_i''}}{\partial x_i}. \end{aligned} \quad (3.10)$$

This averaging has two drawbacks. The averaged mass is not conserved, a term equivalent to a source term appears. Besides, the evaluation of this new term requires modeling, since the average value of the fluctuation product is *a priori* unknown.

#### Mass-weighted or Favre averaging

Favre [Fav69] has introduced a mass-weighted averaging for the variables (also called “Favre averaging”), which are multiplied with the density in the equations to avoid these difficulties:

$$\tilde{f} = \frac{\overline{\rho f}}{\bar{\rho}}, \quad (3.11)$$

$$f = \tilde{f} + f' \text{ and } \tilde{f}' = 0. \quad (3.12)$$

With the Favre averaging, the Navier-Stokes equations retain the same structure than with the Reynolds averaging:

$$\frac{\partial \bar{\rho}}{\partial t} + \frac{\partial \bar{\rho} \tilde{u}_i}{\partial x_i} = 0, \quad (3.13)$$

$$\frac{\partial \bar{\rho} \tilde{u}_i}{\partial t} + \frac{\partial \bar{\rho} \tilde{u}_i \tilde{u}_j}{\partial x_j} = -\frac{\partial \bar{p}}{\partial x_i} + \frac{\partial \tilde{t}_{ij}}{\partial x_j} + \bar{\rho} \tilde{f}_i - \frac{\partial \bar{\rho} \widetilde{u'_i u'_j}}{\partial x_j} \quad \forall i \in [1, 2, 3], \quad (3.14)$$

$$\frac{\partial \bar{\rho} \tilde{y}_k}{\partial t} + \frac{\partial \bar{\rho} \tilde{y}_k \tilde{u}_j}{\partial x_j} = \frac{\partial}{\partial x_j} \left( \bar{\rho} \frac{\nu}{Sc_k} \frac{\partial \tilde{y}_k}{\partial x_j} \right) + \bar{w}_k - \frac{\partial \bar{\rho} \widetilde{y'_k u'_j}}{\partial x_j} \quad \forall k \in [1, n]. \quad (3.15)$$

In momentum and species transport equations, a new term appears due to the non-linearity of the Navier-Stokes equations. The terms  $\left( \bar{\rho} \widetilde{u'_i u'_j} \right)_{,j}$  and  $\left( \bar{\rho} \widetilde{y'_k u'_j} \right)_{,j}$  are relevant for the non-reactive flow modeling, they are described in the next paragraph. The term  $\bar{w}_k$  is related to the reactive flow modeling, it is the focus of the next chapters.

To switch from the Favre-averaging to the Reynolds-averaging, Reynolds fluctuations are required:

$$\bar{\rho} \tilde{f} = \bar{\rho} \bar{f} + \overline{\rho'' f''}. \quad (3.16)$$

It makes the comparison between experiments and simulations difficult. Measurements deliver Reynolds-averaged results, whereas simulations deliver Favre-averaged values. Velocity profiles through the flame front are likely to lead to discrepancies between the two averaging methods, since density fluctuations are maximum around the flame front.

### Turbulent viscosity

Enhancement of the actual diffusion by turbulence in the fluid has been illustrated in section 2.2.2 (p.17). For the modeling of the unknown term  $\left( \bar{\rho} \widetilde{u'_i u'_j} \right)$ , this idea has been introduced:

$$\left( \widetilde{u'_i u'_j} \right) \approx -\nu_t \left( \frac{\partial \tilde{u}_i}{\partial x_j} + \frac{\partial \tilde{u}_j}{\partial x_i} \right). \quad (3.17)$$

This closure is using the averaging values and a so-called *turbulent viscosity*  $\nu_t$  to evaluate the unknown term. It is also worth noting that the closed term correlates with the local averaged strain  $\tilde{D}_{ij} = \frac{1}{2}(\tilde{u}_{i,j} + \tilde{u}_{j,i})$ .

For species turbulent diffusion  $\left( \bar{\rho} \widetilde{y'_k u'_j} \right)$ , the same gradient assumption is made. Postulating a turbulent Schmidt number  $D_{k,t} \equiv \nu_t / Sc_{k,t}$ , a similar expression is obtained:

$$\left( \bar{\rho} \widetilde{y'_k u'_j} \right) \approx -\bar{\rho} \frac{\nu_t}{Sc_{k,t}} \frac{\partial \tilde{y}_k}{\partial x_j}. \quad (3.18)$$

The possible drawback of this gradient assumption is the so-called *counter-gradient diffusion* discussed in section 6.1.3 (p.93).

### 3.2.2 Turbulent variables and non-reactive models

The turbulent viscosity  $\nu_t$ , introduced with the previous closure Eq. (3.17), has still to be evaluated. Formulations or models based on different turbulent variables have been developed for this aim. A fairly exhaustive review of RANS models has been compiled by Piquet [Piq99](p. 102-141). In the following section, type of models are mentioned.

#### Class of RANS turbulence models

Using dimensional considerations, the turbulent viscosity should scale with the product of the integral length scale with the fluctuation:

$$\nu_t \sim u' l_t.$$

Practically, most models estimate the turbulent kinetic energy  $k \sim u'^2$  with another turbulent variable in order to evaluate  $\nu_t$ :

- *Mixing length* or *no-equation* model. It has been employed for the first RANS models like the Baldwin-Lomax model. This formulation is based on a local equilibrium between the turbulent production and dissipation. The value obtained is independent on the surrounding values and on the flow history, which is disputable for most of flows, as stressed by Piquet [Piq02](p. 221).
- *One-equation* model. For this class of model the turbulent viscosity is calculated by solving a transport equation for the turbulent kinetic energy, and by modeling a length information to permit the closure. The Spalart-Allmaras model has been for example largely used in the aeronautics industry for design of turbomachine blades.
- *Two-equation* model. These are the most popular turbulence models for industrial applications, and are implemented as default turbulence models in CFD software. They are based mostly on two transport equations for the turbulent kinetic energy  $k$  with the turbulent dissipation  $\varepsilon$  or the turbulent frequency  $\omega$ : respectively  $k - \varepsilon$  or  $k - \omega$  models.
- *Reynolds stress* model. The main drawback of 0- up to 2-equation models is the implicit hypothesis of isotropy and homogeneity of turbulence. The six averaging correlations  $\left(\overline{\rho u'_i u'_j}\right)$ , which appear in the momentum transport equations, are indeed modeled with one value for the turbulent viscosity, as defined in Eq. (3.17). This value is independent on the direction, so that the eventual anisotropy and inhomogeneity of turbulence is not taken into account. Deriving further the averaged Navier-Stokes equations, transport equations for the Reynolds stress components can be formulated. This type of model has the advantage of modeling anisotropic flows more accurately. The detriment is the increase of required transport equations from two to six.

### 3.2.3 RANS combustion modeling

As already explained in section 3.1.2 (p.43) about DNS, chemical scales are finer than turbulent scales for most industrial burners. For RANS modeling of turbulent combustion, it implies that the mesh, which is designed according to the geometrical scales, is much too coarse to resolve any flame structure. In RANS equations, the difficulty consists in correctly evaluating the averaged reactive term of the species mass fraction transport equations. Three main approaches of RANS modeling of premixed turbulent combustion have been developed for this purpose:

- Chemical representation: species mass fractions
- Progress variable approach
- Level-set approach or  $G$ -equation.

Most LES combustion models have been adapted from RANS modeling. The same approaches have been used, so that they are detailed in the next section, relative to the LES modeling.

## 3.3 LES modeling

LES modeling differs from RANS modeling by the formalism: The transport equations are filtered (with a low-pass filter) and not averaged. It means that the lowest wave numbers are resolved, and the highest must be modeled. In the next sections, filtering and filters are presented, LES models (for cold flow) for the closure of the highest wave numbers are described, before giving a review of LES combustion models.

*In the following chapters,*

- *only LES equations are employed. The same notation  $\bar{f}$  and  $\tilde{f}$  as for the RANS equations have been used to avoid introduction of multiple notations.*
- *only the Favre filtering is employed. For this reason, a simple ' is used for its notation, in order to simplify notations.*

### 3.3.1 Filters and cut-off scales

$\bar{f}$  is the filtered variable, and  $f''$  the high wave number part for any fluctuating variable  $f$ .  $\tilde{f}$  is the filtered mass-weighted variable, and  $f'$  its high wave number part. By analogy with RANS, one directly writes with Favre filtering:

$$\tilde{f} = \frac{\rho f}{\bar{\rho}} \quad (3.19)$$

$$f = \tilde{f} + f' \quad (3.20)$$

Considering the mathematical formalism, there are two possibilities to filter a signal that is known (see for example Poinso and Veynante [PV05](p. 162), or Pope [Pop00](p. 561)). The most convenient is to work directly with the *spectral space representation* of this filter. In this case the signal is considered with its Fourier transform, and filtering amounts to cut-off the highest wave numbers above the cut-off wave number  $\kappa_c$  (cut-off scale  $\Delta_c$ ):

$$\bar{\rho} \widetilde{f(x)} = \int (\rho f)_\kappa(x) F(\kappa) d\kappa \quad (3.21)$$

$$F(\kappa) = \begin{cases} 1 & \text{if } \kappa < \kappa_c = \frac{\pi}{\Delta_c} \\ 0 & \end{cases} \quad (3.22)$$

In CFD, the Fourier decomposition of the solution is rarely known, since the solution is calculated in physical space. In this case the filtering is achieved by taking a weighted average of the solution over a given volume using the filter kernel  $F$ :

$$\bar{\rho} \widetilde{f(x)} = \int \rho(x') f(x') F(x - x') dx' \quad (3.23)$$

Typically, two different filters are used in the physical space representation:

- The Gaussian filter:

$$F(x) = F(x_1, x_2, x_3) = \left( \frac{6}{\pi \Delta_c^2} \right)^{3/2} \exp \left[ -\frac{6}{\Delta_c^2} (x_1^2 + x_2^2 + x_3^2) \right] \quad (3.24)$$

- The box-filter:

$$F(x) = F(x_1, x_2, x_3) = \begin{cases} \frac{1}{\Delta_c^3} & \text{if } |x_i| \leq \frac{\Delta_c}{2} \\ 0 & \end{cases} \quad (3.25)$$

An important consequence of these expressions is that the filtered part of the fluctuations can be non zero, when the filter kernel  $F$  is not a projector:  $F \times F \neq F$ , such as for the Gaussian filter.

In the case of CFD software, an extension of the box filter is employed. Theoretically, the box filter is only defined for Cartesian meshes, for which the directions  $x_1$ ,  $x_2$ ,  $x_3$  are perfectly defined. Practically, for structured as well as for unstructured meshes, directions are not considered, and the filter kernel expression simply reads:

$$F(x) = \begin{cases} \frac{1}{\Delta^3} & \text{in the considered cell of volume vol} \\ 0 & \text{outside} \end{cases} \quad (3.26)$$

where  $\Delta$  is defined as the typical length of the cell  $\Delta \equiv \text{vol}^{1/3}$ , so that the cut-off wave number directly depends on the cell size :  $\kappa_c = \frac{\pi}{\Delta}$ .

Besides, the filtering operation is *implicitly* delivered through the mesh discretization in CFD software, as justified by Kim [Kim04](p. 3). Compared to the signal theory, for which frequencies of a complete signal are suppressed by filtering, the problem is inverse when solving the filtered Navier-Stokes equations. The signal is resolved from the transport

equations and the mesh. According to the mesh refinement, only a part of the real signal can be reconstructed, so that only the *sampled signal* is computable. Fluctuations with smaller wave length than the grid size cannot be predicted, they are implicitly filtered. Nevertheless, their effect has to be modeled in the filtered equations. The Navier-Stokes equations can be correctly resolved only if all scales are considered, because of the non-linearity of the convection term.

### 3.3.2 LES Models

As already written, the filtered Navier-Stokes equations conserve the same formalism as RANS equations. Models are again based on the evaluation of a *subgrid turbulent viscosity* to close the unknown terms. The subgrid turbulent viscosity models the diffusion effect of the smallest turbulent eddies, which are not explicitly resolved. Compared to RANS simulations, LES modeling is expected to improve the prediction of turbulent phenomena, and consequently of the averaged flow. The distinctive feature of LES is the explicit computation of the largest turbulent structures, which essentially depend on the geometry. LES modeling is concerned on the smallest scales only, which effect is not expected to depend on the geometry. A universal formulation, i.e. geometry independent, may be acceptable. Two LES models largely employed during this work are presented, and their implementation in *Fluent* is described. The description of a third model, the Mixed Scale Model (MSM), and its implementation in *Fluent* have been included in section A.3.3 (p.217). Its use is specially relevant with the TF combustion model, but has not been yet completely validated. For a complete review on LES models for non-reactive incompressible flows, see Sagaut [Sag01].

#### Smagorinsky model

The Smagorinsky model [Sma63] is the first LES model, and was developed for meteorological applications. The closure is algebraic, and does not require any transport equation to represent subgrid turbulence. The evaluation of the turbulent viscosity is based on the filtered shear stress  $\tilde{S} = (2\widetilde{D_{ij}D_{ij}})^{1/2}$ :

$$\nu_t = (C_s \Delta)^2 \tilde{S}, \quad (3.27)$$

where  $C_s$  is a model constant, which should take values between 0.1 and 0.2.

The model is known to be dissipative especially near the walls. A limitation for the viscosity is included in *Fluent*, according to the Smagorinsky-Lilly model [FLU05] (p. 46, Chap. 11):

$$\begin{aligned} \nu_t &= L_s^2 \tilde{S}, \\ L_s &= \min \{Kd; C_s \Delta\}. \end{aligned} \quad (3.28)$$

$C_s = 0.1$  is taken as default value,  $d$  is the distance to the nearest wall, and  $K = 0.4187$  the von Karman constant.

The two main drawbacks of the model remain the constant  $C_s$ , which should be modified for each configuration, and the sole dependence on the filtered strain rate. Germano and Lilly [Ger92, Ger96, Lil92] have proposed a dynamic model using a test filter to automatically adapt the local value of the constant  $C_s$ .

### Turbulent kinetic energy

With this model, the subgrid turbulent viscosity depends on the subgrid kinetic energy  $k_{sgs}$ :

$$\nu_t = C_k k_{sgs}^{1/2} \Delta. \quad (3.29)$$

The closure is achieved by solving a transport equation for the subgrid turbulent kinetic energy, as expressed by Kim [Kim04](p. 6-7):

$$\frac{\partial k_{sgs}}{\partial t} + \frac{\partial \tilde{u}_j k_{sgs}}{\partial x_j} = -\tau_{ij} \frac{\partial \tilde{u}_i}{\partial x_j} - C_\epsilon \frac{k_{sgs}^{3/2}}{\Delta} + \frac{\partial}{\partial x_j} \left[ (\nu_t + \nu) \frac{\partial k_{sgs}}{\partial x_j} \right] \quad (3.30)$$

within  $C_\epsilon$  and  $C_k$  are determined dynamically according to the Germano's identity [GPMC91, Ger92, Ger96].

This method enables to take the *history* (the time effect) into consideration thanks to the transport equation. It also correlates the viscosity with the local subgrid turbulent energy, rather than the strain rate. Backscatter of kinetic energy is thus expected to be modeled. Compared to the Smagorinsky model, the strain rate acts as a source term for turbulence, rather than directly evaluating turbulent velocity, which is more physical. The drawback of this model is naturally the extra transport equation to solve.

## 3.4 LES premixed combustion models

This section gives an overview of LES combustion models. Distinction between combustion representation and closure models is stressed. In the next chapters, the Thickened Flame (TF) model, the Turbulent Flame speed Closure (TFC) model and the Subgrid scale Flame Closure (SFC) model are detailed, so that there are just mentioned in this part. In conclusion, reasons for choosing these models are given.

### 3.4.1 Modeling approach and closure strategies

Before starting with the presentation of LES models for the premixed turbulent combustion, *combustion representations* and *closures* are presented. There are namely three main manners to describe premixed flames: species mass fractions (with reduced or detailed mechanisms), progress variable and level-set approach. Although the distinction between these three categories is sometimes tenuous, closures differ. For example, species mass fraction approach with one species can be compared to the progress variable approach.

Closure for species mass fraction approach is mostly formulated with a simplified Arrhenius approximation, whereas closure for progress variable is often based on a turbulent flame speed. The level-set approach is also using evaluation of a turbulent flame speed, like the progress variable approach, but it is derived for the displacement of an iso-value in the flow, rather than to evaluate a combustion rate as made with the progress variable approach.

For each of these representations, filtering implies the closure of the subgrid scale transport, and of the reactive terms. The subgrid scale transport is mostly approximated with a gradient assumption, and this term is modeled as a turbulent diffusion. Closure of the reactive term depends on the type of representation. There are different strategies for this closure: adaptation of Arrhenius formulation, evaluation of a turbulent flame speed, use of the fractal theory, consideration based on the flame wrinkling or flame surface density. The next three paragraphs briefly present the different types of flame description, and which type of closures are typically associated. The last paragraph displays the different coupling between closure and representations.

#### **Chemical representation: species mass fractions**

The computation of the species mass fraction transport equations is the most natural representation of combustion, since it describes the quantity of each species at any time and position. According to the chemical reaction mechanism a large or reduced number of species can be computed. In most industrial applications, turbulent mixing is of greater importance than the detailed chemical description, so that reduced reaction mechanisms have been used. Besides, considering the scale difference between the mesh and the flame front thickness, it is illusory to expect to correctly compute distribution of radicals. To reduce the CPU-cost, and optimize the potential of the combustion modeling, new representations of the flame structure have been developed.

#### **Progress variable approach**

The progress variable approach is a pragmatic simplification of the chemical representation. The flame front structure is no more described in terms of species, but a unique variable describes the presence of unburnt or burnt gas. It implies some hypotheses with diffusion coefficients and Lewis numbers, they are detailed in section 5 (p.69). The available information is therefore the position and eventually the thickness of the flame brush. The progress variable approach is normally well adapted for the adiabatic perfectly premixed combustion, but it can be extended for more general cases as detailed in section 5 (p.69). Two models using this approach are also investigated in this thesis: the TFC-LES in section 6 (p.87), and the SFC model in section 7 (p.99).

representation	species	progress variable	level-set approach
modified Arrhenius formulation	TF, EDC, FM		
turbulent flame speed		LES-TFC, SFC	$G$
flame surface density		FSD	
fractal theory	FM	SFC	

**Tab. 3.1:** Representation and closure strategies

### Geometrical representation: Level-set approach or $G$ -equation

This type of approach corresponds to a geometrical description. The flame is not considered physically. A transport equation for a variable  $G$  is resolved and the flame position is associated to a certain value of  $G_0$  as described by Peters [Pet00]. Based on the local flame propagation mechanisms, a turbulent flame speed relation is derived for the averaged representation in order to describe the displacement of the iso-value  $G_0$ .

#### Associated closure strategies

Some closures can be used with different approaches. For example a closure for the turbulent flame speed is required both for models based on the progress variable, or based on the level-set approach. Table 3.1 (p.52) presents a synopsis of possibilities.

Closures for the three different approaches are successively presented. The progress variable approach is separated in two parts. The first one describes the standard models, the second one describes the models based on the flame surface density. Consequently, the next four sections respectively present models for the species mass fraction approach, for the progress variable approach, for the progress variable with flame surface density, and for the level-set approach.

### 3.4.2 Models based on species mass fractions

The TF model belongs to this category, it is detailed in chapter 4.

#### Mixing-controlled reaction rate

Fureby and Löfström [FL94] present a model based on the species mass fractions with an Arrhenius formulation extended for turbulent flames. The evaluation of the reaction rates employs a multi-reaction mechanism ( $\dot{w}_j$  is the reaction rate of the  $j$ -th reaction,  $\nu_{i,j}$  the stoichiometric coefficients of the species  $i$  for the reaction  $j$ ):

$$\dot{m}_i = M_i \sum_{j=1}^n (\nu_{i,j}^P - \nu_{i,j}^R) \dot{w}_j. \quad (3.31)$$

This laminar consideration is modified to take into account the influence of turbulent mixing:

$$\tilde{m}_i = M_i \sum_{j=1}^n (v_{i,j}^P - v_{i,j}^R) \min \{ \tilde{w}_j; \tilde{w}_{mix} \}. \quad (3.32)$$

Two possible contributions are considered for the reaction rate. A first contribution  $\dot{w}_{kin}$  is kinetically controlled (Arrhenius type), and a second contribution  $\dot{w}_{mix}$  is mixing-controlled. The filtered Arrhenius type contribution  $\tilde{w}_{kin}$  is evaluated according to Eq. (3.31) using the filtered temperature and mass fractions. Naturally, it implies some discrepancies, because of passage from laminar variables to filtered variables. This should be compensated with the second contribution  $\dot{w}_{mix}$ . The mixing-controlled term  $\tilde{w}_{mix}$  is assumed to be equivalent to the turbulent time calculated at the subgrid scale  $t_\Delta$ :

$$\tilde{w}_{mix} = \frac{\bar{\rho}}{t_\Delta} \left( \underbrace{\min_{i \in P} \left\{ \frac{\tilde{y}_i}{v_{i,j} M_i} \right\}} - \underbrace{\min_{i \in R} \left\{ \frac{\tilde{y}_i}{v_{i,j} M_i} \right\}} \right), \quad (3.33)$$

$$\text{with } t_\Delta \sim \frac{\Delta}{k_{sgs}}. \quad (3.34)$$

The reaction rate is limited by turbulent mixing in zones of low turbulence intensity, where  $t_\Delta$  is large. Inversely, the reaction is limited by the chemical aspect in the zone of high turbulence intensity. For example, it reduces excessive reaction rates in strain rate regions, like it may be the case with progress variable approach closures, as discussed with the LES-EBU model in the following, or with the TFC-LES model in section 6 (p.87). Advantage of this model is the use of the Arrhenius formulation which makes the use of any species number possible. A drawback is that the interaction between turbulence and flame is not really investigated. Fureby and Löfström have validated their model with a one-step, a two-step and a three-step mechanism [FL94] (p. 1259) using reaction rate expressions from Westbrook and Dryer [WD81] against experimental results obtained on the Volvo test-rig by Sjunnesson et al. [SNM91, SHL92] also presented in section 8.1.5 (p.150).

### Eddy dissipation concept model

The *Eddy Dissipation Concept (EDC)* has been developed by Magnussen [Mag81] to model the interaction between turbulence and chemistry in RANS context. The fine structures of turbulence are considered as a homogeneous reactor, which exchanges energy and mass with the fluid. The EDC model requires:

- A measure of the fine structures denoted with  $\star$
- A model for the intermittent behavior of the fine structures
- An evaluation of the mass exchange within the fine structures
- An evaluation for the molecular mixing and the reaction process.

Rydén et al. [REO93] propose such an EDC-model for LES modeling. The reactor concept models the effect of the turbulent scales included between the fine scale  $\star$  and subgrid scale  $\Delta$ . The difficulty consists in measuring the fine structures. For this purpose, the turbulence spectrum is modeled as a sequence of eddies, which vorticity  $\omega_n = u_n/l_n$  should fulfill between different levels  $n$ :

$$\omega_{n+1} = 2\omega_n. \quad (3.35)$$

It is equivalent to a series description, where the first term  $\omega_0$  represents the whole spectrum, and the highest  $\omega_\star$  only the fine structure level. Evidently, one can discuss the previous relation, and question about the factor 2, which seems to be unjustified. Actually, in the inertial range where  $\varepsilon = \varepsilon_n = u_n^3/l_n$ , it is always possible to find smaller eddies with a larger vorticity  $\omega_n = u_n/l_n$  than a reference. The factor 2 is just selected for mathematical convenience. Supposing isotropic turbulence and equilibrium for the dissipation between different scales, Rydén et al. [REO93] estimate the dissipation at the level  $n$ :

$$\varepsilon_n = \zeta^2 (12\omega_n u_{n+1}^2 + 15\nu\omega_n^2), \quad (3.36)$$

within  $\zeta = 0.177$  is a model constant. Expressing the dissipation at the fine structure level  $\varepsilon_\star$  and the whole dissipation  $\varepsilon$ , sum of the dissipation at each level, Rydén et al. [REO93] (p. 4) obtain a measure of the velocity and length of the fine structures as function of the Kolmogorov scale:

$$u_\star = \left(\frac{5}{16\zeta^2}\right)^{1/4} u_\eta \approx 1.78u_\eta, \quad (3.37)$$

$$l_\star = (125\zeta^2)^{1/4} \eta \approx 1.41\eta. \quad (3.38)$$

As expected, these eddies are larger than the Kolmogorov eddies. Defining an intermittency factor  $\gamma_\star = (u_\star/u')^3$ , Rydén et al. [REO93] express the mass transfer rate  $R_{i,\star}$  according to the fine structure, and finally filtered reaction rate  $\tilde{R}_i$  from Arrhenius expression. Unfortunately, the development of this model part is not detailed enough in the paper.

### Fractal Model

Giacomazzi et al. [GBF99, GBF00, GBB04] have developed a model named *Fractal Model (FM)* based on a species approach, and using the Fractal theory described in appendix A.1 (p.205). The fractal dimension  $\mathcal{D}$  is employed to determine the part of turbulent structures in the cell volume, in order to extend the Arrhenius expression for turbulent combustion, and to evaluate the filtered reaction rate  $\tilde{w}$ . Estimation of the volume fraction  $\gamma^\star$ , that the dissipative turbulent structures occupy in cells, should enable the evaluation of the subgrid effect for turbulent reactive flows. The volume fraction  $\gamma^\star$  of the fine structures is evaluated as product of the volume fraction  $\gamma_{tot}$  of the turbulent structures, with the fraction of fine structures  $\gamma_{N_\eta}$ :

$$\gamma^\star \equiv \gamma_{N_\eta} \cdot \gamma_{tot}, \quad (3.39)$$

$$\gamma^\star = \gamma_{N_\eta} \cdot \left(\frac{\Delta}{\eta}\right)^{\mathcal{D}-3}. \quad (3.40)$$

In the publications by Giacomazzi et al. [GBF99, GBF00, GBB04], the model has been coupled to a global mechanism. The reaction rate is estimated using the Arrhenius formulation and the *volume fraction of the fine structures*  $\gamma^*$  [GBF00](p. 395):

$$\tilde{w} = \gamma^* A_i [F]^{\alpha_i} [Ox]^{\beta_i} \exp \frac{-E_{a_i}}{\mathcal{R}T}. \quad (3.41)$$

### 3.4.3 Models based on the progress variable

#### LES-EBU model

The model is relevant for *high turbulent intensities*  $Re_t \gg 1$ , where the chemical time is considered infinitely small ( $Da \gg 1$ ). The formulation of its source term is essentially estimated according to turbulence, rather than to chemical considerations. In the LES context, the reactive term reads:

$$\dot{w} = C_{EBU} \bar{\rho} \frac{1}{t_\Delta} \tilde{c} (1 - \tilde{c}) \quad (3.42)$$

where  $t_\Delta = \Delta / u_{sgs}$  is the subgrid turbulent time scale, and  $C_{EBU}$  a model constant. Like for RANS modeling, this formulation has the main drawback to depend on the turbulent time, and thus on the subgrid turbulent velocity. The reaction rate is over-predicted in zones with high strain rates. This model may be coupled with an Arrhenius formulation to exploit benefits of both modelings, as achieved by Rydén et al. [REO93] with the EDC-model.

#### Flame wrinkling

Motivation of such models is to evaluate the flame wrinkling due to turbulence, in order to estimate the actual flame surface, and then the actual reaction rate. Duwig and Fuchs [DF05] have developed a model for the progress variable approach using a flame wrinkling factor. With the hypothesis that the mesh is much coarser than the reaction layer, the reaction rate is represented with a Dirac function  $\delta(x)$ . Starting from the one-dimensional progress variable filtered transport equation for a laminar flame, and applying a Gaussian filter kernel (see Eq. (3.24)) of size  $\Delta$ , the filtered reaction rate reads:

$$\tilde{w}_c = \rho_u S_l \overline{\delta(x)} = \rho_u S_l \sqrt{\frac{1}{\pi}} \frac{1}{\Delta} \exp \left( -\frac{6x^2}{\Delta^2} \right). \quad (3.43)$$

The product  $\rho_u S_l$  ensures the correct global reaction rate along the flame. This formulation may be difficult to adapt in commercial solvers, for which filter kernels are mostly box filter kernels rather than Gaussian filter kernels.

The explicit influence of the filter size  $\Delta$  in the source term  $\tilde{w}_c$  requires to parametrize the r.h.s. of the three-dimensional  $\tilde{c}$  transport equation:

$$\frac{\partial \bar{\rho} \tilde{c}}{\partial t} + \frac{\partial \bar{\rho} \tilde{u}_i \tilde{c}}{\partial x_i} = \frac{\rho_u S_l \Delta}{a_\Delta} \frac{\partial^2 \tilde{c}}{\partial^2 x_i} + \frac{\rho_u S_l}{\Delta} \Pi_c(\tilde{c}, a_\Delta). \quad (3.44)$$

$\Pi_c$  is a normalized reaction rate, which is evaluated a priori from precomputed tables. A dimensionless parameter  $a_\Delta$  is defined by Duwig and Fuchs [DF05](p. 1493) to characterize the filtered flame structure according to the mesh refinement. A simple interpretation for this term is a ratio of diffusion and chemical times relevant at the grid size:

$$\begin{aligned} a_\Delta &= \frac{t_{d,\Delta}}{t_{c,\Delta}} = \frac{\Delta^2}{D} \cdot \frac{S_l}{\Delta} \sim \frac{\Delta^2}{S_l \delta_l} \cdot \frac{S_l}{\Delta}, \\ a_\Delta &\sim \frac{\Delta}{\delta_l}. \end{aligned} \quad (3.45)$$

This parameter is small  $a_\Delta \ll 1$  for fine meshes, for which the structure of the flame can be directly solved, since the chemical time in the cell is much larger than the diffusion. This parameter is large  $a_\Delta \gg 1$  for typical LES simulations, where the mesh is much larger than the flame thickness.

For the thickened flame regime, two modifications allow to model the effect of subgrid scale eddies. The laminar flame speed is multiplied with a wrinkling factor  $S_l \rightarrow \Xi S_l$  both in diffusion and reaction rate terms, and the dimensionless factor  $a$  is based on the thickened flame:

$$a_\Delta = \frac{\Delta}{\delta_l + (\Xi - 1)\delta_t}. \quad (3.46)$$

Duwig and Fuchs approximate the parameter  $\Xi$  and  $\delta_t$  with:

$$\Xi = 1 + \frac{u_{sgs}}{S_l}, \quad (3.47)$$

$$\delta_t \approx 1.5 \times \delta_l. \quad (3.48)$$

Some ideas of this model are similar to the ones used with the TF model, as detailed in section 4 (p.61).

### 3.4.4 Progress variable and Flame Surface Density models

Flame Surface Density (FSD) models are mostly used with the progress variable approach in order to evaluate the reaction term  $\widetilde{w}_c$ . The flame surface density  $\Sigma$  estimates the flame surface area per unit volume, i.e. the *relative quantity of flame surface* within each cell. The flame surface is a relevant information for combustion modeling: The burning rate correlates with it, since the wrinkling of the flame increases the burning rate.

In order to express the reaction term, the flame surface density  $\Sigma$  is related to the progress variable  $c$  by the relation:

$$\Sigma = |\nabla c| \delta (c^* - c), \quad (3.49)$$

where  $c^* = 0.5$  is the value of the progress variable taken at the flame surface.

The filtered turbulent reaction rate can be determined using:

$$\widetilde{w}_c = \rho_u S_{t|s} \widetilde{\Sigma}, \quad (3.50)$$

where  $S_{t|_s}$  is the average turbulent flame speed along the surface. This formulation is an interesting *alternative* to the two classical progress variable formulations:  $\widetilde{w}_c \sim |\nabla \tilde{c}|$ , and  $\widetilde{w}_c \sim \tilde{c}(1 - \tilde{c})$ . The advantage of this decomposition is to separate the pure thermochemical aspects modeled with  $S_{t|_s}$ , from the turbulent/combustion interactions modeled with  $\Sigma$ , according to Poinso and Veynante [PV05](p. 224).

For the evaluation of the flame surface density  $\Sigma$ , there are different strategies using algebraic relations, a similarity model or a transport equation.

### Algebraic relations

In this case, the evaluation is based on the progress variable. Boger et al. [BVBT98] have developed an algebraic model for the LES modeling using a DNS analysis:

$$\tilde{\Sigma} = 4\beta \frac{\tilde{c}(1 - \tilde{c})}{\Delta}, \quad (3.51)$$

where the parameter  $\beta$  depends on the subgrid scale flame front wrinkling [BVBT98](p. 923). With this algebraic closure, the model is similar to classical progress variable approach using  $\tilde{c}(1 - \tilde{c})$ . The difficulty consists in evaluating correctly a length scale for dimensional reasons, in this case  $4\beta/\Delta$ .

### Similarity models

Knikker et al. [KVM02] have developed a flame surface density similarity model. The closure is achieved using a similarity method (test filter  $\hat{\cdot}$ ):

$$\tilde{\Sigma} - 4\sqrt{\frac{6}{\pi}} \frac{\tilde{c}(1 - \tilde{c})}{\Delta} \approx c \left[ \frac{\widehat{\tilde{c}(1 - \tilde{c})}}{\Delta} - \frac{\hat{\tilde{c}}(1 - \hat{\tilde{c}})}{\hat{\Delta}} \right], \quad (3.52)$$

to avoid the resolution of the transport equation for the filtered flame surface density  $\tilde{\Sigma}$ . The second term of the l.h.s., which corresponds to the resolved flame surface, as well as the term on the r.h.s. in brackets are known. The constant  $c$  must be determined in order to estimate  $\tilde{\Sigma}$ . Its evaluation is achieved using the fractal theory, described in section A.1 (p.205). The resolved flame surface density scales with the mesh size and the inner cut-off length  $\xi_i$  according to the relation Eq. (A.1):

$$4\sqrt{\frac{6}{\pi}} \frac{\tilde{c}(1 - \tilde{c})}{\Delta} \approx \tilde{\Sigma} \left( \frac{\Delta}{\xi_i} \right)^{2-\mathcal{D}}, \quad (3.53)$$

$$\text{so that: } c \approx \frac{1}{1 - \left( \frac{\hat{\Delta}}{\hat{\xi}_i} \right)^{2-\mathcal{D}}} 4\sqrt{\frac{6}{\pi}} \left[ \left( \frac{\Delta}{\xi_i} \right)^{\mathcal{D}-2} - 1 \right]. \quad (3.54)$$

$\mathcal{D}$  is the fractal dimension. This model has the drawback of requiring an evaluation of the inner cut-off scale. Knikker et al. have expressed it using the simple relation  $\xi_i \approx 3\delta_l^0$ .

### Transport equations

Hawkes and Cant [HC01] have presented a LES model with two transport equations for the progress variable  $c$  and the flame surface density  $\Sigma$ . The resolution of the progress variable allows the description of the flame by determining burnt and unburnt zones. The estimation of the flame surface density with an extra transport equation should offer a more accurate evaluation of the reaction rate in order to resolve the progress variable.

Tabor and Weller [TW04] have also developed a model based on two transport equations, one for the progress variable (actually  $1 - c$ ) and one for the subgrid scale flame front wrinkling defined with:

$$\Xi = \tilde{\Sigma}/|\nabla\tilde{c}|.$$

The use of  $\Xi$  requires more caution than  $\tilde{\Sigma}$ , since the definition of the variable is conditioned by the presence of the flame front  $|\nabla\tilde{c}| \neq 0$ .

#### 3.4.5 Level-set approach: G-equation

This model has been introduced by Peters for RANS modeling [Pet00]<sub>(p. 109)</sub> and then adapted for the LES modeling. This approach has been also mostly employed by Pitsch and Duchamp de Lageneste [DP00, DP01, DP02, Pit06, PD02]. This model consists in a geometrical description of the flame. A *passive scalar*  $G$  is resolved with the help of its transport equation, where an iso-surface  $G_0$  of the field represents the flame front. Peters [Pet99] employs the value  $G_0 = 0$  and imposes  $|\nabla G(x, t)| = 1$ , so that  $G$  corresponds to a distance to the flame. The basic propagation equation for the scalar  $G$  reads:

$$\rho \frac{\partial G}{\partial t} + \rho \mathbf{u} \cdot \nabla G = \rho S_d |\nabla G|, \quad (3.55)$$

where  $S_d$  stands for the flame displacement speed.

The adaptation of this model to different turbulent combustion regimes depends on the relevant evaluation of  $S_d$ . First, an evaluation has been proposed for the corrugated flame regime based on the laminar stretched flame theory (see section 2.3.4 (p.29)). Peters [Pet00]<sub>(p. 91, 104)</sub> has extended it for both the corrugated flame regime and the thickened flame regime:

$$\rho \frac{\partial G}{\partial t} + \rho \mathbf{u} \cdot \nabla G = \rho S_l |\nabla G| - \rho D \kappa |\nabla G|. \quad (3.56)$$

Locally, the stretched flame displacement speed is numerically close to the unstretched laminar flame speed  $S_l$  as demonstrated by Peters [Pet00]<sub>(p. 106)</sub>. The diffusion  $D \kappa |\nabla G|$  stands for the effect of the Kolmogorov eddies which can penetrate the flame front and induce the local curvature  $\kappa$ . With Favre filtering the propagation equation for the scalar  $G$  reads:

$$\bar{\rho} \frac{\partial \tilde{G}}{\partial t} + \bar{\rho} \tilde{\mathbf{u}} \cdot \nabla \tilde{G} = \bar{\rho} S_t |\nabla \tilde{G}| - \bar{\rho} (D + D_t) \tilde{\kappa} |\nabla \tilde{G}|. \quad (3.57)$$

$D_t$  is the subgrid turbulent viscosity due to the closure of the unknown turbulent transport term  $\overline{\nabla \cdot \mathbf{u}' G'}$ .  $S_t$  is a turbulent flame speed introduced to replace the unclosed term  $\overline{\rho S_l |\nabla G|}$ .

A model for the turbulent flame speed  $S_t$  is therefore required. Duchamp de Lageneste and Pitsch [DP01](p. 98) [PD02](p. 2004) [Pit05](p. 597) have used the following expression:

$$\frac{S_t}{S_l} = -\frac{c_1}{Sc_t} \frac{\nu_t}{D} \frac{S_l}{u'_\Delta} + \sqrt{\left(\frac{c_1}{Sc_t} \frac{\nu_t}{D} \frac{S_l}{u'_\Delta}\right)^2} + c_2 \frac{\nu_t}{Sc_t D}. \quad (3.58)$$

Values for the model constants  $c_1$  and  $c_2$  has been evaluated by Duchamp de Lageneste and Pitsch [DP00]. This expression is derived from the one developed by Peters [Pet99] for RANS modeling. Naturally, the *closure for the turbulent speed has to be distinguished from the level-set approach*. It would be interesting to compute the level-set approach with another turbulent flame speed closure, for example: TFC-LES and SFC closures described and derived respectively in section 6 (p.87) and section 7 (p.99). Or reciprocally, computing progress variable approach models, mostly using a turbulent flame speed closure, with this estimation of  $S_t$  would allow the distinction between the quality of this approach, and the quality of the turbulent flame speed closure.

A theoretical drawback is due to the use of the flame displacement speed. As this velocity only represents the displacement speed of the iso-value of  $G$  coinciding with the flame front, the equation is also only valid on the flame front, i.e. for  $G = G_0$ . A computational difficulty of the level-set approach consists in the so-called *reinitialization procedure*. As already explained, Peters defines  $G$  as *a distance* to the flame by imposing  $|\nabla \tilde{G}| = 1$ . This condition must be valid for any point at any time, so that the reinitialization procedure developed for level-set approach of two-phase flow simulations by Sussman et al. [SSO94] has to be executed at each time-step and for each cell.

### 3.5 Choice of the Thickened Flame (TF), Turbulent Flame speed Closure (TFC-LES) and Subgrid Flame Closure (SFC) models

In literature, comparisons of LES combustion models are rare, so that it is difficult to evaluate and choose models without testing them. In the last sections, most of the known models have been presented, and their hypothesis stressed and discussed when possible. Only subjective or intuitive suggestions could be delivered, so that the TF and TFC-LES models have been chosen for practical reasons.

The G-equation model was of interest. It has not been selected, because the implementation of the renormalization procedure without access to *Fluent* source codes would not have been feasible. The TF model has been selected, because it has been largely validated against industrial applications, although only with the solver *AVBP*. The TFC-LES has been chosen for two main reasons. It is based on the progress variable approach, which requires a reduced CPU-effort. The TFC-RANS model has been largely used in our research group, also with our own implementation in *Fluent*, so that pro and cons of this model were already known. After testing these two models, the need for a new model for the progress variable approach has motivated the development of the SFC model.



## 4 Thickened Flame model

The *Thickened Flame (TF) model* has been developed and validated conjointly at the *ECP-EM2C* (Chatenay-Malabry, France) and the *CERFACS* (Toulouse, France) by Colin et al. [CDVP00, Col00]. It has been employed for simulations of gas turbines and turbomachines by Colin, Selle et al. [Col00, SLP<sup>+</sup>04], as well as for car engines by Moureau et al., Soulère and Thobois et al. [MBAP04, Sou03, TRS<sup>+</sup>05] implemented in the code *AVBP* [CER]. To our knowledge and except in our own works [DHP05, DP07], only results of the TF model used with the code *AVBP* have been published.

The formulation of the model for the reaction term is based on a straightforward physical idea. But the mathematical development induces a complex closure because of the formulation of the filtered reaction rate. It is based on a higher order derivative operator, which is difficult to evaluate for commercial solvers like *Fluent*, since intern derivative routines are not available for users.

The aim of this chapter is to present the model and its particularities. A formulation identical to the original model is proposed and implemented in *Fluent*. The limitation which is imposed on the mesh structure is discussed. A slightly modified formulation, referred as TF' for convenience, is proposed in the second section. This new version allows simulations with any grids, while remaining close to the original model motivation. The thermochemical characteristics used with the TF/TF' models, as well as detailed explanations on the implementation with the so-called UDFs, are given, respectively, in appendix A.2 (p.206) and appendix A.3 (p.212).

The model and the complete justification of its formulation are described in detail by Colin et al. [Col00, CDVP00].

### 4.1 Principle of the TF model

In this section, the thickened flame model is introduced. The underlying idea of the model, i.e. artificial thickening of the flame in order to resolve it on the computational grid, is presented first. Then, it is explained why an *efficiency function*  $E$  must be introduced to compensate for the reduced surface area of the thickened flame. In order to compute  $E$ , the intensity of velocity fluctuations  $u'_{\Delta_e}$  at a test filter scale  $\Delta_e$  must be estimated. Difficulty to achieve this estimation in *Fluent* is discussed.

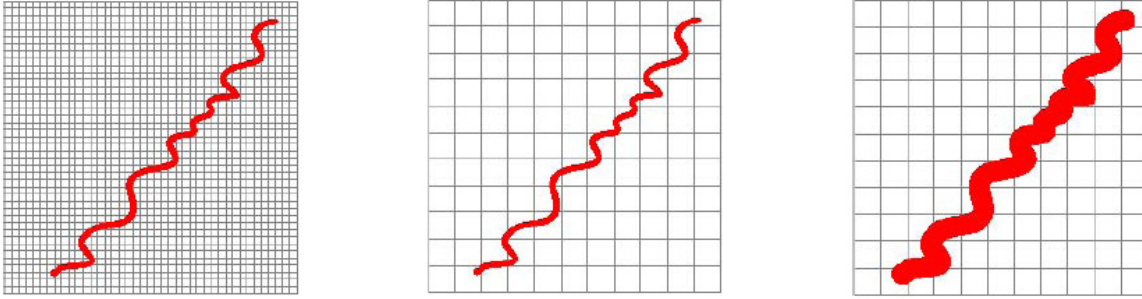


**Fig. 4.1:** Numerical thickening with the TF model: Real flame with DNS mesh (left), real flame with LES mesh (center) and thickened flame with LES mesh (right)

#### 4.1.1 Artificial thickening of the flame

The TF-LES model belongs to the most recent models for turbulent premixed combustion, which are developed *especially* for LES simulations, as proposed by Colin et al. [CDVP00], Flohr and Pitsch [FP00], Giacomazzi et al. [GBB04], and Durand et al. [DPGS07]. In such models, a closure must be invoked for the filtered reaction rate, because LES grids are not fine enough to resolve the flame front explicitly. This is particularly true for industrial applications, where Reynolds numbers are high. The TF model is based on the idea to artificially thicken the flame front, so that the thickened flame can be explicitly computed. This is simply represented in Figure 4.1 (p.62): The difference of refinement between a LES and a DNS grid is displayed. The impossibility to resolve explicitly the flame front with the LES is revealed. The aim is therefore to thicken the flame while maintaining its propagation velocity. Maintaining the flame speed is of importance, since it influences the stabilization and position of the flame in the flow. Considering the scaling of laminar flame speed  $S_l^0$  and thickness  $\delta_l^0$  with molecular diffusivity  $D$  and reaction rate  $\dot{w}$ :

$$S_l^0 \sim \sqrt{D\dot{w}}, \quad (4.1)$$

$$\delta_l^0 \sim \frac{D}{S_l^0} \sim \sqrt{\frac{D}{\dot{w}}}, \quad (4.2)$$

this modification of the flame structure may be realized by increasing the diffusivity  $D$  by a factor  $F > 1$ , while decreasing the reaction rate by the same factor. It follows that for the thickened flame (superscript “1”):

$$S_l^1 = S_l^0, \quad (4.3)$$

$$\delta_l^1 = F\delta_l^0 \sim \frac{FD}{S_l^0}. \quad (4.4)$$

However, the thickening of the flame from  $\delta_l^0$  to  $\delta_l^1$  modifies the interaction between combustion and turbulence. For example, the Damköhler number  $Da$ , defined as the ratio between turbulent and chemical times in section 2.4.2 (p.35), is decreased by a factor  $F$

when the flame is thickened:

$$\begin{aligned} \text{Da} &= \frac{t_t}{t_c} \sim t_t \dot{w} \\ \Rightarrow \text{Da}^1 &= \frac{1}{F} \text{Da}^0. \end{aligned} \quad (4.5)$$

The thickened flame is thus less sensitive to turbulent eddies.

The artificial thickening of the flame has eventually two effects:

- The first effect corresponds to the aim of the model. The filtered reaction rate  $\widetilde{w}_1$  is distributed over a larger region in space than the real reaction rate  $\dot{w}_0$ , such that it can be resolved on the computational grid
- Secondly, turbulent eddies in the range of scales  $[\delta_l^0; \delta_l^1]$  cannot wrinkle the thickened flame (while they do wrinkle the real flame), such that the effective flame surface and therefore the overall reaction rate, which scales as the product of flame surface and burning velocity, is reduced.

An efficiency function  $E$  is thus introduced in the TF model to compensate for this undesired effect so that:

$$\widetilde{w}_1 = \frac{E}{F} \widetilde{w}_0. \quad (4.6)$$

The reaction rate  $\widetilde{w}_0$  is evaluated from the Arrhenius formulation using the filtered variables. The chemical mechanism employed is described in appendix A.2 (p.206). With influence of the thickening factor  $F$  and the efficiency function  $E$ , species transport equations read:

$$\frac{\partial \bar{\rho} \tilde{y}_\alpha}{\partial t} + \frac{\partial \bar{\rho} \tilde{u}_i \tilde{y}_\alpha}{\partial x_i} = \frac{\partial}{\partial x_k} \left( E F D_\alpha \frac{\partial \tilde{y}_\alpha}{\partial u_k} \right) + \frac{E}{F} \tilde{w}_\alpha.$$

#### 4.1.2 The efficiency function

The efficiency function aims at compensating the reduced flame surface, induced by the flame thickening. However, instead of expressing the actual flame surface itself, a dimensionless wrinkling factor  $\Xi$  is introduced to evaluate the required efficiency function  $E$ . It represents the ratio of the flame surface to its projection in the propagating direction. the wrinkling  $\Xi$  is larger for the real flame than for the thickened flame, since the former counts more small scale cusps, which increase the surface as depicted in Figure 4.2 (p.64).

Colin et al. [CDVP00] propose the following expression for the wrinkling factor  $\Xi$ , based on earlier work by Meneveau and Poinso [MP91]:

$$\Xi = 1 + \alpha \frac{u'_{\Delta_e}}{S_l^0} \Gamma \left( \frac{\Delta_e}{\delta_l}, \frac{u'_{\Delta_e}}{S_l^0} \right), \text{ where} \quad (4.7)$$

$$\alpha = \frac{2 \ln 2}{3 c_{ms} (\text{Re}_t^{1/2} - 1)} \text{ and } c_{ms} = 0.28. \quad (4.8)$$

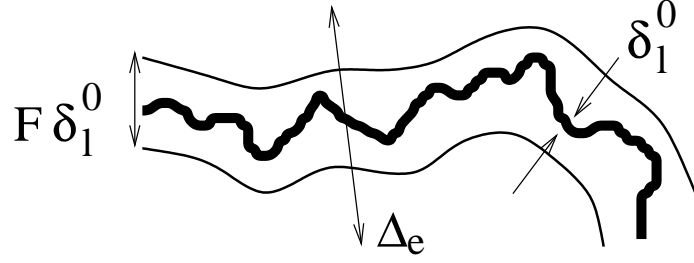


**Fig. 4.2:** Scales  $\delta_l^0$ ,  $\delta_l^1$  and  $\Delta_e$

The term  $\alpha u'_{\Delta_e} / S_l^0 \Gamma$  expresses the increase of flame wrinkling due to turbulent stretch, where  $\Delta_e$  is a test filter length scale. This test filter should bring an observation scale at the thickened flame for the similarity method employed in the following, so that

$$\Delta_e = \delta_l^1 = F \delta_l^0 > \Delta \quad (4.9)$$

appears as a reasonable choice.  $\Delta_e$  must be strictly larger than  $\Delta$ , and possibly comparable to the thickened flame scale, in order to extract fluctuations between the grid scale and the thickened flame scale for the evaluation of the efficiency function  $E$ , as justified by Colin et al. [CDVP00] (p. 1853). The velocity  $u'_{\Delta_e}$  is an evaluation of velocity fluctuations at the test scale  $\Delta_e$ . Its estimation, using a similarity assumption, is detailed in the next section.

The function  $\Gamma$  stands for the dimensionless stretch of a flame with flame velocity  $S_l^0$  and thickness  $\delta_l$  submitted to the action of a range of vortices as introduced by Meneveau and Poinso [MP91]:

$$\Gamma \left( \frac{\Delta_e}{\delta_l^i}, \frac{u'_{\Delta_e}}{S_l^0} \right) \approx 0.75 \exp \left[ -1.2 \left( \frac{u'_{\Delta_e}}{S_l^0} \right)^{-0.3} \right] \left( \frac{\Delta_e}{\delta_l^i} \right)^{2/3}. \quad (4.10)$$

Finally the efficiency function  $E$  is expressed as the ratio between the wrinkling factor  $\Xi$  of the real flame with  $\delta_l = \delta_l^0$  and that of the thickened flame with thickness  $\delta_l^1$ :

$$E = \frac{\Xi_{|\delta_l=\delta_l^0}}{\Xi_{|\delta_l=\delta_l^1}} > 1. \quad (4.11)$$

The wrinkling factor  $\Xi$  and the efficiency function  $E$  are plotted qualitatively in Figure 4.3 (p.65) as a function of  $\delta_l$ , suggesting that the wrinkling factor can be quite large for  $\delta_l \ll \Delta_e$ . The impact of  $u'_{\Delta_e}$  on the efficiency function  $E$  is weak, because both  $\Xi_{|\delta_l^0}$  and  $\Xi_{|\delta_l^1}$  increase with  $u'_{\Delta_e}$ . It is helpful to consider a situation typical for turbulent combustion at high Reynolds numbers. Then it is possible to choose a test filter scale sufficiently large to have  $u'_{\Delta_e} / S_l^0 \gg 1$ , such that the exponential function in Eq. (4.10) approaches unity. In this limit, the wrinkling factor tends to

$$\Xi \rightarrow \alpha \frac{u'_{\Delta_e}}{S_l^0} \left( \frac{\Delta_e}{\delta_l^0} \right)^{2/3}, \quad (4.12)$$

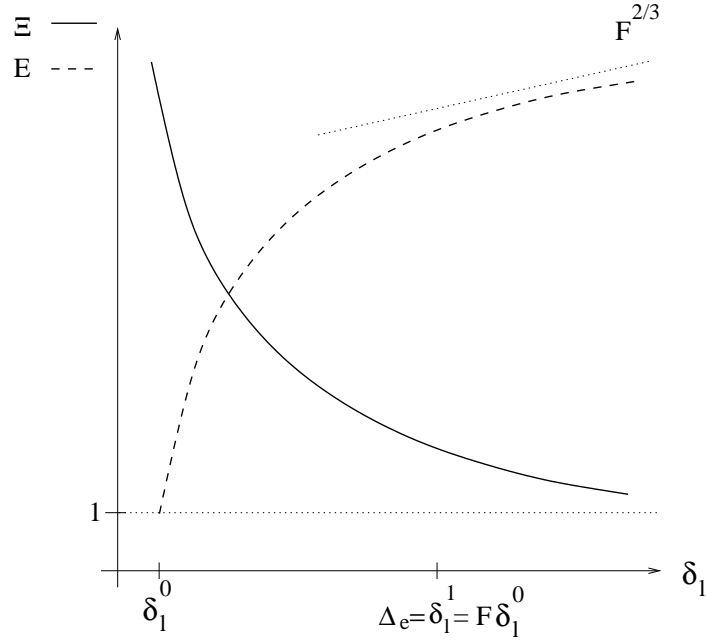


**Fig. 4.3:** Wrinkling factor  $\Xi$  and efficiency function  $E$

and the efficiency function  $E$  scales with

$$E \sim \left( \frac{\delta_l^1}{\delta_l^0} \right)^{2/3} = F^{2/3}. \quad (4.13)$$

Indeed, in this limit the value of the test filter velocity  $u'_{\Delta_e}$  has no effect on the efficiency function.

#### 4.1.3 Velocity fluctuation at the test-filter

The norm of the velocity fluctuation  $u'_{\Delta_e}$  relative to the filter scale  $\Delta_e$  has still to be evaluated. Its calculation is discussed in detail by Colin et al. [CDVP00](p. 1853). This is a non-trivial problem, since this velocity fluctuation does not correspond to the grid size  $\Delta$ , but to the filter size  $\Delta_e$ . The Smagorinsky model [Sma63] as well as more complex turbulent kinetic energy transport equation models [FLU05] [Kim04](p. 6) cannot directly deliver the fluctuation at the filter scale level  $\Delta_e$ . Explicit filtering *at the scale*  $\Delta_e$  would be most precise, but computationally expensive and complicated, since a large number of cells may be required for this procedure. A similarity assumption according to Bardina et al. [BFR80] has been finally retained by Colin et al.:

$$u'_{\Delta_e} \sim OP(\tilde{\mathbf{u}}) \sim |(\tilde{\mathbf{u}} - \hat{\mathbf{u}})|. \quad (4.14)$$

$\tilde{\mathbf{u}}$  represents the numerical solution of the velocity field, and  $\hat{\mathbf{u}}$  the explicit filtered field. To circumvent the employ of an explicit filter,  $\hat{\mathbf{u}}$  is written as a Taylor series function of

the box-filter kernel  $G$  with cut-off scale  $\Delta_e$  as presented by Sagaut for a one-dimensional case [Sag01]<sub>(p. 162)</sub>:

$$\hat{u} = \int_{-\infty}^{+\infty} G(x-y) \widetilde{u}(y) dy \quad (4.15)$$

$$\hat{u} = \tilde{u} + \frac{1}{24} \Delta_e^2 \left( \frac{\partial^2 \tilde{u}}{\partial^2 x} \right) + \dots, \quad (4.16)$$

thanks to the symmetry and conservation properties of the filter kernel  $G$ , the first derivative of  $\tilde{u}$  cancels out. This interesting result makes the approximation of the explicit filter by a second order discretization operator possible:

$$u'_{\Delta_e} \sim \Delta_e^2 \left| \frac{\partial^2 \tilde{u}}{\partial^2 x} \right|. \quad (4.17)$$

This operator can be generalized to a three-dimensional case:

$$u'_{\Delta_e} \sim \Delta_e^2 \left| \frac{\partial^2 \tilde{u}_i}{\partial^2 x_j} \vec{x}_i \right| = \Delta_e^2 \left| \begin{array}{c} \frac{\partial^2 \tilde{u}}{\partial^2 x} + \frac{\partial^2 \tilde{u}}{\partial^2 y} + \frac{\partial^2 \tilde{u}}{\partial^2 z} \\ \frac{\partial^2 \tilde{v}}{\partial^2 x} + \frac{\partial^2 \tilde{v}}{\partial^2 y} + \frac{\partial^2 \tilde{v}}{\partial^2 z} \\ \frac{\partial^2 \tilde{w}}{\partial^2 x} + \frac{\partial^2 \tilde{w}}{\partial^2 y} + \frac{\partial^2 \tilde{w}}{\partial^2 z} \end{array} \right|. \quad (4.18)$$

A vorticity operator can be conjointly applied to remove the dilatational part (related to the divergence) of velocity. Colin et al. [CDVP00] have finally obtained an equivalent expression for the filter velocity:

$$u'_{\Delta_e} = c \frac{\Delta_e^2 \Delta}{24} \left| \epsilon_{ijk} \frac{\partial^3 \tilde{u}_k}{\partial^2 x_l \partial x_j} \vec{x}_i \right| \quad (4.19)$$

where they approximate  $c \approx 2$  according to Cook's [Coo97] similarity model based on isotropic homogeneous turbulence. The factor  $\Delta_e$  appears because of the Taylor series development of the filter at this scale. The factor  $\Delta$  appears because of the derivation operation at the grid scale due to the vorticity.

Evidently, this operator requires a third order derivative of the velocity. The evaluation of this term in *Fluent*, as well as in other commercial solvers, is *not trivial*. For example only the gradient (i.e. the first derivative of the velocity) can be known using UDFs in *Fluent*. The complexity to implement the TF model is thus mostly due to the term  $u'_{\Delta_e}$ . The algorithm especially developed to achieve this discretization is described in appendix A.3.1 (p.212).

## 4.2 Finite-volume based evaluation of test filter velocity: TF' model

The implementation of the TF model, identical to the original formulation of Colin et al. [CDVP00], requires a (non-uniform) cartesian mesh in a commercial solver. Our aim is now to present an alternative strategy for evaluating the filter velocity  $u'_{\Delta_e}$  with any mesh.

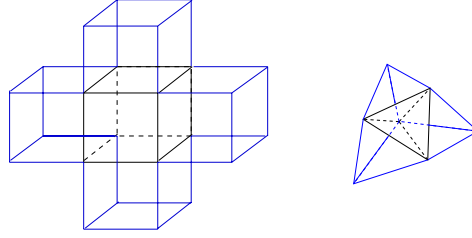


**Fig. 4.4:** Test filter with the face-sharing neighbor cells

In the work by Colin et al. [CDVP00], the development in discrete Taylor series has naturally led to the use of a finite difference approximation. For an unstructured formulation, it makes more sense to develop the scale similarity method with a finite volume approximation. An explicit filtering is required to achieve it. The new formulation, named TF' for convenience, is described in the following. In appendix A.3.3 (p.217), the practical implementation of the TF' model conjointly with the MSM turbulence model, also based on an explicit filter, is proposed.

The velocity fluctuation  $u'_{\Delta_e}$  is evaluated by directly using the *scale similarity* assumption according to Bardina et al. [BFR80] without any discrete filter operator. The dilatational part of the field is again suppressed by writing the analog expression with the rotational operator:

$$u'_{\Delta_e} = c\Delta |\nabla \times (\tilde{\mathbf{u}} - \hat{\mathbf{u}})| = c\Delta |\nabla \times \tilde{\mathbf{u}} - \nabla \times \hat{\mathbf{u}}|. \quad (4.20)$$

The difficulty consists in evaluating the curl of the filtered velocity  $\nabla \times \hat{\mathbf{u}}$ . This operator is different (except if the mesh is uniform) from the filtered vorticity:

$$\nabla \times \hat{\mathbf{u}} \neq \widehat{\nabla \times \mathbf{u}}. \quad (4.21)$$

The evaluation can be achieved by developing the filter using its linear definition:

$$\hat{\mathbf{u}} = \frac{\sum_k \tilde{\mathbf{u}}_k \text{vol}_k}{\sum_k \text{vol}_k} \quad (4.22)$$

where  $\tilde{\mathbf{u}}_k$  and  $\text{vol}_k$  are respectively the velocity vector and volume of each cell surrounding the cell of interest. In this work, cells having a common surface are selected, i.e. six cells for hexahedral meshes and four for tetrahedral meshes as depicted in Figure 4.4 (p.67).

Equivalent filter formulations could be naturally employed. However, the gain in precision would not justify the increased implementation complexity and memory-cost.

The vorticity of the filtered velocity is then:

$$\nabla \times \hat{\mathbf{u}} = \epsilon_{ijk} \frac{\partial \hat{u}_k}{\partial x_j} \vec{x}_i = \begin{pmatrix} \frac{\partial \hat{u}_2}{\partial y} - \frac{\partial \hat{u}_1}{\partial z} \\ \frac{\partial \hat{u}_3}{\partial z} - \frac{\partial \hat{u}_2}{\partial x} \\ \frac{\partial \hat{u}_1}{\partial x} - \frac{\partial \hat{u}_3}{\partial y} \end{pmatrix} \quad (4.23)$$

As an example, the derivative with respect to  $y$  of the  $z$ -component of the filtered velocity is developed by exploiting the linearity of the derivation operator (note that the Einstein summation notation is not used here):

$$\begin{aligned}\frac{\partial \hat{w}}{\partial y} &= \frac{\partial}{\partial y} \left( \frac{\sum_k \tilde{w}_k \text{vol}_k}{\sum_k \text{vol}_k} \right) = \left( \sum_k \text{vol}_k \right)^{-2} \left( \frac{\partial \sum_k \tilde{w}_k \text{vol}_k}{\partial y} \sum_k \text{vol}_k - \frac{\partial \sum_k \text{vol}_k}{\partial y} \sum_k \tilde{w}_k \text{vol}_k \right) \\ \frac{\partial \hat{w}}{\partial y} &= \left( \sum_k \text{vol}_k \right)^{-1} \left( \sum_k \frac{\partial \tilde{w}_k}{\partial y} \text{vol}_k + \sum_k \frac{\partial \text{vol}_k}{\partial y} \tilde{w}_k \right) \\ &\quad - \left( \sum_k \text{vol}_k \right)^{-2} \left( \sum_k \tilde{w}_k \text{vol}_k \right) \sum_k \frac{\partial \text{vol}_k}{\partial y}.\end{aligned}\tag{4.24}$$

The non-uniformity of the mesh makes the expression more complicated. For uniform meshes, each derivative of the volume naturally cancels out, and only the first term remains, which correspond to  $\nabla \times \hat{\mathbf{u}} = \widehat{\nabla \times \mathbf{u}}$ .

Disposing of the three components of the explicit filtered vorticity  $\nabla \times \hat{\mathbf{u}}$ , and of the vorticity  $\nabla \times \tilde{\mathbf{u}}$  enables the evaluation of the filtered velocity  $u'_{\Delta e}$ . This procedure may seem complexer than the original expression. However, it is more flexible in *Fluent*, and can be adapted for any mesh thanks to the finite volume formulation. Details on the implementation are given in appendix A.3.2 (p.215).

### 4.3 Conclusion

The difficulty to implement the TF model in a commercial solver, without modifying the source code has been stressed. For this reason, a modified formulation TF' has been proposed. The two formulations are compared and validated against two other models in section 8 (p.139).

In section A.3.3 (p.217), the choice of the cold turbulence model used with the TF model, and its implementation in *Fluent* are discussed. Beside the Smagorinsky and turbulent kinetic energy transport equation models, for which the validation has been achieved in section 8 (p.139), a third turbulence model, the Mixed Scale Model by Sagaut [Sag01] (p. 101), is considered. Unfortunately, its complete validation was not feasible during this thesis.

## 5 Progress variable approach

As explained in section 3.4 (p.50), there are several representations of combustion, and for each of them different models have been developed. The previous chapter has detailed the TF model, which is based on the species approach.

The aim of this chapter is to present a second representation: The *progress variable* approach. The chemical description is replaced with only one variable. The adiabatic perfectly premixed case is presented in the first section 5.1 (p.69) as introduction. In the case of the lean inhomogeneously premixed combustion, defined in section 2.3.1 (p.23), the transport equation must be extended to consider the effects of diffusion due to the mixture fraction  $Z$ . In case of a non-adiabatic combustion, solving the energy equation is required, and a sub-model, which takes into consideration thermal quenching in the progress variable equation, is proposed in section 5.3 (p.81).

Two model closures for the progress variable approach, the Turbulent Flame speed Closure (TFC-LES) and the Subgrid Flame Closure (SFC) models, are respectively described and derived in the next two chapters. The main difficulty namely remains the closure of the reactive term in the filtered progress variable transport equation for the LES modeling.

### 5.1 Definitions

In this part, the description of reactive flows using the progress variable approach is introduced with the particular case of an adiabatic perfectly premixed mixture.

The progress variable is usually noted with  $c$ , dimensionless and normalized, so that  $c = 0$  describes an unburnt mixture,  $c = 1$  a burnt mixture, and  $0 < c < 1$  the resolved flame front where combustion occurs. The aim is no longer to study all the species in the flow, but to determine at given location and instant whether the mixture is burnt or unburnt.

#### 5.1.1 Progress variable transport equation

The transport equation for the progress variable reads, according to Zimont et al. [ZL95, ZPBW97]:

$$\frac{\partial \rho c}{\partial t} + \frac{\partial \rho c u_i}{\partial x_i} = \frac{\partial}{\partial x_i} \left( \rho \frac{\nu}{Sc_c} \frac{\partial c}{\partial x_i} \right) + \dot{w}_c. \quad (5.1)$$

This equation describes the local rate of change of the progress variable. The r.h.s. contains the diffusive and reactive terms. For the diffusion coefficient, a Schmidt number for

the progress variable  $Sc_c$  has been introduced. The Schmidt number of nitrogen for the progress variable is selected, since the mixture contains more than 90% of air, i.e. more than 70% of nitrogen  $N_2$ .

For lean perfectly premixed mixture, a simple relation can be written between the fuel mass fraction and the normalized progress variable:

$$c = 1 - \frac{y_f}{y_f^0}, \quad (5.2)$$

where  $y_f$  is the local fuel mass fraction and  $y_f^0$  is the uniform unburnt fuel mass fraction (for a rich mixture an equivalent relation based on the oxygen mass fraction could be written). As long as the Navier-Stokes equations are considered without averaging and filtering, the reaction source term can be directly evaluated from the fuel mass fraction:

$$\dot{w}_c = -\frac{\dot{w}_f}{y_f^0}. \quad (5.3)$$

The evaluation of the filtered reaction rate  $\tilde{w}_c$  in LES modeling is a central topic of this thesis (see the next two chapters).

### 5.1.2 Reference case: adiabatic and perfectly premixed combustion

In the case of the *perfectly premixed* combustion, the source terms for the fuel mass fraction, progress variable and enthalpy are proportional. Additionally, if the process is *adiabatic*, if their diffusion coefficients are also equal, and the fuel Lewis number is assumed to equal one,

$$Le_f \equiv \frac{Sc_f}{Pr} = \frac{a}{D_f} = 1,$$

then these three variables are solutions of the same transport equation, and therefore equivalent.

Consequently, the progress variable can be also defined as a linear function of the temperature:

$$c = 1 - \frac{y_f}{y_f^0} = \frac{T - T_u}{T_{ad} - T_u}. \quad (5.4)$$

Using the perfect gas law for incompressible flows (see Eq. (2.13)) leads to the similar relation with the density:

$$\rho = \rho_u(1 - c) + c\rho_b. \quad (5.5)$$

Therefore, in the case of the *adiabatic perfectly premixed combustion* and neglecting the effect of differential diffusion between enthalpy and species, the progress variable allows to evaluate the local temperature and density. Compared to the isothermal case, only the progress variable has to be solved. The feedback of the combustion on the flow is achieved by modifying the density according to Eq. (5.5).

In the following, the modifications required to employ the progress variable approach in general cases are described.

## 5.2 Inhomogeneously premixed combustion

The distinction between the non-perfectly, the inhomogeneously and the partially premixed combustion has been defined in section 2.3.2 (p.23). The mathematical formalism presented in this section should be valid for both inhomogeneously and partially premixed combustion. The non-perfectly case can be considered as a part of the inhomogeneously case with the formalism used, so that in the following, there are only references to inhomogeneously and partially premixed flames. Some further hypotheses and simplifications are made for the inhomogeneously premixed case, which is treated in more details with the simulation of the TD1 burner in section 8.3 (p.173). To model inhomogeneously and partially premixed turbulent combustion, the progress variable formulation must be adapted.

First the transport equation Eq. (5.1), which has been presented for a perfect premixed mixture, is no longer valid since three additional terms must be considered. In the case of the lean premixed combustion (i.e. for the inhomogeneously premixed case, but not the partially premixed case), only one of these three terms is required.

Secondly, the evaluation of the laminar flame speed, employed in the reaction term closure, must be adapted, since it is no more uniform. It must depend on the local mixture fraction  $Z$  (defined in section 2.3.2 (p.24)), and also eventually on its fluctuation.

### 5.2.1 Extended transport equation for the progress variable

In this part, contributions of several authors are used and discussed to extend the progress variable formulation from the perfectly premixed to the inhomogeneously premixed combustion. As defined in section 2.3.1 (p.23), inhomogeneously and partially premixed combustion are related to local variations of the air-fuel mixture. These variations should be considered with the progress variable approach.

It has been demonstrated by Domingo, Vervisch and Bray, as well as illustrated by Duwig and Fuchs [DVB02, DVR05, BDV05, DF04, DF05], that the progress variable approach, as it has been previously presented for the perfect premixed case, is neither valid for the inhomogeneously, nor for the partially premixed combustion. Scalar dissipation terms due to the non-uniform mixture fraction appear in the transport equation for the progress variable.

The correct transport equation for the progress variable is analytically derived from the fuel mass fraction transport equation. The fuel mass fraction  $y_f(\mathbf{x}, t)$  is defined as function of the progress variable  $c(\mathbf{x}, t)$  and of the mixture fraction  $Z(\mathbf{x}, t)$  as defined by Bray et al. [BDV05](p. 433, Eq.3):

$$y_f(\mathbf{x}, t) = y_f \{c(\mathbf{x}, t), Z(\mathbf{x}, t)\}. \quad (5.6)$$

The partial derivatives for the fuel mass fraction therefore depends on the progress variable and on the mixture fraction (for one-dimension case):

$$\frac{\partial y_f}{\partial x} = \frac{\partial y_f}{\partial c} \frac{\partial c}{\partial x} + \frac{\partial y_f}{\partial Z} \frac{\partial Z}{\partial x} \quad (5.7)$$

$$\frac{\partial}{\partial x} \left( \frac{\partial y_f}{\partial c} \right) = \frac{\partial^2 y_f}{\partial^2 c} \frac{\partial c}{\partial x} \frac{\partial c}{\partial x} + \frac{\partial^2 y_f}{\partial c \partial Z} \frac{\partial Z}{\partial x} \frac{\partial c}{\partial x} + \frac{\partial y_f}{\partial c} \frac{\partial^2 c}{\partial^2 x} \quad (5.8)$$

$$\text{and } \frac{\partial}{\partial x} \left( \frac{\partial y_f}{\partial Z} \right) = \frac{\partial^2 y_f}{\partial^2 Z} \frac{\partial Z}{\partial x} \frac{\partial Z}{\partial x} + \frac{\partial^2 y_f}{\partial Z \partial c} \frac{\partial c}{\partial x} \frac{\partial Z}{\partial x} + \frac{\partial y_f}{\partial Z} \frac{\partial^2 Z}{\partial^2 x}. \quad (5.9)$$

The second derivative counts five terms:

$$\frac{\partial^2 y_f}{\partial^2 x} = \frac{\partial^2 y_f}{\partial^2 c} \frac{\partial c}{\partial x} \frac{\partial c}{\partial x} + \frac{\partial^2 y_f}{\partial^2 Z} \frac{\partial Z}{\partial x} \frac{\partial Z}{\partial x} + 2 \frac{\partial^2 y_f}{\partial c \partial Z} \frac{\partial c}{\partial x} \frac{\partial Z}{\partial x} + \frac{\partial y_f}{\partial c} \frac{\partial^2 c}{\partial^2 x} + \frac{\partial y_f}{\partial Z} \frac{\partial^2 Z}{\partial^2 x}. \quad (5.10)$$

Finding the expression of the complete progress variable transport equation may not be intuitive, and deserves to be detailed. The fuel transport equation can be expanded by replacing the partial derivatives of the fuel mass fraction  $y_f$  by their expressions:

$$\begin{aligned} & \rho \left( \frac{\partial y_f}{\partial c} \frac{\partial c}{\partial t} + \underbrace{\frac{\partial y_f}{\partial Z} \frac{\partial Z}{\partial t}}_2 \right) + \underbrace{y_f \frac{\partial \rho}{\partial t}}_1 + \rho u \left( \frac{\partial y_f}{\partial c} \frac{\partial c}{\partial x} + \underbrace{\frac{\partial y_f}{\partial Z} \frac{\partial Z}{\partial x}}_2 \right) \\ & + \underbrace{y_f \frac{\partial}{\partial x} (\rho u)}_1 = w_i + \left( \frac{\partial y_f}{\partial c} \frac{\partial c}{\partial x} + \underbrace{\frac{\partial y_f}{\partial Z} \frac{\partial Z}{\partial x}}_2 \right) \frac{\partial}{\partial x} (\rho D) \\ & + \rho D \left( \frac{\partial^2 y_f}{\partial^2 c} \frac{\partial c}{\partial x} \frac{\partial c}{\partial x} + \frac{\partial^2 y_f}{\partial^2 Z} \frac{\partial Z}{\partial x} \frac{\partial Z}{\partial x} + 2 \frac{\partial^2 y_f}{\partial c \partial Z} \frac{\partial c}{\partial x} \frac{\partial Z}{\partial x} + \frac{\partial y_f}{\partial c} \frac{\partial^2 c}{\partial^2 x} + \underbrace{\frac{\partial y_f}{\partial Z} \frac{\partial^2 Z}{\partial^2 x}}_2 \right). \end{aligned} \quad (5.11)$$

The two terms under-braced with "1" cancel thanks to the continuity equation. The four terms under-braced with "2" cancel thanks to the transport equation for the mixture fraction  $Z$ , if the hypothesis of an identical diffusion coefficient  $D$  for fuel mass fraction  $y_f$ , progress variable  $c$  and mixture fraction  $Z$  is made. By dividing the remaining terms of the previous equation by  $\frac{\partial y_f}{\partial c} \neq 0$ , the progress variable transport equation valid for premixed and diffusion flames yields:

$$\begin{aligned} \frac{\partial \rho c}{\partial t} + \frac{\partial \rho u c}{\partial x} &= \frac{\partial}{\partial x} \left( \rho D \frac{\partial c}{\partial x} \right) + \frac{1}{\frac{\partial y_f}{\partial c}} \dot{w}_f \\ &+ \frac{\rho D}{\frac{\partial y_f}{\partial c}} \left( \frac{\partial^2 y_f}{\partial^2 c} \frac{\partial c}{\partial x} \frac{\partial c}{\partial x} + \frac{\partial^2 y_f}{\partial^2 Z} \frac{\partial Z}{\partial x} \frac{\partial Z}{\partial x} + 2 \frac{\partial^2 y_f}{\partial c \partial Z} \frac{\partial c}{\partial x} \frac{\partial Z}{\partial x} \right). \end{aligned}$$

This equation can be derived similarly for a three-dimensional case:

$$\begin{aligned} \frac{\partial \rho c}{\partial t} + \frac{\partial \rho c u_i}{\partial x_i} &= \frac{\partial}{\partial x_i} \left( \rho \frac{v}{S c_c} \frac{\partial c}{\partial x_i} \right) + \dot{w}_c \\ &+ \frac{1}{\frac{\partial y_f}{\partial c}} \left( \frac{\partial^2 y_f}{\partial^2 c} \rho D \frac{\partial c}{\partial x_i} \frac{\partial c}{\partial x_i} + \frac{\partial^2 y_f}{\partial^2 Z} \rho D \frac{\partial Z}{\partial x_i} \frac{\partial Z}{\partial x_i} + 2 \frac{\partial^2 y_f}{\partial c \partial Z} \rho D \frac{\partial c}{\partial x_i} \frac{\partial Z}{\partial x_i} \right). \end{aligned} \quad (5.12)$$

The analytical, but unpracticable, relation  $\dot{w}_c = 1/\frac{\partial y_f}{\partial c} \dot{w}_f$  is a generalization of Eq. (5.3) for inhomogeneously and partially premixed combustion. In section 5.2.2 (p.74), further properties of lean inhomogeneously premixed combustion permits to express the factor  $1/\frac{\partial y_f}{\partial c}$  as function of the mixture fraction  $Z$ .

The three new terms in the r.h.s. (second line) in Eq. (5.12) describe changes due to scalar dissipation, in the literature they are often denoted as:

$$\chi_c \equiv D \vec{\nabla} c \cdot \vec{\nabla} c = \frac{\partial c}{\partial x_i} \frac{\partial c}{\partial x_i}, \quad (5.13)$$

$$\chi_Z \equiv D \vec{\nabla} Z \cdot \vec{\nabla} Z = \frac{\partial Z}{\partial x_i} \frac{\partial Z}{\partial x_i}, \quad (5.14)$$

$$\chi_{Z,c} \equiv D \vec{\nabla} Z \cdot \vec{\nabla} c = \frac{\partial c}{\partial x_i} \frac{\partial Z}{\partial x_i}. \quad (5.15)$$

To discuss and illustrate the role of each of these three terms, the progress variable is expressed as a function of the mixture fraction and the fuel mass fraction, as suggested by Duwig et al. [DSFT05](p. 7) [DF04](p. 2):

$$c = \frac{y_f - y_f^u(Z)}{y_f^b(Z) - y_f^u(Z)}. \quad (5.16)$$

$y_f$ ,  $y_f^b$  and  $y_f^u$  are respectively the local, burnt and unburnt mass fraction of fuel and are functions of the mixture fraction  $Z$ . This relation remains general, but includes the *hypothesis of linearity* between the progress variable  $c$  and the mass fraction  $y_f$ .

The first consequence of this assumption is that the partial derivative  $\frac{\partial^2 y_f}{\partial^2 c}$  cancels, and that the *first term*  $\rho \chi_c \frac{\partial^2 y_f}{\partial^2 c}$  is no more acting.

The *second term* associated to  $\chi_Z$  is a pure scalar dissipation term, which is commonly used in non-premixed combustion modeling. It allows the progress variable to keep a constant value with pure mixing. Without this term, a problem can occur: If two zones of burnt gas ( $c=1$ ) at two different mixture fraction  $Z_1$  and  $Z_2$  are mixing, the resulting zone of a fluid has a mixture fraction  $Z' = (Z_1 + Z_2)/2$  and still contains burnt gas so that  $c' = 1$ . Or using the definition of  $c$  in the mixture:

$$c' = \frac{y_f(Z_3) - y_f^u(Z_3)}{y_f^b(Z_3) - y_f^u(Z_3)} = \frac{\frac{y_f^b(Z_1) + y_f^b(Z_2)}{2} - y_f^u(Z_3)}{y_f^b(Z_3) - y_f^u(Z_3)}$$

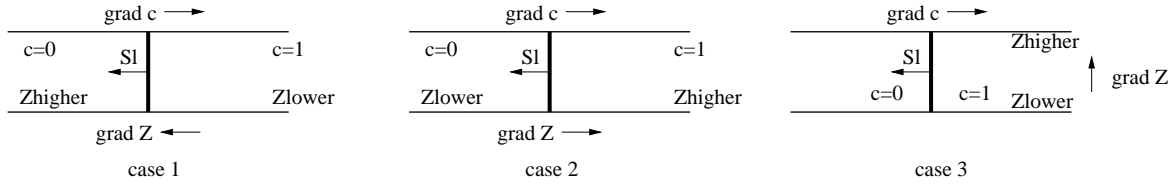


**Fig. 5.1:** Influence of the cross-scalar dissipation term  $\chi_{Z,c}$

so that this relationship gives  $c' = 1$  if:

$$\frac{y_f^b(Z_1) + y_f^b(Z_2)}{2} = y_f^b(Z_3)$$

i.e. if the *burnt mass fraction*  $y_f^b$  is a linear function of the mixture fraction  $Z$ , which may be not the case. This demonstrates that pure mixing can raise difficulties.

The *third term* associated to  $\chi_{Z,c}$  is the so-called *cross-scalar dissipation* term. It depends on the direction of propagation of the flame compared to the gradient direction of the mixture fraction. The effect of this term can be easily understood considering three simple configurations of a rectangular tube in which a flame is propagating (Figure 5.1 (p.74)). In the first case a mixture is achieved, so that the flame is propagating in the direction of an increasing mixture fraction  $Z$ .  $\chi_{Z,c}$  is negative (the gradients are of opposite direction), and its associated factor in the transport equation is positive for *lean mixtures* (the reason is justified in the next section 5.2.2 (p.74)) but negative for rich mixtures. Therefore in this case the global term tends to decrease the source term for lean mixtures, and to increase it for rich mixtures. In the last case where the mixture fraction gradient is oriented in the vertical direction, its scalar product with the flame propagation direction is zero, so that this term does not act.

## 5.2.2 Case of the lean inhomogeneously premixed combustion

### Simplifications for the lean case

Compared to the general case, the lean combustion case allows a few more simplifications. A still more explicit relationship given by Bray et al. [BDV05](p. 434) for the progress variable can be used taking advantage of the direct dependence of mass fraction to mixture fraction:

$$c(\vec{x}, t) = \frac{y_f(\vec{x}, t) - y_f^0 Z}{y_f^b(Z(\vec{x}, t)) - y_f^0 Z} \quad (5.17)$$

In this work, the fuel mass fraction in the fuel supply stream is considered as pure methane or pure propane:  $y_f^0 = 100\%$ . The fuel mass fraction is zero in the burnt gas:  $y_f^b(Z(\vec{x}, t)) \equiv 0$  and  $\frac{\partial y_f^b}{\partial Z} = 0$ . The expressions for  $c$  and the two left scalar and cross-scalar dissipation

terms can be simplified to:

$$c(\vec{x}, t) = 1 - \frac{y_f(\vec{x}, t)}{Z(\vec{x}, t)} \quad (5.18)$$

$$\Leftrightarrow y_f = Z(1 - c). \quad (5.19)$$

The progress variable is the complement to one of the actual fuel mass fraction  $y_f$  divided by the unburnt fuel mass fraction  $Z$ . Reciprocally, the fuel mass fraction can be expressed as the unburnt mass fraction at the local position  $Z$  reduced from its burnt part. Its singularity for  $Z = 0$  (case of pure air) is handled considering Eq. (5.19) since  $Z = 0$  implies  $y_f = 0$  for any value of  $c$ .

Deriving the partial derivatives of  $y_f$ ,  $\frac{\partial y_f}{\partial c} = -Z$  and  $\frac{\partial^2 y_f}{\partial z \partial c} = -1$ :

$$\frac{1}{\frac{\partial y_f}{\partial c}} \rho \chi_Z \frac{\partial^2 y_f}{\partial^2 Z} = 0, \quad (5.20)$$

$$\frac{1}{\frac{\partial y_f}{\partial c}} \rho \chi_{Z,c} \frac{\partial^2 y_f}{\partial Z \partial c} = 2 \frac{\rho}{Z} \chi_{Z,c}. \quad (5.21)$$

Finally, the transport equation for the progress variable in the case of *lean inhomogeneously premixed combustion* differs only of one term from the transport equation in the perfectly premixed case:

$$\frac{\partial \rho c}{\partial t} + \frac{\partial \rho c u_i}{\partial x_i} = \frac{\partial}{\partial x_i} \left( \rho \frac{v}{S c_c} \frac{\partial c}{\partial x_i} \right) + \dot{w}_c + 2 \frac{\rho}{Z} \chi_{Z,c} \quad (5.22)$$

Going back to the statement at the end of the previous section 5.2.1 (p.71), it has been demonstrated that  $\frac{\partial y_f}{\partial c}$  is negative (the fuel is consumed when the progress variable is increasing), and  $\frac{\partial^2 y_f}{\partial z \partial c}$  is also negative in the lean case. The sign of the extra term  $1 / \frac{\partial y_f}{\partial c} \cdot \rho \chi_{Z,c} \frac{\partial^2 y_f}{\partial Z \partial c} = 2 \frac{\rho}{Z} \chi_{Z,c}$  is thus the same as the sign of  $\chi_{Z,c}$ , i.e. positive when the flame propagates toward leaner mixture (see case 2 in Figure 5.1 (p.74)).

### Influence of mixture fraction fluctuations

For illustration, the flame front in Figure 5.1 (p.74)(case2) is considered. It is defined with the iso-value  $c = 0.5$ , so that marginal cases with  $c = 1$  or  $c = 0$ , for which the respective value  $y_f = 0$  and  $y_f = Z$ , are avoided. It is progressing in the rectangular tube into lower mixture fraction zone and in a non-moving flow  $\mathbf{u} = \vec{0}$ .

The purpose is to characterize how the inhomogeneity of mixture fraction  $Z$  can modify the progress variable. For definiteness a point of the flame front is tracked between two instants  $t_1$  and  $t_2$  so that:

$$\begin{aligned} c(t_1) &= c(t_2) = 0.5, \\ Z(t_1) &< Z(t_2). \end{aligned}$$

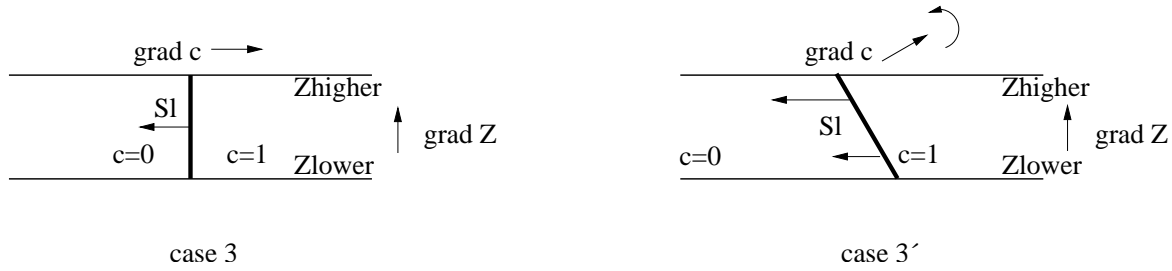


**Fig. 5.2:** Another inhomogeneously premixed configuration

In the lean premixed case, a reduction of the mixture fraction leads to a decrease of the laminar flame speed and thus to a decrease of the reactive source term:

$$w_c(Z(t_2)) < w_c(Z(t_1)),$$

so that the reactive term would lead to a reduction of the progress variable  $c$ .

This may be slightly compensated by the cross-scalar dissipation term. The gradients of the progress variable and the mixture fraction being in the same direction, the cross-scalar dissipation term would lead to an increase of  $c$  since  $Z(t_2) < Z(t_1)$  appear in the denominator:

$$2 \frac{\rho}{Z(t_2)} \chi_{Z,c} > 2 \frac{\rho}{Z(t_1)} \chi_{Z,c}.$$

Considering the third academic example with the rectangular tube and the mixture fraction gradient oriented in the vertical direction in Figure 5.2 (p.76): The reaction rate  $\dot{w}_c$  is higher in the zone where the mixture is richer, so that the flame front will tend to turn and to be inclined in respect with the horizontal axis. The progress variable gradient will therefore rotate and tend to align with the mixture fraction gradient. The global source term  $w_c + 2\rho/Z\chi_{Z,c}$  is thus still more increasing, the extra term  $1/\frac{\partial y_f}{\partial c} \rho \chi_{Z,c} \frac{\partial^2 y_f}{\partial Z \partial c}$  is not at all acting with a balancing effect as it might have been initially guessed.

For inhomogeneously premixed combustion cases, the cross-scalar dissipation term  $2\rho/Z\chi_{Z,c}$  may become non negligible (and positive) when the flame front reaches the zone where  $Z$  becomes zero, since the two gradients of  $c$  and  $Z$  are non zero and almost parallel as shown in Figure 5.3 (p.77).

### 5.2.3 Influence on the laminar flame speed

Turbulent reaction models (RANS and LES) for the progress variable are often closed using the local ratio between the turbulent and laminar flame speeds  $S_t$  and  $S_l$ .

#### Influence of the mixture fraction

As detailed in part section 2.3.3 (p.26), the laminar flame speed depends on the fuel (methane, propane, kerosene, ...), on the equivalence ratio  $\Phi$ , and on the unburnt temperature

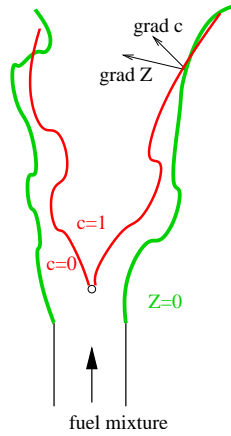


**Fig. 5.3:** Cross-scalar dissipation term with a V-Flame burner

$T_u$  and pressure  $p$ :  $S_l(F, \Phi, T_u, p)$ . All present simulations have been carried out at atmospheric pressure  $p = p^0$  and at the same unburnt temperature for each burner. But varying equivalence ratio values have been investigated: Either as a configuration parameter for the perfectly premixed burners (Volvo test-rig and PSI burners), or as a *local* variable for the inhomogeneously premixed burner TD1. In this section, the focus is placed on the dependence of the laminar flame speed  $S_l$  to the mixture fraction  $Z$  and the equivalence ratio.

In the case of a perfectly premixed mixture  $S_l$  has a constant value in the whole domain, and therefore can be given as constant parameter in the model. For the partially premixed burners, the mixture fraction is changing with space and time, so that the laminar flame speed must be expressed explicitly with the mixture fraction  $Z$ . There are typically two manners of achieving this:

- Finding a polynomial or any continuous function which delivers  $S_l(Z)$
- Having a table of values for  $Z$  and  $S_l$  and interpolating for any value of  $Z$  during the calculation.

These functions or tables are extracted for one gas at a unique couple of unburnt temperature and pressure conditions, therefore the mixture fraction is the only variable.

Here, a polynomial approximation of the laminar flame speed of a methane-air mixture at the reference pressure and temperature and for different mixture ratio has been calculated using values reproduced in Table 5.1 (p.78) and the algorithm *polyfit* from *Matlab*. The coefficients of the polynomial are given as evaluated with *Matlab* (i.e. without any round-off), since this would lead to discrepancies comparing to the solution:

$$\begin{aligned}
 S_l(\lambda) = & 3.5890252 \times 10^3 \lambda^{15} - 5.1605065 \times 10^4 \lambda^{14} + 3.2526170 \times 10^5 \lambda^{13} - 1.1598564 \times 10^6 \lambda^{12} \\
 & + 2.4681343 \times 10^6 \lambda^{11} - 2.7789706 \times 10^6 \lambda^{10} + 5.2139180 \times 10^6 \lambda^8 - 8.2519854 \times 10^6 \lambda^7 \\
 & + 5.6442169 \times 10^6 \lambda^6 - 3.3940305 \times 10^6 \lambda^4 + 3.0609669 \times 10^6 \lambda^3 - 1.3743672 \times 10^6 \lambda^2 \\
 & + 3.2794755 \times 10^5 \lambda - 3.3218682 \times 10^4.
 \end{aligned} \tag{5.23}$$

$\lambda$	0.60	0.65	0.75	0.80	0.90	1.00	1.10	1.20	1.30	1.40	1.50	1.60	1.70	1.80	1.876
$\phi$	1.67	1.54	1.33	1.25	1.11	1.00	0.91	0.83	0.77	0.71	0.67	0.63	0.59	0.56	0.53
$Z(\times 10^2)$	8.85	8.23	7.21	6.79	6.08	5.51	5.03	4.63	4.29	4.00	3.74	3.51	3.31	3.14	3.01
$S_I(\lambda)$	0	0.10	0.30	0.40	0.43	0.42	0.37	0.28	0.20	0.15	0.10	0.07	0.035	0.01	0

**Tab. 5.1:**  $S_I(\lambda)[m/s]$  for methane at  $T_u = 300$  K and  $p = 1$  bar from Hirsch [Hir02](p. 13)

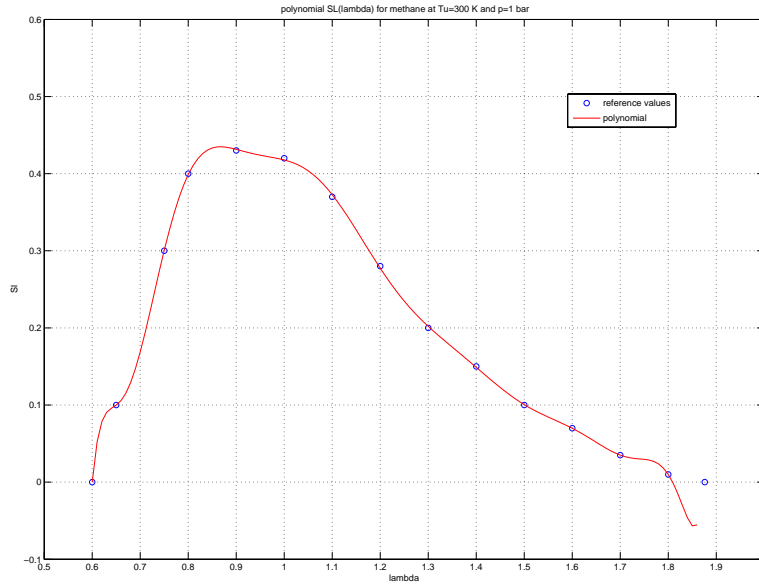


**Fig. 5.4:** Polynomial for  $S_I(\lambda)$

Note that this polynomial is not used directly in *Fluent*. It only permits to calculate with *Matlab* the table  $\tilde{S}_I(\tilde{Z}, Z_{sgs})$ , which is used with *Fluent*, as detailed in the next section. It delivers a curious trend for the lowest AFR values ( $\lambda \approx 0.65$ ), which is not problematic for this work, since only the lean combustion ( $\lambda > 1$ ) is of interest. At the other side the value of  $S_I$  must be clipped to zero for  $\lambda > 1.84$ , i.e.  $\phi < 0.54$ . This is also not compelling, since this value corresponds about to the lean blow-off value.

### Need to account for mixture fraction fluctuations

The relation  $S_I(Z)$  should not be directly transposed to  $S_I(\tilde{Z})$  in the LES modeling, since  $\tilde{Z}$  is a filtered value. The mixture fraction fluctuations have to be taken into consideration, in order to model this variation around the filtered value. The reference laminar flame speed value must coincide with the type of modeling. With RANS modeling, it can be based on the averaged mixture fraction  $\tilde{Z}$  and its fluctuation. With LES modeling, the laminar speed flame value should be a representative value of the filtered solution and of the subgrid-scale value.

Keich et al. [KRG98](p. 299) have developed such a model in the steady RANS context for

car engines. They solved the mean mixture fraction  $\tilde{Z}$ , and include the influence of its Favre-averaged variance  $Z_{rms}^2 = \widetilde{Z'^2}$  to evaluate the laminar flame speed. The formulation is inspired by Peters [Pet97] (p. 93-94), considering the mean value of  $S_l$  as a stochastic value:

$$\bar{S}_l(\tilde{Z}, \widetilde{Z'^2}) = \int_0^1 S_l(Z) P_Z(\tilde{Z}, \widetilde{Z'^2}) dZ. \quad (5.24)$$

$P_Z(\tilde{Z}, \widetilde{Z'^2})$  is a joint probability density function of  $\tilde{Z}$  and  $\widetilde{Z'^2}$ , see Pope [Pop85]. It may be based on the so-called Beta- and Gamma-functions (defined to be an extension of the factorial to complex and real number arguments as explained by Hackbusch et al. [HSZ96] (p. 124, 599):

$$P_Z(\tilde{Z}, \widetilde{Z'^2}) = Z^{\alpha-1} (1-Z)^{\beta-1} \frac{\Gamma(\gamma)}{\Gamma(\alpha)\Gamma(\beta)} \quad (5.25)$$

$$\text{with } \alpha = \tilde{Z}\gamma, \beta = (1-\tilde{Z})\gamma, \text{ and } \gamma = \frac{\tilde{Z}(1-\tilde{Z})}{\widetilde{Z'^2}} - 1.$$

The numerical evaluation of this expression is difficult, because the Gamma-function lead to large values when the fluctuations  $\widetilde{Z'^2}$  are very small. Since, this occurs more with LES modeling than with RANS modeling, details for the most adapted mathematical formulation and the estimation of the function are given in appendix A.4 (p.221).

### Fluctuations with the LES modeling: fpdf-functions

The approach presented for the RANS context must be adapted using the Favre filtered mixture fraction  $\tilde{Z}$  and its subgrid scale fluctuation  $Z_{sgs}$  in order to calculate the *filtered laminar flame speed* noted  $\tilde{S}_l$ . As the use of  $\tilde{S}_l$  corresponds to a statistical property, like in the RANS-case, the concept of filter probability density function (fpdf) must be employed. A fpdf stands namely for the average of *filtered density functions* (fdf, see Pope [Pop90] (p. 595-596) [Pop00] (p. 630-631) for the original definition) of realizations giving the same filtered result, according to Fox [Fox03] (p. 108-110). Actually the same presumed shape can be attributed for fpdf of LES modeling than for pdf for RANS modeling as justified by Pitsch [Pit06] (p. 457). In the following the mathematical function  $P_Z$  is still employed in order to evaluate the filtered laminar flame speed  $\tilde{S}_l$ .

### Evaluation of $Z_{sgs}$

Methods to evaluate the subgrid mixture fraction fluctuations  $Z_{sgs}$  have been principally developed for the simulations of diffusion flames, since the mixture fraction is the main variable used to represent these flames. In literature essentially two ways of evaluations can be found:

- Use of a gradient assumption
- Use of a test filter.

The use of the gradient assumption is similar to the gradient assumption for evaluating the turbulent diffusion in section 3.2.1 (p.44). The subgrid variance scales proportionally with the filtered mixture fraction gradient:

$$Z_{sgs}^2 = c_Z \Delta^2 |\nabla \tilde{Z}|^2. \quad (5.26)$$

The constant  $c_Z$  can be determined analytically or dynamically. A dynamic formulation is proposed by Pitsch [Pit06](p. 459), Pierce and Moin [PM98] for example. A constant value can be used for simplification:  $c_Z = 0.13$  is advised by Forkel and Janicka [FJ00](p. 165).

A test filter can also be employed to evaluate the fluctuation  $Z_{sgs}$ . The formulation by Forkel and Janicka has been retained here [FJ00]. The mixture fraction at the test filter is calculated according to:

$$\hat{Z}_0 = \frac{1}{12} \left( 6\tilde{Z}_0 + \sum_k \tilde{Z}_k \right). \quad (5.27)$$

As presented in Eq. (4.22) and illustrated in Figure 4.4 (p.67),  $\tilde{Z}_0$  is the mixture fraction at the considered cell,  $\tilde{Z}_k$  are the values at the neighbor cells (sharing a face with the considered cell). The approximation for the subgrid variance yields using the same weighting:

$$Z_{sgs}^2 \approx \frac{1}{12} \left[ 6 \left( \tilde{Z}_0 - \hat{Z}_0 \right)^2 + \sum_k \left( \tilde{Z}_k - \hat{Z}_0 \right)^2 \right]. \quad (5.28)$$

This procedure is particularly interesting in this work, since it is using the same explicit test filter as already developed and implemented for the TF' model in section 4.2 (p.66).

The test filter procedure for estimating  $Z_{sgs}$  has been only employed, if already used in the computation for another purpose. Else, the gradient assumption with the constant  $c_Z = 0.13$  has been used in order to reduce the CPU-effort.

#### Table for $\tilde{S}_l(\tilde{Z}, Z_{sgs})$ and interpolation

The retained method consists in evaluating a large matrix of values of the laminar flame speed before the calculation, and in interpolating the desired value during the simulation.

The function Eq. (5.25) has been programed and evaluated in *Matlab*, with the evaluation of the laminar flame speed using the polynomial Eq. (5.23). A matrix  $201 \times 499$  has been produced varying  $\tilde{Z}$  in the range  $[0;0.1]$  with a step  $\Delta\tilde{Z} = 5 \cdot 10^{-4}$ , and  $Z_{sgs}$  in the range  $[3 \cdot 10^{-5}; 10^{-2}]$  with a step  $\Delta Z_{sgs} = 2 \cdot 10^{-5}$ . The result is depicted in Figure 5.5 (p.81). When the fluctuation is increasing, the maximum laminar flame speed is obtained for richer mixture.

During the simulation, the interpolation is based on the normalized coordinates  $(\zeta_{\tilde{Z}}; \zeta_{Z_{sgs}})$

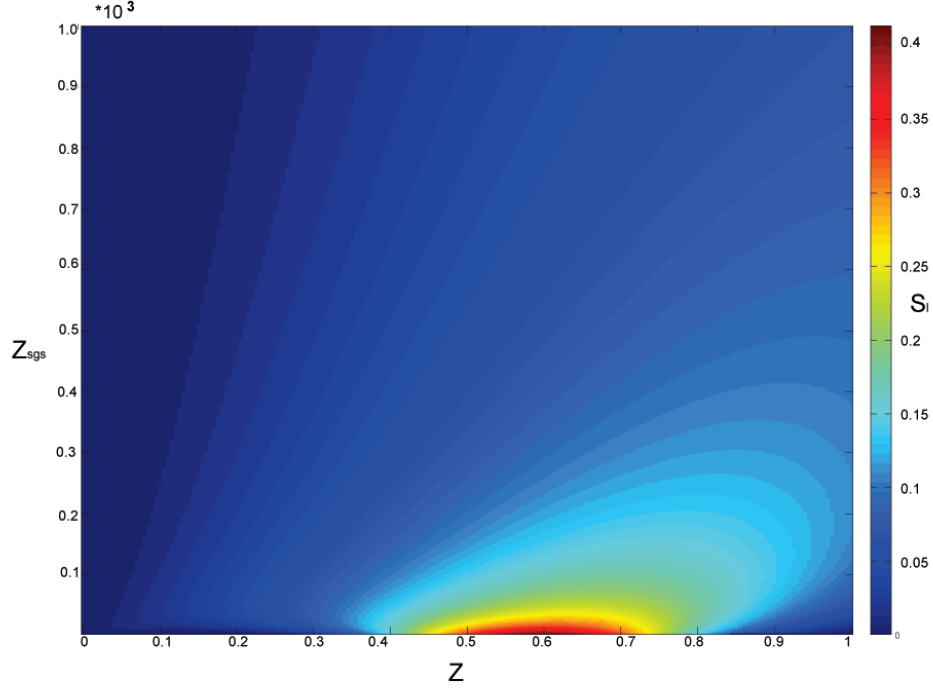


**Fig. 5.5:** Filtered laminar flame speed  $\tilde{S}_l(\tilde{Z}, Z_{sgs})$

of the desired couple  $(\tilde{Z}; Z_{sgs})$  in a matrix four-point box:

$$Z_i < \tilde{Z} < Z_{i+1} \rightarrow \zeta_{\tilde{Z}} = \frac{\tilde{Z} - Z_i}{Z_{i+1} - Z_i},$$

$$Z'_j < Z_{sgs} < Z'_{j+1} \rightarrow \zeta_{Z_{sgs}} = \frac{Z_{sgs} - Z'_j}{Z'_{j+1} - Z'_j}.$$

The laminar flame speed is then evaluated in *Fluent*:

$$\tilde{S}_l(\tilde{Z}, Z_{sgs}) \approx S_l(i, j) + (S_l(i+1, j) - S_l(i, j))\zeta_{\tilde{Z}} + (S_l(i, j+1) - S_l(i, j))\zeta_{Z_{sgs}} + [(S_l(i+1, j+1) - S_l(i, j+1)) - (S_l(i+1, j) - S_l(i, j))]\zeta_{\tilde{Z}}\zeta_{Z_{sgs}}. \quad (5.29)$$

If the subgrid fluctuation is smaller than the minimal value tabulated ( $Z_{sgs_{min}} = 3 \cdot 10^{-5}$ ), the fluctuation is considered zero: The filtered laminar flame speed depends only on the filtered mixture fraction  $\tilde{Z}$ .

### 5.3 Non-adiabatic combustion

For most industrial configurations, combustion chambers are closed, with cooled walls, so that the flow is not adiabatic. In such cases, the linear relation between the progress

variable from one side, the temperature Eq. (5.4) and the density Eq. (5.5) from the other side is no more valid. The enthalpy transport equation has to be resolved to take the energy exchange into account. This aspect is explained in the first section 5.3.1 (p.82), where the focus is placed on the lack of feedback to the progress variable. In the second section 5.3.2 (p.82), the notion of *enthalpy index* is presented. In the third part the enthalpy index is expressed in order to include a feedback into the progress variable transport equation.

### 5.3.1 Enthalpy loss term

For a non-adiabatic configuration, the enthalpy equation must be slightly modified to include the effect of energy losses. This exchange of energy with the outer side of the thermodynamical system, constituted by the fluid in the burner, might be also a gain of energy. The non-adiabaticity is mostly due to cooled walls, losses are considered and noted  $w_{HL}$ . In the enthalpy transport equation, losses are modeled with a negative source term. Whereas the reactive term is a volume source term, the non-adiabatic term is modeled with a surface term. The term  $w_{HL}$  is acting only at the boundary conditions (typically walls as already suggested) of the system. There are two ways of modeling this effect:

- Considering directly a flux of enthalpy  $F_H$  at the wall or boundary condition
- Considering a constant temperature at the wall or boundary condition.

The second possibility has been used for the test-cases.

Taking into consideration the energy loss is still not sufficient to model correctly a non-adiabatic burner with the progress variable approach. With the chemical representation, the reactive terms are evaluated with the Arrhenius formulation, and thus strongly dependent on the temperature. On the contrary, the progress variable approach has been initially developed for adiabatic case, where the temperature does not appear in the source term for the progress variable. Consequently, losses of enthalpy, which locally lead to lower temperature, are not acting on the progress variable. A model to include this effect in the progress variable transport equation is described in section 5.3.3 (p.84). In the next section 5.3.2 (p.82), the notion of *enthalpy index* introduces a useful formalism.

### 5.3.2 Enthalpy index

Wenzel et al. [WHZ06]<sup>(p. 5)</sup> have introduced the notion of *enthalpy index* in order to give a measure of the *local non-adiabaticity* in a flow:

$$\mathcal{S}_h \equiv \frac{h - h_u}{h_{ad} - h_u}, \quad (5.30)$$

where  $h$  is the local enthalpy,  $h_{ad}$  the enthalpy in the adiabatic configuration and  $h_u$  the enthalpy at the unburnt temperature  $T_u$ . This index give a normalized value of the enthalpy:  $\mathcal{S}_h = 1$  under adiabatic conditions, and  $\mathcal{S}_h = 0$  for maximum heat loss. The index can

be evaluated locally, so that for each point of the burner the *level of adiabaticity* can be evaluated.

$h_u$  is the enthalpy of the unburnt mixture:

$$h_u = h_0(T^0, p^0) + \int_{T^0}^{T_u} c_p(T) dT. \quad (5.31)$$

$h_0(T^0, p^0)$  is the reference enthalpy of the mixture, taken at the standard reference temperature  $T^0 = 298.15$  K and standard reference pressure  $p^0$ .  $c_p$  the specific calorific coefficient of the mixture. The adiabatic enthalpy can be expressed in two different ways:

$$h_{ad} = h_0(T^0, p^0) + \int_{T^0}^{T_{ad}} c_p(T) dT \quad (5.32)$$

$$h_{ad} = h_0(T^0, p^0) + \int_{T^0}^{T_u} c_p(T) dT + \Delta H^0 Z \quad (5.33)$$

where  $T_{ad}$  is the adiabatic temperature,  $\Delta H^0$  the specific reaction enthalpy.  $\Delta H^0$  is evaluated as the enthalpy produced by 1 kg of fuel, so that it is multiplied with the local mixture fraction  $Z$  defined in section 2.3.2 (p.24). The first expression Eq. (5.32) describes the sensible enthalpy of the mixture which has reached the adiabatic temperature. The second expression Eq. (5.33) represents the enthalpy in terms of sensible enthalpy of the cold mixture plus the enthalpy delivered by combustion. This second term leads to the formulation of the local enthalpy  $h$ :

$$h = h_0(T^0, p^0) + \int_{T^0}^T c_p(T) dT + (1 - c)\Delta H^0 Z \quad (5.34)$$

where  $T$  is the local temperature and  $c$  the local progress variable. This expresses the enthalpy as the sum of the local sensible enthalpy due to the temperature  $T$  plus the *potential* reaction enthalpy (considering how much the mixture is already burnt, and how much may still burn). The enthalpy index can reach  $\mathcal{S}_h = 1$  for different combinations of values  $(T, c)$ , but two are of particular interest:

- The mixture is not burnt:  $c = 0$ , and the local temperature is the unburnt temperature  $T = T_u$
- The mixture is completely burnt  $c = 1$  and the local temperature has reached the adiabatic temperature  $T = T_{ad}$ .

Using the previous relations, the enthalpy-index reads:

$$\mathcal{S}_h = \frac{\int_{T_u}^T c_p(T) dT + (1 - c)\Delta H^0 Z}{\Delta H^0 Z} = \frac{1}{\Delta H^0 Z} \int_{T_u}^T c_p(T) dT - (1 - c). \quad (5.35)$$

The enthalpy-index is thus different from unity, if the local temperature cannot reach anymore the adiabatic temperature with the remaining fuel to burn.

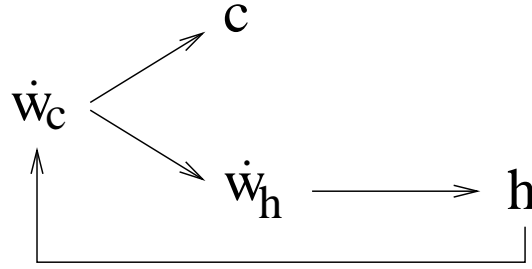


**Fig. 5.6:** Feedback enthalpy to progress variable

### 5.3.3 Feedback enthalpy-progress variable

When locally the flow is not adiabatic and the losses significant (too much energy has been exchanged with cooled walls for example), the flame may not ignite. The aim of this part is to formulate in a simple way this idea, to express a feedback from the enthalpy to the progress variable transport equation.

A reference enthalpy or a reference enthalpy-index is required to predict if the combustion can occur. The inner layer temperature  $T_i$ , which stands for the transition between the chain-branching and chain-breaking reactions as described by Peters [Pet00](p. 27), is taken as reference temperature. From the temperature  $T_i$ , the reference enthalpy-index  $\mathcal{S}_{h_i}$  can be estimated. During the computation, if the actual enthalpy-index is lower than the reference enthalpy-index, then the inner layer temperature cannot be reached and the chain-breaking reactions do not start, so that the combustion cannot occur.

The enthalpy-index  $\mathcal{S}_{h_i}$  corresponding to the inner layer temperature  $T_i$  is evaluated with:

$$\mathcal{S}_{h_i} = \frac{\int_{T_u}^{T_i} c_p(T) dT}{\Delta H^0_z}. \quad (5.36)$$

If the enthalpy-index becomes smaller than this reference value, then the reactive term for the enthalpy equation is set to zero, as well as the source term of the progress variable transport equation:

$$\mathcal{S}_h < \mathcal{S}_{h_i} \Rightarrow \dot{w}_c = 0 \text{ and } \dot{w}_h = 0. \quad (5.37)$$

The numerical value of the inner layer temperature approximated by Müller et al. [MBP97](p. 351) and related to the activation energy is used:

$$T_i = -E_a \ln\left(\frac{p}{B}\right) \quad (5.38)$$

where  $p$  is the operative pressure,  $E_a$  the activation energy and  $B$  a parameter. For methane and propane, Müller et al. use the parameters referenced in Table 5.2 (p.85). With this approximation, the inner layer temperature depends only on the pressure. Numerically, the inner layer temperature is  $T_i = 1219.90$  K at  $p = 1$  bar for methane mixture. The associated enthalpy-index  $\mathcal{S}_{h_i}$  depends on the unburnt temperature. In the following, numerical examples are given for the *PSI burner*, which is one of the test-case for this thesis

fuel	$B$ [bar]	$E_a$ [K]
CH <sub>4</sub>	$3.1557 \times 10^8$	23873.0
C <sub>3</sub> H <sub>8</sub>	$2.2501 \times 10^6$	17223.5

**Tab. 5.2:** Parameters for the inner layer temperature

and has been simulated with this sub-model in section 8.2 (p.156):

$$\begin{aligned} T_i &= 1219.90 \text{ K} \\ T_u = 673 \text{ K} \Rightarrow \mathcal{S}_{h_i} &= 0.48. \end{aligned}$$

The polynomial (temperature dependent, but not mixture dependent) calorific coefficient  $c_p(T)$ , already listed in Table 2.1 (p.14) in section 2.1.3 (p.13), has been used.

To avoid any numerical difficulties in *Fluent*, a ramp function, depicted in Figure 5.7 (p.86), for the feedback is implemented instead of the step function near the inner-layer value. The slope is a function of the unburnt, adiabatic and inner-layer temperature ratios. For example, a relatively large difference between adiabatic and inner-layer temperatures should indicate a relatively low activation energy in Eq. (5.38), and therefore a slower reaction rate with a smoother influence of the temperature. The coefficient is set to 0.5 at the inner-layer enthalpy-index, the value 2.5 is an arbitrary coefficient which controls the stiffness, this gives following values for the slopes (for the PSI burner):

$$2.5 \frac{T_{ad} - T_u}{T_{ad} - T_i} = 2.5 \frac{1882 - 673}{1882 - 1219.90} \approx 4.57. \quad (5.39)$$

It follows:

$$\dot{w}_{c,feedback} = \dot{w}_c \cdot \begin{cases} 0, & \text{for } \mathcal{S}_h < 0.37 \\ 0 < 0.5 + 4.57(\mathcal{S}_h - \mathcal{S}_{h_i}) < 1, & \text{for } \mathcal{S}_h \in [0.37; 0.59] \\ 1, & \text{for } \mathcal{S}_h > 0.59 \end{cases} \quad (5.40)$$

This model makes a feedback, and also a complete interaction from the enthalpy equation to the progress variable transport equation possible (see Figure 5.6 (p.84)). If the enthalpy-index is namely low enough to locally reduce or prevent the mixture from burning, the progress variable source term tends to zero. Consequently the reactive source term for the enthalpy becomes also zero, because of  $w_h = \Delta H^0 \cdot Z \cdot w_c$ . By this way an equilibrium is reached between enthalpy and progress variable, and this allows to model *thermal quenching* near walls with the progress variable approach.

To conclude two comments regarding the enthalpy-index should be pointed out:

- The enthalpy-index  $\mathcal{S}_h$  is not strictly required for this model, since the criterion is based on the enthalpy potentially available. Nevertheless it represents a useful and flexible indicator for the evaluation of the minimal enthalpy which allows combustion to occur.

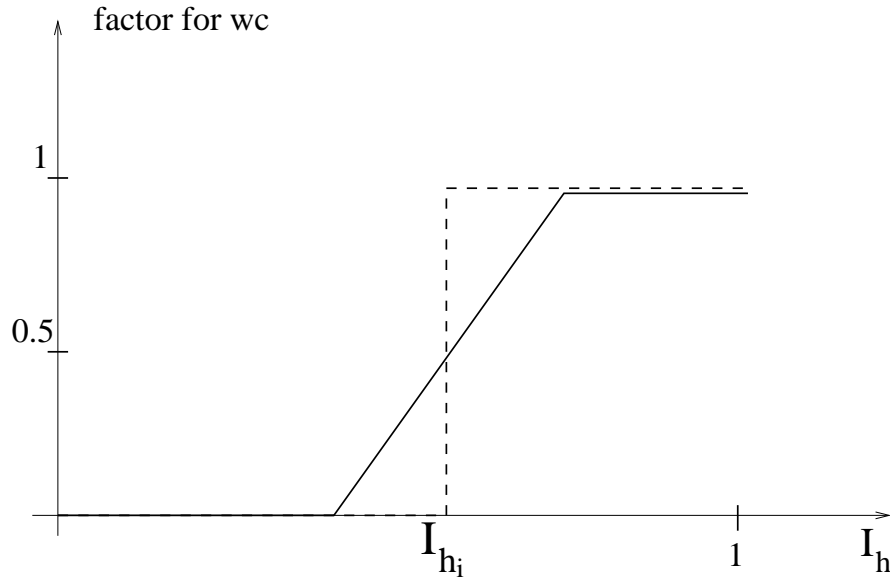


**Fig. 5.7:** Ramp function for the feedback

- The enthalpy-index  $\mathcal{S}_h$  has been implicitly defined using the internal enthalpy, whereas according to the first law of thermodynamics the total enthalpy should be considered. For the PSI burner, neglecting the kinetic energy of the flow  $h_d$  induces a very small error, since it amounts to:

$$h_d = \frac{1}{2} \rho u^2 \approx \frac{1.2 \cdot 40^2}{2} \approx 1040 \text{ J/kg}, \quad (5.41)$$

whereas the reference intern enthalpy is

$$h_{ref} = \int_{T_0}^{T_u} c_p(T) dT \approx 400000 \text{ J/kg}, \quad (5.42)$$

so that the relative error is smaller than 0.25%.

## 5.4 Conclusion

In this part, the progress variable approach, as possible combustion representation, has been described. Starting from its original definition for the perfectly premixed adiabatic combustion, the formulation has been extended to the lean inhomogeneously premixed non-adiabatic case. Only, the estimation of the reaction rate has still been eluded. Two closures for it are presented in the next two chapters: respectively the TFC-LES model, and the SFC model.

# 6 Turbulent Flame speed Closure model

Es lohnt sich, die Entdeckungen anderer zu studieren, dass für uns selbst eine neue Quelle für Erfindungen entspringt.

G. W. Leibniz

The Turbulent Flame speed Closure (TFC) model is a closure model for the reaction rate using the progress variable approach. The original model developed by Zimont for RANS modeling is presented. Then, its adaptation to LES modeling by Flohr and Pitsch is discussed.

## 6.1 Original model with RANS turbulence modeling

The purpose of this part is to detail the development of the *Turbulent Flame speed Closure* model (TFC model) by Zimont [Zim79] for RANS context. It should permit a better comprehension and assessment of its adaptation for LES modeling by Flohr and Pitsch [FP00]. Besides, some of Zimont's ideas have been used to develop the *Subgrid Flame Closure* derived in section 7 (p.99).

### 6.1.1 Gradient formulation of the source term

The model closure was first presented for RANS modeling in 1995 by Zimont and Lipatnikov [ZL95](p. 7). The Favre-averaged transport equation for the progress variable with RANS reads:

$$\frac{\partial \bar{\rho} \tilde{c}}{\partial t} + \frac{\partial \bar{\rho} \tilde{c} \tilde{u}_i}{\partial x_i} = \frac{\partial}{\partial x_i} \left( \bar{\rho} \frac{\nu_t}{Sc_c} \frac{\partial \tilde{c}}{\partial x_i} \right) + \rho_u S_t \left| \vec{\nabla} \tilde{c} \right|. \quad (6.1)$$

This is a classical RANS transport equation, except that the laminar diffusion is not taken into account (this topic is discussed in the following). A first modeling step has been included, since the averaged reactive term has been written as:

$$\tilde{w}_c = \rho_u S_t \left| \vec{\nabla} \tilde{c} \right|. \quad (6.2)$$

$\left| \vec{\nabla} \tilde{c} \right|$  is the magnitude of the gradient of the progress variable,  $S_t$  is the mean turbulent flame speed.  $S_t$  must be modeled, and depends on local turbulent parameters as well on chemical characteristics of the mixture.  $\rho_u$  is the unburnt density, and is required to

achieve a correct closure for a one-dimensional case (this is discussed in the following paragraph).

The gradient formulation has a beneficial effect for CFD simulations. The resolved flame thickness  $\delta$  has no effect on the source term  $\tilde{w}_c$ , as demonstrated for a one-dimensional flame:

$$\begin{aligned} \int_{x_0}^{x_0+\delta} \tilde{w}_c dx &= \rho_u S_t \int_{x_0}^{x_0+\delta} \frac{\partial \tilde{c}}{\partial x} dx \\ \Leftrightarrow \forall \delta : \int_{x_0}^{x_0+\delta} \tilde{w}_c dx &= \rho_u S_t [\tilde{c}]_{x_0}^{x_0+\delta} = \rho_u S_t. \end{aligned} \quad (6.3)$$

It uncouples the resolved turbulent flame velocity  $S_t$  from the resolved flame thickness  $\delta$ . According to the actual flame thickness, the refinement of the mesh, the gradient  $|\vec{\nabla} \tilde{c}|$  in the flame front is more or less steep (and corollary resolved with more and less cells), but it remains without effect on the resolved flame velocity  $S_t$  and the reaction rate  $\tilde{w}_c$ . This enables the TFC model to be robust, contrary to most combustion models. The drawback of this formulation is that the actual thickness of the flame cannot be estimated.

Historically, Zimont and Lipatnikov [ZL95] did not derive the equation Eq. (6.1) from a species transport equation, but from a convection-diffusion equation for the progress variable at constant density and steady turbulent burning velocity:

$$\frac{\partial \tilde{c}}{\partial t} = D_t \frac{\partial^2 \tilde{c}}{\partial x^2} - S_t \frac{\partial \tilde{c}}{\partial x}. \quad (6.4)$$

Extending Eq. (6.4) to a three-dimensional flow with variable density [ZL95](p. 997) should describe a flame front moving with the velocity  $S_t$ , whose averaged thickness  $\delta_t$  increases with the turbulent diffusion. Three topics are discussed in the following:

- Why  $\rho_u$  is required in the source term
- Why the laminar diffusion is not taken into consideration
- How to evaluate the turbulent flame speed  $S_t$ .

The last topic, the evaluation of the turbulent flame speed  $S_t$ , is detailed in the next section 6.1.2 (p.89).

#### Needs for $\rho_u$

In the source term  $\tilde{w}_c = \rho_u S_t |\vec{\nabla} \tilde{c}|$ , the presence of density is required for dimensional reasons. The value of the density  $\rho_u$  is imposed by considering the case of a one-dimensional flame propagating in a stagnant and steady flow. The integration of the continuity equation Eq. (2.1) within the flame front implies:

$$\begin{aligned} \int_{x_0}^{x_0+\delta} \frac{\partial \bar{\rho}}{\partial t} + \frac{\partial \bar{\rho} \tilde{u}_x}{\partial x} dx &= 0 \\ \Leftrightarrow \rho_b u_b &= \rho_u S_t, \end{aligned} \quad (6.5)$$

within  $x_0$  is the unburnt extremity of the flame front:  $\forall t, c(x_0, t) = 0$  of the flame front, and  $\delta$  the flame thickness:  $\forall t, c(x_0 + \delta, t) = 1$ . This condition warrants mass conservation through the flame front, defining  $u_b$  as the velocity in the burnt gas. Similarly, the progress variable transport equation Eq. (6.1) can be integrated within the flame front, and only  $\rho_u$  can satisfy both relations Eq. (6.5) and Eq. (6.6):

$$\begin{aligned} \int_{x_0}^{x_0+\delta} \frac{\partial \bar{\rho} \tilde{c}}{\partial t} + \frac{\partial \bar{\rho} \tilde{u}_x \tilde{c}}{\partial x} dx &= \int_{x_0}^{x_0+\delta} \frac{\partial \bar{\rho} D_t \frac{\partial \tilde{c}}{\partial x}}{\partial x} + \rho_u S_t \frac{\partial \tilde{c}}{\partial x} dx \\ \Rightarrow [\bar{\rho} \tilde{u}_x \tilde{c}]_{x_0}^{x_0+\delta} &= \left[ \bar{\rho} D_t \frac{\partial \tilde{c}}{\partial x} \right]_{x_0}^{x_0+\delta} + \rho_u S_t [\tilde{c}]_{x_0}^{x_0+\delta} \\ \Rightarrow \rho_b u_b &= \rho_u S_t. \end{aligned} \quad (6.6)$$

The diffusion term  $\left[ \bar{\rho} D_t \frac{\partial \tilde{c}}{\partial x} \right]_{x_0}^{x_0+\delta}$  cancels using the continuity of  $\frac{\partial \tilde{c}}{\partial x}$  at  $x_0$  and  $x_0 + \delta$ :

$$0 = \frac{\partial \tilde{c}}{\partial x} \Big|_{x < x_0} = \frac{\partial \tilde{c}}{\partial x} \Big|_{x > x_0}, \text{ and } \frac{\partial \tilde{c}}{\partial x} \Big|_{x < x_0 + \delta} = \frac{\partial \tilde{c}}{\partial x} \Big|_{x > x_0 + \delta} = 0.$$

This is supported by experimental results. Lipatnikov and Chomiak [LC02](p. 35-36) have shown that for different burners and flame locations the progress variable according to a dimensionless distance (characterizing the flame front thickness) is similar to the error function. Therefore the partial derivative  $\frac{\partial \tilde{c}}{\partial x}$  cancels at both extremities of the flame front.

### Absence of the laminar diffusion

Zimont and Lipatnikov insist that the TFC model is invalid for the case  $u' \ll S_l$  and  $D_t \approx D$ , i.e. for laminar or low turbulent flames [ZL95](p. 998, Eq. 9). Under the assumption  $D_t \gg D$ , the laminar diffusion is simply neglected, which is completely coherent with the formulation of the model valid for the thickened flame regime. For the TFC model with LES modeling, this assumption is commented in section 6.2 (p.94).

### 6.1.2 Turbulent flame velocity $S_t$

The only remaining unclosed term for the modeling of the source term is the turbulent velocity  $S_t$ . Although the topic of this work is the LES combustion modeling, the theory detailed by Zimont [Zim79] for the RANS-TFC model is described here. The concepts presented by Zimont are worth being understood and reformulated for a deeper comprehension. The derivation of the averaged flame speed  $S_t$  is achieved in two steps. The first step consists in evaluating the *flamelet velocity*, and the second step in deducing the *brush velocity*, which corresponds to the turbulent flame velocity  $S_t$ .

#### Flamelet velocity

The TFC model is developed for the thickened flame regime. According to Zimont, the flames display a structure of flamelets thicker than a laminar flame  $b_{nt} > \delta_l$ , and propagate

with a velocity larger than the laminar flame speed  $u_{nt} > S_l$  in this regime. These properties are local and depend on the mixture properties as well as on the local flow turbulence<sup>1</sup>. Zimont makes the hypothesis that the turbulent eddies can enter the flame front and potentially the inner reaction zone. The purpose is thus to determine which eddies can enter the flame front, and how they can make the flame thicker. Zimont et al. [ZPBW97](p. 3) formulate the idea of “*an engulfment of larger and larger vortices up to a certain size, until an equilibrium*” is reached. The exercise consists in expressing the relations between the flamelet characteristics  $u_{nt}$  and  $b_{nt}$ , and the turbulence characteristics, such as energy  $E(\kappa)$  and integral length scale  $l_t$ . Considering the energy spectrum in the inertial range  $E(\kappa) = \varepsilon^{2/3} \kappa^{-5/3}$  with the condition  $l_t \gg b_{nt} \gg \eta$  (thickened flame regime), the velocity pulsation  $u'_{nt}$  and length scale  $L_{nt}$  of the eddies, which can enter the flame front, should fulfill:

$$u'_{nt}{}^2 \approx \int_{1/b_{nt}}^{\infty} E(\kappa) d\kappa \sim \varepsilon^{2/3} b_{nt}^{2/3} \quad (6.7)$$

$$L_{nt} \approx \frac{\int_{1/b_{nt}}^{\infty} \kappa^{-1} E(\kappa) d\kappa}{\int_{1/b_{nt}}^{\infty} E(\kappa) d\kappa} \sim b_{nt}. \quad (6.8)$$

This makes the evaluation of the turbulent thermal diffusivity in the front possible:

$$a_{nt} \sim u'_{nt} L_{nt} \sim \varepsilon^{1/3} b_{nt}^{4/3}. \quad (6.9)$$

Implicitly, Zimont makes the usual assumption that the chemical reaction time in the flame front is the same as in the laminar case  $t_c$ . Consequently, the velocity and thickness of the flame front can be evaluated using the turbulent thermal diffusivity:

$$u_{nt} \sim \sqrt{\frac{a_{nt}}{t_c}}, \quad (6.10)$$

$$b_{nt} \sim \sqrt{a_{nt} t_c}. \quad (6.11)$$

The last expressions Eqs. (6.10)(6.11) can be written as a function of the integral length scale  $l_t$  and turbulent velocity  $u'$  using the rate of dissipation of turbulent energy in the inertial range  $\varepsilon \sim u'^3/l_t$ :

$$u_{nt} \sim u' \sqrt{\frac{t_c}{t_t}}, \quad (6.12)$$

$$b_{nt} \sim l_t \left(\frac{t_c}{t_t}\right)^{3/2}, \quad (6.13)$$

$$a_{nt} \sim u' l_t \left(\frac{t_c}{t_t}\right)^2 \sim a_t \left(\frac{t_c}{t_t}\right)^2. \quad (6.14)$$

These expressions allow the local description of flamelet characteristics in terms of mixture chemical property  $t_c$  and local turbulence parameters  $u'$ ,  $t_t$  and  $l_t$ . The flamelet velocity scales with the inverse square root of the Damköhler number  $Da \equiv t_t/t_c$ .

---

<sup>1</sup>in the subscript "nt", "t" stands for turbulent, and "n" for normal, since a normal propagation velocity can be defined for each thickened flamelet

### Brush and burning velocity

Since for RANS modeling the average turbulent flame velocity  $S_t$  is required for the model closure, this last step consists in evaluating  $S_t$  using the flamelet velocity  $u_{nt}$ . Zimont's evaluation is based on the averaged ratio of flamelet surfaces to the normal direction of propagation of the turbulent flame [Zim79](p. 308):

$$S_t = u_{nt} \frac{\overline{\delta S}}{\delta S_0} > u_{nt}, \quad (6.15)$$

where  $\delta S$  is the flamelet front area and  $\delta S_0$  its projected area normal to the direction of the flame propagation. This unclosed term is statistically equal to the ratio between the standard deviation  $\Sigma$  of the local flamelet position ( $z=z(x,y)$ ) submitted to turbulence, and  $\Lambda$  the scale related to the flame front surface:

$$\frac{\overline{\delta S}}{\delta S_0} = \frac{\Sigma}{\Lambda}. \quad (6.16)$$

The variance of the flame position  $\Sigma^2 = \overline{(z - \bar{z})^2}$  can be seen as the result of turbulent diffusion:

$$\Sigma^2 \approx D_t t \approx (u' l_t) t \quad (6.17)$$

with the condition that the time  $t$  belongs to the range:

$$t_t \sim \frac{l_t}{u'} < t < \frac{l_t}{u_{nt}} \sim t_t \text{Da}^{1/2}. \quad (6.18)$$

This condition ensures that the statistical averaging is relevant in terms of turbulence time scale (left inequality), and that the reduced displacement of the front (right inequality) enables consideration of the same fluid particles as justified by Zimont et al. [ZPBW97](p. 3-4).

Zimont expresses  $\Lambda/b_{nt}$  using the Pi-theorem with the ratios  $u' t/b_{nt}$ ,  $u'/u_{nt}$  and  $l_t/b_{nt}$  [Zim79](p. 308):

$$\frac{u' t}{b_{nt}} = G_1 \left( \frac{u' t}{b_{nt}}, \frac{u'}{u_{nt}}, \frac{l_t}{b_{nt}} \right). \quad (6.19)$$

Similarity of Eqs. (6.12)(6.13) allows the elimination of the ratio  $u'/u_{nt}$  to keep  $l_t/b_{nt}$ . To maintain the condition of stationarity of  $S_t$  and using the facts that:

- $u' t/b_{nt}$  is the only factor displaying an explicit dependence to  $t$
- $\Sigma$  scales with  $t^{1/2}$ ,

the term  $u' t/b_{nt}$  must also scale with the power of 1/2:

$$\frac{u' t}{b_{nt}} = \sqrt{\frac{u' t}{b_{nt}}} G_2 \left( \frac{l_t}{b_{nt}} \right). \quad (6.20)$$

Zimont demonstrates that the function  $G_2$  can only be constant of order unity [Zim79](p. 309), because its argument  $l_t/b_{nt}$  is very large for the thickened flame regime (which implies  $u_{nt} \ll u'$ ), so that the expression for the flame front surface scale  $\Lambda$  is simply:

$$\Lambda = \sqrt{\frac{u' l_t}{b_{nt}}}. \quad (6.21)$$

Eqs. (6.15), (6.12), (6.17) and (6.21) yield the expression for the averaged flame speed:

$$S_t \sim u' \sqrt{\frac{t_c}{t_t}} \sqrt{\frac{l_t}{b_{nt}}} \sim u' \left(\frac{t_t}{t_c}\right)^{1/4}. \quad (6.22)$$

The averaged flame speed  $S_t$  scales with the Damköhler number to the power of 1/4, whereas the flamelet velocity scales to the power of 1/2.

### Closure for CFD

Within CFD calculations, the last expression Eq. (6.22) is mostly formulated in order to exhibit its ratio with the laminar flame speed  $S_l$ , which is a given parameter precisely known for any gas from tables or correlations, see section 2.3.3 (p.26):

$$\frac{S_t}{S_l} = A \left(\frac{u' l_t}{a}\right)^{1/2} \left(\frac{t_c}{t_t}\right)^{1/4} = A \sqrt{\text{Pr Re}_t} \text{Da}^{-1/4}. \quad (6.23)$$

The constant  $A$  ensures a complete closure for the model, since Eq. (6.22) is based on scaling arguments, but not on numerical value. According the numerous validations of this model against experimental data, a *universal* value for hydrocarbon fuels

$$A = 0.52 \quad (6.24)$$

has been empirically found and adopted. The value of the constant  $A$  for LES is largely discussed in the following.

For the TFC model, a bending function can be used to limit the turbulent flame speed in case of high turbulence intensity. . The turbulent flame velocity is limited by a *stretch factor*  $G$  ( $G S_t$  replacing  $S_t$  in Eq. (6.2)), as developed by Zimont et al. [ZL95, ZPBW97] and Cant and Bray [CB88](p. 793-794):

$$G = \frac{1}{2} \text{erfc} \left\{ -\left(\frac{1}{2\sigma}\right)^{1/2} \ln\left(\frac{\varepsilon_{cr}}{\varepsilon} + \frac{\sigma}{2}\right) \right\}, \quad (6.25)$$

$$\text{with } \sigma = \ln \frac{l_t}{\eta} \text{ and } \varepsilon_{cr} = 15 \nu g_{cr}^2. \quad (6.26)$$

$\sigma$  is the standard deviation of the log-normal distribution of the dissipation rate  $\varepsilon$ . The critical flamelet quench rate  $g_{cr}$  is estimated from laminar flame computations or directly estimated as  $g_{cr} \approx 8.4 S_l^2 / a(T_{ad})$  according to Polifke et al. [PFB00](p. 5), or simply as

$g_{cr} \sim S_l^2/a(T_u) \sim 1/t_c$  as proposed by Zimont et al. [ZPBW97](p. 5). The critical flamelet quench rate generally scales inversely to the chemical time:  $g_{cr} \sim 1/t_c$ . The value of 15 in Eq. (6.39) is a coefficient coming from the isotropic homogeneous turbulence theory [Pet00](p. 16). Thanks to the log-formulation, the general formulation is not sensitive to small discrepancies in the evaluation of  $g_{cr}$ . This part of the TFC model has given satisfying results for burners with high strain rates. This is further discussed for LES modeling in section 6.2.3 (p.96).

### 6.1.3 Counter-gradient diffusion

The classical model for turbulent diffusion based on a gradient assumption has been presented in section 3.2.1 (p.45). In the context of the progress variable approach, a possible drawback appears.

If the hypothesis of an infinitely thin flame front is made, an expression of the Favre averaging can be expressed as function of the conditional variables in burnt and unburnt sides  $\tilde{f}_u$  and  $\tilde{f}_b$ :

$$\bar{\rho} \tilde{f} = \overline{\rho f} = (1 - \tilde{c}) \tilde{f}_u + \tilde{c} \tilde{f}_b. \quad (6.27)$$

Using this expression for the term  $f = c'u'$  (in 1D for simplicity), an expression of the progress variable turbulent diffusion (see Eq. (3.18) and Eq. (6.2)) reads:

$$\begin{aligned} \bar{\rho} \widetilde{c'u'} &= \bar{\rho} \overline{(u - \tilde{u})(c - \tilde{c})} \\ \bar{\rho} \widetilde{c'u'} &= \tilde{c} (1 - \tilde{c}) (\tilde{u}_u - \tilde{u}_b). \end{aligned} \quad (6.28)$$

Contrary to the turbulent diffusion based on the gradient assumption

$$\bar{\rho} \widetilde{c'u'} = -\frac{\mu_t}{Sc_c} \frac{\partial \tilde{c}}{\partial x}, \quad (6.29)$$

the previous expression Eq. (6.28) can take positive values through the flame front, if the gas in the unburnt gas is faster than in the burnt side  $\tilde{u}_u - \tilde{u}_b > 0$ . Evidently, the thermal expansion factor  $\tau = \rho_u/\rho_b - 1$  is quite important for this gas dynamic effect, since it influences the normal velocity component through the flame front. A Bray number  $N_B$  has been introduced by Veynante et al. [VTBM97] to quantify this effect:

$$N_B \equiv \frac{\tau S_l}{u'}. \quad (6.30)$$

Counter-gradient diffusion should appear for larger values than one ( $N_B > 1$ ), and may be neglected with high turbulence intensity burners, i.e. for the thickened flame regime where  $u' \gg S_l$ . This effect appears for the wrinkled flame regime, since it is characterized with  $u' < S_l$ . It may also occur for the corrugated flame regime if  $\tau > \sqrt{\text{Pr} \text{Re}_l / \text{Da}}$  according to Eq. (2.106). In the following, no special model are employed to correct the counter-gradient diffusion. The models are developed for burners in the thickened flame regime or at its limit with the corrugated flame regime, where the previous relation is likely to be fulfilled.

Zimont and Biagioli [ZB02] claim that the TFC model includes implicitly the counter-gradient effect in the source term. The r.h.s. of the modeled equation with the diffusion gradient assumption and the source term would permit to the r.h.s. of the exact equation thanks to a “joint closure”. The idea is promising, but its justification based on the conserved integral reaction rate is not complete [ZB02](p. 83).

## 6.2 Closure LES-TFC

Flohr and Pitsch [FP00] have proposed a fairly straightforward adaptation of the TFC model for the LES modeling. Their closure for the turbulent flame speed is presented in the next sub-section. In this work and contrary to Flohr and Pitsch’s paper [FP00](p. 171, Eq. 2.7), the laminar diffusion  $\nu/S_{c_c}$  is taken into consideration. An identical Schmidt number for laminar and turbulent diffusions is assumed. Neglecting the laminar diffusion can be namely accepted for RANS modeling, because numerically the turbulent diffusion is typically 50 times larger than the laminar one. But, this is not easily acceptable for LES modeling where this ratio is likely to belong to the range [0 – 10]. The filtered transport equation for the progress variable derived from Eq. (5.1) reads:

$$\frac{\partial \bar{\rho} \tilde{c}}{\partial t} + \frac{\partial \bar{\rho} \tilde{c} \tilde{u}_i}{\partial x_i} = \frac{\partial}{\partial x_i} \left( \bar{\rho} \frac{\nu + \nu_t}{S_{c_c}} \frac{\partial \tilde{c}}{\partial x_i} \right) + \tilde{w}_c. \quad (6.31)$$

This is formally the same equation as Eq. (6.1), except that the symbol  $\tilde{\cdot}$  stands for a filtering procedure, instead of an averaging procedure. A gradient-diffusion assumption is made for the turbulent diffusion:

$$\tilde{c} \tilde{u} - \tilde{c} \tilde{u} \approx \frac{\nu_t}{S_{c_c}} \overrightarrow{\nabla} \tilde{c}. \quad (6.32)$$

The eventual consequence of this assumption is discussed in section 6.1.3 (p.93), since this part of the modeling is often a theme of discord in literature.

### 6.2.1 LES-TFC model closure

For the closure of the filtered source term, Flohr and Pitsch [FP00] write similar to the RANS modeling:

$$\tilde{w}_c = \rho_u S_{t_\Delta} \left| \overrightarrow{\nabla} \tilde{c} \right|, \quad (6.33)$$

where  $\tilde{w}_c$  is the filtered source term, and  $S_{t_\Delta}$  the filtered turbulent flame speed. They adapt the closure for this last term to LES modeling under the assumptions that:

- “The turbulent large scales  $u'$  and  $l_t$  only enter Zimont’s analysis via  $\varepsilon \approx u'^3/l_t$  [FP00](p. 172)”
- The dissipation rate  $\varepsilon$  is constant in the inertial range:  $\varepsilon \approx u(l_n)^3/l_n$  for any eddy such as  $l_t > l_n > \eta$

- The grid scale  $\Delta$  belongs to  $[\eta, l_t]$ , and is smaller than the turbulent flame brush thickness  $\delta_t$ .

According to Kolmogorov's energy cascade theory [Kol41, Kol62], the second assumption is completely acceptable with homogeneous turbulence. The first assumption is more disputable, and the assertion looks like an abrupt short-cut compared to Zimont's theoretical developments, even if the ratio  $S_t/S_l$  finally scales with the turbulent dissipation  $\varepsilon$  (see Eq. (6.36)). The third assumption only concerns the design of the mesh and is not problematic.

Consequently, Flohr and Pitsch replace dimensionless numbers based on the turbulent large scales ( $u', l_t$ ) by the ones based on the cut-off scales ( $u_{sgs}, \Delta$ ) and write:

$$\frac{S_{t\Delta}}{S_l} = 1 + A(\text{Re}_\Delta \text{Pr})^{1/2} \text{Da}_\Delta^{-1/4}, \quad (6.34)$$

where  $\text{Re}_\Delta = u_{sgs}\Delta/\nu$  and  $\text{Da}_\Delta = \Delta/(u_{sgs}t_c)$  are respectively the subgrid scale Reynolds and Damköhler numbers. The term 1 has been included to recover the relation  $S_{t\Delta} = S_l$  for zones of lower turbulence, i.e. where the flame regime is no more the thickened flame regime. The filter scale is computed from the cell volume:  $\Delta = \text{vol}^{1/3}$ , and the subgrid scale fluctuation obtained from the Smagorinsky model:

$$u_{sgs} = \frac{\nu_t}{C_s\Delta} = C_s\Delta\sqrt{2\overline{D_{ij}D_{ij}}} \quad (6.35)$$

where  $C_s$  is the Smagorinsky constant. Flohr and Pitsch have maintained the constant value to  $A = 0.52$  for their applications. This is commented in section 6.2.4 (p.97), and illustrated with numerical results in section 8.1 (p.139), section 8.2 (p.156) and section 8.3 (p.173).

### 6.2.2 LES-TFC with turbulent kinetic energy

In order to dissociate the influence of combustion modeling to turbulence modeling in this thesis, the LES-TFC model has been slightly modified to be computed with a transport equation for the turbulent kinetic energy, rather than with the Smagorinsky model. The closure is evaluated with the local mixture and turbulence parameters instead of the dimensionless numbers:

$$\frac{S_{t\Delta}}{S_l} = 1 + Au_{sgs}^{3/4}\Delta^{1/4}t_c^{-1/4}. \quad (6.36)$$

The influence of the subgrid scale velocity  $u_{sgs}$  is obvious, and its correct prediction is decisive for the evaluation of  $S_{t\Delta}/S_l$ . The subgrid turbulent kinetic energy  $k_{sgs}$  is resolved and directly yields the subgrid scale turbulent fluctuation:

$$u_{sgs} = \sqrt{\frac{2}{3}k_{sgs}}. \quad (6.37)$$

### 6.2.3 Bending effect and stretch factor

As presented for the RANS modeling in section 6.1.2 (p.92), an adapted *stretch factor*  $G$  is used to limit the turbulent flame speed in case of high turbulence intensity:

$$G = \frac{1}{2} \operatorname{erfc} \left\{ - \left( \frac{1}{2\sigma_\Delta} \right)^{1/2} \ln \left( \frac{\varepsilon_{cr}}{\varepsilon_\Delta} + \frac{\sigma_\Delta}{2} \right) \right\}, \quad (6.38)$$

$$\text{with } \sigma_\Delta = \ln \frac{\Delta}{\eta} \text{ and } \varepsilon_{cr} = 15\nu g_{cr}^2. \quad (6.39)$$

Similarly to the TFC model,  $\sigma_\Delta$  is the standard deviation of the log-normal distribution of the dissipation rate  $\varepsilon_\Delta$ . The critical flamelet quench rate remains independent of the turbulence model, and should still scale inversely to the chemical time:  $g_{cr} \sim 1/t_c$ .

Actually, the term  $g_{cr}$  is the central point of the model for  $G$ , since its estimation is still arguable with LES, whereas its influence is more sensitive than with RANS modeling. It has a strong influence on the flame attachment for example. In this thesis, the focus is not placed on this parameter evaluation, but on the general formulation of this bending function in order to parameterize its influence in terms of  $Da_\Delta$  and  $Re_\Delta$ :

$$\begin{aligned} \frac{\varepsilon_{cr}}{\varepsilon_\Delta} &\sim \frac{15\nu}{t_c^2} \frac{\Delta}{u_{sgs}^3} = 15 \frac{\nu}{u_{sgs}\Delta} \frac{\Delta^2}{u_{sgs}^2 t_c^2} \\ \Rightarrow \frac{\varepsilon_{cr}}{\varepsilon_\Delta} &\sim 15 \frac{Da_\Delta^2}{PrRe_\Delta} \sim 15 Ka_{t\Delta}^{-2}. \end{aligned} \quad (6.40)$$

Using the relations Eq. (7.5) and Eq. (E.42) which are derived in the section A.5 (p.222) for the box filter:

$$\sigma_\Delta = 0.26 \ln \frac{\Delta}{\eta} = 0.26 \ln \frac{\Delta}{l_t Re_t^{-3/4}} \quad (6.41)$$

$$\sigma_\Delta \approx 0.26 \ln \left[ MR \left( \frac{Re_\Delta}{0.881 MR^{4/3}} \right)^{3/4} \right] \quad (6.41)$$

$$\sigma_\Delta \approx 0.26 \ln (1.10 Re_\Delta^{3/4}). \quad (6.42)$$

In Eq. (6.41) the term  $MR = \Delta/l_t$  which states for the mesh refinement has been included. This variable is actually defined later in section 7.1.2 (p.101), and its utility is explained.

An expression for  $G$  depending on the local Damköhler and Reynolds numbers can be expressed, and plotted in Figure 6.1 (p.97):

$$G(Re_\Delta, Da_\Delta) \approx \frac{1}{2} \operatorname{erfc} \left\{ \frac{-1.387}{\ln^{1/2} (1.10 Re_\Delta^{3/4})} \ln \left[ 15 \frac{Da_\Delta^2}{Re_\Delta} + 0.13 \ln (1.10 Re_\Delta^{3/4}) \right] \right\} \quad (6.43)$$

The turbulent flame speed is reduced with this function when the ratio  $Re_\Delta/(Da_\Delta^2)$  becomes large, i.e. when the Karlovitz number becomes large. This relation corresponds to the bounds of the thickened flame regime  $1 < Da < Re^{1/2}$ . It also indicates that the bending function  $G$  of the TFC model is useful when the local combustion regime is close to the broken reaction zone regime.

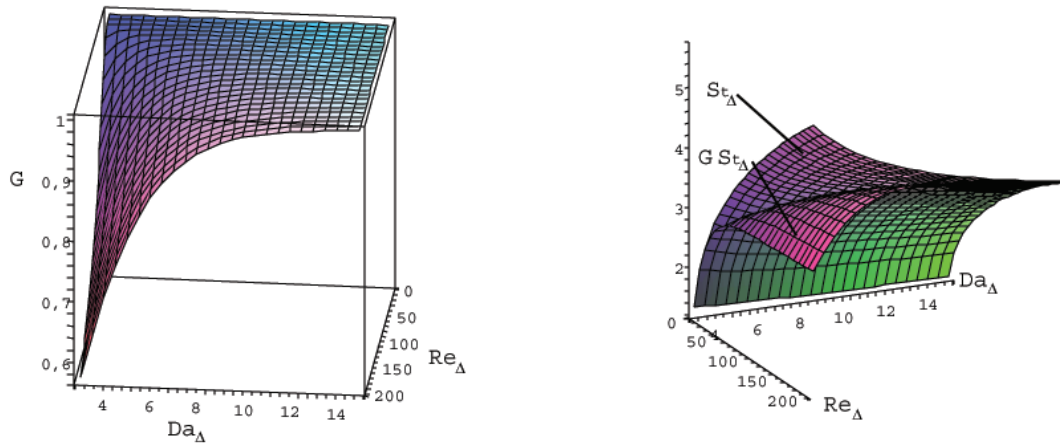


**Fig. 6.1:** Model LES-TFC: stretch effect  $G$  (left) and turbulent flame speed with and without stretch effect (right)

#### 6.2.4 LES-TFC closure drawbacks

Finally, the TFC-LES has two main drawbacks, which are due to the constants  $g_{cr}$  and  $A$ , respectively for the stretch factor and the turbulent flame speed evaluation.

For LES modeling, the stretch factor  $g_{cr}$  should represent the stretch effect only due to subgrid eddies. Its value may therefore be different than its value for RANS modeling for a same case. A model or a precise evaluation for this constant is needed.

Even more problematic is the choice of the constant value  $A$ . For RANS modeling, experience with the model has demonstrated that the value  $A = 0.52$  can be considered as an universal constant. This has not been confirmed for LES modeling. Present results, as well as others obtained by Zimont and Battaglia [ZB06](p. 19), seem to prove that the constant must be adapted for each geometry according to the mesh and the turbulence model (Smagorinsky or turbulent kinetic energy transport equation models).

In the next chapter, a new closure similar to the TFC model is proposed in order to overcome, or to reduce these drawbacks.



## 7 Subgrid Flame Closure model

J'ai toujours dit à mes étudiants : si vous pensez avoir une idée que personne n'a jamais eue, il y a tout lieu de craindre qu'il ne s'agisse d'une sottise. À l'inverse, trouver une de ses propres idées chez un bon auteur du passé est toujours rassurant.

*A. Comte-Sponville, [CS03](p. 48)*

In the previous chapter, the TFC model, developed for the thickened flame regime, has been presented for RANS and LES modeling. Its adaptation to the LES modeling may be less straightforward, considering with more attention the differences between integral scales and subgrid scales. A new closure is thus derived for the resolved burning velocity  $S_{t\Delta}$ , specially conceived for LES modeling. The Subgrid Flame Closure (SFC) model is designed to be valid both for the thickened flame regime and the corrugated flame regime.

The leading idea for this new model is detailed in the first section. Closure is detailed for the thickened flame regime and corrugated flame regime, respectively, in the second and third sections. An extension of the model to treat the bending effect is presented, before describing the general model formulation.

### 7.1 Model concept: subgrid flame closure

#### 7.1.1 Paradoxical difficulty in LES modeling

The difficulty to model the turbulent premixed combustion with LES modeling is essentially due to scale considerations. LES modeling and RANS modeling differ by the consideration of the turbulence. RANS simulations *model and evaluate at each time-step the averaged turbulent scales*: fluctuation velocity  $u'$  and integral length scale  $l_t$ . LES simulations *model and evaluate at each time-step the subgrid fluctuation*  $u_{sgs}$  associated with the mesh size  $\Delta$ . The two quantities  $u'$  and  $l_t$  can be statistically post-processed *only after the simulation*. Whereas LES modeling evaluates turbulent information at finer scales than RANS, it cannot estimate integral turbulent scales  $u'$  and  $l_t$  during calculations. Any LES combustion model should exploit in an optimal way the turbulent information modeled during the simulation: The subgrid fluctuation.

LES combustion modeling requires the introduction of three new flame scales compared to the laminar case, as depicted in Figure 7.1 (p.100):

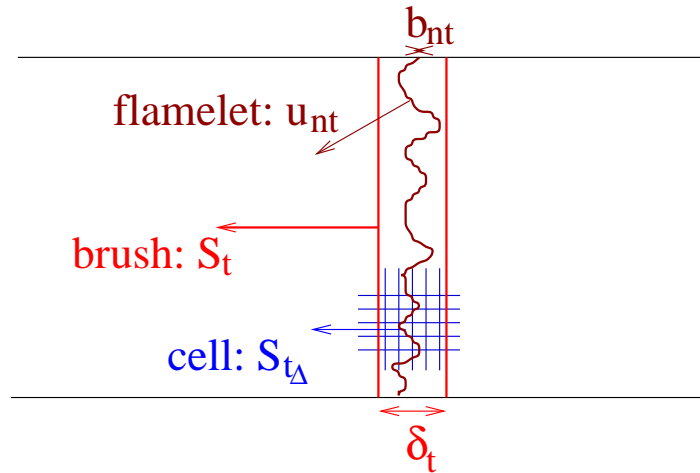


**Fig. 7.1:** Turbulent flame speeds at different observation scales

- As explained in section 2.4.3 (p.37), turbulent eddies tend to modify the structure of the flame front. For the corrugated and thickened flame regimes, the flame front is wrinkled and formed of a collection of (thickened) flamelets. The flamelet thickness  $b_{nt}$ , and flamelet velocity  $u_{nt}$  may be slightly different from the laminar flame properties  $\delta_l$  and  $S_l$ .
- The second scale is larger, and corresponds to the turbulent brush. It refers to the different positions that the flame is occupying during the integral time scale because of the flow fluctuations  $u'$ . The brush thickness  $\delta_t$  may scale with the integral length scale  $l_t$ , as argued by Zimont when developing the TFC model [Zim79]. A brush burning velocity  $S_t$  is associated to the brush, which simply describes the average burning velocity.
- A third scale corresponds to the resolved flame. Its velocity and thickness depend on modeling, as detailed in the following.

The terms “*flame speed*” or “*flame velocity*” refer to the velocity of laminar flames or (thickened) flamelets. The term “*burning velocity*” is used for flame brush, averaged flames and resolved flames, for which a flame velocity cannot be properly defined. It describes a combustion rate, expressing at which averaged velocity burnt gas propagates into unburnt gas.

RANS modeling is coherent in terms of scales with the flame brush, since this approach directly employs the integral scales  $l_t$  and  $u'$ . Because of the mesh property, the flame scale resolved with LES is typically placed between the flamelet and brush scales. The LES closure must therefore deliver a resolved burning velocity  $S_{t\Delta}$  coherent with its resolved thickness.

Two steps are needed in order to achieve this purpose. The first task consists in *evaluating the flamelet thickness  $b_{nt}$  and velocity  $u_{nt}$*  contained in each cell thanks to the subgrid fluctuations. The second step consists in *estimating the resolved burning velocity  $S_{t\Delta}$*  ac-

according to the flamelet, mesh and turbulent properties. This is precisely detailed in section 7.2 (p.104), when developing the closure for the thickened flame regime. The development for the corrugated regime, described in section 7.3 (p.111), is similar.

Similarly to the TFC-LES model and demonstrated by Eq. (6.3) in section 6.1.1 (p.87), the resolved flame front thickness has no effect on the numerical solution, and *its evaluation is not required*, since the SFC model is based on the gradient source term:

$$\tilde{w}_c = \rho_u S_{t_\Delta} \left| \vec{\nabla} \tilde{c} \right|.$$

Although, the SFC model can deliver an estimation of the flamelet thickness  $b_{nt}$ , contrary to the TFC-LES model.

Before detailing the model closure, the subgrid dimensionless Reynolds  $Re_\Delta \equiv u_{sgs}\Delta/\nu$  and Damköhler  $Da_\Delta \equiv t_\Delta/t_c$  numbers are compared to their counter-part turbulent numbers  $Re_t$  and  $Da$ . There are three reasons to derive these relations:

- A closure is developed separately for the corrugated and thickened flame regimes. The regime must locally be identified *during the calculation*, so that the model can switch from one formulation to the other. Normally the two regimes are defined in terms of the turbulent Reynolds  $Re_t$  and Damköhler  $Da$  numbers (see Figure 2.4.3 (p.37)). This must be estimated according to the subgrid dimensionless numbers. The blend function, used to switch from one formulation to the other, is described in section 7.6.1 (p.133) with the complete model formulation.
- For the development of the model, it is supposed that the *mesh is always coarser than the flamelet thickness*:  $\Delta > b_{nt}$  as depicted in Figure 7.2 (p.104). This must be first verified. The condition is expressed in terms of the subgrid dimensionless numbers  $Re_\Delta$  and  $Da_\Delta$ .
- The relation between subgrid and turbulent dimensionless numbers is required in section 7.4 (p.114) and section 7.5 (p.123) dedicated to the modeling of the bending effect and quenching in case of high turbulence intensity.

### 7.1.2 Comparison of subgrid and integral length scales

During LES computations, turbulent Reynolds  $Re_t$  and Damköhler  $Da$  numbers are not known. It is useful to estimate them according to the subgrid dimensionless numbers  $Re_\Delta$  and  $Da_\Delta$ . Two dimensionless numbers are defined to characterize the mesh and to make this evaluation possible:

- $MR \equiv \Delta/l_t < 1$  the *mesh refinement*,
- $RTE \equiv 1 - u_{sgs}^2/u'^2 < 1$  the *resolved turbulent energy*.

The relation between these two numbers requires some mathematical developments, and is derived in appendix A.5 (p.222) for a box-filter:

$$RTE \approx 1 - 0.8 MR^{2/3}. \quad (7.1)$$

This relation can be derived by writing the integral over the eddies length scale of the spectral density energy  $E(\kappa)$  multiplied with the filter function. In the case of the box filter, approximations are required to achieve the numerical computation, contrary to the case of the Gauss and sharp spectral filter illustrated by Pope [Pop00](p. 577).

*The parameters MR and RTE are not used in the model itself, since the mesh refinement is not known during the calculations.* But, they enable to stress and evaluate the difference between the subgrid numbers and the turbulent numbers, when postulating for a mesh refinement. They also permit to demonstrate that the relation  $b_{nt} < \Delta$  is in general fulfilled, i.e. that the mesh size is larger than the (thickened) flamelet, before using this hypothesis to develop the SFC model.

### Subgrid Damköhler number $Da_\Delta$

A relation depending on the mesh refinement between the Damköhler number  $Da$  and the local Damköhler number  $Da_\Delta$  can be established:

$$Da \equiv \frac{t_t}{t_c} = \frac{t_t}{t_\Delta} Da_\Delta \sim \frac{l_t}{u'} \frac{u_{sgs}}{\Delta} Da_\Delta$$

$$Da \sim \frac{\sqrt{1 - RTE}}{MR} Da_\Delta \quad (7.2)$$

$$\Leftrightarrow Da_\Delta \sim \frac{MR}{\sqrt{1 - RTE}} Da. \quad (7.3)$$

Using Eqs. (E.42) and (E.36) with a mesh refinement of five cells <sup>1</sup> to resolve the largest scales  $MR \equiv \Delta/l_t \approx 1/5$ , , it gives numerically:

$$Da_\Delta \approx 1.14 MR^{2/3} Da \quad (7.4)$$

i.e.  $Da \approx 3.32 Da_\Delta$ .

This relation points out discrepancy between integral and subgrid Damköhler numbers. The numerical values obtained during LES simulations are smaller. This is all the more pronounced as the mesh becomes fine. It would lead to problems near walls, where the mesh refinement parameter  $MR \equiv \Delta/l_t$  is drastically reduced.

---

<sup>1</sup>it corresponds to a usual mesh refinement for industrial application, and allows to resolve about 70% of the turbulent energy as demonstrated in appendix A.5 (p.222)

**Subgrid Reynolds number  $Re_\Delta$** 

The same comparison, as achieved in the previous part, is formulated with the Reynolds number:

$$\begin{aligned} \frac{Re_\Delta}{Re_t} &\sim \frac{u_{sgs} \Delta}{u' l_t} \sim MR \sqrt{1 - RTE} \\ \Leftrightarrow Re_t &\sim \frac{Re_\Delta}{MR \sqrt{1 - RTE}} \end{aligned} \quad (7.5)$$

$$\Rightarrow Re_t \approx 1.14 \frac{Re_\Delta}{MR^{4/3}} \text{ with the box-filter} \quad (7.6)$$

$$\Rightarrow Re_t \approx 9.70 Re_\Delta, \text{ with } MR \approx 1/5 \quad (7.7)$$

The discrepancy between subgrid and integral Reynolds numbers is larger than for the Damköhler number. The subgrid Reynolds number corresponds to an approximately order of magnitude smaller value than the turbulent Reynolds number.

Using the definition of  $MR \equiv \Delta/l_t$ , the relation  $Re_\Delta/Re_t \sim MR^{4/3}$  is also useful to show that the subgrid fluctuation is increasing slower than the filter scale compared the respective integral scales  $u'$  and  $l_t$ :

$$\frac{Re_\Delta}{Re_t} = \frac{u_{sgs} \Delta}{u' l_t} \Rightarrow \frac{u_{sgs}}{u'} \sim \left( \frac{\Delta}{l_t} \right)^{1/3}. \quad (7.8)$$

**Subgrid Karlovitz number  $Ka_\Delta$** 

The relation for the Karlovitz number can be demonstrated writing the ratio between Reynolds and Damköhler numbers (see Eqs. (7.5) and (7.2)):

$$\begin{aligned} Ka_t &\sim \frac{\sqrt{\text{Pr} Re_t}}{Da} \sim \sqrt{\frac{1}{\sqrt{1 - RTE} MR}} \frac{MR}{\sqrt{1 - RTE}} \frac{\sqrt{\text{Pr} Re_\Delta}}{Da_\Delta} \\ Ka_t &\sim \frac{MR^{1/2}}{(1 - RTE)^{3/4}} Ka_\Delta \end{aligned} \quad (7.9)$$

Finally using the relation Eq. (E.42) for the box filter:

$$Ka_t \approx 1.21 Ka_\Delta. \quad (7.10)$$

For the Karlovitz number, the ratio between subgrid and turbulent values does not depend on the mesh refinement  $MR$  but only on the mesh structure. Indeed, the Karlovitz number scales with the turbulent dissipation  $\varepsilon$ :

$$\begin{aligned} \frac{Ka_\Delta^2}{Ka_t^2} &\sim \frac{Re_\Delta Da^2}{Da_\Delta^2 Re_t} \sim \frac{u_{sgs}^3 t_c^2}{a \Delta} \frac{a l_t}{u'^3 t_c^2} \\ \Leftrightarrow \frac{Ka_\Delta}{Ka_t} &\sim \sqrt{\frac{\varepsilon_\Delta}{\varepsilon}}. \end{aligned} \quad (7.11)$$

In the inertial range, where the turbulent dissipation  $\varepsilon$  is constant, the Karlovitz number remains constant, and does not depend on the mesh size.

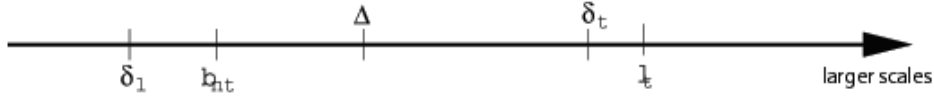


**Fig. 7.2:** Flame and turbulent scales (case  $Da > 1$ )

**Mesh and flamelet sizes: Ratio  $b_{nt}/\Delta$**

In the following, the development of the model is made with the assumption that the mesh is coarser than the flamelet thickness:  $b_{nt} < \Delta$  as depicted in Figure 7.2 (p.104). This condition can be verified using relations Eq. (7.2) and Eq. (6.13) derived by Zimont [Zim79](p. 306). The flamelet thickness scales with the integral length scale and the ratio of chemical and turbulent time scales:

$$\begin{aligned}
 \frac{b_{nt}}{\Delta} &\sim \frac{l_t}{\Delta} \left( \frac{t_c}{t_t} \right)^{3/2} \sim \frac{l_t}{\Delta} Da^{3/2} \\
 \Leftrightarrow \frac{b_{nt}}{\Delta} &\sim Da_{\Delta}^{-3/2} \cdot MR^{1/2} \cdot (1 - RTE)^{-3/4} \\
 \Rightarrow \frac{b_{nt}}{\Delta} &\approx 1.19 Da_{\Delta}^{-3/2} \approx 1.19 \left( \frac{Da}{3.32} \right)^{-3/2}, \quad (7.12) \\
 \text{with} \quad MR &\approx 1/5 \Rightarrow RTE \approx 73\% \text{ for the box filter, see Eq. (E.42).}
 \end{aligned}$$

This hypothesis should almost always be valid for the thickened flame regime, which is bounded with the condition  $Da > 1$ , and also consequently for the corrugated flame regime. This condition might be not fulfilled near the walls, where the mesh becomes finer and the ratio  $Da/Da_{\Delta}$  larger according to Eq. (7.4). This kind of limitation can also be found in the LES-TFC model, as mentioned by Flohr and Pitsch [FP00](p. 172):  $Da_{\Delta} > 3$ .

## 7.2 Closure for the thickened flame regime

In this part, closure of the resolved burning velocity for the thickened flame regime is derived. The thickened flamelet  $b_{nt}$  is supposed too thin to be explicitly resolved with the LES mesh size  $\Delta$ , as discussed previously with Eq. (7.12):

$$b_{nt} < \Delta. \quad (7.13)$$

The following strategy is proposed to obtain the closure of the resolved flame speed  $S_{t_{\Delta}}$  (see Figure 7.1 (p.100) for the flame scales, and Figure 7.3 (p.105) for the model strategy):

- First, the properties of the thickened flame contained in the cell are evaluated: Velocity  $u_{nt}$  and thickness  $b_{nt}$
- Secondly, the resolved burning velocity  $S_{t_{\Delta}}$  is estimated at the cell level using the fractal theory.

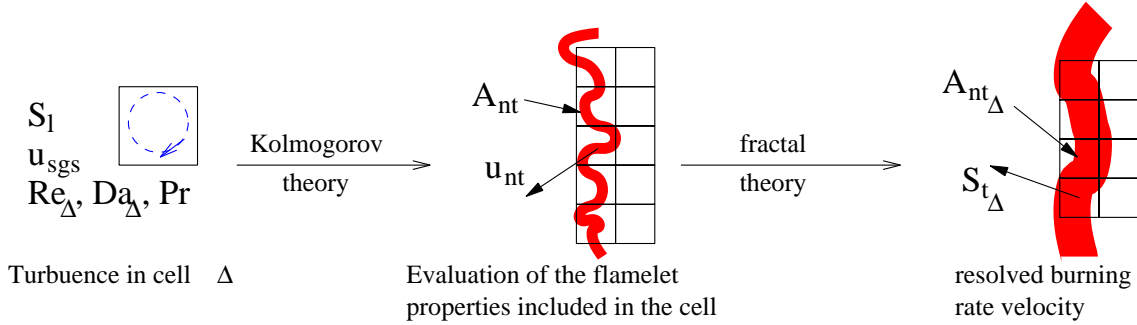


**Fig. 7.3:** Principle of the subgrid flame closure (SFC)

This two-step strategy is comparable to the development of the TFC model for the RANS context by Zimont [Zim79]. He initially evaluated the characteristics (thickness, velocity) of the thickened flamelet as a function of the integral length scale and fluctuation velocity. Secondly, he used arguments based on area ratios to evaluate the characteristics at the brush scale, relevant for RANS modeling.

During LES simulations, information such as integral length scale or turbulent velocity is not known. Consequently, the thickened flamelet characteristics must be evaluated with the available information: grid scale, subgrid-scale velocity and chemical parameters. Zimont [Zim79] derived the characteristics of the flame brush from the flamelet characteristics with an approximation based on the averaged surface of flame. The fractal theory should be more relevant in the LES context, since the difference of scale between the flamelet thickness and the cell scale may be too small to enable a correct averaging.

Compared to the work by Flohr and Pitsch [FP00] for the TFC-LES model, this approach should exploit in a better way LES modeling, since the resolved burning velocity is directly derived from the flamelet scale.

### 7.2.1 Flamelet velocity

As already described in section 2.4.3 (p.38) when detailing the combustion regimes, in the thickened flame regime the Kolmogorov eddies are small enough to enter and thicken the laminar flame front, whereas the largest eddies wrinkle the flame surface. The turbulent flame displays a continuous succession of so-called thickened flamelets. The largest eddies which are able to enter and thicken the laminar flame have a size  $l(n)$  and a velocity  $u(n)$ , which are comparable with the properties of the thickened flamelet:

$$l(n) \approx b_{nt}, \quad (7.14)$$

$$u(n) \approx u_{nt}. \quad (7.15)$$

Working further with the assumption that the thickened flamelet is completely included in the cell:  $b_{nt} < \Delta$ , the properties of the thickened flamelet must be evaluated from this coarser scale. Using the approximation that the flamelet has a uniform thickness  $b_{nt}$  and

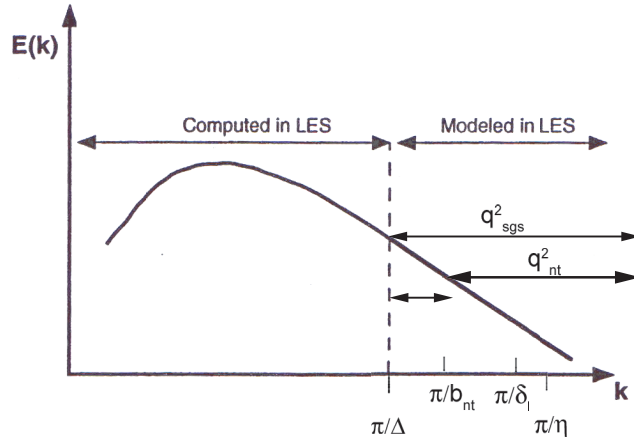


**Fig. 7.4:** Scale and turbulent energy spectrum

a uniform velocity  $u_{nt}$  *within a cell*, these two local characteristic values are evaluated according to Kolmogorov's theory. According to the turbulent energy spectrum, depicted Figure 7.4 (p.106), the largest eddies which enter the flame should satisfy the relation:

$$\begin{aligned} \frac{3}{2} u_{nt}^2 \equiv q_{nt}^2 &\approx \int_{\kappa_{nt}=\pi/b_{nt}}^{\infty} E(\kappa) d\kappa \\ \Leftrightarrow \frac{3}{2} u_{nt}^2 \equiv q_{nt}^2 &\approx \int_{\kappa_{nt}=\pi/b_{nt}}^{\kappa_c=\pi/\Delta} \underbrace{E(\kappa)}_{\kappa^{-5/3} \varepsilon^{2/3}} d\kappa + \underbrace{\int_{\kappa_c}^{\infty} E(\kappa) d\kappa}_{q_{sgs}^2}, \end{aligned} \quad (7.16)$$

within  $q_{nt}^2$  stands for the turbulent kinetic energy included in the range of scales  $[\eta; b_{nt}]$ . This decomposition into two integrals brings some advantages:

- The term  $q_{sgs}^2$  stands for the sub-grid turbulent kinetic energy (tke) which is given by the LES model at each cell. A model which explicitly evaluates the sub-grid turbulent kinetic energy (model with transport equation for tke, or tke-based model) is recommended (see Sagaut [Sag01]), rather than a viscosity-based model (Smagorinsky model [Sma63]).
- The calculation of the first integral of the r.h.s.  $\int_{\kappa_{nt}}^{\kappa_c} \kappa^{-5/3} \varepsilon^{2/3} d\kappa$  is reduced to a small interval (all the more reduced as the grid becomes finer), where the hypothesis of a constant dissipation  $\varepsilon$  (theory of isotropic homogeneous turbulence) is less questionable:

$$\varepsilon \sim \frac{u'(r)^3}{r} \approx \frac{u_{sgs}^3}{\Delta} \sim \varepsilon_{\Delta}. \quad (7.17)$$

Therefore a relation between the flamelet velocity  $u_{nt}$ , size  $b_{nt}$  and the subgrid velocity  $u_{sgs}$  and size  $\Delta$  is obtained:

$$u_{nt}^2 = u_{sgs}^2 - \varepsilon_{\Delta}^{2/3} \pi^{-2/3} (\Delta^{2/3} - b_{nt}^{2/3}). \quad (7.18)$$

Assuming *for the moment* that chemical time scales of the thickened flamelet and the laminar flame are equal:

$$\frac{b_{nt}}{u_{nt}} = t_c \equiv \frac{a}{S_l^2}, \quad (7.19)$$

two equations are available to solve the two unknowns  $u_{nt}$  and  $b_{nt}$ :

$$\begin{aligned} u_{nt}^2 &= u_{sgs}^2 - \varepsilon_{\Delta}^{2/3} \pi^{-2/3} (\Delta^{2/3} - b_{nt}^{2/3}), \\ b_{nt} &= t_c u_{nt}. \end{aligned}$$

The assumption concerning the chemical time  $t_c$  is not evident (particularly with bending-effect), and discussed in section 7.5.1 (p.124), in order to propose a model valid with stretching.

Using the subgrid Damköhler number  $Da_{\Delta} = \Delta / (u_{sgs} t_c)$  and the relations

$$\begin{aligned} \varepsilon_{\Delta}^{2/3} t_c^{2/3} &= u_{sgs}^{4/3} Da_{\Delta}^{-2/3} \\ \text{and } \varepsilon_{\Delta}^{2/3} \Delta^{2/3} &= u_{sgs}^2, \end{aligned}$$

the first equation can be written as function of the two parameters  $u_{sgs}$  and  $Da_{\Delta}$  and the unknown  $u_{nt}$ :

$$\begin{aligned} u_{nt}^2 &= u_{sgs}^2 - \varepsilon_{\Delta}^{2/3} \pi^{-2/3} \Delta^{2/3} + \varepsilon_{\Delta}^{2/3} \pi^{-2/3} (t_c u_{nt})^{2/3} \\ \Leftrightarrow u_{nt}^2 - \pi^{-2/3} u_{sgs}^{4/3} Da_{\Delta}^{-2/3} u_{nt}^{2/3} + u_{sgs}^2 (\pi^{-2/3} - 1) &= 0. \end{aligned} \quad (7.20)$$

$y = u_{nt}^{2/3}$  appears as the solution of a third order polynomial written in the canonic form  $y^3 + 3py + 2q = 0$ .

### Discriminant

For this kind of polynomial expression, the discriminant  $D$  is defined by:

$$\begin{aligned} D &= p^3 + q^2 \\ \Leftrightarrow D &= \left( -\frac{\pi^{-2/3}}{3} u_{sgs}^{4/3} Da_{\Delta}^{-2/3} \right)^3 + \left( \frac{\pi^{-2/3} - 1}{2} u_{sgs}^2 \right)^2 = u_{sgs}^4 \left[ \left( \frac{\pi^{-2/3} - 1}{2} \right)^2 - \frac{\pi^{-2} Da_{\Delta}^{-2}}{27} \right]. \end{aligned}$$

$$\text{So that: } D > 0 \Leftrightarrow \left( \frac{\pi^{-2/3} - 1}{2} \right)^2 - \frac{\pi^{-2} Da_{\Delta}^{-2}}{27} > 0$$

$$\Leftrightarrow Da_{\Delta} > \frac{2\sqrt{3}}{9} \frac{\pi}{1 - \pi^{-2/3}} \approx 0.230.$$

**Positive discriminant:  $Da_\Delta > 0.230$**

For this type of polynomial with a positive discriminant and a negative value of  $p$ , there is only one real zero  $y$ , according to Hackbusch et al. [HSZ96](p. 649):

$$y = -2P \cosh \beta,$$

$$\text{where: } P = \text{sgn}(q) \sqrt{|p|}, \text{ and: } \beta = \frac{1}{3} \text{arccosh} \frac{q}{P^3}$$

$$P = -\frac{\pi^{-1/3} u_{sgs}^{2/3}}{\sqrt{3} Da_\Delta^{1/3}},$$

$$\beta = \frac{1}{3} \text{arccosh} \left( \frac{3\sqrt{3}}{2} (\pi - \pi^{1/3}) Da_\Delta \right).$$

$$\text{Then } y = \underbrace{\frac{2}{\sqrt{3}} \pi^{-1/3}}_{\approx 0.7884} \frac{u_{sgs}^{2/3}}{Da_\Delta^{1/3}} \cosh \left[ \frac{1}{3} \text{arccosh} \left( \underbrace{\frac{3\sqrt{3}}{2} (\pi - \pi^{1/3}) Da_\Delta}_{\approx 4.36} \right) \right],$$

$$u_{nt} = y^{3/2} \approx 0.7 \frac{u_{sgs}}{\sqrt{Da_\Delta}} \cosh^{3/2} \left[ \frac{1}{3} \text{arccosh} (4.36 Da_\Delta) \right]$$

If  $Da_\Delta < 0.230$  the discriminant is negative and  $4.36 Da_\Delta < 1$  so that  $\text{arccosh}(4.36 Da_\Delta)$  is not defined.

**Negative discriminant:  $Da_\Delta < 0.230$**

In this case there are three real zeros:

$$y_1 = -2P \cos \beta; y_{2,3} = 2P \cos \left( \beta \pm \frac{\pi}{3} \right),$$

$$\text{where: } P = \text{sgn}(q) \sqrt{|p|}, \text{ and: } \beta = \frac{1}{3} \arccos \frac{q}{P^3}.$$

For such a polynomial, the zeros fulfill the two relations:

$$y_1 + y_2 + y_3 = 0$$

$$y_1 y_2 y_3 = -2q.$$

In this case  $q < 0$ , so that only one of the three zeros is positive and physically meaningful (from the first relation it is deduced that one has an opposite sign than the others; from the second relation that only one zero negative is impossible):

$$y = \max \left\{ -2P \cos \beta, 2P \cos \left( \beta \pm \frac{\pi}{3} \right) \right\}$$

$$u_{nt} = y^{3/2}.$$

Only the solution given by the positive discriminant is considered, since the domain of validity for the solution with a negative discriminant is not relevant. The condition  $b_{nt} < \Delta$  namely imposes  $Da_\Delta > 1$  in Eq. (7.12).

### Solution for the flamelet velocity

The flamelet velocity  $u_{nt}$  is therefore evaluated with:

$$u_{nt} \approx 0.7 \frac{u_{sgs}}{\sqrt{Da_\Delta}} \cosh^{3/2} \left[ \frac{1}{3} \operatorname{arccosh}(4.357 Da_\Delta) \right]. \quad (7.21)$$

In CFD calculations, turbulent flame velocities are expressed in terms of the laminar flame speed  $S_l$ :

$$\frac{u_{nt}}{S_l} \approx 0.7 \frac{(\operatorname{Re}_\Delta \operatorname{Pr})^{0.5}}{Da_\Delta} \cosh^{3/2} \left[ \frac{1}{3} \operatorname{arccosh}(4.357 Da_\Delta) \right]. \quad (7.22)$$

The evaluation of the flamelet velocity  $u_{nt}$  has been carried out, the resolved burning velocity  $S_{t_\Delta}$  is estimated in the following.

### 7.2.2 Resolved burning velocity

Compared to RANS modeling, which resolves the flame brush scale  $\delta_t$  as depicted in Figure 7.1 (p.100), LES modeling enables the resolution of finer flame structures. Nevertheless it does not permit to resolve the flamelet structure. Therefore neither the flamelet velocity  $u_{nt}$ , nor the brush burning velocity  $S_t$  are the relevant burning velocities in order to close the filtered progress variable transport equation. In this part, the relevant resolved burning velocity is estimated using the fractal theory.

Assuming that the turbulent flame surface can be considered as a fractal surface as shown by Sreenivasan and Meneveau [SM86, Sre91], the change of observation scale is achieved using the fractal theory, originally presented by Mandelbrot [Man82], and described in section A.1 (p.205).  $u_{nt}$  stands for the thickened flamelet velocity,  $S_{t_\Delta}$  the resolved burning velocity of the turbulent flame,  $b_{nt}$  and  $\Delta$  the respective counter-part observation length scale. For fractal surfaces the observed surface area depends on the resolution of the measurement (see Knikker et al. [KVM02]):

$$A(\xi) \sim \xi^{2-\mathcal{D}}, \quad (7.23)$$

where  $\xi$  is the measurement scale and  $\mathcal{D}$  is the fractal dimension.  $\mathcal{D}$  can take values between 2 and 3, and tends asymptotically to:

$$\mathcal{D} \approx 2.37 \quad (7.24)$$

for high turbulence intensity cases (see Sreenivasan and Meneveau [SM86]), as well as for premixed flames in internal combustion engines as measured by Mantzaras et al. [MFB89], and generally for the thickened flame regime where  $u' \gg S_l$  and  $\operatorname{Re}_t \gg 1$  according to Sreenivasan [Sre91]<sub>(p. 567-568)</sub>. In the present case, the two observations scales

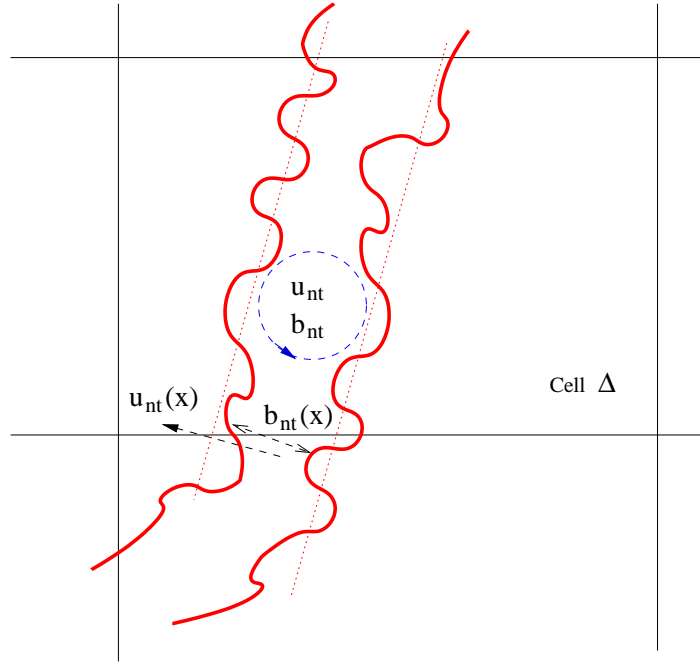


**Fig. 7.5:** Use of the fractal theory

are respectively the thickened flamelet scale  $b_{nt}$  and the grid scale  $\Delta$ :

$$\begin{aligned}
 & \int_{flame} u_{nt} dA = A_{\Delta} S_{t_{\Delta}} \\
 \Rightarrow & u_{nt} \int_{flame} dA \approx A_{\Delta} S_{t_{\Delta}}, \text{ if } u_{nt}(x) \approx u_{nt} = \text{constant within the cell} \\
 \Rightarrow & u_{nt} A_{b_{nt}} \approx A_{\Delta} S_{t_{\Delta}} \\
 \Rightarrow & \frac{S_{t_{\Delta}}}{u_{nt}} \approx \frac{A_{b_{nt}}}{A_{\Delta}} = \left( \frac{b_{nt}}{\Delta} \right)^{2-\mathcal{D}} > 1.
 \end{aligned} \tag{7.25}$$

The approximation  $u_{nt} \approx \text{constant}$  within the cell has already been emphasized, it should be all the more acceptable as the grid size becomes comparable to  $b_{nt}$ .

The expression for the resolved burning velocity is:

$$\begin{aligned}
 S_{t_{\Delta}} & \approx u_{nt} \left( \frac{\Delta}{b_{nt}} \right)^{0.37} \\
 \Leftrightarrow \frac{S_{t_{\Delta}}}{S_l} & \approx 0.7 \frac{(\text{Re}_{\Delta} \text{Pr})^{0.5}}{\text{Da}_{\Delta}^{0.44}} \cosh^{0.945} \left[ \frac{1}{3} \text{arccosh}(4.357 \text{Da}_{\Delta}) \right]
 \end{aligned} \tag{7.26}$$

Note that this expression should not be replaced by a truncated Taylor series: The term  $\text{arccosh}$  does not bring particular CPU-effort, as illustrated with the complete SFC model in section 8.4 (p.182).

The resolved burning velocity  $S_{t_\Delta}$  stands for the burning rate relevant for the filtered progress variable reaction rate, whereas  $u_{nt}$  is an evaluation of the flamelet velocity contained in the cell.

### 7.3 Closure for the corrugated flame regime

The main purpose of this thesis is to develop a model which is efficient and precise for the thickened flame regime which is related to high Reynolds flows and thus to many of industrial applications. Nevertheless, a corresponding and coherent formulation for the corrugated flame regime is also required, since industrial burners are likely to display both regimes of turbulent premixed flames.

In the corrugated flame regime, characterized by a Karlovitz number smaller than unity  $Ka_t < 1$ , no turbulent eddies can enter the flame front. The flamelet structure is therefore similar to the laminar flame structure (same velocity  $S_l$ , same thickness  $\delta_l$ ), except that the flame front surface is wrinkled.

#### 7.3.1 Resolved burning velocity

The geometric relation Eq. (7.25) from the fractal theory is still valid, but must be formulated with the length and velocity scales of the corrugated flame:

$$\frac{S_{t_\Delta}}{S_l} = \frac{A_{\delta_l}}{A_\Delta} = \left(\frac{\delta_l}{\Delta}\right)^{2-\mathcal{D}} > 1. \quad (7.27)$$

Compared to the thickened flame regime case, where a constant value  $\mathcal{D} \approx 2.37$  is assumed because of the associated high turbulence intensity, more caution is required for this case. North and Santavicca [NS90] have derived an empirical parametrization of  $\mathcal{D}$  based on  $u'$  and  $S_l$ :

$$\mathcal{D} = \frac{2.05}{\frac{u'}{S_l} + 1} + \frac{2.35}{\frac{S_l}{u'} + 1}. \quad (7.28)$$

Lipatnikov and Chomiak [LC99](p. 3) have developed from this expression a formulation adapted for LES modeling:

$$\mathcal{D} = \max \left\{ 2; \min \left[ a + \frac{b}{2} \left( \ln \frac{\Delta}{L_G} + 2 \ln Ka_t + \ln(c + Ka_t^\beta) \right); \frac{7}{3} \right] \right\} \quad (7.29)$$

where  $L_G \equiv S_l^3/\varepsilon$  is the Gibson scale. Using the relation:

$$\frac{\Delta}{L_G} \sim \frac{u_{sgs}^3}{S_l^3} \sim \left( \frac{\text{Pr Re}_\Delta}{\text{Da}_\Delta} \right)^{3/2} \quad (7.30)$$

the relation Eq. (7.29) is reformulated in terms of Damköhler and Reynolds numbers:

$$\mathcal{D} = \max \left\{ 2; \min \left[ a + \frac{b}{2} \left( \frac{3}{2} \ln \frac{\text{Pr Re}_\Delta}{\text{Da}_\Delta} + 2 \ln \frac{\sqrt{\text{Pr Re}_\Delta}}{\text{Da}_\Delta} + \ln \left[ c + \left( \frac{\sqrt{\text{Pr Re}_\Delta}}{\text{Da}_\Delta} \right)^\beta \right] \right); \frac{7}{3} \right] \right\}. \quad (7.31)$$

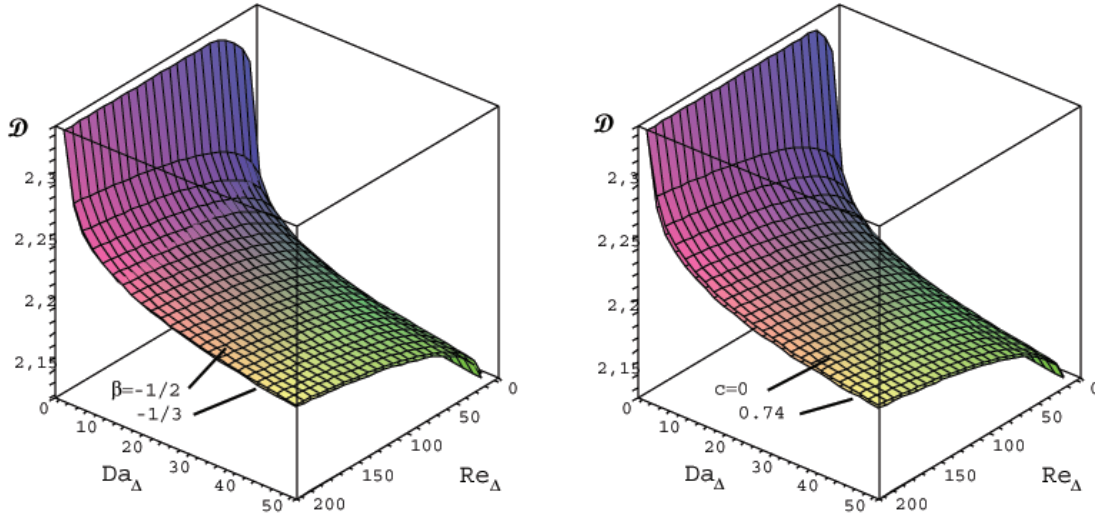


**Fig. 7.6:** Influence of the constant  $\beta$  (left) and  $c$  (right)

Lipatnikov and Chomiak [LC99](p. 3) have obtained the best fit against experimental data with the constants:

$$a = 2.196 \text{ and } b = 0.018.$$

For the evaluation of the inner cutoff, see definition in Figure A.1 (p.206),  $e_i \approx \delta_l(c + \text{Ka}_t^\beta)$ , the constant  $\beta$  may take values in the range  $[-1/2; -1/3]$  as reported by Gülder and Smallwood [GS95](p. 114). Except for the model proposed by Poinso et al. where  $c = 0.74$  (see review by Gülder and Smallwood [GS95](p. 111)), this constant does not appear, i.e.  $c = 0$ . In order to select a couple of values for  $(\beta, c)$ , two different plots of the function are displayed in Figure 7.6 (p.112):

- Influence of  $\beta$  (left plot):  $\beta = -1/2$  and  $\beta = -1/3$  with  $c = 0$ ,
- Influence of  $c$  (right plot):  $c = 0$  and  $c = 0.74$  with  $\beta = -1/2$ .

For the range of selected values  $\text{Re}_\Delta$  and  $\text{Da}_\Delta$ , as well as for a larger one (not displayed here), the choice of the parameter values are not significant on the value of the fractal dimension  $\mathcal{D}$ , so that the following values are retained in the following:

$$\beta = -1/2 \text{ and } c = 0.$$

The Figure 7.6 (p.112) also displays the general behavior of the function  $\mathcal{D}(\text{Re}_\Delta, \text{Da}_\Delta)$ . For low Reynolds numbers the function  $\mathcal{D}$  tends to 2, which is particularly interesting for the model. For very low Reynolds numbers, i.e. for quasi laminar flows, the power argument  $(2 - \mathcal{D})$  tends to zero. Consequently, the resolved burning velocity tends naturally to the laminar speed  $S_l$ , without any extra parameter or need for reformulating the ratio under the form  $S_{t_\Delta}/S_l = 1 + f(\text{Re}_\Delta, \text{Da}_\Delta)$ . For high turbulent Reynolds numbers and moderate Damköhler numbers, the value tends to  $\mathcal{D} \approx 7/3 \approx 2.37$  which is the limit value for high turbulent intensities.

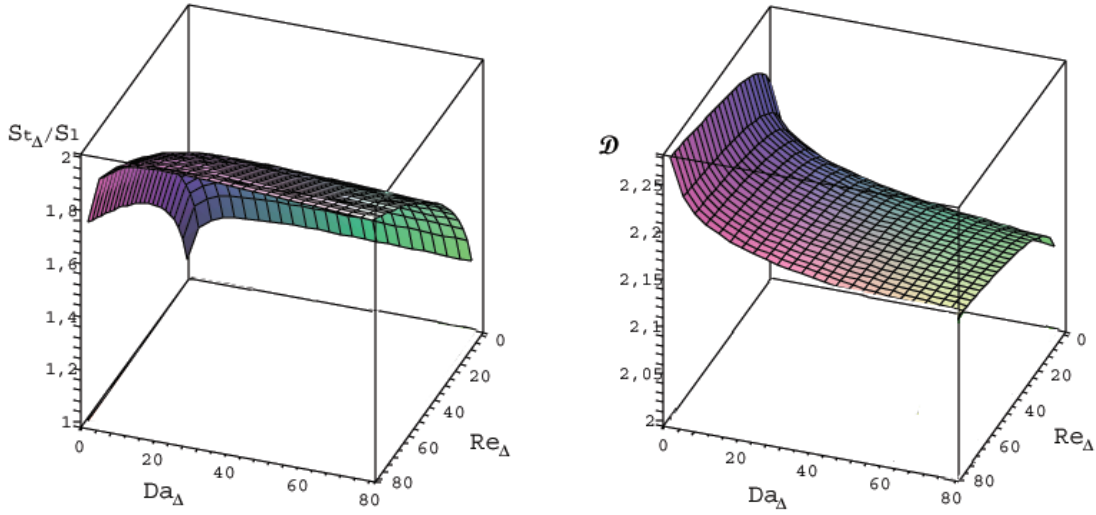


**Fig. 7.7:** Variation of  $S_{t_\Delta}/S_l$  with  $Da_\Delta$  (left) and corresponding values of  $\mathcal{D}$  (right)

Combining Eqs. (7.27), (7.31) and formulating:

$$\frac{\Delta}{\delta_l} \sim \sqrt{\text{Pr Re}_\Delta \text{Da}_\Delta}, \quad (7.32)$$

a closure for the turbulent burning rate at the cell level can be formulated for the corrugated flame regime:

$$\frac{S_{t_\Delta}}{S_l} \approx (\text{Pr Re}_\Delta \text{Da}_\Delta)^{\frac{\mathcal{D}-2}{2}}. \quad (7.33)$$

### 7.3.2 Fractal dimension

Contrary to the case of the thickened flame regime, where the fractal dimension  $\mathcal{D} = 2.37$  is constant, it varies for the corrugated flame regime, depending both on the Damköhler and Reynolds numbers.

The ratio  $S_{t_\Delta}/S_l = f(Da_\Delta, \text{Re}_\Delta)$  mostly decreases with the Damköhler number  $Da_\Delta$ , like for the thickened flame regime. This tendency is achieved due to the strong dependence of  $\mathcal{D}$  on  $Da_\Delta$ , although the power argument  $(\mathcal{D} - 2)/2$  is positive and that  $Da_\Delta$  appears in the numerator of the ratio. This cannot be proved analytically by deriving  $S_{t_\Delta}/S_l$  because of the definition of  $\mathcal{D}$  with the operators min and max.

Nevertheless, comparing the functions  $S_{t_\Delta}/S_l$  in parallel with  $\mathcal{D}$  in Figure 7.7 (p.113) shows that  $S_{t_\Delta}/S_l$  only increases with  $Da_\Delta$  for maximum values of  $\mathcal{D} \approx 2.37$ . This corresponds to high values of  $\text{Re}_\Delta$  compared to  $Da_\Delta$ , i.e. to the thickened flame regime for which another closure is used. For larger values of the Damköhler numbers, the function  $S_{t_\Delta}/S_l$  is a decreasing but almost constant function of  $Da_\Delta$ . The resolved burning velocity depends essentially on the subgrid Reynolds number  $\text{Re}_\Delta$  for the corrugated flame regime.

## 7.4 Modeling bending effect and quenching with CFD

The formulation of the SFC model has been developed for the corrugated and thickened flame regimes. Before the integration of these two different formulations in a global model in the last section 7.6.1 (p.133), the possible occurrence of the so-called *bending effect* and *quenching*, already presented in section 2.4.3 (p.37), must be considered. These two effects are well known from experiments (see for example Peters [Pet99]). They correspond respectively to a decrease of the burning rate and a local extinction of the flame when increasing the turbulence intensity  $u'$ . Their understanding and modeling are still one of the major issues of turbulent combustion modeling.

In this section, an overview of the modeling, essentially for RANS simulations, achieved for the bending effect is presented. The notions of strain and stretch are presented. In the next section 7.5 (p.123), a modification of the SFC model is developed to take into consideration bending effect and quenching.

### 7.4.1 Strain, stretch, bending effect and quenching

As already explained, the bending effect describes the stagnation or decrease of the ratio  $S_t/S_l$ , when increasing the turbulence intensity  $u'$ . The quenching describes the next step, i.e. the local extinction of the flame front when the flame is too much disturbed by the flow fluctuations. These two effects are thus a consequence of turbulent fluctuations, and a result of the deformation of the flame structure by the eddies.

In the following, the word *strain* refers to the local deformation of the flow. The word *stretch*, more descriptive, refers to the deformation to which the flame front is submitted. This distinction is made for clarity, although there is not always such particular agreement in the literature.

In short, bending effect and quenching are caused by stretch, and flame stretch is a consequence of the flow strain. After a mathematical definition of strain and stretch, the next section 7.4.2 (p.115) describes the possible causes for stretch. The third section 7.4.3 (p.117) describes the estimation of the stretched due to the turbulence. section 7.4.4 (p.120) describes how to model the bending effect and quenching:

$$\text{strain} \Rightarrow \text{flame stretch} \Rightarrow \begin{cases} \text{bending effect} \\ \text{quenching} \end{cases}$$

#### Strain

The strain is defined with the symmetric tensor of deformations  $\bar{\bar{S}}$ , since it describes linear deformation and does not consider rotational deformations:

$$D_{ij} \equiv \frac{1}{2} \left( \frac{\partial u_i}{\partial x_j} + \frac{\partial u_j}{\partial x_i} \right) \quad (7.34)$$

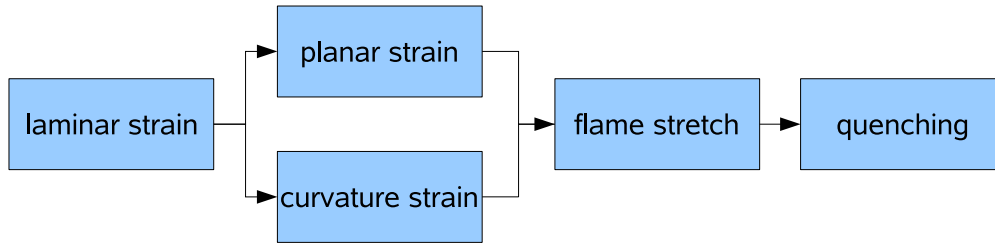


**Fig. 7.8:** Stretch with a laminar flow

and the linear deformation rate  $d$  in the direction  $\mathbf{t}$  reads (see Sini [Sin00](p. 49)):

$$\begin{aligned} d &= \mathbf{t} \cdot \bar{\mathbf{S}} \cdot \mathbf{t} \\ d &= t_i D_{ij} t_j. \end{aligned} \quad (7.35)$$

Strain is mostly considered through its tensor magnitude, the strain rate  $S$ :

$$S \equiv \sqrt{2D_{ij}D_{ij}}. \quad (7.36)$$

One should not oversee that the strain is a three-dimension vector, and that using the magnitude of this vector constitutes some approximation, at least some loss of information.

In case of a single eddy of size  $r$  and velocity  $u(r)$ , the strain simply reads:

$$S_r \sim \frac{u(r)}{r}. \quad (7.37)$$

This definition is naturally mostly employed when evaluating the strain due to turbulence in the following.

### Stretch

Flame stretch has been defined as a measure of the local flame surface rate of change by Karlovitz et al. [KJKW54]:

$$K \equiv \frac{1}{A} \frac{dA}{dt}, \quad (7.38)$$

where  $A$  is the local flame surface. The definition of the local and instantaneous stretch  $K$  is the same in all the literature, but its evaluation differs between authors and still remains an open question.

#### 7.4.2 Causes for stretch and contributions to stretch

The stretch and its effects have already been detailed for a laminar configuration in section 2.3.4 (p.29). This type of stretch is referred in the following as *laminar stretch* and should be generated by the mean flow structure (see Figure 7.8 (p.115)).

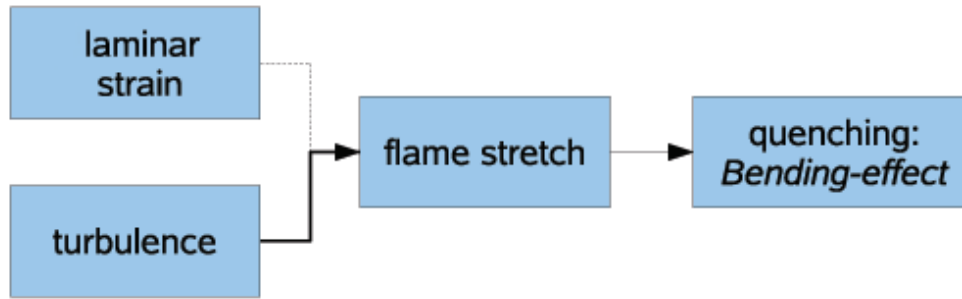


**Fig. 7.9:** Stretch with the whole turbulence modeled

In case of a turbulent flame, the mechanisms which can lead to stretch and quenching are more complex. The nature of turbulence implies that its generated strain is unsteady and due to the whole spectrum of eddies. Each eddy is likely to stretch the flame more or less depending on its size and velocity.

In the literature concerning the modeling of stretch for turbulent flames, the influence of the mean flow structure, which is comparable with the laminar stretching, is eluded. The reason for this is that the whole spectrum of turbulent eddies (RANS approach) has been considered, which is expected to produce much more strain than the configuration itself (strain due to a classical back-step configuration for example). The contribution of turbulence to stretch is likely to hide the contribution of the mean flow structure (laminar stretching in Figure 7.9 (p.116)).

This last sentence implicitly stresses three issues for the present LES modeling:

- How to consider the stretch within a LES simulation, i.e. how to consider the influence of a part of the turbulence?
- What is, for turbulence, the relation between stretch and strain, do all eddies have the same influence on the flame stretch?
- How to estimate the effect of the non-resolved stretch?

Actually these three questions can be summed up in: How to characterize the stretch induced by an eddy to the flame front. With LES as depicted Figure 7.10 (p.117), the effect of the smallest eddies to the flame front stretch must be modeled.

Finally, if the flame stretch induced by an eddy is known, its effect on the reaction rate must be estimated:

$$\text{eddy } (r, u(r)) \Rightarrow \text{stretch} \Rightarrow \begin{cases} \text{bending effect} \\ \text{quenching} \end{cases}$$

Before formulating a new sub-model for the SFC model in section 7.5 (p.123), a review of the accomplished work (essentially in terms of RANS modeling) is presented.

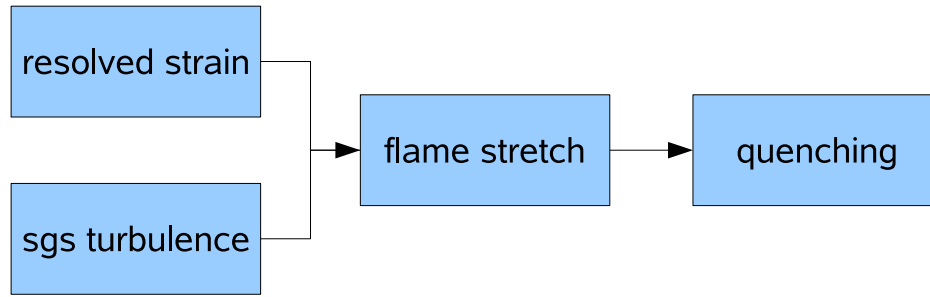


**Fig. 7.10:** Stretch with the LES modeling

### 7.4.3 Turbulence to stretch

In the literature, several estimations for the stretch induced by turbulence have been presented. Some of them are based on a unique turbulent scale, whereas other are formulated considering spectrum of scales.

#### Dependence on single scales

The evaluation of the flame stretch  $K$  defined with Eq. (7.38) has been based both on the smallest and on the largest scales of the turbulence. Cant and Bray [CB88] (p. 793, Eq. 14) relate it to the turbulent Karlovitz number  $Ka_t$ , defined by Eq. (2.80) and Eq. (2.100) based on the Kolmogorov scales:

$$K = Ka_t \frac{S_l}{\delta_l}, \quad (7.39)$$

so that the stretch is evaluated with the smallest scales:

$$K \equiv \frac{1}{A} \frac{dA}{dt} = \left( \frac{\varepsilon}{\nu} \right)^{1/2} \sim \frac{1}{t_\eta}. \quad (7.40)$$

Earlier, the stretch has been often related to the smallest eddies since they generate the highest strain  $S$ , their small size produces high gradients (see section 2.2.1 (p.15)).

Candel et al. [CP90] base their evaluation on the largest scale using dissipation  $\varepsilon$  and turbulent kinetic energy  $k$ :

$$K = \frac{\varepsilon}{k} \sim \frac{u'}{l_t}. \quad (7.41)$$

#### Multi-scale dependence

A complete approach has been proposed by Meneveau and Poinsoot according to their well-known observation [MP91] (p. 321): “scales close to  $\eta$  dominate the strain, does not

mean that they will also control flame stretch” . They have estimated how much turbulent eddies are stretching the flame, starting from the influence of a pair of isolated eddies to conclude with the influence of the whole spectrum of turbulence on the flame stretch. A first interesting result is the expression of the stretch  $K(r)$  caused by each size of eddies proportional to its inverse characteristic time  $u(r)/r$  and to an *efficiency correction function*<sup>2</sup>  $C(r/\delta_l)$ . The function  $C(r/\delta_l)$  relates the strain to the effective stretch. It depends on the ratio of the eddy size to the laminar flame front thickness  $\delta_l$  [MP91](p. 316):

$$\frac{1}{A} \frac{dA}{dt} = C \left( \frac{r}{\delta_l} \right) \frac{u(r)}{r}. \quad (7.42)$$

The function  $C$  was obtained using DNS calculations (see again Meneveau and Poinso [MP91] for more details) and numerically fitted to:

$$C \left( \frac{r}{\delta_l} \right) = 10^{-\frac{0.545}{s+0.364}}, \quad (7.43)$$

$$\text{within } s = \log \frac{r}{\delta_l}. \quad (7.44)$$

This fitting function  $C$  is not mathematically defined for the value:

$$s < -0.364,$$

$$\text{which corresponds to: } r < 0.44 \delta_l. \quad (7.45)$$

The fitting function  $C$  is sharply decreasing for still values of  $r$ , so that the function can be considered to be zero for  $r < 0.44 \delta_l$  (see Figure 7.11 (p.119)). The eddies smaller than about half the laminar flame thickness do not actually stretch the flame.

Considering that an eddy of size  $r$  describes a local distribution of velocity  $u(r, x)$  depending on the local position  $x$  because of the intermittent nature of turbulence, Meneveau and Poinso express this velocity  $u(r, x)$  using an instantaneous local dissipation:

$$u(r, x) = [r \varepsilon_r(x)]^{1/3}. \quad (7.46)$$

Employing a *multi-fractal formalism*, they statically relate the local dissipation  $\varepsilon_r(x)$  to the averaged value  $\tilde{\varepsilon}$  usually available with RANS modeling for example:

$$\varepsilon_r(x) = \tilde{\varepsilon} \left( \frac{r}{l_t} \right)^{\alpha(x)-3}. \quad (7.47)$$

$\alpha$  is a fractal parameter, which probability density function  $P_r(\alpha)$  depending from the eddy size  $r$  is given by<sup>3</sup>:

$$P_r(\alpha) = \sqrt{\frac{\ln \left( \frac{l_t}{r} \right)}{2\pi\mu}} \left( \frac{r}{l_t} \right)^{\frac{(\alpha-3-\mu/2)^2}{2\mu}}, \text{ with } \mu = 0.26. \quad (7.48)$$

---

<sup>2</sup>at the origin of the efficiency function defined for the TF model  $E$ , see Eq. (4.11)

<sup>3</sup>note that the notation of [MP91](p. 320, Eq.15) can lead to confusion with  $1/2\mu$

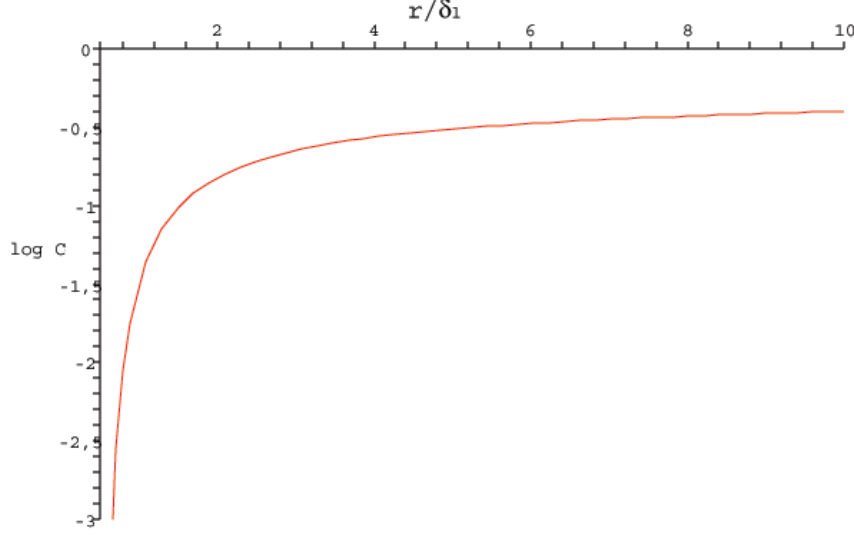


**Fig. 7.11:** Efficiency function  $C(r/\delta_l)$

Developing Eqs. (7.46) and (7.47), the local strain  $S_r(x)$  and stretch  $K_r(x)$  induced by an eddy of size  $r$  read:

$$S_r(x) = \frac{u(r, x)}{r} = l_t^{-2/3} \tilde{\varepsilon}^{1/3} \left( \frac{r}{l_t} \right)^{-2/3 + (\alpha(x)-3)/3},$$

$$S_r(x) = \sqrt{\frac{\tilde{\varepsilon}}{\nu}} \text{Re}_t^{-1/2} \left( \frac{r}{l_t} \right)^{-2/3 + (\alpha(x)-3)/3} \quad \text{and,} \quad (7.49)$$

$$K_r(x) = c_{ms} C\left(\frac{r}{\delta_l}\right) S_r(x). \quad (7.50)$$

The local strain  $S_r(x)$  has been normalized with small scales  $\sqrt{\tilde{\varepsilon}/\nu}$  (using  $\tilde{\varepsilon} = u'^3/l_t$ ) for comparison with Eq. (7.40) in the following. Meneveau and Poinso [MP91] have introduced the constant  $c_{ms} \approx 0.28$  to fit with asymptotic results.

The mean stretch, induced by eddies of size  $r$ , is obtained using the pdf  $P_r(\alpha)$  and by integrating (this can be achieved with *Maple*):

$$\tilde{K}_r = \int_{-\infty}^{\infty} K_r(\alpha) P_r(\alpha) d\alpha \quad (7.51)$$

$$\tilde{K}_r = c_{ms} C\left(\frac{r}{\delta_l}\right) \sqrt{\frac{\tilde{\varepsilon}}{\nu}} \text{Re}_t^{-1/2} \int_{-\infty}^{\infty} \sqrt{\frac{\ln(l_t/r)}{2\pi\mu}} \left(\frac{r}{l_t}\right)^{\frac{-2+(\alpha(x)-3)}{3} + \frac{(\alpha-3-\mu/2)^2}{2\mu}} d\alpha$$

$$\tilde{K}_r = c_{ms} C\left(\frac{r}{\delta_l}\right) \sqrt{\frac{\tilde{\varepsilon}}{\nu}} \text{Re}_t^{-1/2} \left(\frac{r}{l_t}\right)^{-2/3 + \mu/9}. \quad (7.52)$$

After a numerical integration on the size  $r$  of the eddies, Meneveau and Poinso [MP91] obtain the total stretch  $\tilde{K}$ , and compare it to the strain due to small scales, and to the one due to the largest scales. The two main results are:

- The measure of the stretch evaluated from the Kolmogorov scales  $K \approx \sqrt{\tilde{\varepsilon}/\nu}$  in Eq. (7.40) overestimates in all cases the stretch  $\tilde{K}$  [MP91](p. 322, Fig. 9) obtained with the efficiency function  $C(r/\delta_l)$ . As already stressed, the smallest eddies cause strain which is not efficiently converted into flame stretch.
- The ratio  $\Gamma_K = \tilde{K}/(\tilde{\varepsilon}/\tilde{k})$  is strongly dependent on the ratio  $l_t/\delta_l$ , but not on  $u'/S_l$  [MP91](p. 323, Fig. 10), when comparing to large scales. This ratio does not actually appear explicitly in the expression for  $\Gamma_K$ , but only in the limit of the integral, if  $l_t/\delta_l$  becomes large.

#### 7.4.4 Stretch to quenching

In the previous part, a short literature review for the evaluation of the stretch produced by turbulence as been presented. Models for the bending effect and quenching effect are now described.

Cant and Bray [CB88] have proposed an interesting model to evaluate the effect of stretch on the mean reaction rate. The authors consider that the mean reaction rate is linearly decreasing with the instantaneous viscous dissipation  $\varepsilon$  up to a limit value  $\varepsilon_q$  for which the flame is quenched (see again Cant and Bray [CB88](p. 794, Eq. 20)):

$$\frac{w(\varepsilon)}{w(0)} = \begin{cases} 1 - \frac{\varepsilon}{\varepsilon_q}, & \text{for } \varepsilon \leq \varepsilon_q \\ 0, & \text{for } \varepsilon \geq \varepsilon_q \end{cases}, \quad (7.53)$$

where  $w(0)$  corresponds to the reaction rate without any stretching<sup>4</sup>, and

$$\varepsilon_q = \nu \left( \text{Ka}_{tq} \frac{S_l}{\delta_l} \right)^2 \quad (7.54)$$

is evaluated using the Karlovitz number  $\text{Ka}_{tq}$  for which the laminar flame is quenched. The actual reaction rate  $w$  can be calculated writing the pdf  $P(\varepsilon)$  as a log-normal distribution according to Kolmogorov's theory:

$$P(\varepsilon) = \frac{1}{\sqrt{2\pi}\sigma\varepsilon} \exp \left\{ -\frac{1}{2\sigma^2} \left( \ln \frac{\varepsilon}{\tilde{\varepsilon}} - \frac{1}{2}\sigma^2 \right)^2 \right\} \quad (7.55)$$

$$w(\varepsilon) = w(0) \int_0^\infty \frac{w(\varepsilon)}{w(0)} P(\varepsilon) d\varepsilon, \quad (7.56)$$

in which  $\tilde{\varepsilon}$  is the mean viscous dissipation delivered typically by a RANS turbulence model and  $\sigma$  the standard deviation. This formulation has the crucial advantage (in terms of modeling) to have an analytical solution:

$$w(\varepsilon) = \frac{w(0)}{2} \left[ \text{erfc} \left( \frac{\ln \frac{\varepsilon}{\tilde{\varepsilon}} - \frac{1}{2}\sigma^2}{\sqrt{2}\sigma} \right) - \underbrace{\frac{\varepsilon}{\tilde{\varepsilon}} \text{erfc} \left( \frac{\ln \frac{\varepsilon}{\tilde{\varepsilon}} + \frac{1}{2}\sigma^2}{\sqrt{2}\sigma} \right)}_{\text{not used in TFC}} \right] \quad (7.57)$$

<sup>4</sup> $w(0)$  is actually used for clarity since Cant and Bray proposed their own reaction rate closure, but their model for the quenching can be used with any other reaction rate closure

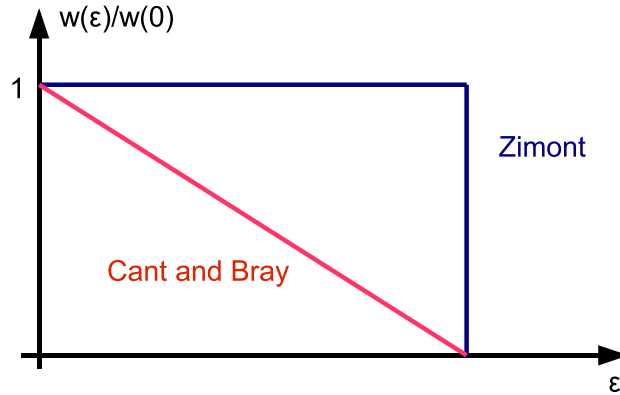


**Fig. 7.12:** Function  $w(\varepsilon)/w(0)$

since the complementary error function  $\text{erfc}$  can be approximated. The model of quench probability proposed by Zimont and Lipatnikov [ZL95] for the TFC model, and its adaptation for the TFC-LES model presented in section 6.2.3 (p.96) are actually a simplified version of this formulation. The reaction rate ratio  $w(\varepsilon)/w(0)$  is simply modeled with (see Figure 7.12 (p.121)):

$$\frac{w(\varepsilon)}{w(0)} = \begin{cases} 1, & \text{for } \varepsilon \leq \varepsilon_q \\ 0, & \text{for } \varepsilon \geq \varepsilon_q \end{cases}, \quad (7.58)$$

with  $\sigma^2 = 0.26 \ln l_t/\eta$ .

To conclude, the model developed by Meneveau and Poinso [MP91] goes further considering more precisely the effect of each eddy on the stretch. But contrary to the model by Cant and Bray [CB88], consequence for the reaction rate has not been derived.

#### 7.4.5 Strategy for developing a bending effect sub-model with the SFC model

The purpose of this part is to summarize and discuss the different possible strategies, which may be employed to develop a sub-model for bending effect and quenching with the SFC model. The main purpose is to develop a sub-model, which is *physically embedded* in the SFC model formulation, rather than which corrects the initial model prediction by multiplying it with an extra factor. A second purpose consists in avoiding the use of quench parameters, because they are difficult to be defined precisely, and therefore to be estimated. In the following, the overview of strategies employed in literature demonstrates that a new strategy must be developed to follow these two purposes.

Two different physical variables have been mostly employed:

- The strain rate (or the stretch) with dimension [1/s], related to the rate of change of area of the flame front, can be compared with the inverse of the chemical time  $t_c$

- The viscous dissipation, whose dimension is  $[\text{m}^2/\text{s}^3]$ , is equivalent to a specific power.

Strategies based on these two variables are presented in the next two paragraphs. The effect of stretch on the reaction rate distribution may be also used. This strategy is presented in the third paragraph.

### Criterion based on flame stretch

The use of the strain rate to develop a model seems to be fairly intuitive thanks to its direct relation to a time and its direct evaluation for each eddy of size  $r$  and velocity  $u(r)$ :

$$S_r \sim \frac{u(r)}{r}. \quad (7.59)$$

A model for bending effect and quenching based on this variable should compare the local flame front stretch to a reference value, which represents the maximum deformation of the flame before quenching. Tasks therefore consist in:

- Quantifying the stretch to which the flame front is submitted, because of the unresolved eddies as well as the larger eddies included in the filtered flow
- Predicting an eventual quenching because of this stretch. Therefore the stretch must be evaluated and compared to a limit value known to provoke quenching, or to prevent the flame from burning normally.

In order to evaluate the stretch produced locally by the subgrid scale eddies and the resolved front, the results derived in the previous section 7.4.4 (p.120) according to the original work by Meneveau and Poinso [MP91] could be used. The stretch due to the largest eddies which are encountered in the resolved strain must be evaluated, as well as the stretch generated by the mean flow.

Finally, a *quenching limit*, expressed as a strain or a Karlovitz number, must be integrated in the model. For example Cho et al. [CCO06] have numerically investigated the definition for an universal extinction Karlovitz number for different fuel (among methane and propane). Takita et al. [TYUM06] have carried out a similar study with experimental investigations. One of the drawbacks of using such results is that these studies are based on a typical flame configuration (for example so-called fresh to burnt configuration, or fresh to fresh configuration), which does not always correspond to the investigated flame configurations. The second drawback is to know if extinction stretch rate studies are transposable to turbulent premixed flames. And that is why a sharp dependence to this limit i.e. complete reaction rate or quenching may be problematic.

Nevertheless Van Oijen et al. [VBGD05](p. 71, Eq.9) [GODG<sup>+</sup>02] have developed a formulation for a Karlovitz number based on the stretch, such as the mass burning rate is decreasing linearly with this number, and tested for DNS simulations of spherically expanding flames in the thin reaction zone and broken reaction zone regime.

**Criterion based on dissipation rate**

The viscous dissipation can bring some useful physical information based on the kinematic energy of the eddies:

$$\varepsilon_r \sim S_r u(r)^2 \sim \frac{u(r)^3}{r}. \quad (7.60)$$

A physical interpretation is difficult with such a variable, which is a product of a strain and a kinetic energy.

As previously presented, this type of criterion to limit the burning velocity in case of high turbulence intensity has been presented by Cant and Bray [Bra79, CB88] and adapted and largely used within the TFC (RANS as well as LES version) model by Flohr, Lipatnikov, Pitsch, Polifke and Zimont [ZL95, ZPBW97, PFB00, FP00]. Like stretch based criterion, a drawback is the need for a critical value. A critical dissipation rate has to be known a priori from numerical or experimental investigation. However, due to statistical considerations of the fluctuating nature of the strain rate  $\varepsilon$  [ABL88], the error on such a criterion value for the quenching is weaker.

**Criterion based on the reaction rate distribution**

The stretch has an influence on the thickness and repartition of the reaction rate in the flame front as Law et al., Lolos and Rogg have shown [Law88, LS00, Lol95, Rog88]. Typical configurations of flames for stagnating flows with different Lewis numbers have already been investigated. It shows that the effect, in terms of position and amplitude, of increasing stretch on the reaction rate strongly depends on the Lewis number (see again Law et al. [Law88](p. 1390) [LS00](p. 481)). For such configurations and for any Lewis number, increasing stretch leads to a displacement of the flame front in direction of the stagnation surface. The Lewis number has an influence on distribution of the reaction rate, and on the position of extinction according to the distance to the stagnation surface. For a value of the Lewis number  $Le \approx 1$ , which corresponds to a lean mixture of methane, the stretch modifies the position of the flame front without changing the distribution of the reaction rate (except very close to the extinction). Unfortunately, the strong dependence on the Lewis number makes such a criterion disputable.

**7.5 A bending effect and quenching sub-model for the SFC model**

The aim of this section is to develop and present a new sub-model for bending effect and quenching, which is efficiently embedded in the SFC model. The approaches described in the previous section 7.4.5 (p.121) have namely two drawbacks. They are expressed in terms of an additional factor for the turbulent burning velocity (like the stretch factor  $G$  with the TFC model introduced by Zimont and Lipatnikov [ZL95]). They also require quenching parameters estimated in terms of Karlovitz number  $Ka_q$ , or maximum level of dissipation  $\varepsilon_q$  (see Eq. (7.54)). Defining such limit parameters is a topic itself. They should represent

the maximum deformation that the flame front can support, which is difficult to evaluate or to experimentally estimate.

A formulation based on the chemical time is here proposed. In presence of high turbulence intensity, eddies are likely to interfere with combustion and to modify the reactive process according to their turnover time. In presence of turbulence, the chemical time is thus likely to be different from the laminar chemical time  $t_c$ , since the turbulent eddies modify the structure of the flame front. In section 7.2 (p.104) the SFC model has been developed assuming that turbulent and laminar chemical time scales are equal. The present sub-model for the bending effect and quenching consists thus in accounting for the turbulent chemical time.

The first section 7.5.1 (p.124) presents how the turbulent chemical time  $t_c^*$  can be evaluated. This approach requires the definition of a Karlovitz number  $Ka_t^*$  for LES modeling, which is presented in the second section 7.5.2 (p.125). Its estimation also requires a precise measure of the resolved and unresolved contributions to stretch using the ideas presented in the section 7.4.3 (p.117). The last section 7.5.3 (p.131) develops the formulation for the bending effect and quenching embedded in the SFC model.

$$\text{turbulent stretch} \Rightarrow Ka_t^* \Rightarrow t_c^* \Rightarrow \frac{S_{l\Delta}}{S_l}(t_c^*) : \begin{cases} \text{bending effect} \\ \text{quenching} \end{cases}$$

### 7.5.1 Chemical time approach

The turbulent chemical time has been supposed to be equal to the laminar chemical time  $t_c$  in Eq. (7.19), when developing the SFC model for the thickened flame regime. The new sub-model formulation starts from the idea that the chemical time may be different from  $t_c$  in turbulent premixed combustion, because of the action of stretch. Van Oijen et al. [VBGD05](p. 82) have reported that: “*at high turbulence levels the flame stretch effects influence the reaction kinetics.*” In the following, the chemical time in presence of turbulence is noted  $t_c^*$ , so that the actual model closure will be simply modified using  $t_c^*$  instead of  $t_c$ .

Remembering that turbulence is essentially producing strain for the flow, analogy with the effects of strain on laminar flames is employed (see section 2.3.4 (p.29)) to evaluate the flame front stretch.

The stretch has the main effect of modifying the flame speed, so that the actual chemical time is in turn modified. Since the aim of the model is to deliver a turbulent flame speed giving a relevant turbulent reaction term in presence of stretch, the stretched laminar flame speed  $S_{l,cs}$  is selected as reference velocity to replace  $S_l$ :

$$\frac{S_{l,cs}}{S_l} = \frac{1}{1 + Ma Ka_t^*}. \quad (7.61)$$

Eq. (2.83) has been employed and adapted for the present case. The inverse function Eq. (2.83) is more convenient than the linear function Eq. (2.81). It numerically tends to zero, and avoids negative values for high stretching values.

$Ka_t^*$  is representing, according to Hoffmann [Hof04] (p. 59-60), a “*generalized Karlovitz number which should account for stretch as well as unsteady effect*”. Assuming that a generalized Karlovitz number for the turbulent flame  $Ka_t^*$  is also possible, the previous relation yields the turbulent chemical time  $t_c^*$ :

$$t_c^* = \frac{a}{S_{l,cs}^2} \quad (7.62)$$

$$\frac{t_c^*}{t_c} = (1 + Ma Ka_t^*)^2. \quad (7.63)$$

The notation  $Ka_t^*$  is employed to be consistent with the turbulent chemical time  $t_c^*$ , and to differentiate the generalized Karlovitz number  $Ka_t^*$  defined by Hoffmann from its application in this thesis.

The Markstein number  $Ma$  has been already defined in section 2.3.4 (p.29). The analytical evaluation developed by [MBP97] and [Pet94] is employed. The Markstein number is likely to be positive (except for non-preheated lean mixture of methane-air with higher pressure) according to Müller et al. [MBP97] (p. 356) and Peters [Pet94] (p. 27), so that the turbulent and stretch chemical time is larger than the laminar chemical time:

$$t_c^* > t_c. \quad (7.64)$$

Considering more in detail the closure formulations for the thickened flame regime in Eq. (7.26), as well as for the corrugated flame regime in Eq. (7.33), a Damköhler number  $Da_\Delta^*$  is introduced to express the modified time dependence:

$$Da_\Delta^* \equiv \frac{t_\Delta}{t_c^*} \sim \frac{\Delta}{u_{sgs} t_c^*}. \quad (7.65)$$

In parallel, the formulation of the turbulent flame speed must be expressed using the stretch laminar flame speed  $S_{l,cs}$ , rather than the laminar flame speed  $S_l$ , in order to be relevant:

$$\left. \frac{S_{t_\Delta}}{S_{l,cs}} \right|_{\text{thickened}} \approx 0.7 \frac{(\text{Pr Re}_\Delta)^{0.5}}{Da_\Delta^{*0.44}} \cosh^{0.945} \left[ \frac{1}{3} \text{arccosh} (4.357 Da_\Delta^*) \right] \quad (7.66)$$

$$\left. \frac{S_{t_\Delta}}{S_{l,cs}} \right|_{\text{corrugated}} \approx (\text{Pr Re}_\Delta Da_\Delta^*)^{\frac{2-2}{2}}. \quad (7.67)$$

Compared to the original formulations Eqs. (7.26) and (7.33), the actual resolved burning velocity  $S_{t_\Delta}$  considering the turbulent time scale  $t_c^*$  is reduced.

This sub-model for the bending effect is thus based on the effective turbulent flame time  $t_c^*$ . The evaluation of the required *generalized Karlovitz number* is developed in the next part.

## 7.5.2 Generalized Karlovitz number

In this part, the Karlovitz number required for the turbulent flame time in LES modeling is defined and evaluated, using an adaptation of the work from Meneveau and Poinso [MP91].

**Resolved and unresolved stretch with LES modeling**

The Karlovitz number was originally defined as a dimensionless number based to the chemical time and to the stretch (see for example Williams [Wil84]):

$$Ka_t = K t_c. \quad (7.68)$$

Adapting this definition for the LES modeling and with the previous work based on the evaluation of the stretch  $K$ , it reads:

$$Ka_t^* \approx K_{(S_\Delta + \tilde{S})} t_c \approx (K_{S_\Delta} + K_{\tilde{S}}) t_c. \quad (7.69)$$

The stretch due to the global strain, i.e. to the subgrid strain  $S_\Delta$  and to the filtered strain  $\tilde{S}$  must be considered, and their respective influence are linearly summed up.

Actually the stretch and the strain should contain three contributions for LES modeling:

- The stretch due to the subgrid scale eddies:  $K_{S_\Delta} = K_{S_{[\eta;\Delta]}}$ , where the strain produced by the smallest eddies is large, but its induced stretch may be not so large as already seen in section 7.4.3 (p.117)
- The stretch due to the resolved eddies:  $K_{S_{[\Delta;l_t]}}$  should have the most influence
- The stretch due to the smallest wave numbers:  $K_{S_{[l_t;\infty]}}$  is likely to not really stretch the flame, since the scales are too large compared to the flame thickness.

Taking into account the last two remarks, the stretch due to scales larger than the integral length scale  $[l_t;\infty]$  is neglected with regard to the stretch induced by the large resolved eddies:

$$K_{S_{[\Delta;l_t]}} \gg K_{S_{[l_t;\infty]}}, \quad (7.70)$$

and the stretch due to the large eddies is evaluated using the filtered strain:

$$K_{\tilde{S}} \approx K_{S_{[\Delta;l_t]}} \approx K_{S_{[\Delta;\infty]}}. \quad (7.71)$$

In the next paragraph, the work by Meneveau and Poinso [MP91] is adapted for the LES modeling, in order to evaluate the stretch at the resolved  $K_{S_\Delta}$  and filtered  $K_{\tilde{S}}$  scales. Doing this, the turbulent flame time  $t_c^*$  can be evaluated.

**Adaptation of the model by Meneveau and Poinso**

The relation Eq. (7.52), valid for all turbulent scales, should make the evaluation of the resolved and unresolved stretch for the LES modeling possible. Nevertheless, this approach encounters two difficulties:

- Reformulate the results from Meneveau and Poinso [MP91] by using the information at the grid scale rather than the integral scale

- Cut the integral between the smallest scales and the largest scales into two integrals with a cut-off at the grid scale.

The original evaluation of  $\tilde{K}_r$  is based on the integral length scale of the turbulence  $u'$  and  $l_t$ . It must be first verified that the formalism can be adapted when employing the subgrid scale variables:  $u_{sgs}$  and  $\Delta$ . The factor  $\sqrt{\tilde{\varepsilon}/\nu} \text{Re}_r^{-1/2}$ , relevant when the integral scales are known, is a term in the expression of  $\tilde{K}_r$  in Eq. (7.52) which comes from the evaluation of the strain rate  $S_r(x)$  in Eq. (7.49). It can be similarly evaluated from the grid scale with the classical assumption that the cut-off lies in the inertial range:

$$\varepsilon_r(x) = \varepsilon_\Delta \left(\frac{r}{\Delta}\right)^{\alpha(x)-3} \quad (7.72)$$

$$\text{and } S_r(x) = \sqrt{\frac{\varepsilon_\Delta}{\nu}} \text{Re}_\Delta^{-1/2} \left(\frac{r}{\Delta}\right)^{-2/3+(\alpha(x)-3)/3}. \quad (7.73)$$

Consulting reference articles about multi-fractal and measurement of  $f(\alpha)$  by Sreenivasan and Meneveau [Sre91, MS87a, MS87b, MS89], the distribution function  $P_r(\alpha)$ :

$$P_r(\alpha) = \sqrt{\frac{\ln\left(\frac{L_{ref}}{r}\right)}{2\pi\mu}} \left(\frac{r}{L_{ref}}\right)^{\frac{(\alpha(x)-3-\mu/2)^2}{2\mu}}$$

can be written for any reference size  $L_{ref}$ , provided that  $L_{ref}$  remains *some outer length scale of the problem* [MS89] (p. 103). This logically explains that  $L_{ref} = l_t$  is mostly employed. With LES modeling, the subgrid scale eddy  $\Delta$  is naturally more relevant.

Finally, the formalism developed by Meneveau and Poinot [MP91] in a RANS approach, see Eq. (7.52), can be transferred to the LES modeling, and the mean stretch  $K_r$  induced by an eddy of size  $r < \Delta$  reads:

$$K_r = c_{ms} C \left(\frac{r}{\delta_l}\right) \sqrt{\frac{\varepsilon_\Delta}{\nu}} \text{Re}_\Delta^{-1/2} \left(\frac{\Delta}{r}\right)^{2/3-\mu/9}. \quad (7.74)$$

### Stretch due to the unresolved scales

The resolved and filtered stretch, respectively, must be evaluated separately because of the LES modeling. The stretch produced by the whole turbulent spectrum can be expressed from the integral scales  $l_t$ ,  $\varepsilon$  and  $k$  according to the original evaluation for the normalized stretch by Meneveau and Poinot [MP91] (p. 323, Eq.24). The global stretch cannot be estimated in this way since the integral scales are not known *during a simulation*.

To estimate the respective stretch caused by unresolved scales  $K_{S_\Delta}$  and filtered scales  $K_{\bar{S}}$ , the stretch  $K_r(\alpha)$  should be respectively *integrated* in the ranges  $[\min\{\eta; 0.44\delta_l\}; \Delta]$  and  $[\Delta; l_t]$ . This is not possible for the range  $[\Delta; l_t]$ , since the function  $Pr(\alpha)$  referenced with  $\Delta$  is mathematically not defined for  $r > \Delta$ . An estimation of the stretch due to the resolved scales is proposed in the next paragraph.

The integration is possible for the subgrid scales. Besides, it can be demonstrated that the fitting function that Meneveau and Poinsoot have developed for  $K$  [MP91](p. 322 Eq. 22) is exploitable for LES with some modifications. This fitting function has been actually carried out for the total turbulent stretch  $\Gamma_K$  normalized with the large-scale strain  $\tilde{\varepsilon}/\tilde{k}$  [MP91](p. 323 Eq. 24):

$$\Gamma_K = \frac{K}{\tilde{\varepsilon}/\tilde{k}}. \quad (7.75)$$

This normalization corresponds to the integral part of the expression for  $K$  itself since:

$$\frac{\sqrt{\frac{\varepsilon}{\nu}} \text{Re}^{-1/2}}{\varepsilon/k} = \mathcal{O}(1), \quad (7.76)$$

$$\Rightarrow \Gamma_K \sim \frac{c_{ms}}{\ln 2} \int_{\text{scales}} K_r dr, \quad (7.77)$$

using the relations  $k = 3/2 u'^2$  and  $\varepsilon = u'^3/l_t$ . In the definition of  $K_r$  as previously demonstrated as well as in the integral of  $K$ , the variable  $l_t$  and  $\Delta$  have mathematically the same role, so that one can expand the fitting function to the current case and express the stretch due to the subgrid scales:

$$K_{S_\Delta} \approx \frac{c_{ms}}{\ln 2} \sqrt{\frac{\varepsilon_\Delta}{\nu}} \text{Re}_\Delta^{-1/2} \Gamma_K\left(\frac{\Delta}{\delta_l}\right). \quad (7.78)$$

Compared to the analytical expression given by Meneveau and Poinsoot [MP91](p. 331 Eq. 57), the variable  $l_t/\delta_l$  has been transposed to  $\Delta/\delta_l$ , and the dependence on  $u'/S_l$  neglected (see Figure 7.13 (p.129)):

$$\Gamma_K(s) \approx 10^{-\frac{e^{-(s+0.4)}}{s+0.4} + (1-e^{-(s+0.4)})\left(\frac{2}{3}s-0.11\right)}, \text{ with } s = \log \frac{\Delta}{\delta_l}. \quad (7.79)$$

This will not lead to discrepancy, since the dependence on this variable is fairly weak: The transposition from  $l_t/\delta_l$  to  $\Delta/\delta_l$  is equivalent to translate the result on the left of the figure, where the dependence on  $u'/S_l$  remains very weak.

According to Eq. (7.78) the respective part of the stretch induced by the subgrid scales compared to the whole turbulence can be estimated *off-line*:

$$\frac{K_{S_\Delta}}{K_{S_{[l_t, l_t]}}} \approx \frac{\Gamma_K\left(\frac{\Delta}{\delta_l}\right)}{\Gamma_K\left(\frac{l_t}{\delta_l}\right)} \left(\frac{\text{Re}_t}{\text{Re}_\Delta}\right)^{1/2}, \quad (7.80)$$

$$\frac{K_{S_\Delta}}{K_{S_{[l_t, l_t]}}} \approx \text{MR}^{-2/3} \frac{\Gamma_K\left(\frac{\Delta}{\delta_l}\right)}{\Gamma_K\left(\frac{\Delta}{\delta_l} - \log \text{MR}\right)}, \quad (7.81)$$

considering that  $\log l_t/\delta_l = \log \Delta/\delta_l - \log \text{MR}$ , Eq. (7.5) and naturally  $\varepsilon_\Delta = \varepsilon$  in the inertial range. The mesh refinement, defined in section 7.1.2 (p.101), must be logically introduced, since the subgrid stretch depends on the mesh size.

Evidently, in case of a very low grid refinement  $\text{MR} = 1$ , this function tends to unity since the stretch due to the resolved length scales equals the global turbulence stretch:

$$\lim_{\text{MR} \rightarrow 1} \frac{K_{S_\Delta}}{K_{S_{[l_t, l_t]}}} = 1. \quad (7.82)$$

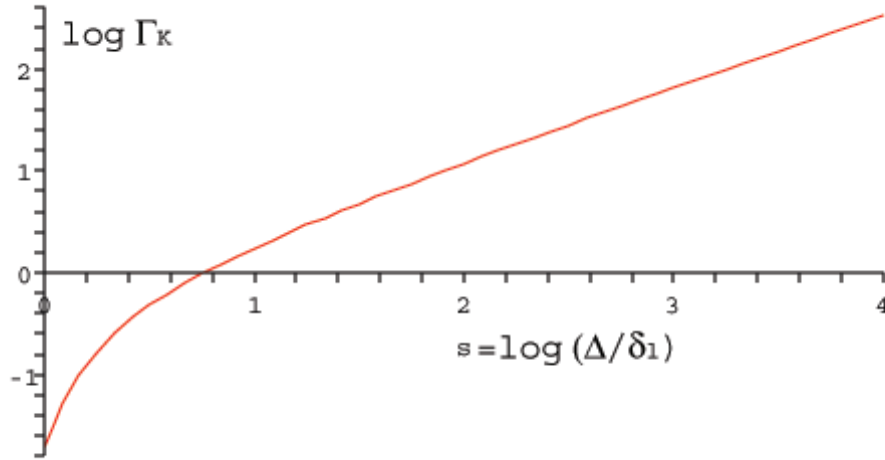


**Fig. 7.13:** Function  $\Gamma_K(\Delta/\delta_l)$  with log-scale

The relative influence of the subgrid scale in the global turbulent stretch  $K_{S_\Delta}/K_{S_{[m,t]}}$  is plotted Figure 7.14 (p.130) for different value of the ratio  $\Delta/\delta_l$  and for different mesh refinement. The influence of the subgrid scale remains smaller than 35% for a standard mesh refinement  $MR = 1/5$ .

### Global stretch

The contribution of the unresolved scales has been detailed. For the subgrid scales the stretch is evaluated according the results established with Eqs. (7.78) and (7.81):

$$K_{S_\Delta} \approx \frac{c_{ms}}{\ln 2} \sqrt{\frac{\varepsilon_\Delta}{\nu}} \text{Re}_\Delta^{-1/2} \Gamma_K\left(\frac{\Delta}{\delta_l}\right)$$

within one factor can be separately estimated:

$$\sqrt{\frac{\varepsilon_\Delta}{\nu}} \text{Re}_\Delta^{-1/2} \sim \frac{u_{sgs}}{\Delta} \sim \frac{1}{t_\Delta}. \quad (7.83)$$

Thus the stretch generated by the unresolved eddies  $K_{S_\Delta}$  scales with the inverse of the local turbulent time  $t_\Delta$  and with the function  $\Gamma_K$  (defined Eq. (7.79)) which rapidly increases with the ratio  $\Delta/\delta_l$  (see Figure 7.13 (p.129)).

The contribution of the resolved eddies must be also evaluated. A similar estimation can be expressed for  $K_{\tilde{S}}$ . Expressing the relation between stretch and strain for large ratios  $r/\delta_l$ , a constant value 0.4 is approximated for the efficiency function so that:

$$K_{\tilde{S}} \approx 0.4 c_{ms} \tilde{S} \approx 0.1 \tilde{S}. \quad (7.84)$$

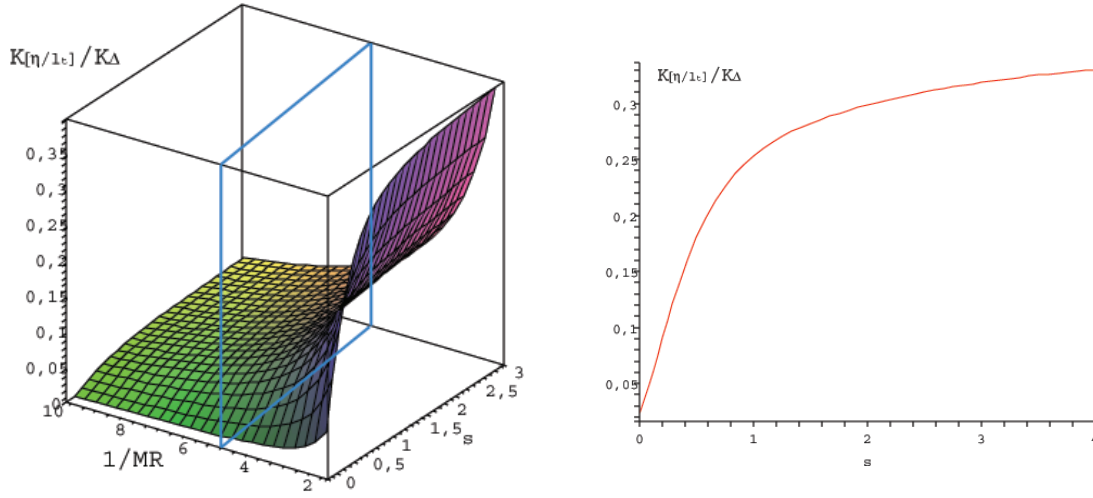


**Fig. 7.14:** Influence of the subgrid scale in the turbulent stretch  $K_{S\Delta} / K_{S[\eta; t]}$  (left) with particular case  $MR = 1/5$  (right)

Supposing the use of the Smagorinsky turbulence model, see Eq. (3.27), the subgrid turbulent time  $t_\Delta$  can be evaluated with the filtered strain rate  $\tilde{S}$ :

$$\frac{1}{t_\Delta} \sim \frac{u_{sgs}}{\Delta} \sim C_s \tilde{S}, \quad (7.85)$$

this numerically leads to:

$$K_{\tilde{S}} \approx \frac{1}{t_\Delta}. \quad (7.86)$$

Finally, the global stretch in LES modeling  $K_{(S_\Delta + \tilde{S})}$  can be estimated, and consequently the generalized Karlovitz number  $Ka_t^*$ , required to express the turbulent flame time  $t_c^*$ , using Eqs. (7.69), (7.78), (7.84), and  $c_{ms} / \ln 2 \approx 0.4$ :

$$K_{(S_\Delta + \tilde{S})} \approx \frac{1 + 0.4 \Gamma_K \left( \frac{\Delta}{\delta_l} \right)}{t_\Delta},$$

$$\text{then } Ka_t^* \approx \left( 1 + 0.4 \Gamma_K \left( \frac{\Delta}{\delta_l} \right) \right) \frac{t_c}{t_\Delta}.$$

This approximation of the generalized Karlovitz number  $Ka_t^*$  is only valid with the Smagorinsky model. It has the advantage of stressing the dependence on the subgrid Damköhler number  $Da_\Delta^{-1} = \frac{t_c}{t_\Delta}$ , similarly to the turbulent Karlovitz number (see Eq. (2.105)). But its numerator  $\sqrt{\text{Pr Re}_\Delta}$  is replaced with a function of the stretch induced by the turbulence:

$$\left( 1 + 0.4 \Gamma_K \left( \frac{\Delta}{\delta_l} \right) \right) \text{ instead of } \sqrt{\text{Pr Re}_\Delta}.$$

Using a transport equation for the turbulent kinetic energy, the original evaluation based on the strain rate to evaluate  $K_{\tilde{S}}$  should be used:

$$K_{(S_{\Delta}+\tilde{S})} \approx 0.1\tilde{S} + 0.4 \frac{\Gamma_K(\frac{\Delta}{\delta_l})}{t_{\Delta}}, \quad (7.87)$$

$$\text{then } \text{Ka}_t^* \approx \left( 0.1\tilde{S} + 0.4 \frac{\Gamma_K(\frac{\Delta}{\delta_l})}{t_{\Delta}} \right) t_c \quad (7.88)$$

### 7.5.3 Sub-model for the bending effect

Using a LES model with a  $k$ -transport equation instead of the Smagorinsky model as advised in section 7.2.1 (p.105), one can conclude with the evaluation of the turbulent chemical time  $t_c^*$ :

$$t_c^* = t_c (1 + \text{Ma } \text{Ka}_t^*)^2 \quad (7.89)$$

$$t_c^* = t_c \left[ 1 + \text{Ma} \left( 0.1\tilde{S} + 0.4 \Gamma_K \left( \frac{\Delta}{\delta_l} \right) \frac{u_{sgs}}{\Delta} \right) t_c \right]^2. \quad (7.90)$$

In the following, the Damköhler number  $\text{Da}_{\Delta}^*$  based on  $t_c^*$

$$\text{Da}_{\Delta}^* \equiv \frac{t_{\Delta}}{t_c^*} = \frac{\text{Da}_{\Delta}}{(1 + \text{Ma } \text{Ka}_t^*)^2} \leq \text{Da}_{\Delta} \quad (7.91)$$

replaces the subgrid Damköhler number based on the laminar chemical time, so that the bending effect is naturally embedded in the model closure by taking the stretched laminar flame speed as reference. The formulations Eq. (7.90) and (7.91) asymptotically tend with a high stretching to respective values:

$$\lim_{\text{Ka}_t^* \rightarrow \infty} t_c^* = \infty \quad (7.92)$$

$$\lim_{\text{Ka}_t^* \rightarrow \infty} \text{Da}_{\Delta}^* = 0. \quad (7.93)$$

The decrease of the local Damköhler number would lead to a larger ratio  $S_{t_{\Delta}}/S_{l,cs}$  in Eq. (7.66), but the stretched flame speed  $S_{l,cs}$  is decreasing faster than this ratio, so that the resolved burning velocity  $S_{t_{\Delta}}$  tends to zero. If quenching locally occurs, it would appear because the local stretched flame speed  $S_{l,cs}$  is reduced to zero.

As a conclusion, eluding the modeling formalism to go back to a physical interpretation, turbulence has actually two effects on the flame structure which compete against each other:

- Modification of the preheating zone due to the turbulent diffusion
- Modification of the reaction zone due to the stretch.

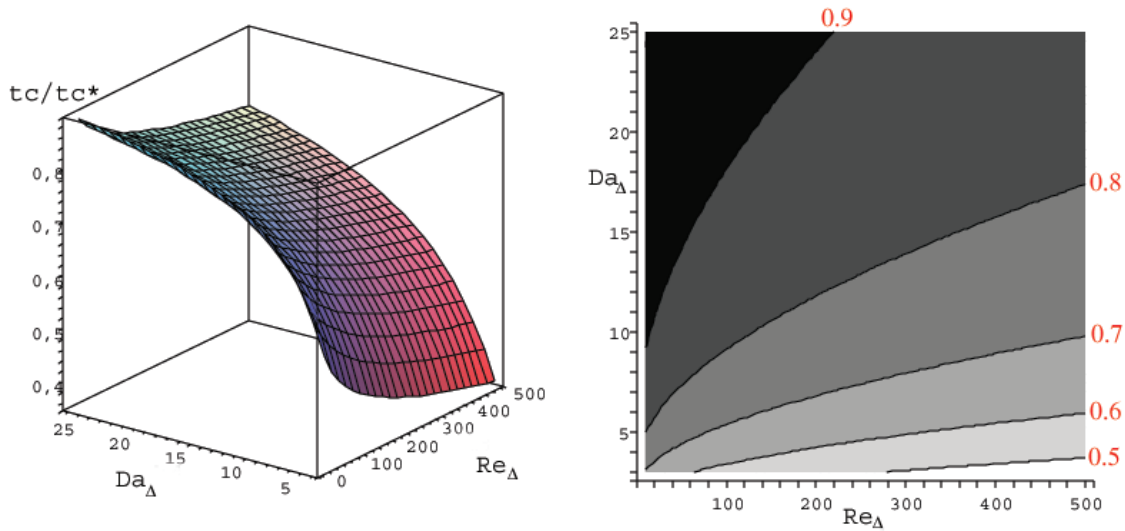


**Fig. 7.15:** Bending-effect correction: Ratio  $t_c/t_c^*$  ( $Ma = 0.69$ ), 3D-plot (left) and contour-plot (right)

For low and moderate turbulence intensity, only the first effect has an active role. The pre-heating zone of the flame front is altered, which leads to an enhancing diffusion process and thus to a faster local turbulent burning velocity. When the turbulence intensity becomes higher, the second effect is no more negligible, the inner structure of the flame is modified. This leads to a modified reference flame speed  $S_{l,sc} < S_l$ , and to a modified turbulent chemical time  $t_c^* > t_c$ . The Damköhler number based on the effective turbulent chemical time  $t_c^*$  is smaller than the original one:  $Da_\Delta^* \leq Da_\Delta$ , which tends to enlarge the ratio  $S_{t_\Delta}/S_{l,sc}$ .

On the other hand, the decrease of  $S_{l,sc}$  is large, so that globally the resolved burning velocity  $S_{t_\Delta}$  is reduced and may be quenched. The ratio  $t_c/t_c^* = Da_\Delta^*/Da_\Delta$  is displayed for illustration for a range of Damköhler and Reynolds numbers in Figure 7.15 (p.132) with  $Ma = 0.69$  and the approximation Eq. (7.85). The averaged ratio  $t_c/t_c^*$  is also displayed for a computation with the Paul Scherrer Institut burner, validation case in section 8.2 (p.156), in Figure 7.16 (p.133). The ratio decreases up to  $t_c/t_c^* \approx 0.6$  in zone of high turbulent intensities: at the burner mouth, and downwards where the flame is flapping, producing turbulence.

The bending-effect only appears, when comparing the turbulent burning velocity to the unstretched laminar flame speed. Basing the ratio to the stretched laminar flame speed *associated with its relevant time scale*, this effect is no more displayed. To conclude, the chemical time scale must be also modified to avoid a closure which should underestimate the turbulent flame speed, by actually overcompensating the bending-effect (see presentation by Weiss [Wei06]).

This sub-model for the quenching and the bending effect could be improved concerning the evaluation of the strain rate. The unsteady effects due to the strain rate variation could

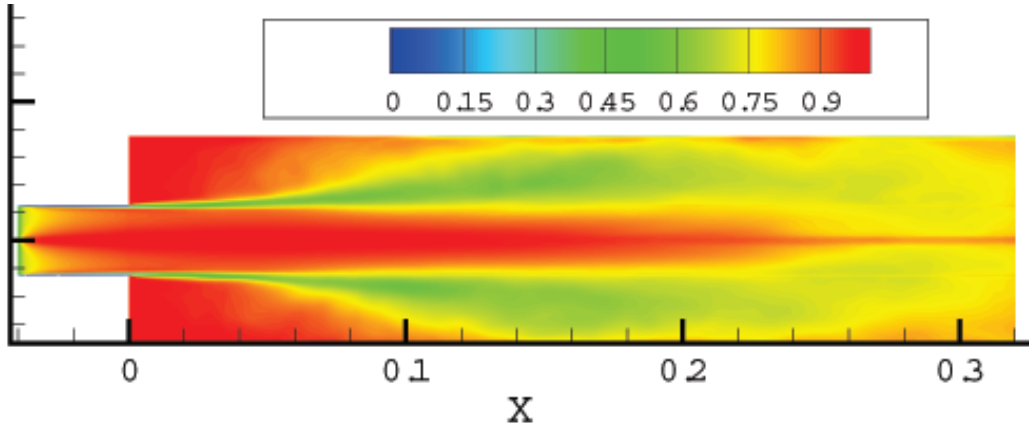


**Fig. 7.16:** Bending-effect correction: Ratio  $t_c/t_c^*$  with the PSI burner ( $\text{Ma} = 0.69$ )

be considered for example, as suggested by Flohr and Pitsch [FP00](p. 173). An evaluation based on the time derivative of  $\tilde{S}$  might be developed for example. But experimental data about such an effect are still missing. A precise evaluation of the stretch induced by the resolved eddies  $K_{\tilde{s}}$  may bring the best numerical improvement.

The dependence to the Markstein number could be also investigated in details. During the validation with the Volvo test-rig in section 8.1 (p.139), the theoretical value for the propane  $\text{Ma} \approx 6.7$  has been set to a lower value, so that the flame can stabilize in the wake of the flame holder. A possible explanation could be the use of *only one Markstein value* for the two contributions to stretch in the actual model:

$$t_c^* = t_c \left[ 1 + \text{Ma} \left( 0.1\tilde{S} + 0.4 \frac{\Gamma_K \left( \frac{\Delta}{\delta_l} \right)}{t_{\Delta}} \right) t_c \right]^2. \quad (7.94)$$

## 7.6 SFC model formulation

### 7.6.1 Blend function and model formulation

A synopsis of the SFC model is illustrated in appendix A.7 (p.226), in order to give an overview of the implementation.

#### Blend function

A fast and smooth transition between the *corrugated and thickened flame regime* formulations is required. A blend function is included to switch between the two established

closures Eqs. (7.66) and (7.67):

$$\begin{aligned} \left. \frac{S_{t_\Delta}}{S_l} \right|_{\text{thickened}} &= 0.7 \frac{S_{l,cs}}{S_l} \frac{(\text{Re}_\Delta \text{Pr})^{0.5}}{\text{Da}_\Delta^{\star 0.44}} \cosh^{0.945} \left[ \frac{1}{3} \text{arccosh} (4.357 \text{Da}_\Delta^{\star}) \right] \\ \left. \frac{S_{t_\Delta}}{S_l} \right|_{\text{corrugated}} &= \frac{S_{l,cs}}{S_l} (\text{PrRe}_\Delta \text{Da}_\Delta^{\star})^{\frac{\mathcal{D}-2}{2}} \end{aligned}$$

for  $\text{Ka}_\Delta \in [0.1, 1]$ :

$$\alpha = \tanh(2\text{Ka}_\Delta^2) \quad (7.95)$$

$$\frac{S_{t_\Delta}}{S_l} = \alpha \left. \frac{S_{t_\Delta}}{S_l} \right|_{\text{thickened}} + (1 - \alpha) \left. \frac{S_{t_\Delta}}{S_l} \right|_{\text{corrugated}} \quad (7.96)$$

The current definition has been retained by comparing different functions with *Maple*. Two main criteria have been selected for this choice:

- A rapid transition from one formulation to the other (stiff zone where  $\alpha \approx 0.5$ )
- Smooth changes near the zone of dominant influence ( $\alpha \approx 0$  or  $\alpha \approx 1$ ).

Figure 7.17 (p.135) displays the blend function  $\alpha$  as a function of the Reynolds and Damköhler numbers compared to the constant value 0.5. For illustration on the r.h.s. the function  $\alpha$  is compared with the simple function  $\tanh(\text{Ka}_\Delta)$ . As desired the gradients are smooth where  $\alpha \approx 0$  or  $\alpha \approx 1$  and steeper for the transition for the retained function. For illustration Figure 7.18 (p.135) depicts the local blend function for the PSI burner. It appears that the model burns in the corrugated flame regime at the plenum entry, and then rapidly in the thickened flame regime since the fluctuations are increasing downwards.

### 7.6.2 Comparison with the TFC model

The results of simulations with the TF, TFC-LES and SFC models are discussed in the next two chapters. The goal of this part is to compare *a priori* the TFC-LES and SFC model closures using the analytical model formulations.

#### General comparison

The TFC-LES model is naturally a reference model for the current proposed SFC model. Both of them are formulated for the progress variable approach, and developed to deliver the resolved burning velocity at the cell scale. They differ in the closure formulation and on the way to achieve it. They are nevertheless based on the same principles: the existence of thickened flamelets and their interactions with turbulence. Whereas the TFC-LES model should be only valid for the thickened flame regime, the SFC is composed of a two part formulation, in order to simulate correctly both thickened flame and corrugated flame

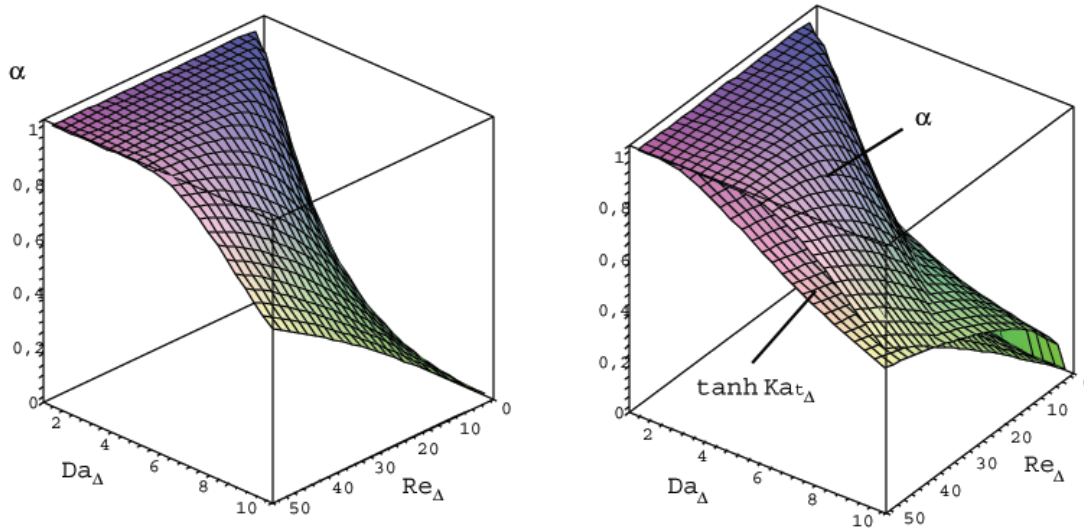


**Fig. 7.17:** Blend function  $\alpha = \tanh(2Ka_\Delta^2)$  (left), and  $\alpha$  compared to the function  $\tanh Ka_\Delta$  (right)

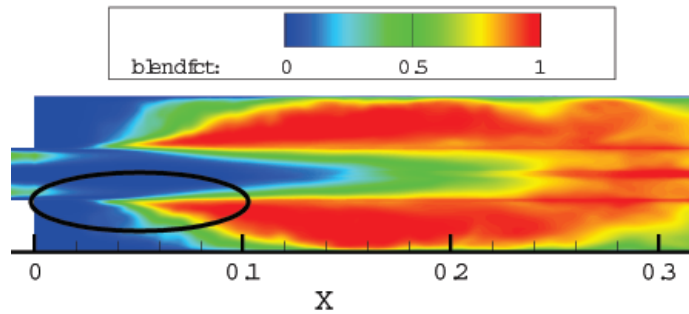


**Fig. 7.18:** Blend function with the PSI burner; marked zone: Transition between the corrugated and thickened flame regimes

regimes. For this reason, it is interesting to look at the ratio  $S_{t_\Delta}/S_l$  (effect of bending effect has been included, for TFC-LES refer to Eq. (6.43)) given by the two models in Figure 7.19 (p.136). The largest discrepancy appears for the domain with large Damköhler number and moderate Reynolds number, i.e. for the corrugated regime in Figure 7.20 (p.136). In the thickened flame regime, the two models deliver similar values of the ratio  $S_{t_\Delta}/S_l$ . The non-validity of the TFC-LES model for values  $Da_\Delta < 3$  is also stressed in Figure 7.20 (p.136), as explained in section 7.2 (p.104) and by Flohr and Pitsch [FP00](p. 172). The ratio  $S_{t_\Delta}/S_l$  is indeed suddenly increasing. The SFC model is mathematically defined for small values up to  $Da_\Delta \approx 0.23$  (see paragraph section 7.2.1 (p.108)), but physically up to  $Da_\Delta \approx 1$  (see Eq. (7.12)).

A remarkable result is that the two models predict the maximum locations of the ratio  $S_{t_\Delta}/S_l$  for about the same values ( $Re_\Delta, Da_\Delta$ ) (see Figure 7.19 (p.136) as well as Figure 7.20

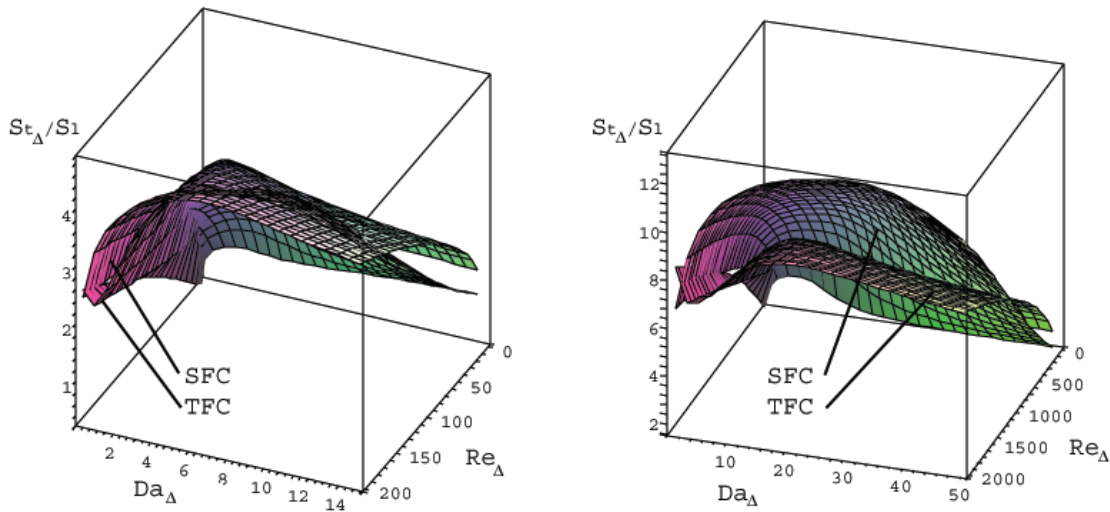


**Fig. 7.19:** SFC and TFC models with bending-effect correction for a reduced (l.h.s.) and a large (r.h.s.) range of values ( $Re_\Delta, Da_\Delta$ ) ( $Ma = 0.69, g_{cr} = 1/t_c$ )

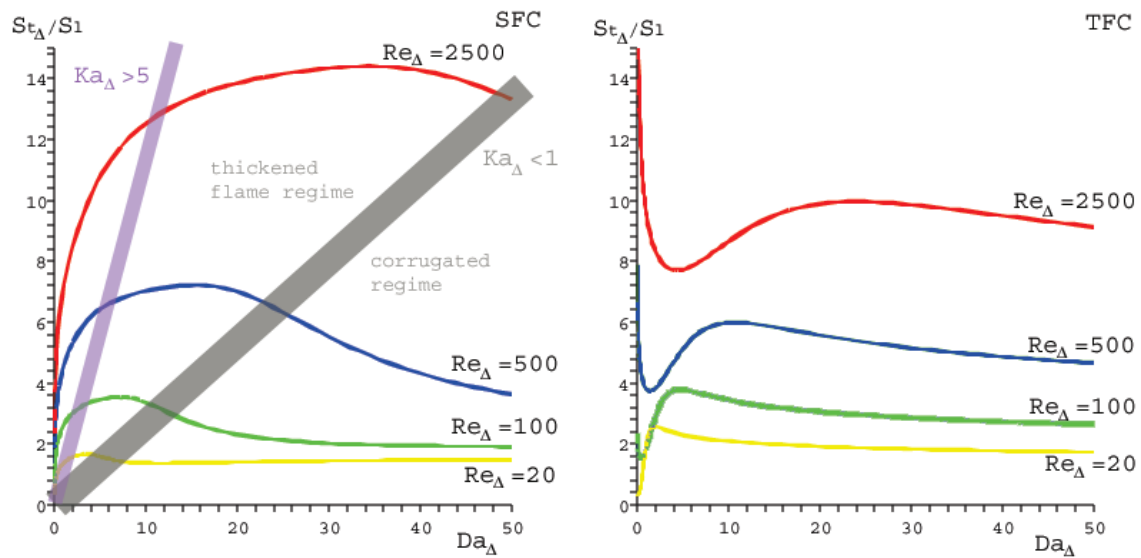


**Fig. 7.20:** Quantitative evolution of  $S_{t_\Delta}/S_l$  for the models SFC (left) and TFC (right) models with bending-effect correction (for  $Ma = 0.69, g_{cr} = 1/t_c$ )

(p.136)). These values are obtained along the line  $Ka_\Delta = \sqrt{Re_\Delta}/Da_\Delta \approx 2 - 3$ . The maximum value of  $S_{t_\Delta}/S_l$  occurs in the thickened flame regime near the limit with the corrugated regime, where the bending effect does not strongly act, and does not limit the ratio  $S_{t_\Delta}/S_l$  (see Figure 6.1 (p.97) and Figure 6.1 (p.97) with the TFC-LES model).

Figure 7.21 (p.137) indicates that the discrepancy between the two models reaches 30 % in the domain displayed. The SFC tends to predict larger resolved flame speed for flows with increasing turbulence. The influence of the subgrid Reynolds number is stronger than the

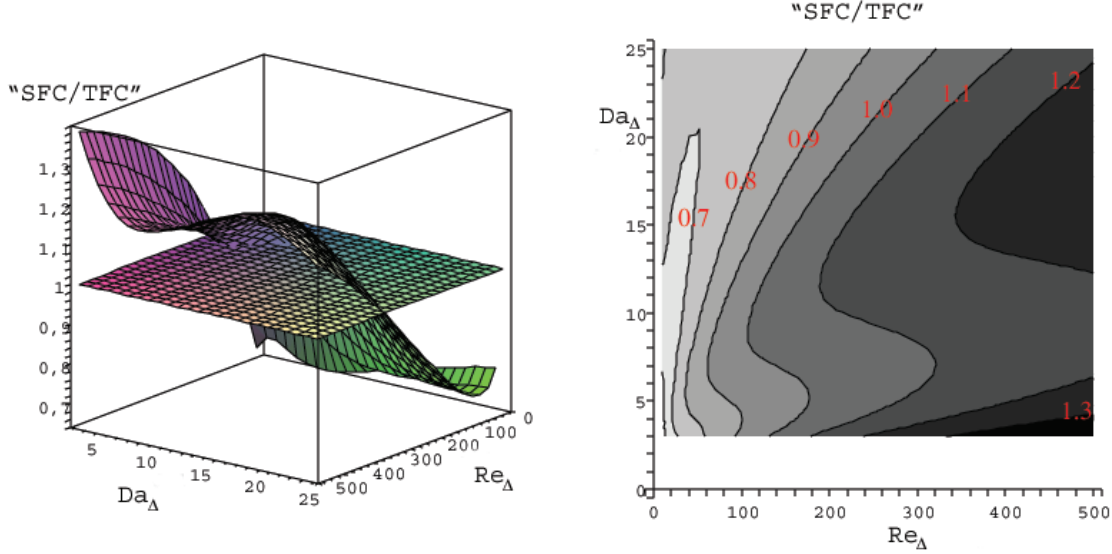


**Fig. 7.21:** Ratio  $S_{t_{\Delta}}^{SFC} / S_{t_{\Delta}}^{TFC}$  with the models SFC and TFC-LES with bending-effect correction, with 3D-plot (left) and contour-plot (right) (for  $Ma = 0.69$ ,  $g_{cr} = 1/t_c$ )

influence of the subgrid Damköhler number.

### Reynolds number dependence

This similarity for the model behavior should have been expected since their formulations in the thickened flame regime have the same dependence on the Reynolds number  $\sqrt{Re_{\Delta}}$ . If the trends are qualitatively similar in Figure 7.20 (p.136) with increasing Reynolds numbers, the ratio  $S_{t_{\Delta}} / S_l$  is larger with the SFC model, because of the different factor depending on the Damköhler number. They also differ by the presence of the additional term 1 in the TFC-LES model to recover the property  $S_{t_{\Delta}} / S_l = 1$  for flow with low turbulence intensity. This property is more naturally achieved by the SFC model with the help of the model for corrugated regime, as explained in section 7.3.1 (p.111).

### Damköhler number dependence

The main difference is the explicit influence of the subgrid Damköhler number  $Da_{\Delta}$ :

$$\frac{S_{t_{\Delta}}^{SFC}}{S_{t_{\Delta}}^{TFC-LES}} \sim \frac{1}{Da_{\Delta}^{0.19}} \cosh^{0.945} \left[ \frac{1}{3} \operatorname{arccosh} (4.357 Da_{\Delta}) \right] \quad (7.97)$$

In this ratio, the additional term 1 of the TFC-LES model has been omitted, so that only the thickened flame regime can be considered for which the term  $\frac{\sqrt{Re_{\Delta} Pr}}{Da_{\Delta}^{0.25}}$  is preponderant, with small values of the Damköhler number or large values of the Reynolds number. In Figure 7.22 (p.138) the function given by Eq. (7.97) is represented. The discrepancy reaches

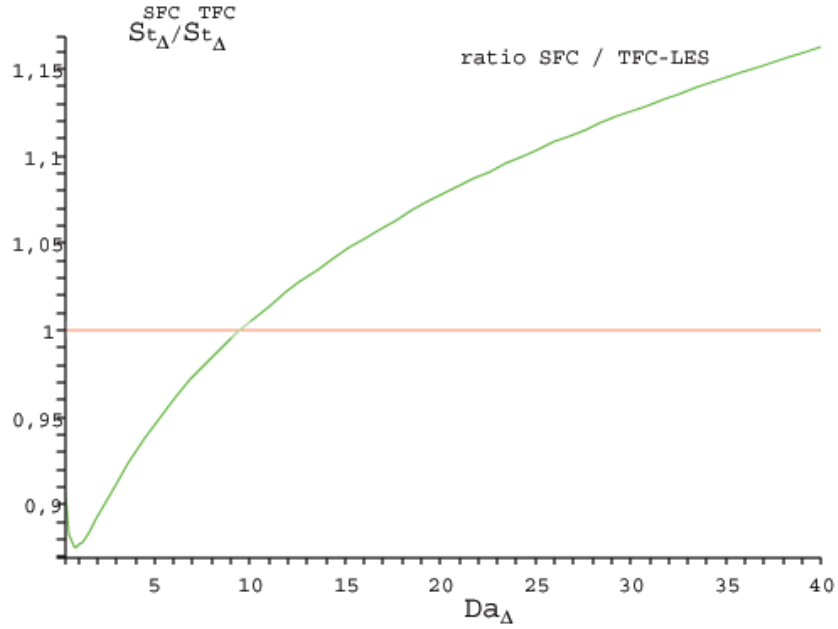


**Fig. 7.22:** Influence of the Damköhler number in SFC and TFC-LES models: Eq. (7.97) (without bending effect)

$\pm 15\%$  and the SFC model tends to predict higher values of the ratio  $S_{t_\Delta}/S_l$  for increasing  $Da_\Delta$  values. For values  $Da_\Delta < 1$ , the particular behavior of the TFC model is identified by the local minimal value of the ratio  $S_{t_\Delta}^{SFC}/S_{t_\Delta}^{TFC-LES}$ . This numerical comparison is indicative, since it has been made based on the model formulations *without bending effect corrections*. However, the present comparison highlights clearly the qualitative dependence on the Damköhler number.

### Conclusion

The two models TFC-LES and SFC mainly differ by the term  $Da_\Delta^{-0.19} \cosh^{0.945} [1/3 \operatorname{arccosh}(4.357 Da_\Delta)]$ , which increases with  $Da_\Delta$ . Remembering the definition  $Da_\Delta = t_\Delta/t_c = \Delta/(u_{sgs} t_c)$ , the SFC model tends to predict larger resolved burning velocity when meshes become coarser, since  $u_{sgs}$  is increasing slower than  $\Delta$ , as demonstrated with Eq. (7.8). Discussion on the model constant  $A$  for the TFC-LES model in section 8.1.2 (p.143), namely indicates that the constant  $A$  should be tuned up according to test-cases, and also to meshes. This more complex and explicit dependence on  $Da_\Delta$ , due to the accurate consideration of the flame characteristics in the cell, is likely to enable the SFC constant to be not mesh dependent.

## 8 Results and discussions

Die Natur macht keine Sprünge.

*G. W. Leibniz*

Comparisons of experimental and numerical results are presented for three burners. The first test-case, the so-called Volvo test-rig, has allowed the validation of the TF' model, presented in chapter 4, and its comparison to the TF model. Simplifications of the geometry (periodicity) have made the computations faster. The second test-case, the PSI burner presented in section 8.2 (p.156), permits to compare precisely the three different combustion models. The third test-case, the TD1 burner presented in section 8.3 (p.173), allows the validation of the progress variable approach for inhomogeneously premixed combustion both with TFC-LES and SFC closures.

### 8.1 Volvo test-rig

This burner has been selected as a validation case for three main reasons. It displays a perfect premixed turbulent flame, for which mean and rms variables are available, so that velocity profiles can be precisely compared with simulations. Furthermore, the relatively simple geometry makes the use of a cartesian mesh possible. This property is required for the validation of the TF model adaptation for *Fluent*, presented in section 4.2 (p.66). Moreover, the use of periodic conditions on the spanwise direction reduces the number of required cells, and thus CPU-effort and memory requirement. This burner test-rig has been investigated by Sjunnesson et al. [SNM91, SHL92] and has been already employed as validation case for other LES publications [FL94, GBB04, REO93, ZB06].

#### 8.1.1 Experiments and geometry

##### Experimental set-up and results

The Volvo test-rig is a typical afterburner configuration with a triangular cross section bluff body (side length: 40 mm) as flame holder. The burner consists of a one-meter combustor straight channel (downstream of the flame holder) with a rectangular cross section  $240 \times 120$  mm. The vertical side cut of the flame holder is mounted 318 mm from the inlet, so that the actual combustion chamber is 682 mm long. Measurements have been achieved under atmospheric conditions  $P = 1$  bar and  $T = 288$  K with an inlet velocity

$u = 17$  m/s (mass flow rate  $\dot{m} \approx 600$  g/s) and 3-4% of turbulence intensity. The turbulent Reynolds number is about  $Re_t \approx 2 \times 10^3$ , considering that the integral length scale has the half size of the flame holder  $l_t \approx 2$  cm, and that the velocity fluctuation is  $u' \approx 2$  m/s near the flame holder. A mixture of air and propane at an equivalence ratio  $\phi = 0.65$  (implies that  $S_l \approx 0.17$  m/s) has been employed. This leads to a Damköhler number  $Da \approx 10$ , and to a turbulent Karlovitz number  $Ka_t \approx 4$ , indicating that the combustion may occur in the thickened flame regime rather than in the corrugated flame regime (see definition section 2.4.3 (p.37) and resolved flame front in Figure 8.2 (p.141)). Other sets of parameters have been considered (inlet temperature  $T_{in} = 600$  K, equivalence ratio  $\phi = 0.85$ ), they are not reported here.

Velocity measurements have been achieved using Laser Doppler anemometry (LDA) in axial and transversal directions. Profiles for mean and rms values are available for different sections at  $x = 15, 38, 61, 150$  and  $376$  mm (counted from the flame holder, see Figure 8.3 (p.142)). Reynolds averaged temperature has been measured with a Coherent Anti-Stokes Raman Scattering system (CARS) at  $x = 150, 350$  and  $550$  mm by Sjunnesson et al. [SNM91, SHL92].

### Flow field

The main characteristic of the flow is the recirculation zone behind the bluff body, as depicted Figure 8.1 (p.140)). The flame can stabilize in the region of reduced velocity (see Figure 8.2 (p.141)). The inlet turbulence intensity amounts 3-5 %. In the wake of the flame holder, the shear layer generates turbulence. The turbulence intensity in the burning region is higher, and does not directly depend on the inlet parameters. This flame is a so-called *developing turbulent flame*, which means that the brush thickness of the flame becomes larger with distance to the stabilization point. Simultaneously, the flame approaches the

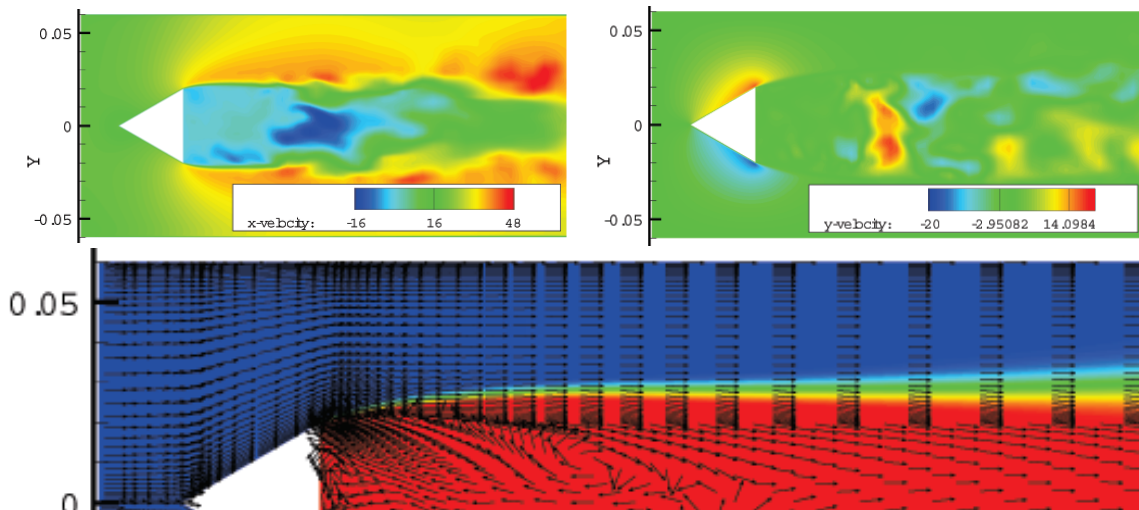


**Fig. 8.1:** Flow structure behind the bluff body: instantaneous x- and y-velocities (top, left and right), and mean velocity vectors and progress variable (bottom, half picture)

bottom and top walls.

### 8.1.2 Modeling and boundary conditions

#### Domain and mesh

The mesh is structured, and the part downstream of the flame holder, where the flame stabilizes, is even Cartesian as recognized with the vector plot in Figure 8.1 (p.140) (the density of vectors is reduced compared to the mesh refinement). Periodic boundary conditions in spanwise direction have been used to reduce the transverse direction to one third ( $\dot{m} \approx 200$  g/s), and to limit the number of required cells (see Figure 8.3 (p.142) for experimental dimension). The inlet part before the bluff body has been reduced to 20 mm. Finally, the mesh counts about 600,000 cells in the whole domain. The walls (flame holder and upper and bottom walls) are explicitly resolved by placing first cells to obtain a value  $y^+ < 3 - 5$ . The mesh has been designed in a way that the upstream half ( $x < 500$  mm) is fine such that turbulent eddies can be resolved with at least 5 cells:  $\Delta_x/l_t < 1/5$ . The downstream part of the mesh ( $x > 500$  mm) is coarser  $\Delta_x/l_t \approx 1/3$  to use less cells. Actually, a coarser mesh in the axial direction would lead to inappropriate aspect ratios cells.

#### Fluid properties

The propane-air mixture is considered as incompressible. Its molar mass is constant and non-dependent on the local mixture  $M = 29.0$  g/mole. The density according to the ideal gas law (see Eq. (2.13)) reads at the reference atmospheric pressure  $p_0$ :

$$\rho(T) = \frac{p_0}{\mathcal{R} T}. \quad (8.1)$$

The laminar dynamic viscosity is temperature dependent and evaluated using Sutherland's law, as given in *Fluent* [FLU05]:

$$\mu(T) = 1.7894 \left( \frac{T}{273.11 \text{ K}} \right)^{3/2} \frac{273.11 + 110.56 \text{ K}}{T + 110.56 \text{ K}} [\text{kg}/(\text{m s})]. \quad (8.2)$$

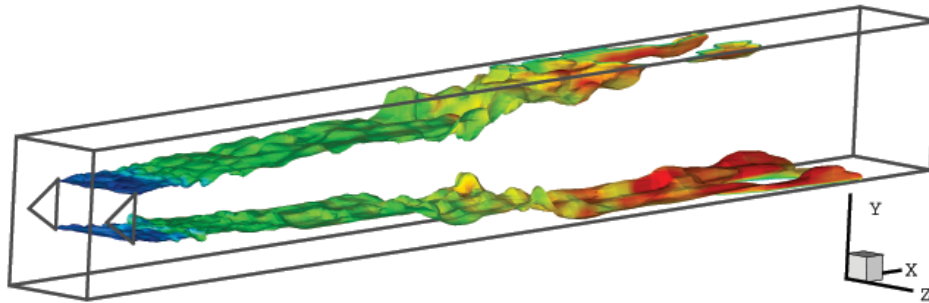


**Fig. 8.2:** Flame front ( $c = 0.5$ )

The calorific coefficient is given by the polynomial presented in Table 2.1 (p.14) for the three models. The thermal conductivity has the constant value  $\lambda = 0.0242 \text{ W/(m K)}$  for the TFC-LES and SFC simulations. For the TF model, the thickening factor is taken into consideration for the energy equation, so that the thermal conductivity is evaluated according to the relation Eq. (B.12).

### Boundary conditions

There are four types of boundary conditions for the computational domain. The inlet is modeled with the option “velocity inlet”, the outlet with the “pressure outlet” option and the structure walls with “wall” option from *Fluent* 6.2. The periodic conditions are treated automatically. The parameters for the UDS scalars, as well as the turbulent parameters, differ according to the combustion model. Simulations with the TFC-LES model have been achieved with the Smagorinsky model, and simulations with the SFC and TF model with the subgrid turbulent kinetic energy transport equation model, as will be explained later. The generic flow parameters are given in Table 8.1 (p.143), and the specific parameters, which depends on the combustion model, are listed in Table 8.2 (p.144). These parameters directly correspond to the experimental values. The subgrid turbulent kinetic energy at the inlet has been set to a larger value, since *Fluent* is damping the turbulence at the inlet. Considering that  $u' = TI \cdot U_{in} \approx 0.85 \text{ m/s}$ , and that about 60 % of the turbulent kinetic energy is resolved, one should employ  $k_{sgs} \approx 40\% \cdot 3/2 u'^2 \approx 0.51 \text{ m}^2/\text{s}^2$ .

The combustion parameters are imposed with Dirichlet condition (specified value) at the inlet, and with Von Neumann condition (specified flux) at the outlet and walls.

### Numerical parameters

The time-step has been set to  $\Delta t = 5 \cdot 10^{-6} \text{ s}$ , and results have been averaged for the simulation time  $\Delta T = 0.08 \text{ s}$ , larger than the convective time  $T_c \approx 0.05 \text{ s}$ . The transport equations have been solved to the second order, with central differencing scheme for the momentum, pressure and energy equations, and upwind differencing scheme for the UDSs equations.

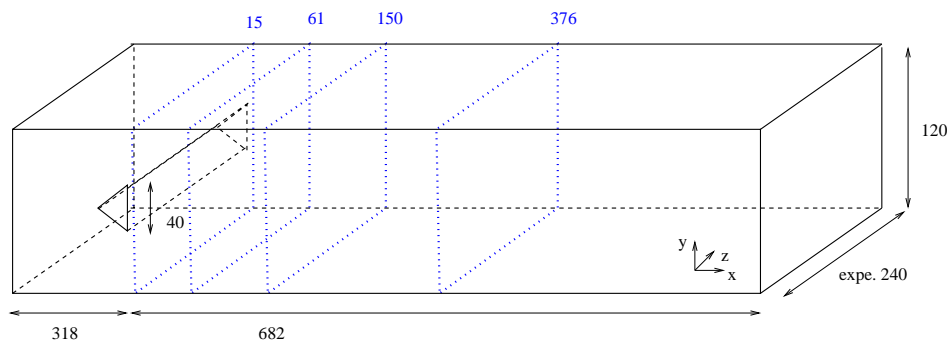


**Fig. 8.3:** Experimental test-rig dimensions and velocity measurements sections

### Special model parameters

For the TFC-LES model, only results with the Smagorinsky turbulent model and the constant  $A = 0.52$  (see Eq. (6.34)) are shown for the comparison. Nevertheless simulations have been tested with three different configurations:

- $A = 0.52$  and Smagorinsky model
- $A = 0.52$  and the transport equation
- $A = 0.77$  and Smagorinsky model.

Like the TF and SFC models, the TFC-LES model has been also implemented conjointly with the tke transport equation. Unfortunately, it has delivered results with too much reaction rate near the walls. The flame is burning back along the top and bottom walls. Reduced values of the stretch factor  $g_{cr}$  (see section 6.39 (p.96)) have not permitted to correct this, and to get satisfying results. In regards to the CPU-time required to achieve these different tests, no further computations of the TFC-LES with this turbulence model have been carried out.

As detailed in section 6.2.4 (p.97), the *universality* of the constant  $A$  for the TFC-LES model has not been proved. The value  $A = 0.77$  permits to achieve a complete combustion in the channel:

$$\int w_c \dot{c}(t) dv = \int \rho_u S_t |\nabla c| dv \approx 200 \text{ g/s.} \quad (8.3)$$

With the constant  $A = 0.52$  only  $\int w_c \dot{c}(t) dv \approx 140 \text{ g/s}$  is reached. Zimont and Battaglia [ZB06](p. 19) have used the value  $A = 1.2$  for testing this case with exactly the same conditions. This demonstrates the TFC-LES model constant  $A$  is not only case-dependent, but also mesh-dependent, and probably also dependent on the turbulence model.

Boundary condition	Parameter	Value
Inlet	"Velocity inlet"	
	Velocity	17 m/s
	Temperature	288 K
	Turbulence intensity	5%
	Integral length scale	4 cm
	subgrid tke	$1.1 \text{ m}^2 / \text{s}^2$
Outlet	"Pressure outlet"	
	Gauge pressure	0 Pa
	Backflow Temperature	1300 K
	subgrid tke	$1.1 \text{ m}^2 / \text{s}^2$

**Tab. 8.1:** Flow boundary conditions for the Volvo test-rig

Inlet		
TFC-LES and SFC	UDS-0	$c = 0$
TF	UDS-0	$y_F = 0.0283$
	UDS-1	$y_{CO} = 0$
Outlet and wall		
TFC-LES and SFC	UDS-0	$\frac{\partial c}{\partial n} = 0$
TF	UDS-0	$\frac{\partial y_F}{\partial n} = 0$
	UDS-1	$\frac{\partial y_{CO}}{\partial n} = 0$

**Tab. 8.2:** Boundary conditions for the combustion models, Volvo test-rig

### 8.1.3 Validation of the TF model

This part presents the validation of the TF' model described in section 4.2 (p.66) compared to the original TF model. Three versions of the TF models have been computed:

- The TF standard model associated with the Smagorinsky turbulent model
- The TF' model associated with the Smagorinsky turbulent model
- The TF' model associated with the tke transport equation.

Only the first two versions with the Smagorinsky turbulent model should be required for the validation of the version TF'. The third version informs on the influence of the turbulence model on the combustion modeling. The velocity profiles in axial and transversal directions are briefly compared for three sections  $x = 15, 61$  and  $150$  mm. A more complete description and explanations for the discrepancies are given in the next section, when comparing the TFC, TF' and SFC models. The focus is namely here placed on the similarity between the numerical results.

#### Section $x = 15$ mm: Figure 8.4 (p.146)

For this section directly placed behind the flame holder, the axial and transversal mean velocity profiles of the three versions are similar and close to the experimental results. The level of fluctuations are too low.

#### Section $x = 61$ mm: Figure 8.4 (p.146)

For this section the main axial and transversal velocity profiles are still similar for the three versions of the TF model, but display more discrepancies compared to the experimental results. The two TF' versions deliver better prediction of the transversal rms velocity profile.

**Section  $x = 150$  mm: Figure 8.4 (p.146)**

The averaged numerical results are fairly satisfying in this section, even less precise near the walls for the transversal direction. There are no discrepancies between the three versions. The prediction of the axial fluctuations is fairly good, slightly better with the TF'-tke version. The transversal fluctuations are well predicted with the TF version, contrary to the previous section.

**Temperature profiles: Figure 8.5 (p.147)**

The results for the TF and TF' models are identical. The TF'-tke model delivers for the last section ( $x=550$  mm) a slightly different profile, and actually a poorer agreement compared to the experiments.

**Conclusion**

The predictions of the three versions of the TF model are very close. The TF and TF' deliver the same prediction in terms of mean velocity profiles, as well as for the temperature prediction. The TF'-tke does not bring noticeable changes. This shows that the turbulence model has not much effect on the simulation quality. The TF' formulation seems similar to the original model, and its implementation in *Fluent* is satisfying.

**8.1.4 Comparison of the TFC-LES, TF' and SFC models**

For the TF model, which has been validated in three different configurations in the last section (TF-Smagorinsky, TF'-Smagorinsky and TF'-tke), only the results with the version TF'-tke are displayed here. The SFC model has been also used conjointly with the tke transport equation for the reasons given in section 7.2.1 (p.105). The TFC-LES model has been computed with the Smagorinsky model for the reasons given in section 8.1.2 (p.143).

In the following, results of mean and rms velocity profiles at the sections  $x = 15, 61, 150$  and  $376$  mm are presented in the axial and transversal directions, and compared to the experimental results. The results for  $x = 38$  mm are not given, because they are similar to the results at  $x = 61$  mm for the analysis. Before detailing each result, a global trend can be given: None of the three models is surpassing the others. In general the TF' and SFC models predict in a better way the profile for the first three sections  $x = 15, 61$  and  $150$  mm. The TFC model gives better results at  $x = 376$  mm. The reason for this unexpected change of trend in the result quality is explained using the temperature profile at  $x = 150, 350$  and  $550$  mm.

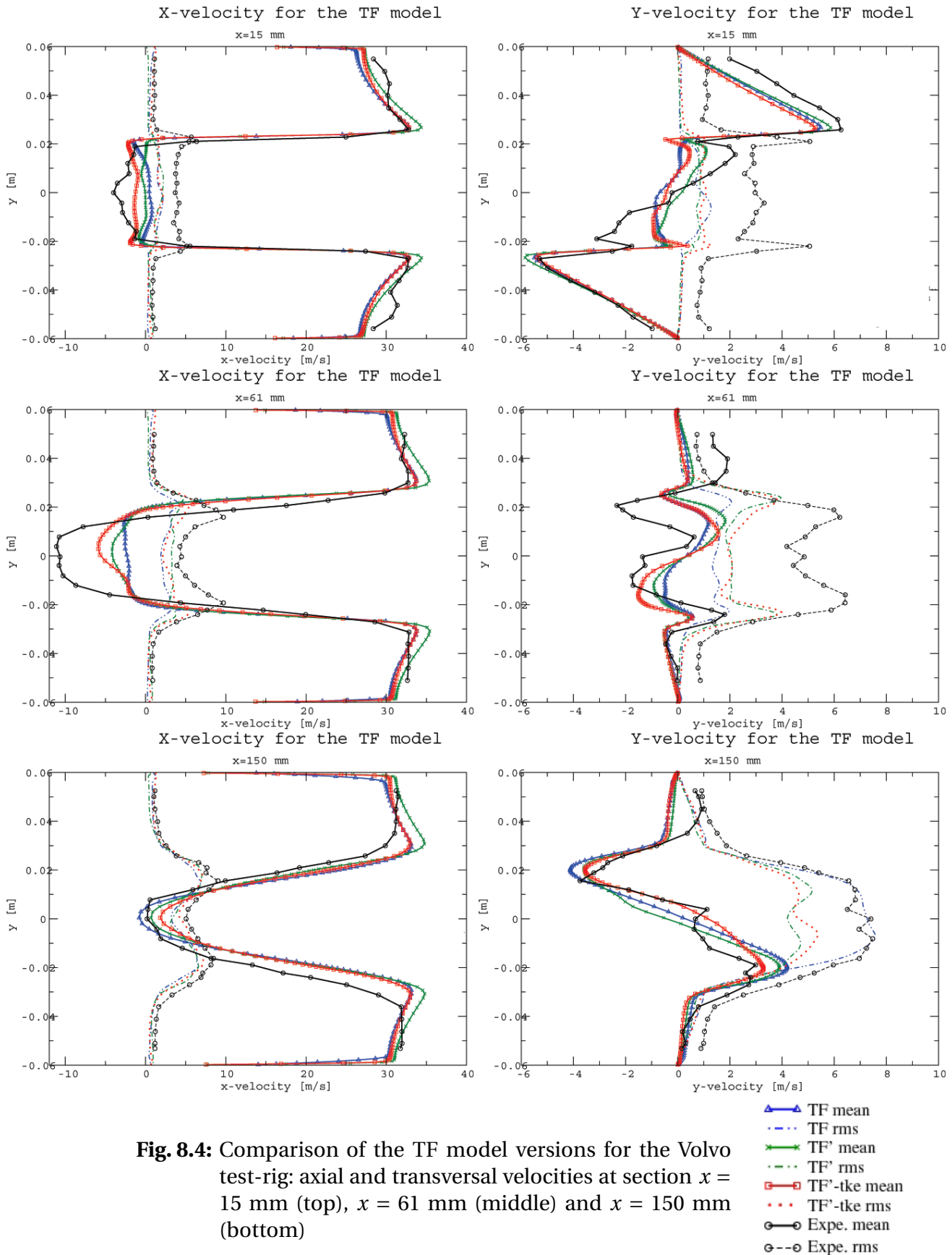


**Fig. 8.4:** Comparison of the TF model versions for the Volvo test-rig: axial and transversal velocities at section  $x = 15$  mm (top),  $x = 61$  mm (middle) and  $x = 150$  mm (bottom)

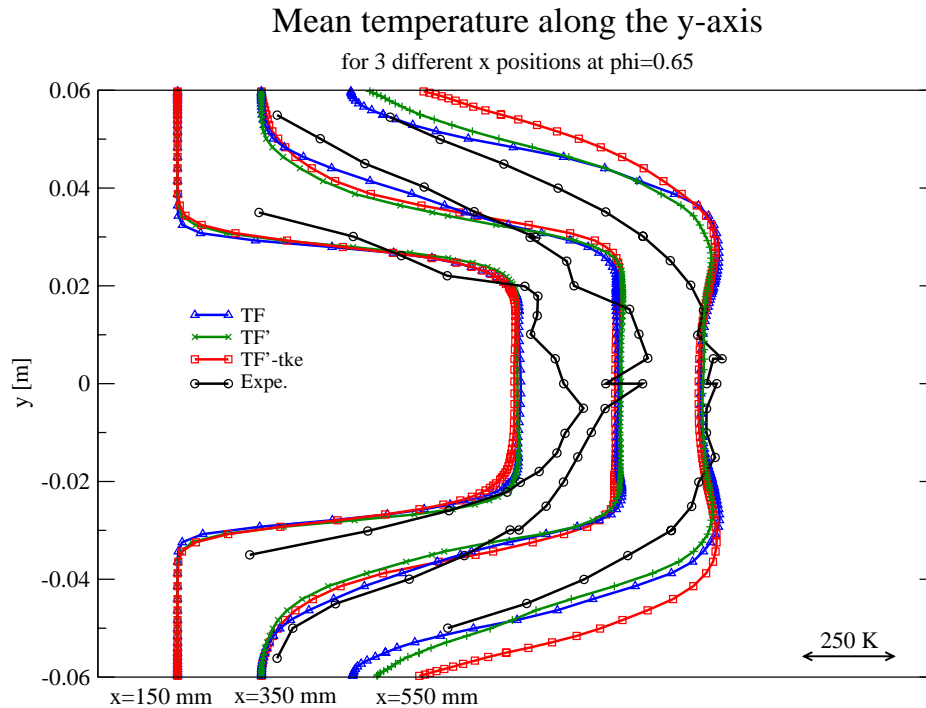


**Fig. 8.5:** Temperature profiles

**Section  $x = 15$  mm: Figure 8.6 (p.151)**

For this first section, the mean axial velocity profiles for the three models are very close and predict almost perfectly the experimental results. Only on the symmetry axis the intensity of the recirculation is strongly underestimated, and the profiles are flat instead of rounded. Concerning the mean transversal velocity, the TFC and SFC models give identical results and close to the experimental ones above and below the flame holder level. Behind the flame holder the SFC model predicts the trend of the velocity, but fails quantitatively. The TFC model predicts inverse trend at the same location. The TF' model yields similar results as the SFC model, but exhibits an offset. Even if the values are not predicted very precisely, the trend given by the experimental results is respected, namely the abrupt change of variation at  $x = \pm 20$  mm.

The level of turbulence is too low behind the flame holder as displayed with the axial and transversal rms velocities. This is probably due to the influence of the inlet boundary placed only a few centimeters upwards of the flame holder. SFC and TF' are delivering nevertheless higher levels thanks to the tke transport equation model.

**Section  $x = 61$  mm: Figure 8.7 (p.152)**

Larger discrepancies between the models appear at this section. The SFC model delivers the best prediction of the recirculation zone. The TFC and TF' models predict it with less intensity (axial mean velocity slightly smaller). For the transversal velocities, experimental

results deliver profiles which are not perfectly averaged nor centered. Nevertheless TF' and SFC predict again the best qualitative results, but with too large peak values for the SFC. The results given by the TFC are too flat.

The level of turbulence is better predicted than in the  $x = 15$  mm case, and almost exactly for the SFC model. Comparing to the first section, the inlet condition has less effect, and the production of turbulence because of the shear layer is dominant. The SFC delivers the same axial and transversal profiles as the experiments. The comparison with the TF' model, which is also using the tke transport equation model, is thus interesting. The TF' model gives similar profiles, but not as accurate as the SFC model. In this section, it seems that the combustion model has the strongest effect on the simulation results. The TFC model yields insufficient turbulence intensity, maybe because of the Smagorinsky model.

#### **Section $x = 150$ mm: Figure 8.8 (p.153)**

For this section the TF' model gives the best predictions both for the mean axial and transverse velocities. Its profiles are very close quantitatively to the experimental ones. The TFC model overpredicts the intensity of the recirculation zone, whereas the SFC model underpredicts it. Concerning the transverse mean velocity, like in the previous case, the TFC model follows the trend with flat profiles, and the SFC slightly overpredicts the peak values at  $x \pm 20$  mm. Possible explanations are suggested in the following paragraph *Conclusions*.

For the turbulence, the SFC still delivers fairly good predictions (particularly for the transversal direction), although it fails for the axial mean velocity. The TF' model yields also very good results. The results with the TFC are better for this section, but still with a too small intensity.

#### **Section $x = 376$ mm: Figure 8.9 (p.154)**

For this section, the best results are given by the TFC model, the TF' and SFC models are not accurate for this section. The flow prediction in the wake of the flame holder is imprecise both in axial and transversal directions.

Results for the turbulent fluctuations are non-precise and of too high intensity.

#### **Temperature profiles: Figure 8.10 (p.155)**

The temperature profiles at the sections  $x = 150, 350$  and  $550$  mm are depicted for the three models. The maximum temperature is correctly predicted with the SFC model, slightly underestimated with the TF' model and significantly underestimated with the TFC-LES model for the last two sections. The discrepancy between the SFC and the TFC-LES models is due to the reduced reaction rate with the TFC-LES model. Namely the energy equation is treated in the same way for both models, computing the enthalpy source term from

the progress variable source term. Discussion on the parameter  $A = 0.52$  of the TFC-LES is required. Zimont and Battaglia [ZB06](p. 18) have used  $A = 1.2$  for this validation case. Concerning the TF' model, temperature and enthalpy in the domain are strongly influenced by the chemical mechanism. The exact reason for the small discrepancy with the experiments is thus difficult to identify.

The temperature profile differs between computations and experiments. A reason for this can be the numerical treatment, which tends to increase the flame thickness (resolved flame as well as brush). The influence of the cooled walls, which cannot be modeled in the present computations (because precise data for the heat flux are not available), may be a reason, too. The temperature predicted by the computations is namely larger than the experimental one, except for the TFC-LES, which gives an incomplete reaction as already discussed.

The excessive temperatures in the downstream section are the reason for the false prediction of the velocity profiles at  $x = 376$  mm for the SFC and TF' models. Considering the conservation of the mass flow rate in a section of the test rig, and neglecting the influence of the  $z$ -direction:

$$\dot{m} = l_z \int \rho(y) u_x(y) dy \quad (8.4)$$

$$\dot{m} \approx \int \frac{u_x(y)}{T(y)} dy. \quad (8.5)$$

This simply demonstrates that the overpredicted temperature in the wake of the flame holder implies an overpredicted axial velocity. The recirculation length, which is slightly underestimated, also tends to increase this effect.

### Conclusions:

As remarked at the beginning of this section, the TF' and SFC are delivering the best results up to the section  $x = 150$  mm. The reason for the non-precise prediction of the TF' and SFC models at  $x = 376$  mm is due to the temperature prediction. The TFC model *paradoxically* benefits at this section of its insufficient reaction rate (see lower temperature at  $x = 350$  mm). Indeed, the results of the TFC-LES with the higher constant value  $A = 0.77$ , which allows to obtain the correct integral reaction rate in the whole domain, display the same trend as the TF' and SFC models at this section. Figure 8.11 (p.155) shows the velocity profiles at  $x = 376$  mm for the TFC-LES model with  $A = 0.52$  and  $A = 0.77$ : The results with the latter value are similar with the results of the SFC and TF' models. This stresses the influence of the reaction rate distribution in the domain to predict correctly both flame position and flow structure.

The SFC model is more precise for the fluctuations predictions. This is not only due to the turbulent model, but also on the combustion model itself. It predicts namely slightly better rms velocity profiles than the TF'-tke model, which is employing the same turbulence model.

The parameter  $Ma \approx 0.7$  for the SFC quenching model presented in section 7.5.3 (p.131) has been maintained like in the methane case. The theoretical value  $Ma \approx 7$  prevents the mixture to burn, because of the influence with the square  $(1 + MaKa_t)^{-2}$  in the model, as suggested and discussed in section 7.5.3 (p.131).

### 8.1.5 Comparison with previous works

The Volvo test-rig has been computed with LES combustion models with the same parameters by Giacomazzi et al. [GBB04], and Zimont and Battaglia [ZB06].

Giacomazzi et al. have produced several LES computations to compare results of a complete three-dimensional case, a case with periodic boundary conditions in spanwise direction, and a two-dimensional case. It demonstrates that a complete 3D simulation brings fairly better prediction than the 3D with periodic BCs. As in the present work there are some discrepancies for the velocity at the section  $x = 150$  and  $376$  mm, there are also due to the temperature profiles. In the case  $x = 376$  mm, the recirculation zone is overpredicted, which logically corresponds to the lower temperature value at  $x = 350$  mm. The results for the axial velocity fluctuations seem fairly accurate compared to the experimental results.

Zimont and Battaglia only display mean results. As already mentioned in section 8.1.2 (p.143), a constant value  $A = 1.2$  has been used and not the reference value  $A = 0.52$ . They find fairly reasonable profiles compared to the experimental results. The mean axial velocity is a little overpredicted. As expected, the temperature in the wake of the bluff body is thus smaller than in the current results, and the profile better predicted. Unfortunately, there are no results depicted for the fluctuations or in the transversal direction.

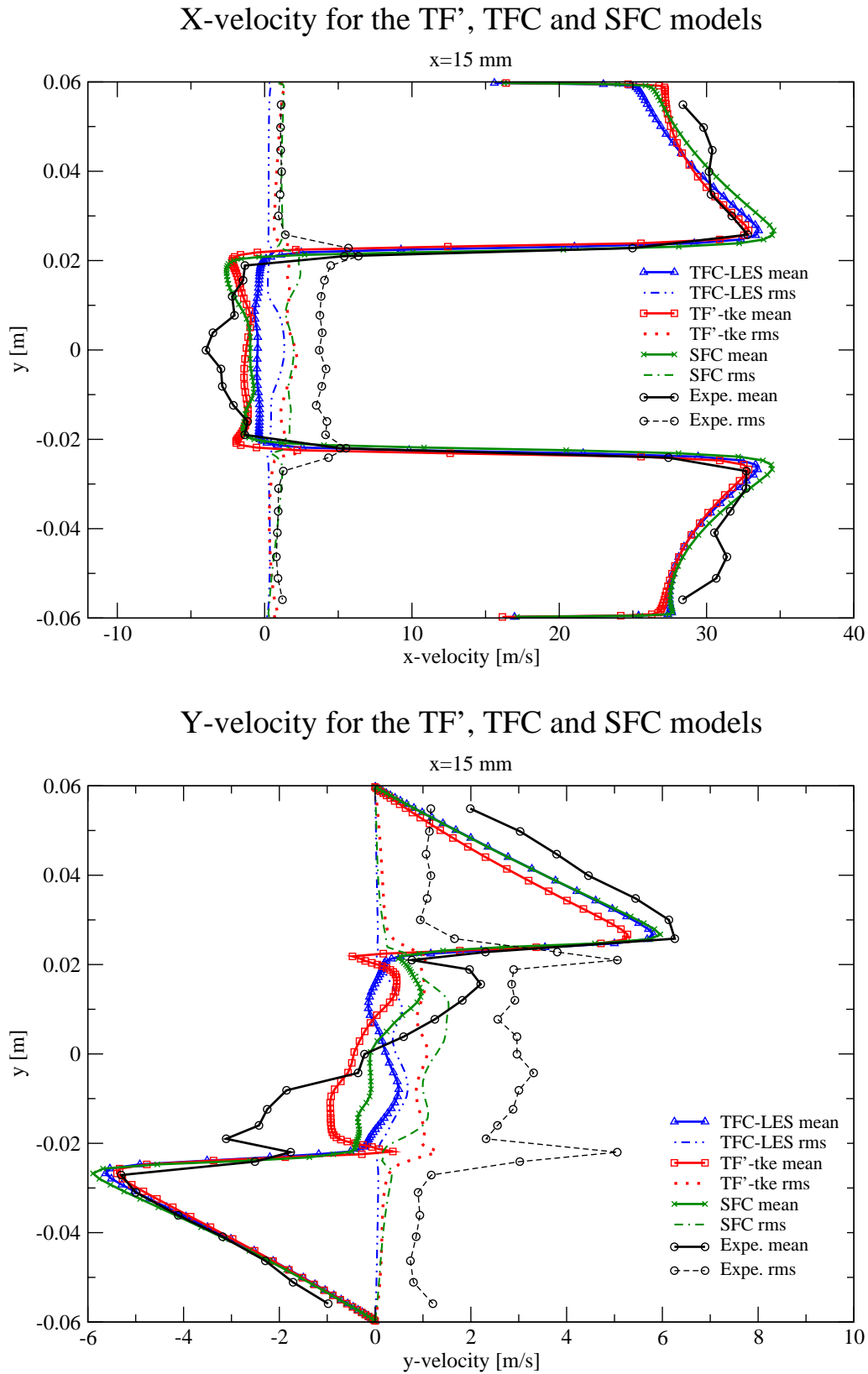


**Fig. 8.6:** Models TFC, TF'-tke and SFC for the Volvo test-rig: axial (top) and transversal (bottom) velocities at section  $x = 15 \text{ mm}$

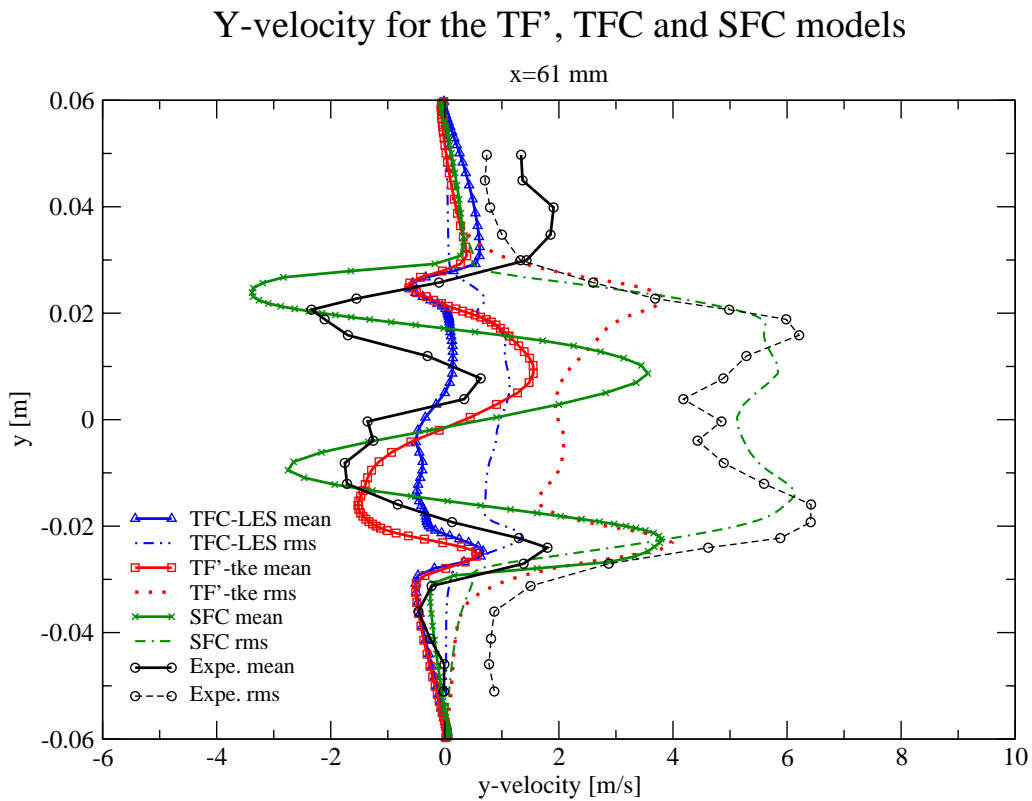
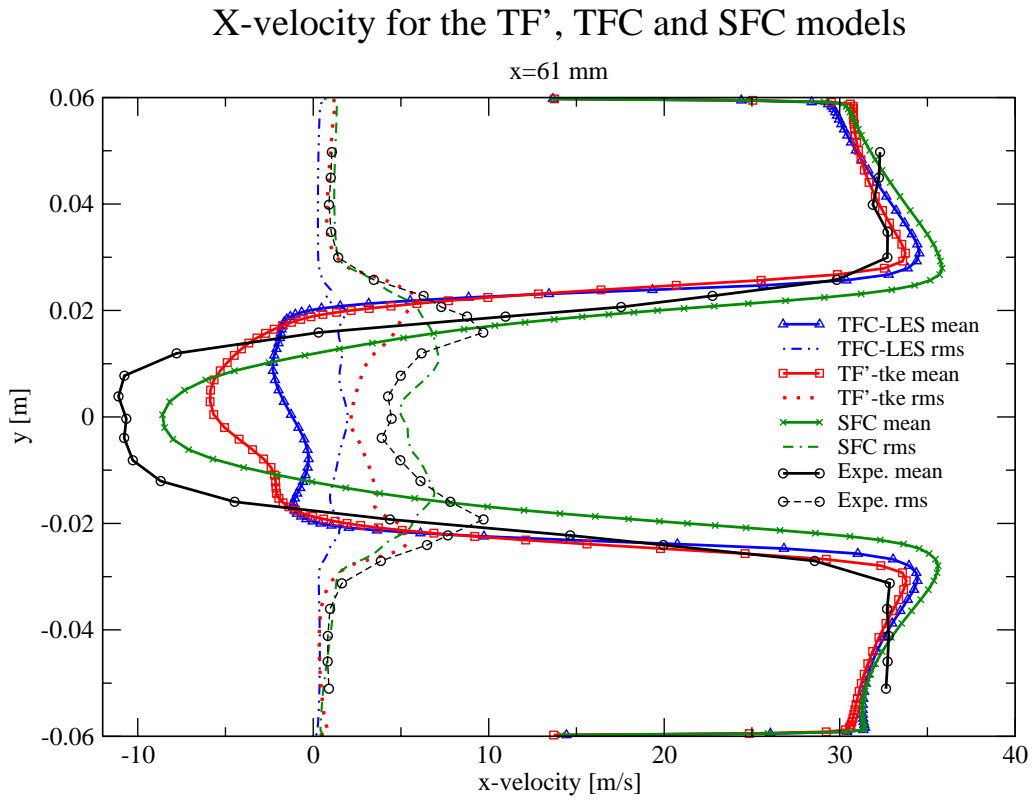


**Fig. 8.7:** Models TFC, TF'-tke and SFC for the Volvo test-rig: axial (top) and transversal (bottom) velocities at section  $x = 61$  mm

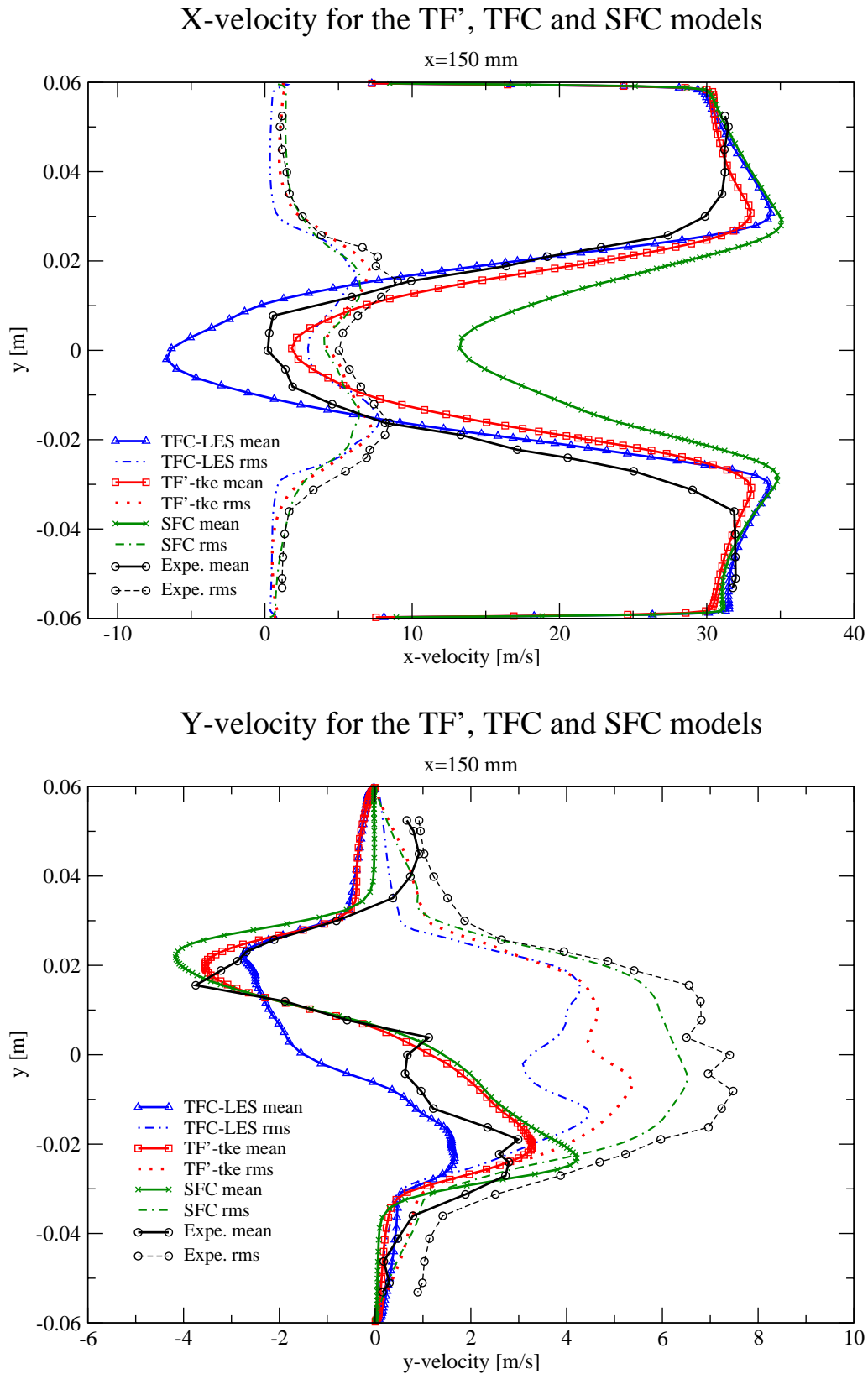


**Fig. 8.8:** Models TFC, TF'-tke and SFC for the Volvo test-rig: axial (top) and transversal (bottom) velocities at section  $x = 150$  mm

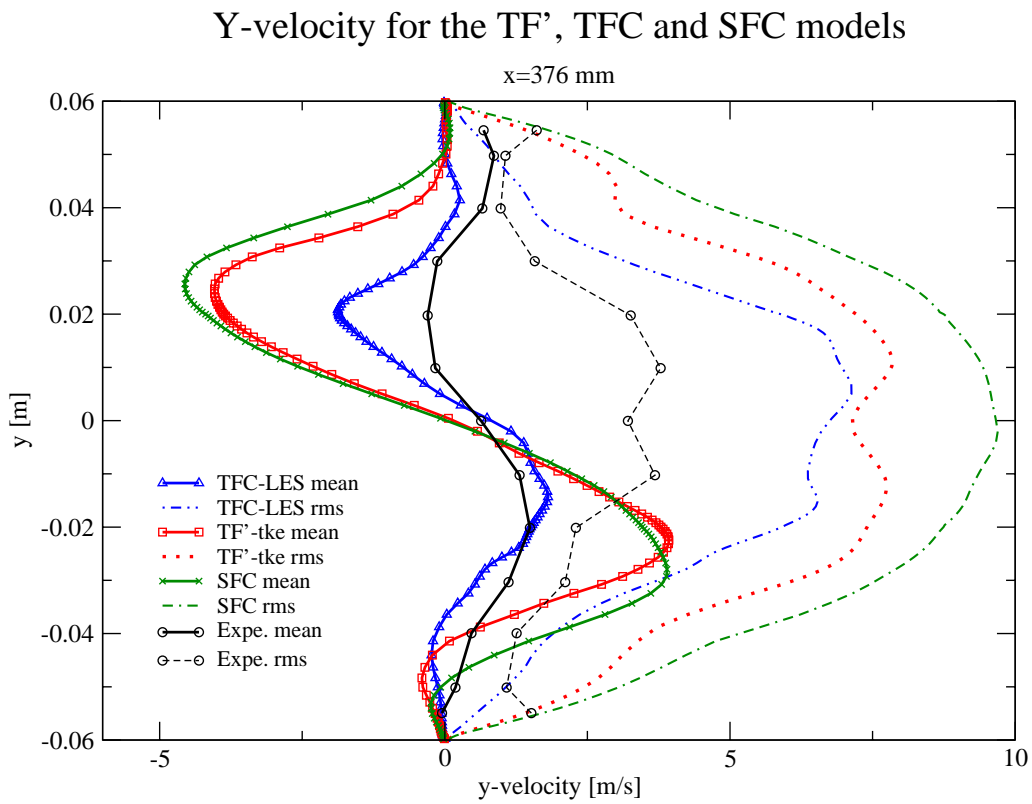
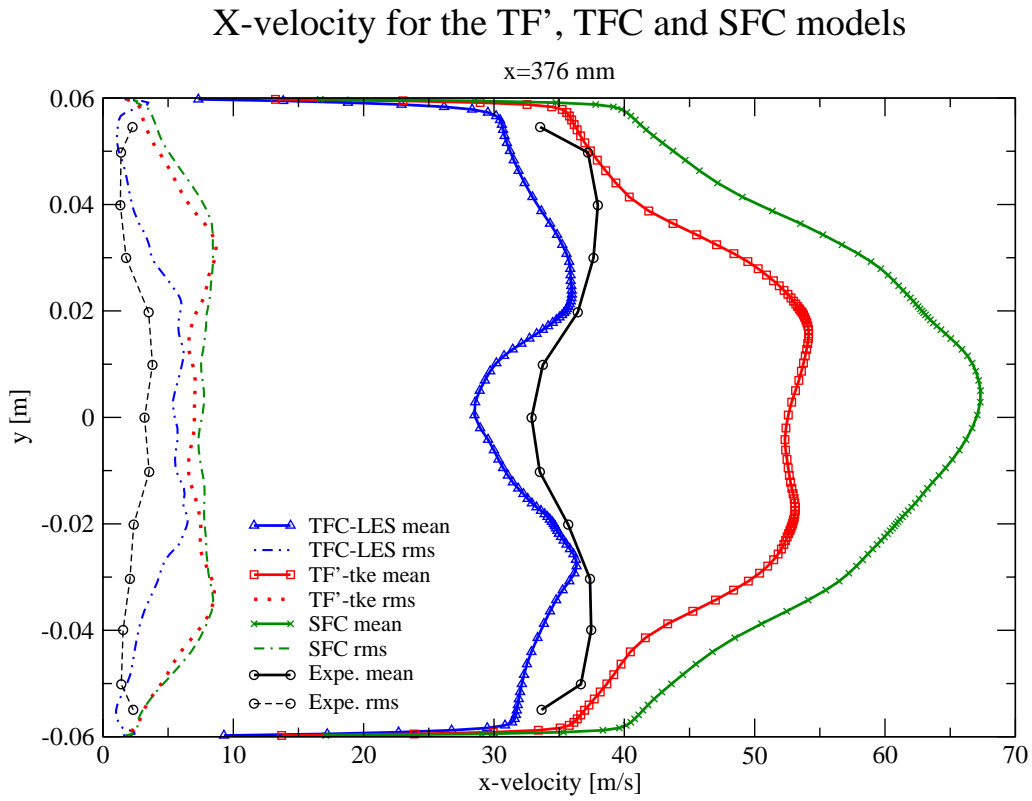


**Fig. 8.9:** Models TFC, TF'-tke and SFC for the Volvo test-rig: axial (top) and transversal (bottom) velocities at section  $x = 376$  mm

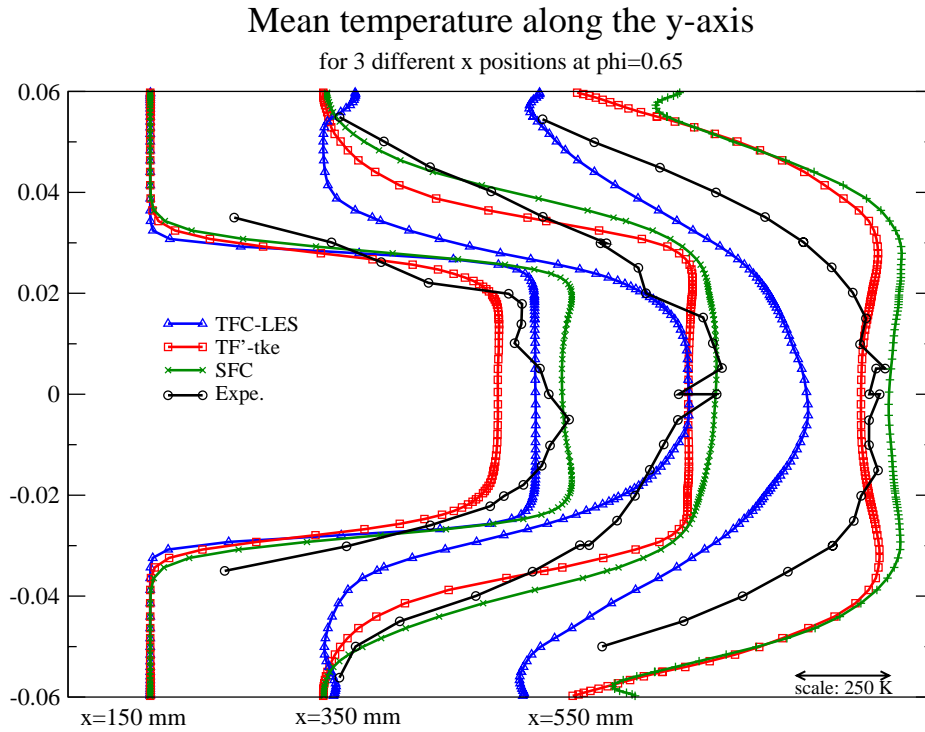


**Fig. 8.10:** Temperature profiles

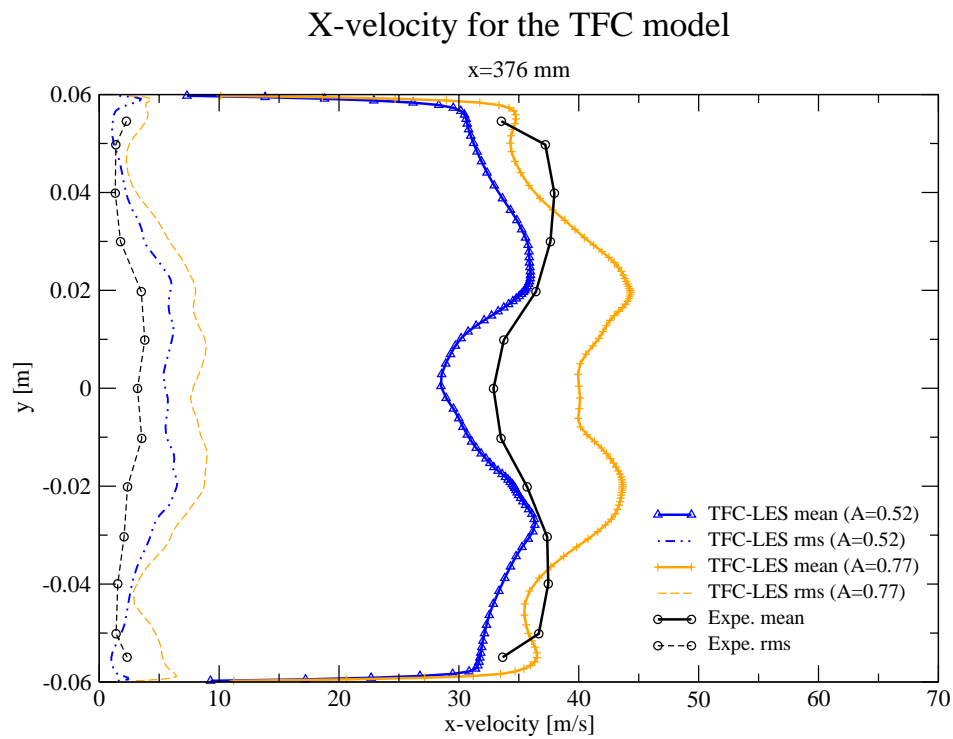


**Fig. 8.11:** Influence of the constant A for the TFC-LES model at section  $x = 376$  mm

## 8.2 Paul Scherrer Institute burner

This burner has already been employed for comparison of several RANS models by Pieringer [Pie02], or a LES model validation by Duwig et al. [DUF<sup>+</sup>06], and a study of flame structure by Griebel et al. [GSS<sup>+</sup>03, GBI<sup>+</sup>05, Sie06]. Non-adiabatic wall boundary conditions are taken into consideration. The cooled walls imply a different treatment of the energy and progress variable equations. An active feedback from the local enthalpy to the progress variable has been implemented for this purpose as detailed in Figure 5.3 (p.81).

### 8.2.1 Experiments and geometry

#### Experimental set-up

This test-rig has been designed for a maximum pressure of 30 bar and a maximum mixture air flow rate of 0.6 m<sup>3</sup>/s, which can be preheated up to 823K. The combustor accepts a maximum thermal power of 400 kW, and maximum temperatures  $T = 1850$  K. The walls are cooled with circulation of air in the liner. The combustion gas is a perfectly homogeneous premixed mixture of methane and air. The flame is stabilized aerodynamically at the passage from the inlet duct to the combustion chamber. The backward facing step generates a recirculation of the burnt gas between the flame and the walls. As depicted in Figure 8.12 (p.157), the duct which constitutes the burner inlet, has a diameter  $d = 25$  mm. The combustion chamber diameter is  $D = 75$  mm, and its length is  $L = 320$  mm.

Concentrations of the species CO, CO<sub>2</sub>, O<sub>2</sub>, NO<sub>x</sub> can be measured with a gas probe located at the exit of the combustor and exhaust gas analysis. Optical measurements with Planar Laser Induced Fluorescence (PLIF) are achieved for the OH and NO concentrations. Transitions of the OH-radical at 285 nm and of OH at 308 nm and 314 nm are collected, as well as the NO transition at 225 nm. Particle Image Velocimetry (PIV) measurements with a spatial resolution of 0.55 mm have been carried out in a symmetry plane by Griebel et al. [GSS<sup>+</sup>03](p. 3), and radial velocity profiles are available for several normal planes. Mean and rms results are computed using 400 samples. Temperature of the exhaust gas are also measured. For more details on the experimental set-up, see Siewert [Sie06](p. 44-55).

#### Experimental results

Different campaigns of measurements (isothermal and with combustion) have been carried out with this burner by Griebel et al. [GSS<sup>+</sup>03, GBI<sup>+</sup>05, Sie06]. The turbulent parameters at the inlet can be modified using four different turbulence grids (two hole diameter 3 and 4 mm, and two blockage ratio 50% and 65%).

Experiments	Isothermal	Combustion
Bulk velocity m/s	20 - 40	40-80
Inlet temperature K	293	673
Pressure bar	1	1-10
Equivalence ratio	-	0.5

**Tab. 8.3:** Experimental conditions

### Flow field

As described by Griebel et al. [GSS<sup>+</sup>03] for the isothermal and atmospheric case, the flow field structure remains the same for different operating conditions. Five main zones can be distinguished as depicted Figure 8.13 (p.158). The *core flow region* corresponds to the jet formed at backward facing step. It is characterized by the highest velocity magnitude and a moderate turbulence intensity. On the side a *recirculation zone* is created where axial velocity is negative. Between the recirculation zone and the core flow region and in the alignment of the duct, a *shear layer zone* is generating turbulence. This zone extends in the radial direction up to  $x/d \approx 5$ . From  $x/d = 5$  up to  $x/d \approx 8$  a *high turbulent zone* is almost completely radially extended and corresponds to the transition from the jet shape to the *dissipation zone* just upwards from the outlet.

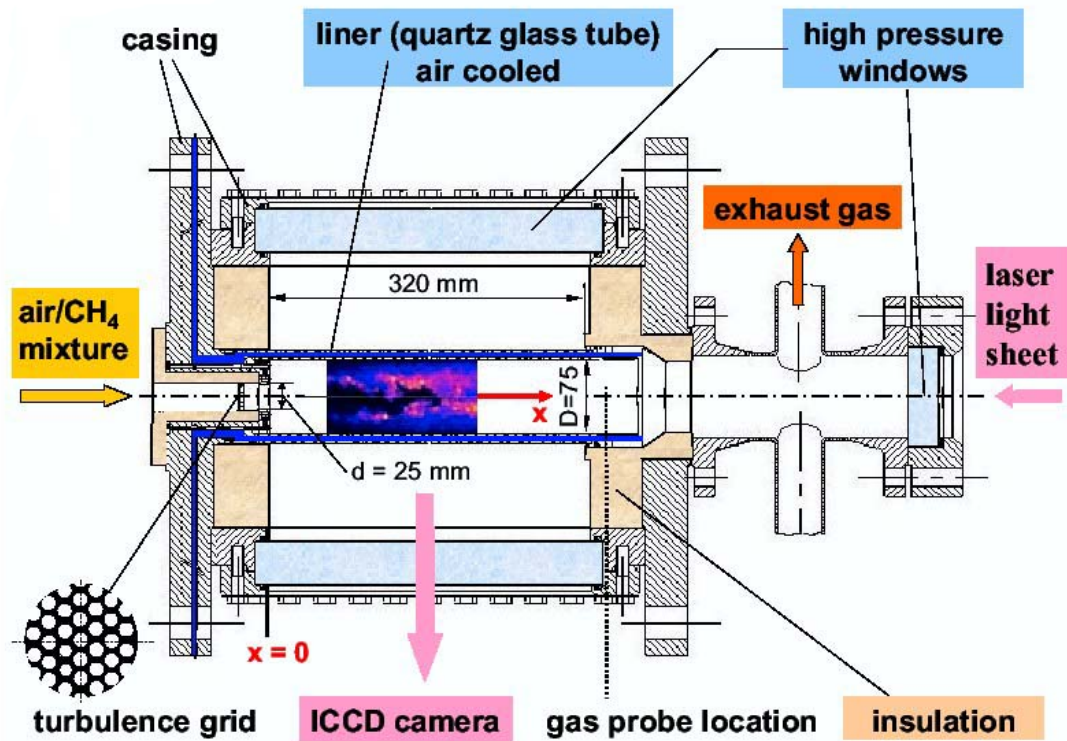


**Fig. 8.12:** PSI burner

### 8.2.2 Modeling and boundary conditions

The simulations are investigated with an inlet velocity  $U = 40$  m/s (mass flow rate 10 g/s), an atmospheric pressure  $p = 1$  bar, an inlet temperature  $T = 673$  K and an equivalence ratio  $\phi = 0.5$ .

#### Domain and mesh

The mesh topology is composed of two coaxial cylinders. The inlet cylinder is 40 mm long, and the combustion chamber has a length of 320 mm like by the experiments. The mesh has been refined to obtain the value  $y^+ \approx 1 - 3$  at walls. To maintain a structured mesh in the whole domain, and avoid the singularity at the axis a squared volume is designed in the center (see Figure 8.14 (p.159) and Sohoni [Soh05](p. 55)). The whole mesh counts 1.8 million cells.

The same *Fluid properties* than for the Volvo test-rig are used, see section 8.1.2 (p.141).

#### Boundary conditions

There are three types of boundary conditions for this domain. The inlet is modeled with the option “velocity inlet”, the outlet with the “pressure outlet” option and the structure walls with “wall” option from *Fluent* 6.2. The parameters for the UDS scalars, as well as the turbulent parameters, differ according to the combustion model. Simulations with

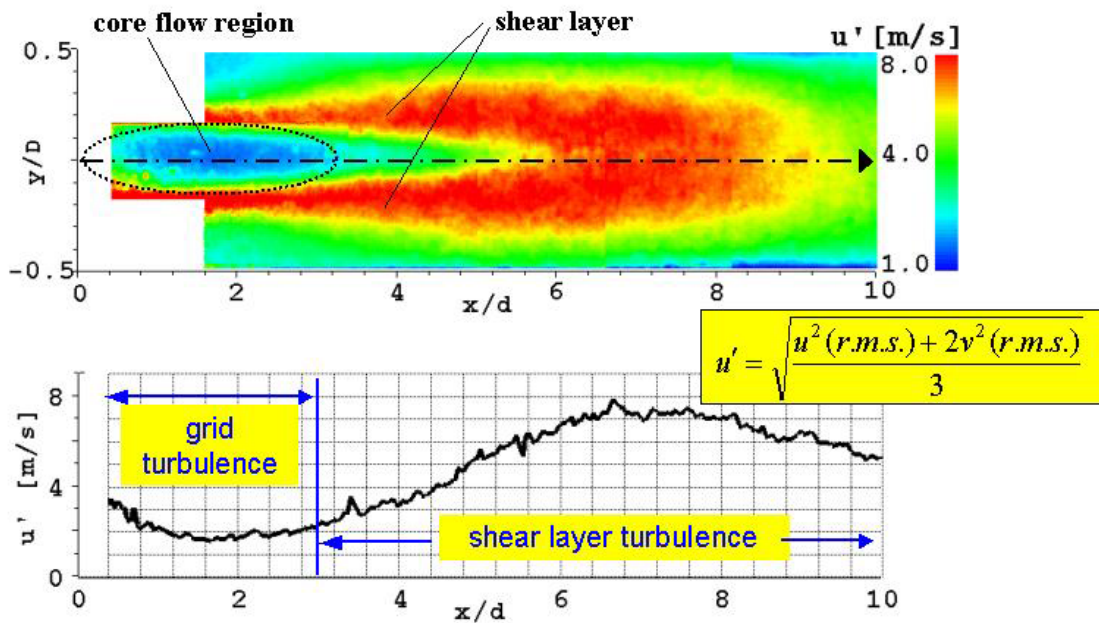


**Fig. 8.13:** Flow structure (cold flow) [Gri05, Soh05]

Boundary condition	Parameter	Value
Inlet	Velocity inlet	
	Velocity	40 m/s
	Temperature	673 K
	Turbulence intensity	10%
	Integral length scale	4 mm
	subgrid tke	$10 \text{ m}^2 / \text{s}^2$
Outlet	Pressure outlet	
	Gauge pressure	0 Pa
	Backflow Temperature	1383 K
	subgrid turbulence intensity	3 %
Walls	Wall with thermal condition	
	Temperature	673 K

**Tab. 8.4:** Flow boundary conditions for the PSI burner

the TFC-LES model have been achieved with the Smagorinsky model, and simulations with the SFC and TF model with the subgrid turbulent kinetic energy transport equation model. The generic flow parameters are given in Table 8.4 (p.159), and the specific parameters, which depends on the combustion model, are listed in Table 8.5 (p.160). Like for the Volvo test-rig (see section 8.1.2 (p.142)), the subgrid turbulent kinetic energy has been slightly overestimated at the inlet.

A constant temperature at the walls has been imposed. Previous simulations have been carried out with a wall heat flux of  $30 \text{ kW/m}^2$ . This value has been calculated according to the global heat loss  $H_w = 22 \text{ kW}$  (according to Griebel, and reported by Sohani [Gri05, Soh05]) exchanged to the cooling fluid divided by the total combustion chamber wall surface  $S_w = 7.54 \cdot 10^{-2} \text{ m}^2$ . Because the combustion does not occur in the vicinity of the walls and because this heat flux is large enough, these simulations have given wall temperature close to the inlet temperature. For this reason, a constant temperature thermal condition has been retained since it is numerically more stable.

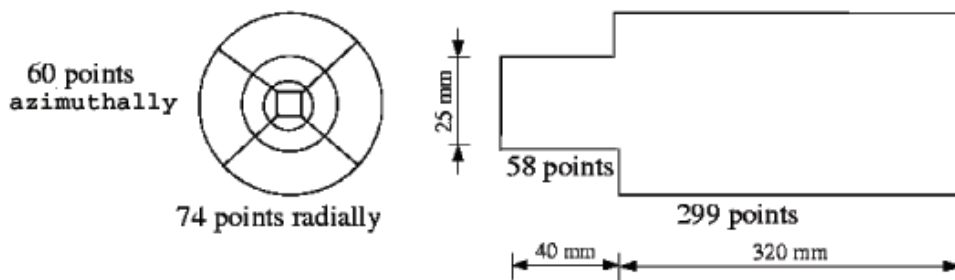


**Fig. 8.14:** Mesh structure

Inlet		
TFC-LES and SFC	UDS-0	$c = 0$
TF	UDS-0	$y_F = 0.0283$
	UDS-1	$y_{CO} = 0$
Outlet and wall		
TFC-LES and SFC	UDS-0	$\frac{\partial c}{\partial n} = 0$
TF	UDS-0	$\frac{\partial y_F}{\partial n} = 0$
	UDS-1	$\frac{\partial y_{CO}}{\partial n} = 0$

**Tab. 8.5:** Boundary conditions for the combustion models, PSI burner

The combustion parameters are imposed with Dirichlet condition (specified value) at the inlet, and with Von Neumann condition (specified flux) at the outlet and walls as indicated in Table 8.5 (p.160).

### 8.2.3 Comparison of the TFC-LES, TF' and SFC models

Profiles of axial and transversal (mean and rms) velocities are compared at five sections:  $x/d = 0, 3, 5, 7$  and  $9$ , with  $d = 25$  mm. Mean values of the progress variable  $c$  are also compared at the same sections. This should demonstrate the capability of the models to predict the position and thickness of the turbulent flame brush.

The three models give fairly good agreement with the experimental results. The flame structure (computed with SFC) Figure 8.15 (p.160) is very folded. Both mean and rms predictions are more satisfying than with the Volvo test-rig. There may be three reasons for this: The relatively finer mesh employed for the PSI burner, the complete 3D-simulation (without periodic conditions), and the configuration of the flame, which is closed.

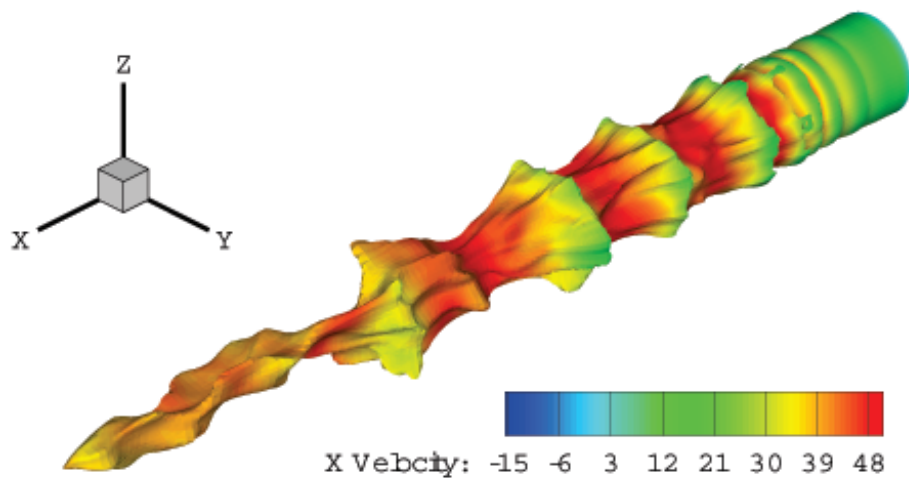


**Fig. 8.15:** Flame structure: iso-value  $c = 0.5$  colored with axial velocity

The TF' and SFC models predict more precise results than the TFC-LES model. In this case, the three models have been computed without changing any model constants. Besides, the experimental results have been collected after computing. This comparison reveals the capacity of each model to deliver accurate results without adapting any parameters.

For the simulations, results have been exported in a two-dimensional plane cutting the cylindrical geometry in *Fluent*. Because of the mesh structure with the square part in the center, *Fluent* is exporting points which are not mesh points, but only intersections of the cutting-plane with the geometry. In order to retain only the mesh points, successive points with a distance smaller than  $\Delta y = 1.15 \cdot 10^{-2}$  mm have been filtered out. This tolerance corresponds to the refinement at the wall. After this procedure, 163 points have been exported for each section. This equals about the actual number of points in a section as depicted in Figure 8.14 (p.159).

Two observations relative to the statistical averaging for the computations, and concerning all sections can be made before detailing the velocity results. The number of samples retained  $n = 400$  to obtain the mean and rms values seem relevant. The rms profiles in both axial and transverse directions are namely fairly symmetrical, which is a good indicator of the statistical post-processing quality. Nevertheless, the mean axial velocities show not perfectly symmetrical results near the walls. Recirculation zones in the vicinity of walls are namely slightly different. It is probably due to a very low-frequency flap oscillation of the recirculation zone compared to the convective time of the burner (see for illustration the computed axial velocity field with the SFC model in Figure 8.16 (p.162)). It may be an effect due to the axisymmetrical Kelvin-Helmholtz eddies which develop, see Figure 8.15 (p.160). Unfortunately, this phenomenon has not been further investigated in the experiments. To average completely this phenomenon, a still larger simulation time  $\Delta T \gg 0.04 \text{ s} = 5T_c = 5L/U$  should be required.

#### **Section $x/d = 0$ : Figure 8.17 (p.166)**

Velocity profiles at the exit of plenum are correct for the mean value in the axial direction. Nevertheless, the profile at the center is not precise because of the low level of turbulence at the inlet. This is evident at the radius  $r = 17.5$  mm, i.e. at the section change.

The results for the transverse direction are not convincing. Again rms fluctuations are too low for the simulations.

The discrepancy for the rms fluctuations is probably due to the inlet boundary conditions of *Fluent*. Turbulence seems to be damped in the inlet cylinder before entering the plenum.

#### **Section $x/d = 3$ : Figure 8.18 (p.167)**

The results for this section are quite good for the three models. The maximum mean axial value are correctly predicted. The TFC-LES model does not predict the recirculation zone

near the walls. The SFC and TF' models predict it. The TF' model gives the most accurate profile shape comparing to the experimental profile, with the round form at the center.

The SFC and TF' models also predict quite accurately the axial fluctuations.

The three models deliver the trend for the transverse mean and rms velocity. Again SFC and TF' models give a better agreement for the fluctuations.

Contrary to the section  $x/d = 0$ , the rms fluctuations are better predicted, since the inlet boundary conditions are not acting so much, compared to the high shear stress at the plenum mouth.

### Section $x/d = 5$ : Figure 8.19 (p.168)

The results for the axial profiles are similar to the section  $x/d = 3$ . SFC and TF' models predict fairly correctly the profile in terms of recirculation zone at the walls and maximum values. The TF' model remains more accurate for the shape in the center part. The results of rms fluctuations are also very correct for these two models.

A reason for the better prediction of the flame shape with the TF' model is probably the prediction of the flame position in Figure 8.22 (p.171). For the sections  $x/d = 3$  and  $x/d = 5$ , the TF' model results are much more close to the experimental results than the other two models.

For the transverse results, it seems that the time simulation was not large enough. The mean values are not symmetrical. The TF' model delivers a precise profile in the bottom

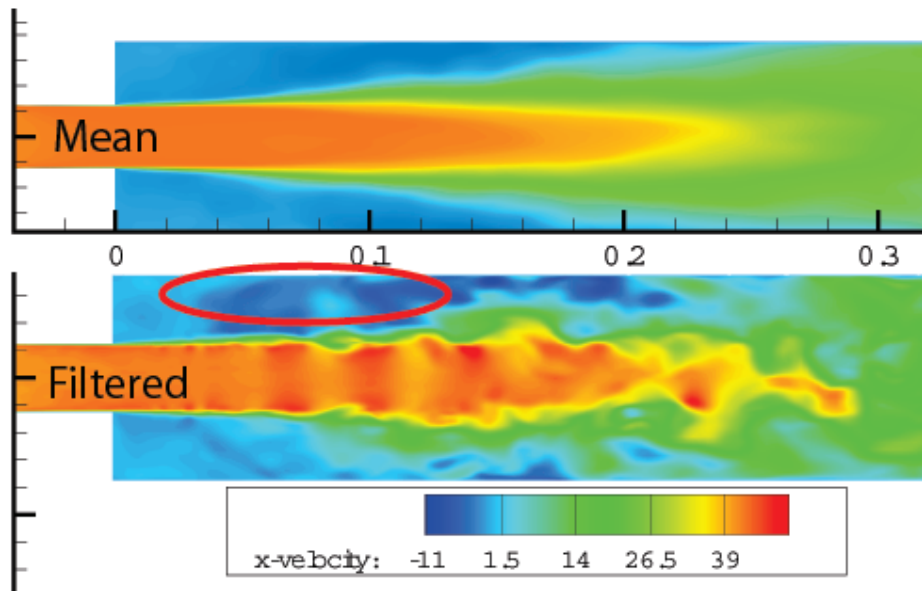


**Fig. 8.16:** Mean (top) and sample (bottom) axial velocity (SFC model); marked zone: Fluctuating recirculation zone

part ( $r < 0$ ) but not on the top part ( $r > 0$ ). The SFC model delivers the best trend for the fluctuations.

**Section  $x/d = 7$ : Figure 8.20 (p.169)**

At this section, the mean axial velocity profile with the TFC-LES model is fairly imprecise, although the rms values are correct. The discrepancy with the experiments is due to the combustion model, rather than to the turbulence model. The SFC model gives the most accurate mean and rms axial profiles, even if the TF' model results remain closer to the experimental results near the walls.

The SFC model gives also the best predictions for the transverse velocity. The mean velocity trend is well predicted.

**Section  $x/d = 9$ : Figure 8.21 (p.170)**

This last section confirms the previous comments. The SFC model predicts very accurately the mean axial velocity profile shape, and fairly correctly the trend for the transverse direction.

The TFC-LES model overpredicts the axial velocity at the axis, whereas the TF' underpredicts it.

The axial rms fluctuations display more discrepancy than in the previous sections. The most correct predictions are given by the TFC-LES model, although it has been employed with the Smagorinsky turbulence model. In the transverse direction, the SFC model delivers the most exact trend.

**Flame position, progress variable: Figure 8.22 (p.171)**

For the experiments, results of the progress variable with  $p = 1$  and  $p = 5$  bar are displayed. During the experiments, better measurements have been namely obtained with the case  $p = 5$  bar than the case  $p = 1$  bar, because of too high signal intensities and consequently reflections in the latter case. Generally for this burner, the pressure has not given any influence on the flame position as mentioned by Griebel [Gri06], so that position of the experimental flame at  $p = 5$  bar is taken as reference.

For the TF' model, the progress variable has been directly calculated from the mass fraction of methane according to Eq. (5.2) since the mixture is perfectly premixed.

The profile for the progress variable has been partially described by comparing the velocity profiles. The discrepancy at  $x/d = 0$  between models and experiments is due to the fact that computational results have been exported 2 mm downstream. For the sections  $x/d = 3$  and  $x/d = 5$ , the TF' model is the most accurate. The slant of the progress variable against the radius, and therefore the brush thickness, is the most exact for this model.

For the sections  $x/d = 7$  and  $x/d = 79$  the SFC model is more precise. Like for the Volvo test-rig, it seems that the TFC-LES model with the default constant  $A = 0.52$  predicts too low reaction rates in the burner. The value of the progress variable is namely fairly small compared to the experimental results. The SFC benefits from its better prediction of the flame for the last sections, as already commented for the velocity profiles.

With the observation of the computed mean and rms temperature fields in Figure 8.23 (p.171) and Figure 8.24 (p.172), the position of the flame front and the brush thickness can be qualitatively compared between the models. The three models deliver very different results. The TFC-LES tends to deliver a similar distribution shape to the SFC model, but translated downstream. It is the reason for the imprecise flame position with the TFC-LES model. The distribution of the reaction rate is not correctly placed. The TF' and SFC models give maximum values in the same zone, but of different intensities. Actually, the experimental results seem to deliver similar results as the SFC model [GBI<sup>+</sup>05](p. 5) [Sie06](p. 71, spatial distribution of the flame front). The temperature has not been measured during the experimental campaign. Nevertheless, the OH-detection is a good indicator for the position of the flame front, and qualitatively comparable to the temperature fluctuations in Figure 8.24 (p.172).

## Conclusion

Generally the most accurate velocity profile predictions have been given by the TF' and SFC models. The TF' model has the particularity to deliver the most accurate mean axial profile shapes (notably near the center  $r < 20$  mm), but slightly underpredicts the velocity at the axis after the section  $x/d = 5$ .

The transverse mean and rms velocities are better predicted by the SFC model. The TF' model predicts the correct trends, but tends to overestimate the peak values. The SFC model predicts in a better way the heat release distribution, which influences the position and thickness of the flame brush.

The TFC-LES model deliver reasonable results, but less precise than the two other models. Like in the Volvo testcase, it also tends to predict too low reaction rate, and at least not correctly placed. The progress variable is largely smaller than one, whereas the experiments predict an almost complete burnt mixture at  $x/d = 9$ : The predicted flame is too long.

A reason for this might have been the fluctuation values, since the TFC-LES have been computed with another turbulence model than the SFC and the TF'. The TFC-LES combustion model namely predicts a reaction rate which scale with  $u_{sgs}$ . Actually, it must not be the reason. The fluctuations values are namely the most precise compared to the experiments (and also very close to the ones predicted by the other models), where the reaction rate is even too reduced. Again, the TFC-LES model has been not simulated with the tke transport equation model, because the flame has propagated upstream in the inlet. This implies that the constant  $g_{cr}$  should be also adapted according to the turbulence model.

The turbulence models have less influence on the flow structure than the combustion model. This has already been demonstrated in section 8.1.3 (p.144) for the validation of the

TF' model, where both turbulence models have been employed. Reciprocally, an interesting task should be to evaluate how the turbulence model itself, through the prediction of the flame, is influencing the fluctuations of the flow.

As a conclusion for the PSI testcase, the SFC model has delivered the most precise results without tuning parameters. This global result is probably due to an overall more accurate prediction of the heat release. Compared to the TFC-LES model, less reaction rate is produced at the section change, and more downstream with the presence of larger eddies.

The TF' has also given fairly exact predictions. It slightly underpredicts the axial velocity downstream in the burner. Its profile shapes are nevertheless more precise, and round at the axis like for the experiments. It cannot be due to the fluctuation predictions since the results are very similar with the SFC. This is maybe an effect of the dilatational effect which is suppressed thanks to the complex procedure based on the rotational operator.

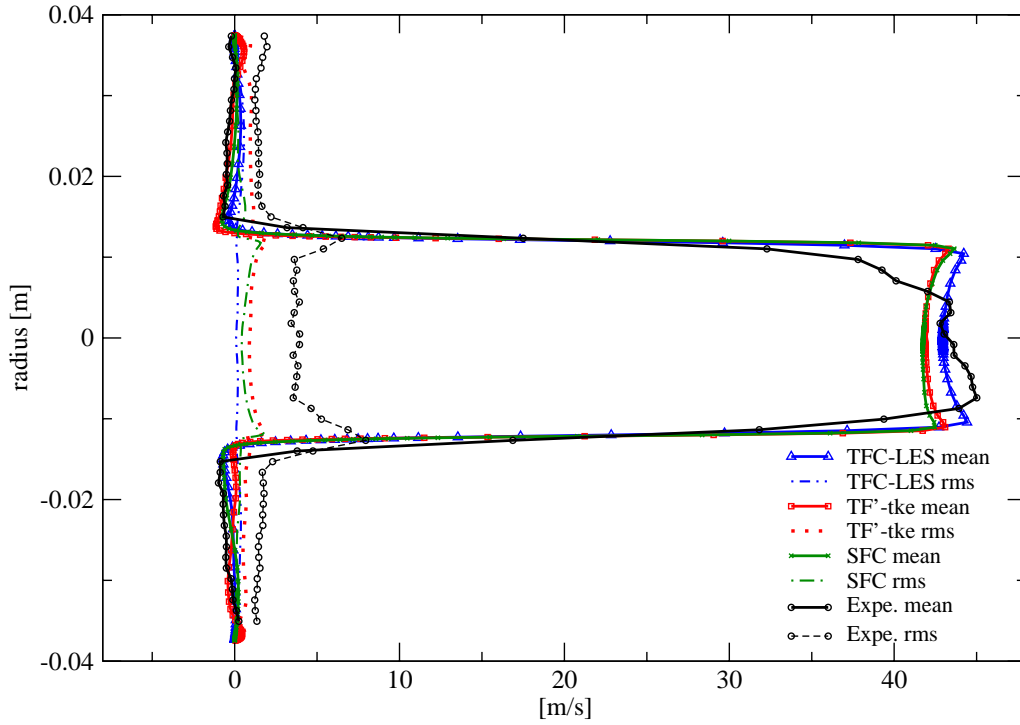
#### 8.2.4 Comparison with other LES simulations

Duwig et al. [DUF<sup>+</sup>06] have numerically investigated the same PSI burner configuration ( $p = 1$  bar,  $T_u = 673$  K) with the LES combustion model presented in section 3.4.3 (p.55). Unfortunately they have essentially considered the isothermal solution. Their reactive results have just been compared to the isothermal numerical mean axial velocity profiles, so that no complete comparison of the combustion model against the experimental results appear. Nevertheless it confirms that the flow structure is similar between isothermal and reactive cases (see section 8.2.1 (p.157) and [DUF<sup>+</sup>06](p. 10)). The jet core in the reactive case is just a little wider because of gas expansion.

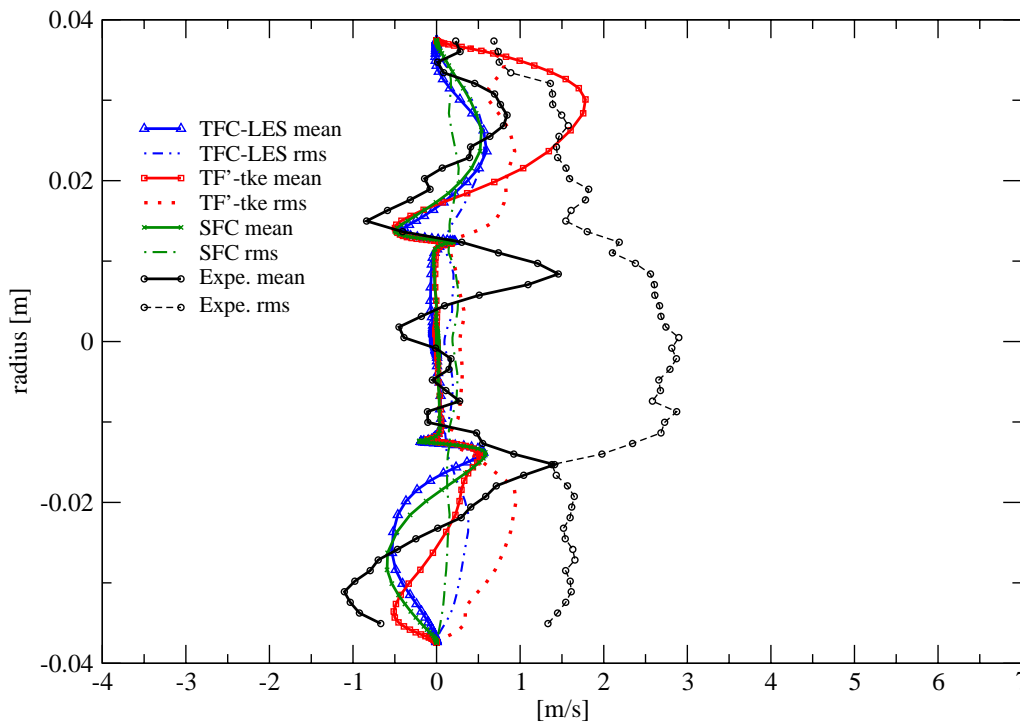
#### 8.2.5 Comparison with other experimental results

The PSI burner has also been experimentally investigated for different pressures. As already cited at the beginning of this part, these results have been used by Pieringer [Pie02, PBP<sup>+</sup>03] for comparison of different RANS models. The TFC-LES and SFC models could be extended in order to model pressure influence, comparatively to the work by Aluri, Dinkelacker and Muppala [MADL05, Kum07] for RANS models with progress variable approach achieved for the project **FortVer**.

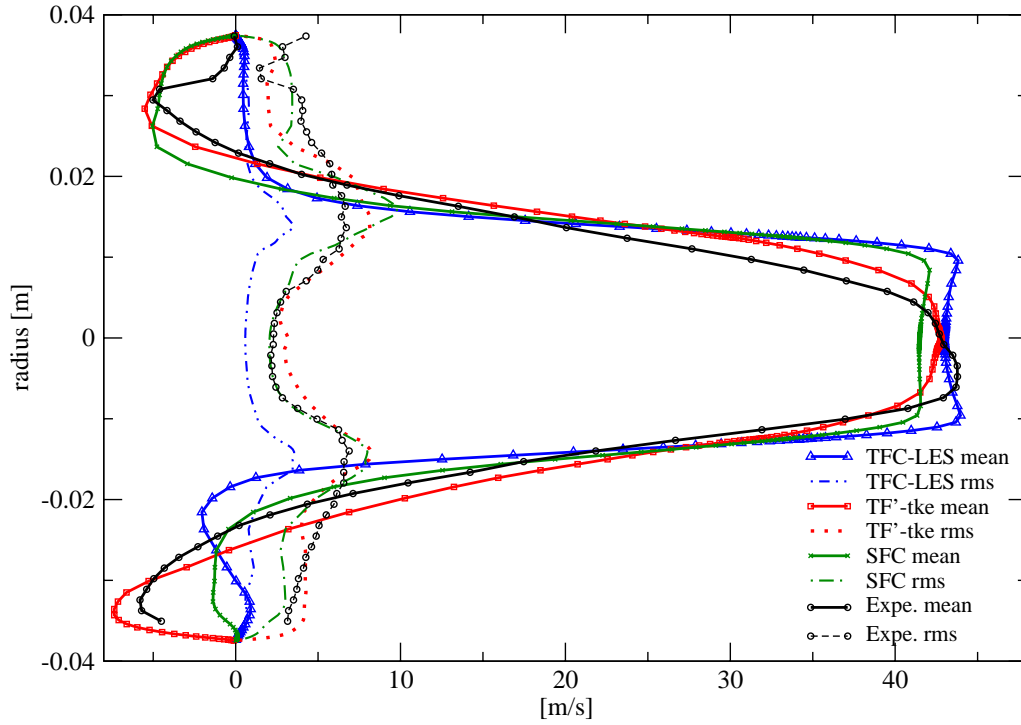
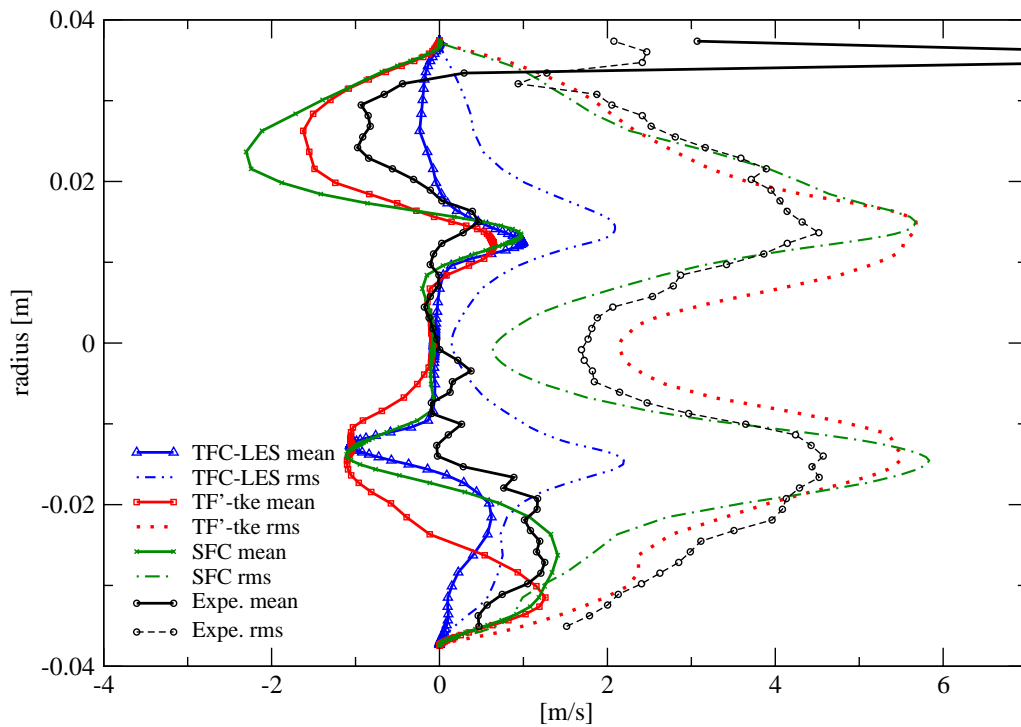
Axial velocity at  $x/d=0$



Transverse velocity at  $x/d=0$

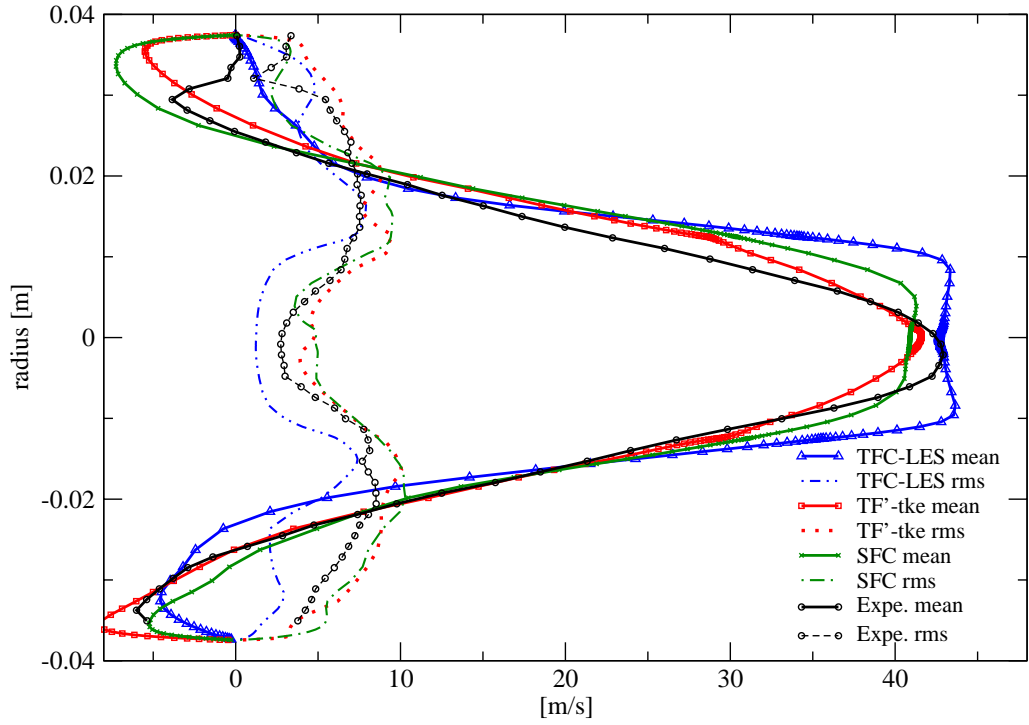


**Fig. 8.17:** Models TFC, TF'-tke and SFC for the PSI burner: axial (top) and transversal (bottom) velocities (m/s) at section  $x/d = 0$ .

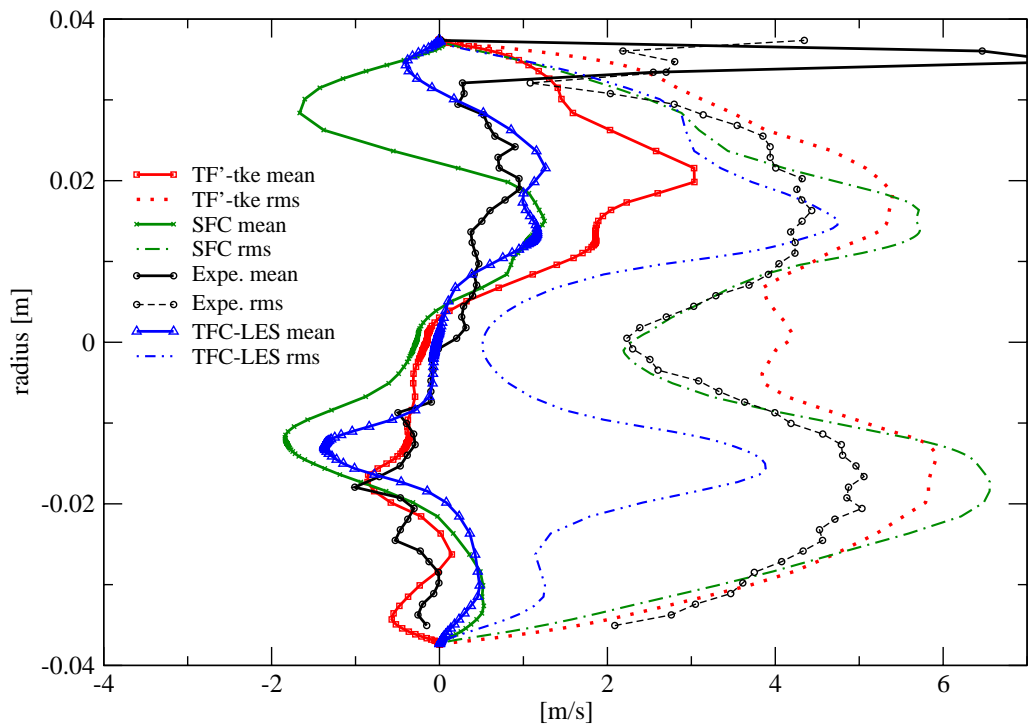
Axial velocity at  $x/d=3$ Transverse velocity at  $x/d=3$ 

**Fig. 8.18:** Models TFC, TF<sup>1</sup>-tke and SFC for the PSI burner: axial (top) and transversal (bottom) velocities (m/s) at section  $x/d = 3$ .

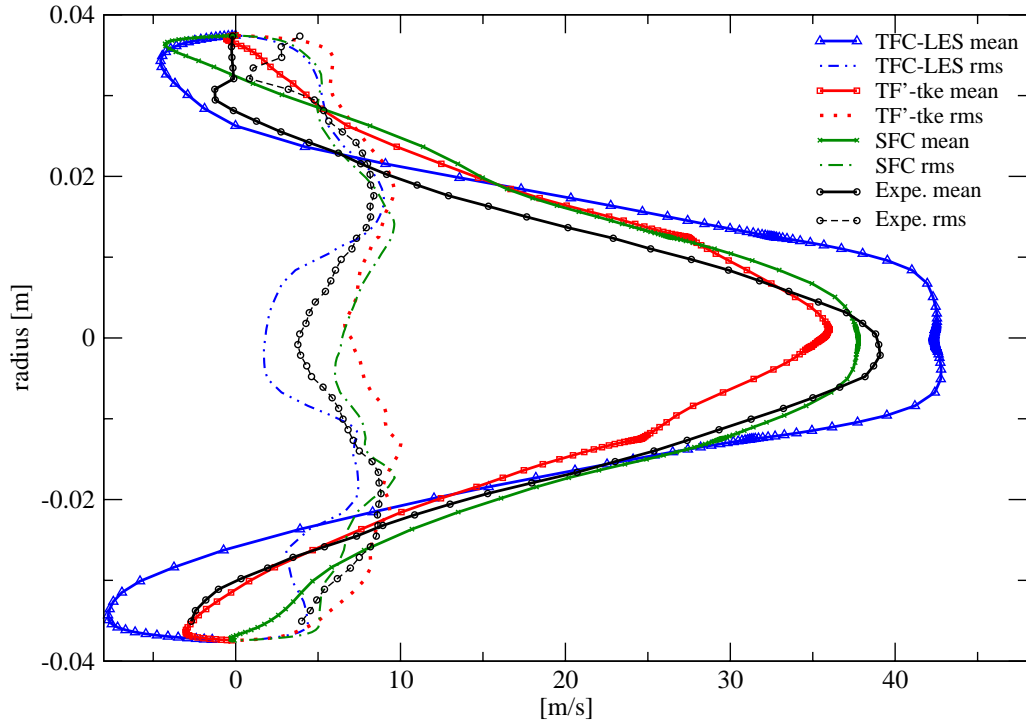
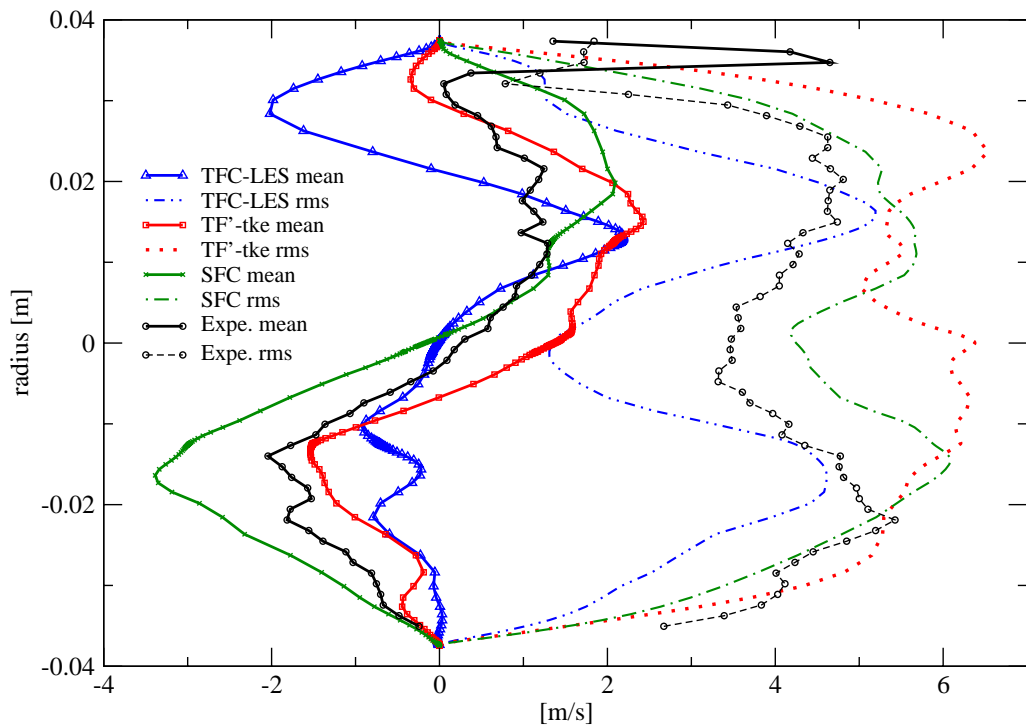
Axial velocity at  $x/d=5$



Transverse velocity at  $x/d=5$

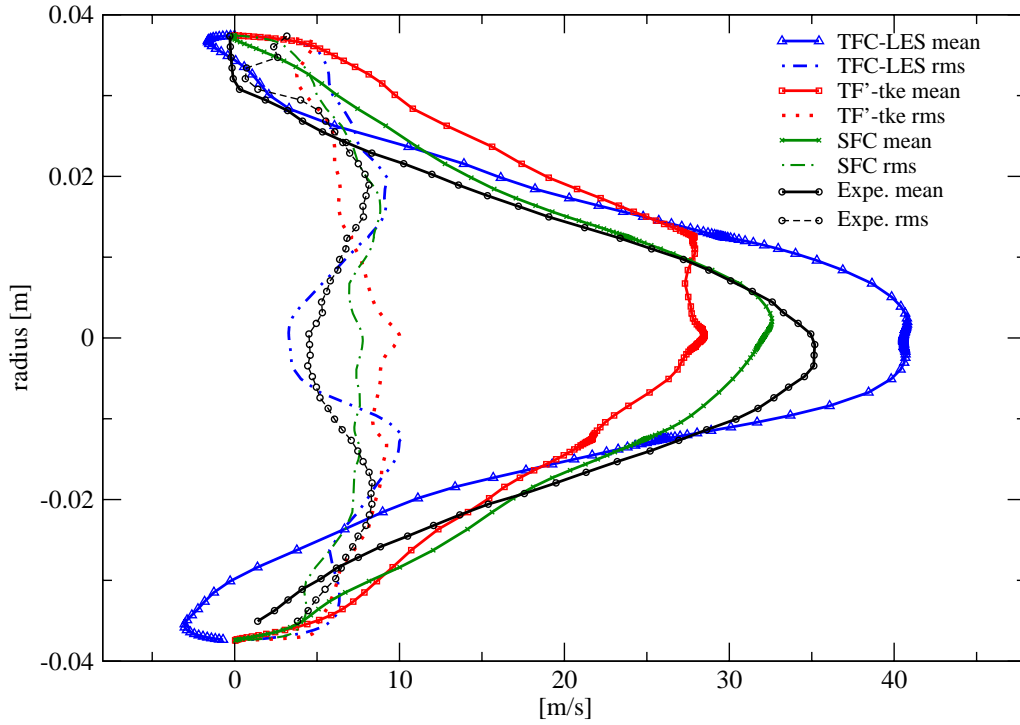


**Fig. 8.19:** Models TFC, TF'-tke and SFC for the PSI burner: axial (top) and transversal (bottom) velocities (m/s) at section  $x/d = 5$ .  
168

Axial velocity at  $x/d=7$ Transverse velocity at  $x/d=7$ 

**Fig. 8.20:** Models TFC, TF'-tke and SFC for the PSI burner: axial (top) and transversal (bottom) velocities (m/s) at section  $x/d = 7$ .

Axial velocity at  $x/d=9$



Transverse velocity at  $x/d=9$

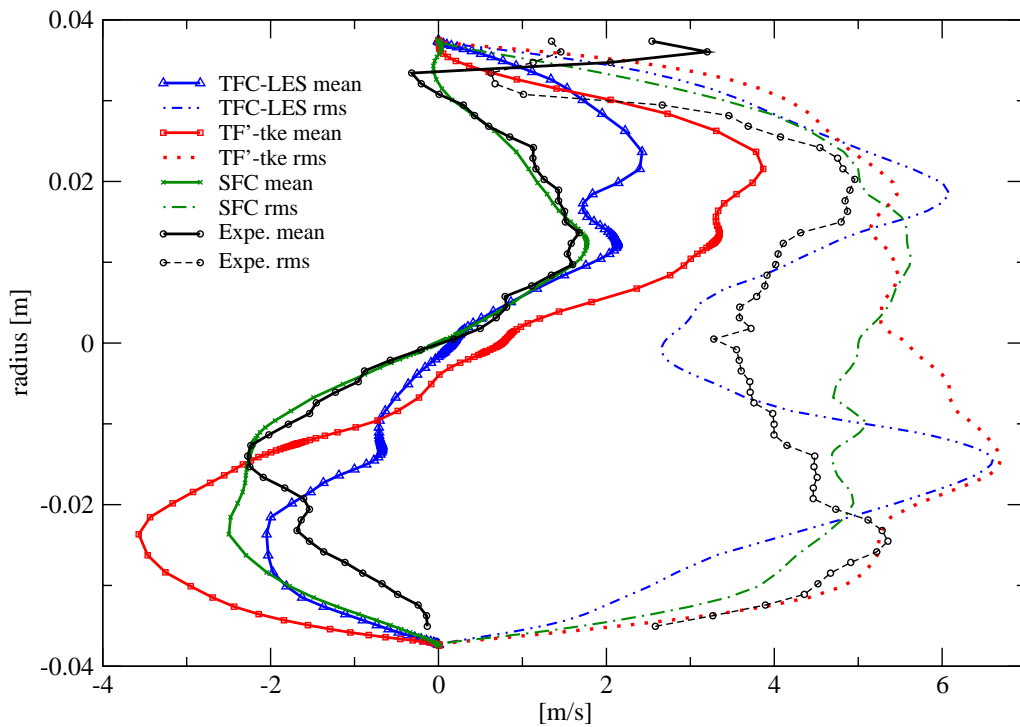


**Fig. 8.21:** Models TFC, TF<sup>2</sup>-tke and SFC for the PSI burner: axial (top) and transversal (bottom) velocities (m/s) at section  $x/d = 9$ .

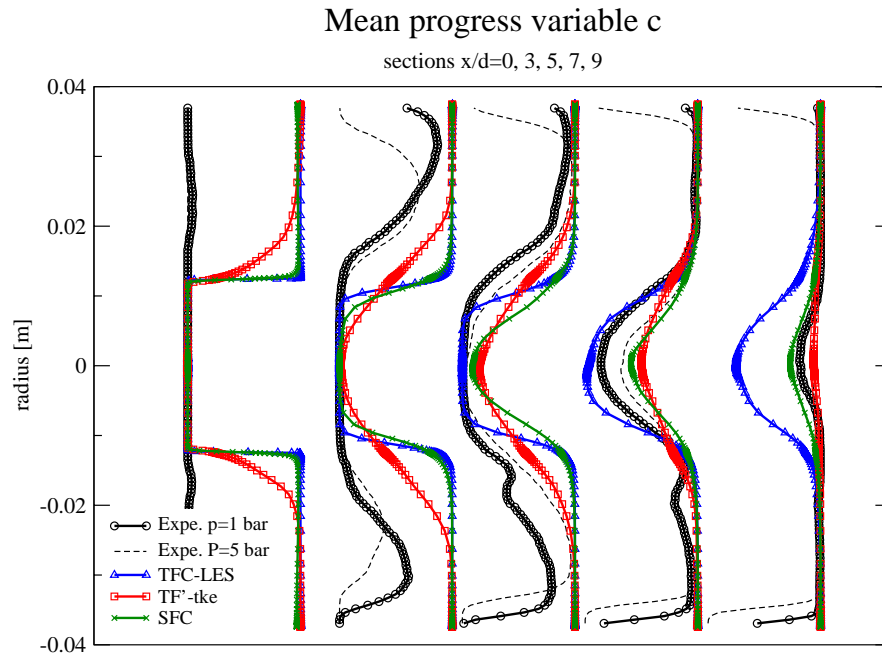


**Fig. 8.22:** Progress variable

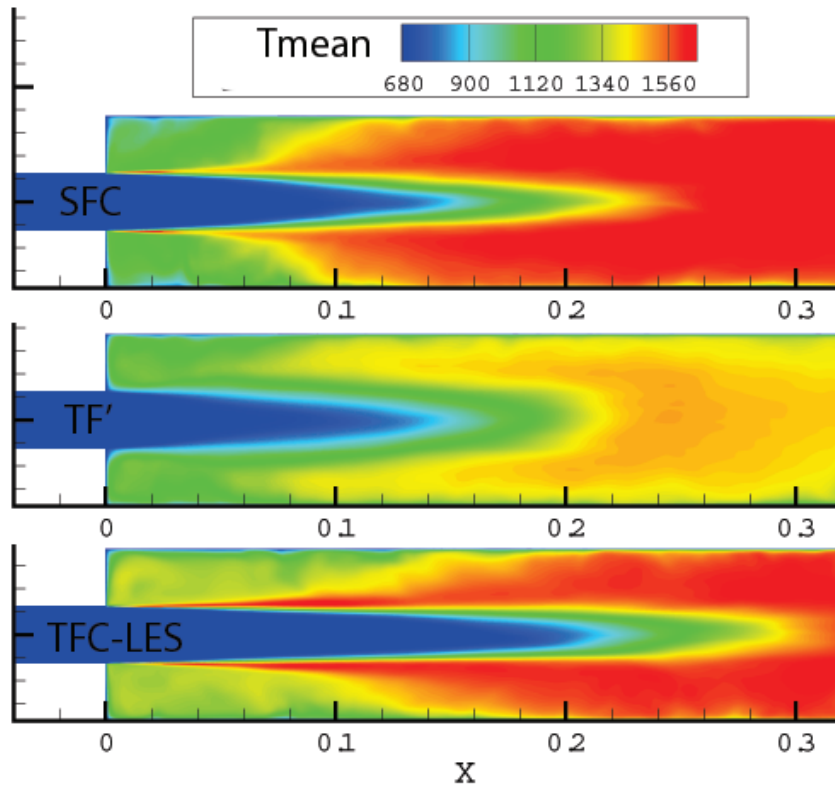


**Fig. 8.23:** Computed mean temperature

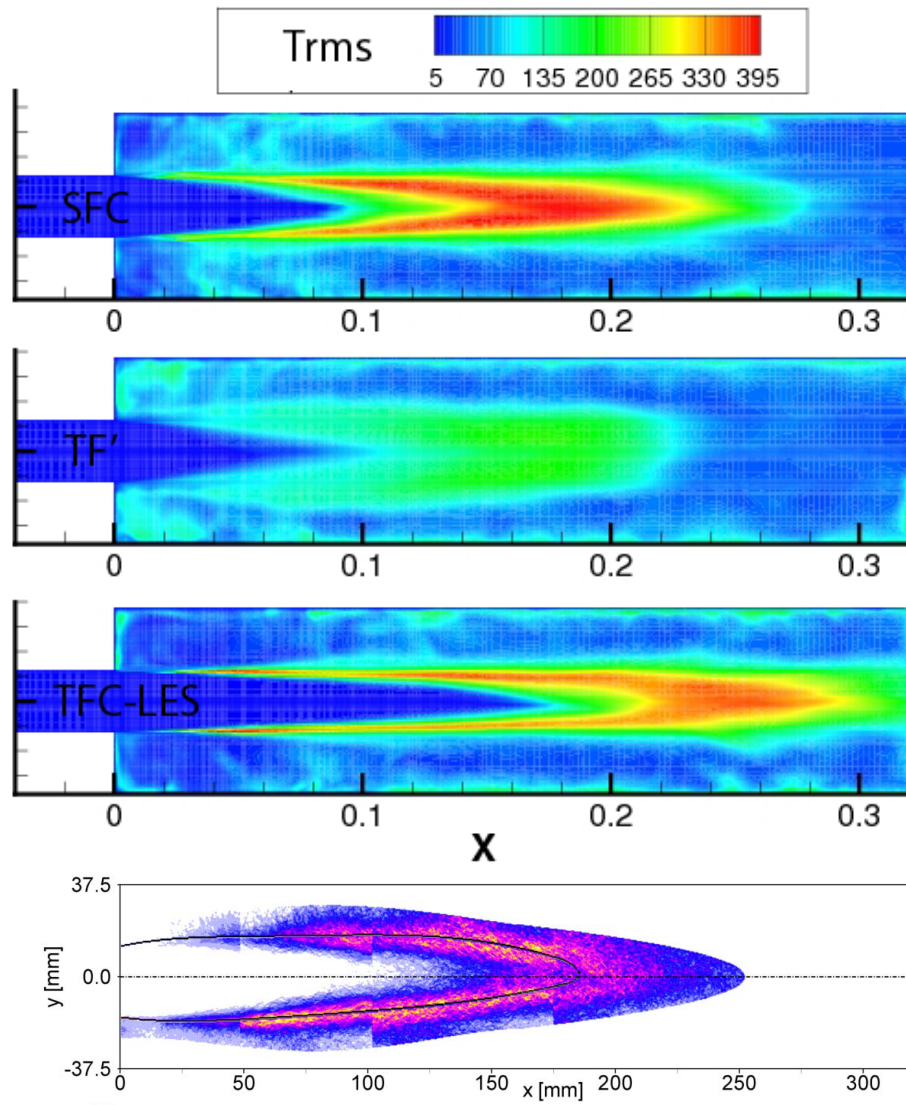


**Fig. 8.24:** Flame front position and flame brush thickness: Computed rms temperature (top), experimental flame front distribution (bottom)

## 8.3 TD1 burner

The TD1 burner is used at the chair of Thermodynamics at the Technische Universität München for the experimental investigation of combustion noise [WWS06, WWS04, WWS05a], and of the heat release spatial coherence for jet and swirl flames by Wäsle and Winkler [WWS05c, WWS05b]. Its modular conception makes the study of flames in closed (for thermo-acoustic study for example), as well as in opened geometries, possible. For this work, unconfined and freely burning flames are investigated. This configuration offers the possibility to validate the TFC-LES and SFC models for inhomogeneously pre-mixed turbulent combustion.

In the first section, the geometry and the setup-facilities are described. In the second section, the computational model and the simulation results are presented.

### 8.3.1 Experiments and geometry

Another advantage of this burner is the presence of the swirler depicted Figure 8.25 (p.174). This swirler is formed of slits which can be partially blocked in order to modify the swirl number. One configuration is considered in the following.

#### Experimental set-up and results

The supply air (with  $\text{TiO}_2$ -seeding for the measurements, which can lead to discrepancy of the reference density) comes from a plenum and goes through the swirler before being injected in the combustor as depicted in Figure 8.25 (p.174). The inner diameter of the nozzle is  $D = 40$  mm, and the diameter of the lance  $d = 16$  mm. The burner can be operated in the range of power 10 – 100 kW, according to the mass flow rate and the mixture property. The configuration considered is a lean methane-air mixture with an equivalence ratio  $\phi = 0.83$ , and a mixture mass flow rate  $\dot{m} = 20$  g/s, which produces 60 kW.

The velocity measurements have been achieved with a high speed PIV system (at repetition rate 1000 Hz). The velocity fields are obtained according to a correlation method. The interrogation area counts  $32 \times 32$  pixels with an overlapping of 50%, so that a spatial resolution of  $\Delta = 1.75$  mm is achieved.

The local density is evaluated after binarizing of Mie scattering images. Particles are injected with the incoming flow with a constant concentration. Unburnt gas corresponds to the high particle concentration, and burnt gas to the low concentration, as a consequence of the thermal gas expansion.

The heat release zones and flame front detection are indicated by the chemiluminescence measurements of the radicals  $\text{OH}^*$  and  $\text{CH}^*$  achieved by Winkler et al. [WWS04, WWS05a].

## Flow field

In the middle region, the recirculation behind the lance allows the flame to stabilize (see Figure 8.27 (p.177)). Since during the experiments the lance temperature does not exceed 500-600 K, the flame is anchored at a thermal quenching distance from about 0.2-0.3 mm (see Lechner [Lec06]). The flame has a length of about 80 mm according to the heat release. There is an entrainment of ambient cold flow essentially from the side. Simulations show that cold flow is also entering the recirculation zone, since the field of mixture fraction  $\tilde{Z}$  displays reduced values.

### 8.3.2 Modeling and boundary conditions

#### Domain and mesh

The computational domain has larger dimensions than the experimental measurement window. The domain length is 120 mm, and its radius 80 mm. The swirler has not been computed to reduce the number of cells and the CPU-effort. 1.8 million cells have namely been employed for the mesh of the opened plenum. Between 1.5 and 2 million cells would be required to mesh precisely the swirler. The advantage for not simulating the swirler is clearly the gain in CPU-requirements. The drawback is that the inlet of the computation is placed directly at the burner exit plane, and can influence the simulations. Mean axial, radial and tangential velocity have been given according to the measurements (realized at 3 mm of the axis) in order to reduce this drawback. An uniform turbulence intensity  $TI = 22.5\%$  has been given at the inlet of the computational domain, according to measurements.

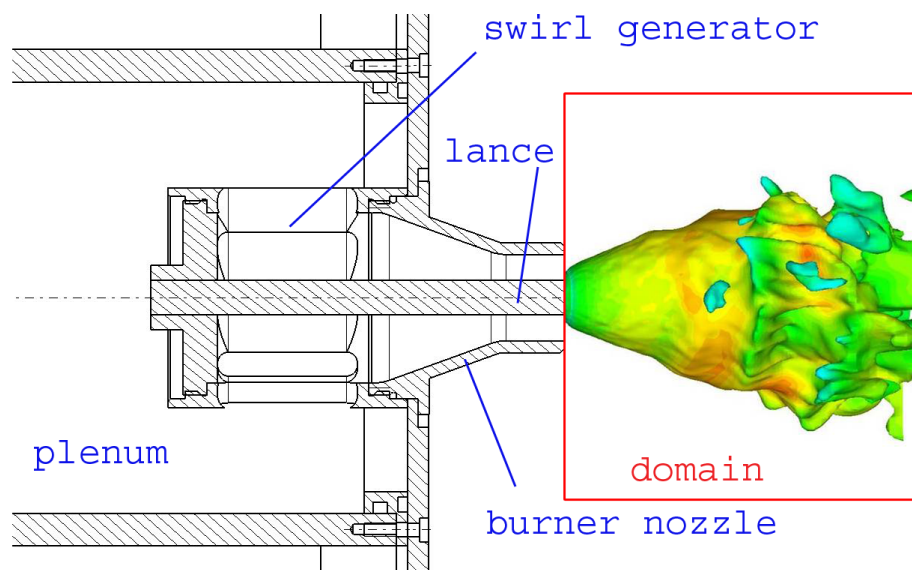


**Fig. 8.25:** TD1 burner (vertical oriented) and computed flame front ( $c = 0.5$ )

The same *Fluid properties* than for the Volvo test-rig are used, see section 8.1.2 (p.141).

### Boundary conditions

Four types of boundary conditions have been employed for this computational domain. The inlet is modeled with the option “velocity inlet” (components of velocity in the three cylindrical directions), the lance with the “wall” option. The bottom part and the two lower thirds of the side are simulated with the “pressure inlet”, since flow can circulate from outside into the domain. The outlet and the third upper part of the side are simulated with the “pressure outlet” option, since flow is likely to go outside of the domain for these parts. The parameters for the UDS scalars as well as the turbulent parameters differ according to the combustion model. Simulations with the TFC-LES model have been achieved with the Smagorinsky model, and simulations with the SFC model with the subgrid turbulent kinetic energy transport equation model. The generic flow parameters are given in Table 8.6 (p.176), and the specific parameters, which depends on the combustion model, are listed in Table 8.7 (p.176).

The combustion parameters are imposed with Dirichlet condition (specified value) at inlet (velocity inlet or pressure inlet) boundary conditions, and with Von Neumann condition (specified flux) at the outlet, pressure outlet and walls as indicated in Table 8.7 (p.176).

### 8.3.3 Discussion

Considering the qualitative results in the vertical plane, the simulations (TFC-LES as well SFC models) capture fairly correctly the structure of the flow, as detailed by Mayerhofer [May06]. The length and thickness (turbulent brush) of the flame are precisely predicted. The velocity fields are also quite identical (see Figure 8.27 (p.177)).

Comparison of the velocity and progress variable profiles let appear the discrepancies.

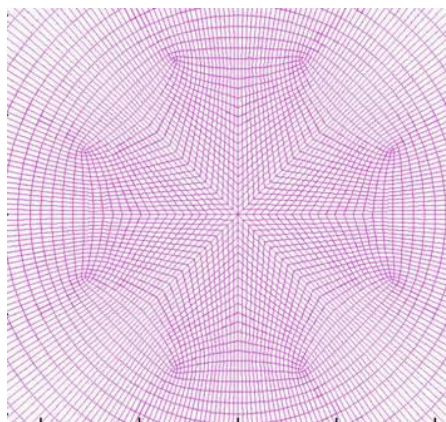


**Fig. 8.26:** Mesh structure at the axis

Boundary condition	Parameter	Value
Inlet	Velocity inlet	
	Velocity components	radial functions (UDF)
	Temperature	293 K
	Turbulence intensity	22.5%
	Integral length scale	4 mm
	subgrid tke	$25 \text{ m}^2 / \text{s}^2$
Side (lower part)	Pressure inlet	
	Gauge total pressure	0 Pa
	Temperature	293 K
	subgrid tke	$1 \text{ m}^2 / \text{s}^2$
Side (upper part)	Pressure outlet	
	Gauge pressure	0 Pa
	Backflow Temperature	300 K
	subgrid tke	$1 \text{ m}^2 / \text{s}^2$
Outlet	Pressure outlet	
	Gauge pressure	0 Pa
	Backflow Temperature	300 K
	subgrid tke	$1 \text{ m}^2 / \text{s}^2$
Lance	Wall with thermal condition	
	Temperature	550 K

**Tab. 8.6:** Flow boundary conditions for the TD1 burner

Inlet		
TFC-LES and SFC	UDS-0	$c = 0$
	UDS-1	$Z = 0.046$
Pressure inlet		
TFC-LES and SFC	UDS-0	$c = 0$
	UDS-1	$Z = 0$
Outlet and wall		
TFC-LES and SFC	UDS-0	$\frac{\partial c}{\partial n} = 0$
	UDS-1	$\frac{\partial Z}{\partial n} = 0$

**Tab. 8.7:** Boundary conditions for the combustion models, TD1 burner

They are displayed at different vertical sections:  $z=7, 18, 28, 45, 66, 86$  and  $107$  mm. The experimental profiles have been translated from  $2$  mm to recover symmetrical results.

**Axial velocity: Figure 8.29 (p.179)**

The mean axial velocity profiles are fairly similar for the TFC-LES and SFC models. The experimental profiles are more rounded in the prolongation of the inlet with larger zones of high axial velocity, particularly up to  $30$  mm. There can be two reasons for this. Turbulence

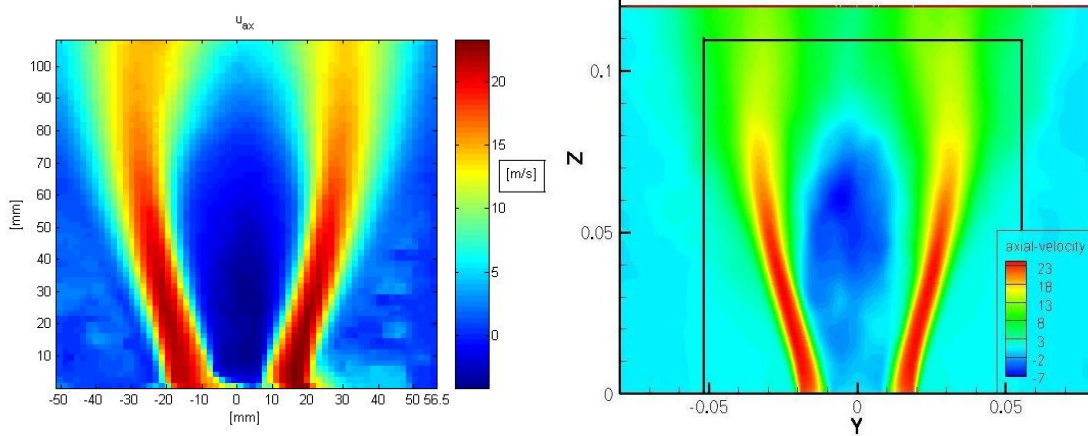


**Fig. 8.27:** Mean axial velocity fields in a vertical plane for experiments (left) and simulations (right)

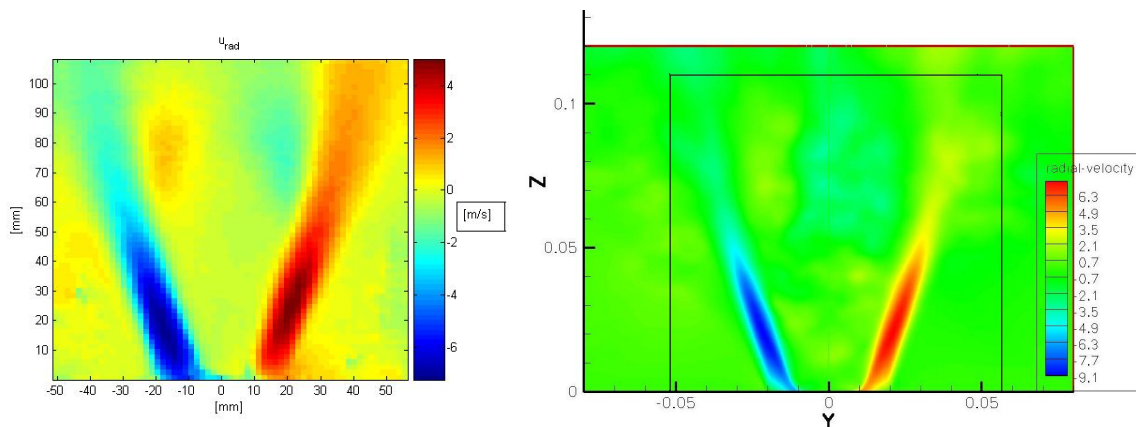


**Fig. 8.28:** Mean radial velocity fields in a vertical plane for experiments (left) and simulations (right)

fluctuations may be too weak for the simulations, so that there is less momentum transfer from a radial position to the other. The second reason can be the relative proportion of momentum between the axial velocity and the radial or azimuthal.

The results for the axial velocity fluctuations tend to demonstrate the first idea. Near the inlet and up to  $z=30$  mm, the simulations predict insufficient level of turbulence. This is particularly true for the radial position  $r=5-15$  mm, where the discrepancy of mean axial velocity appears. The rms values with the models as well as for the experiments are not perfectly symmetric, which is probably due to a too reduced number of samples.

#### Radial velocity: Figure 8.30 (p.180)

Again the two models deliver quasi identical results for the mean radial velocity profiles. They are also very close from the measurements. The qualitative comparison in Figure

8.28 (p.177) stresses the good prediction of the flow structure. The locations with the highest values are well predicted, even if the peak values are underpredicted.

**Progress variable: Figure 8.31 (p.181)**

The profiles from the measurements are relevant up to  $z=66$  mm only. For higher values, the concentration of Mie-particles becomes insufficient to ensure correct binarization, as mentioned in section 8.3.1 (p.173). This is due to the mixture with the ambient air which does not contain Mie, and reduces the Mie-particles concentration. Similarly, values at high radial values are not defined.

The results of simulations are identical for the mean progress variable profile. Compared to the experiments, they predict the correct flame brush thickness, since the slant of the curves are identical for all the profiles (for which the experimental results are relevant). However the simulations deliver a position of the flame with a radial offset. This corresponds to the discrepancy with the axial velocity. The flame front is placed where the radial derivative of axial velocity occurs. In the same way the maximum values of the rms progress variable are offset on the outer direction.

**Conclusion**

For the TD1 burner, the TFC-LES and SFC models deliver similar results. The prediction for the entrainment of fresh air on the side and the strong influence of the inlet boundary conditions are preponderant compared to the combustion model. Qualitative results are very interesting, the flow structure is accurately predicted. Comparison of velocity profiles show some small discrepancies.

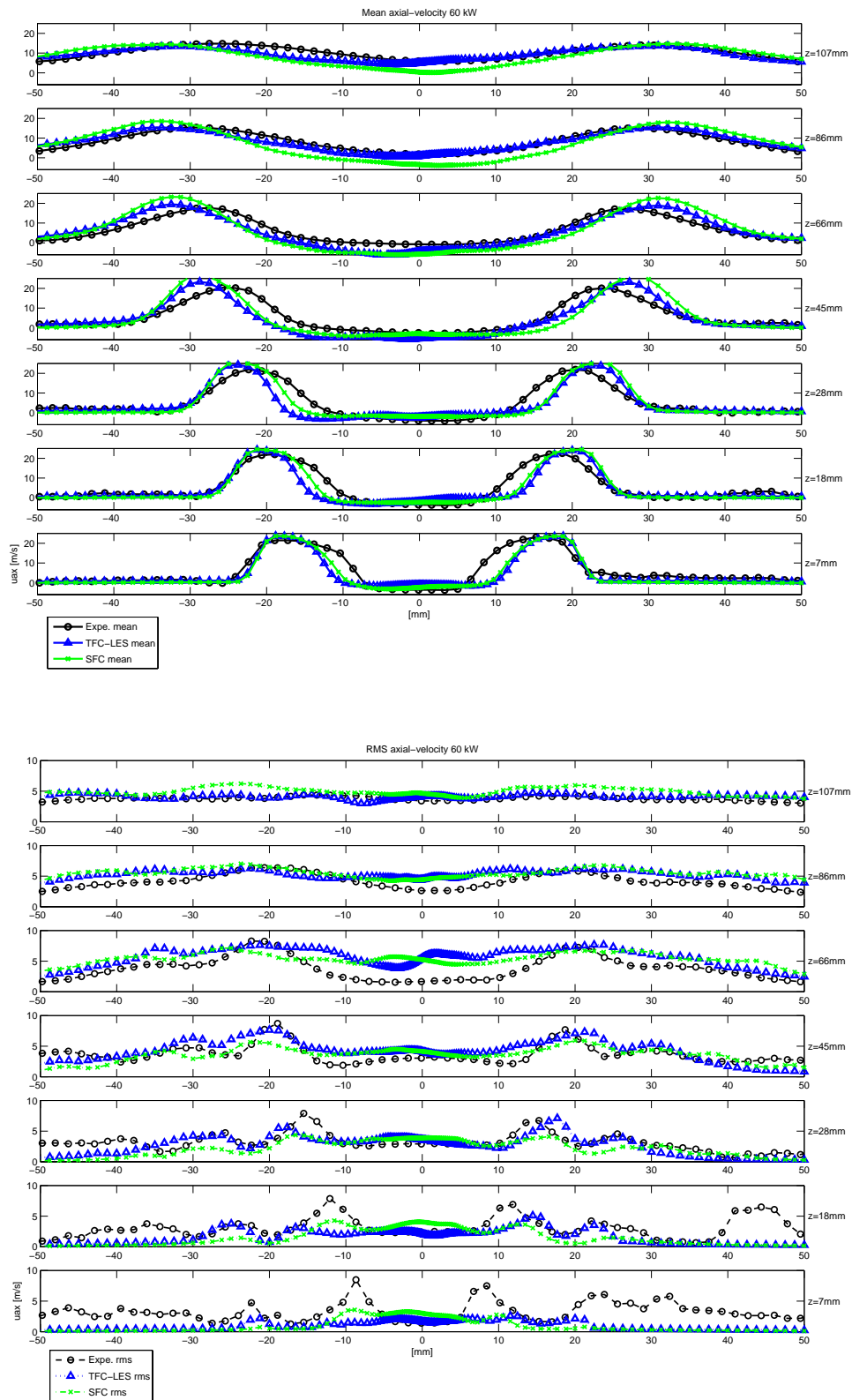
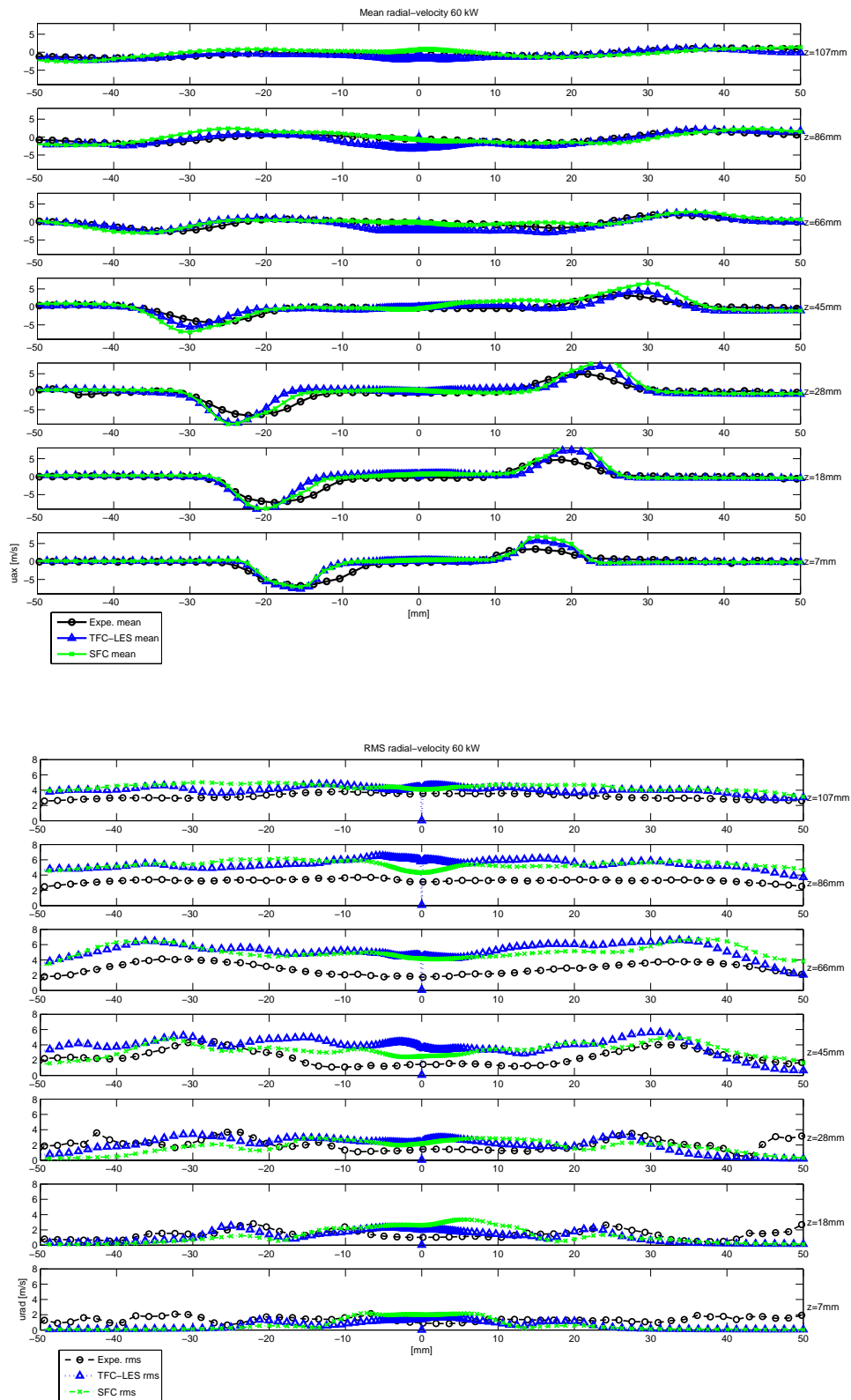


Fig. 8.29: Mean (top) and rms (bottom) axial velocity for different vertical sections



**Fig. 8.30:** Mean (top) and rms (bottom) radial velocity for different vertical sections

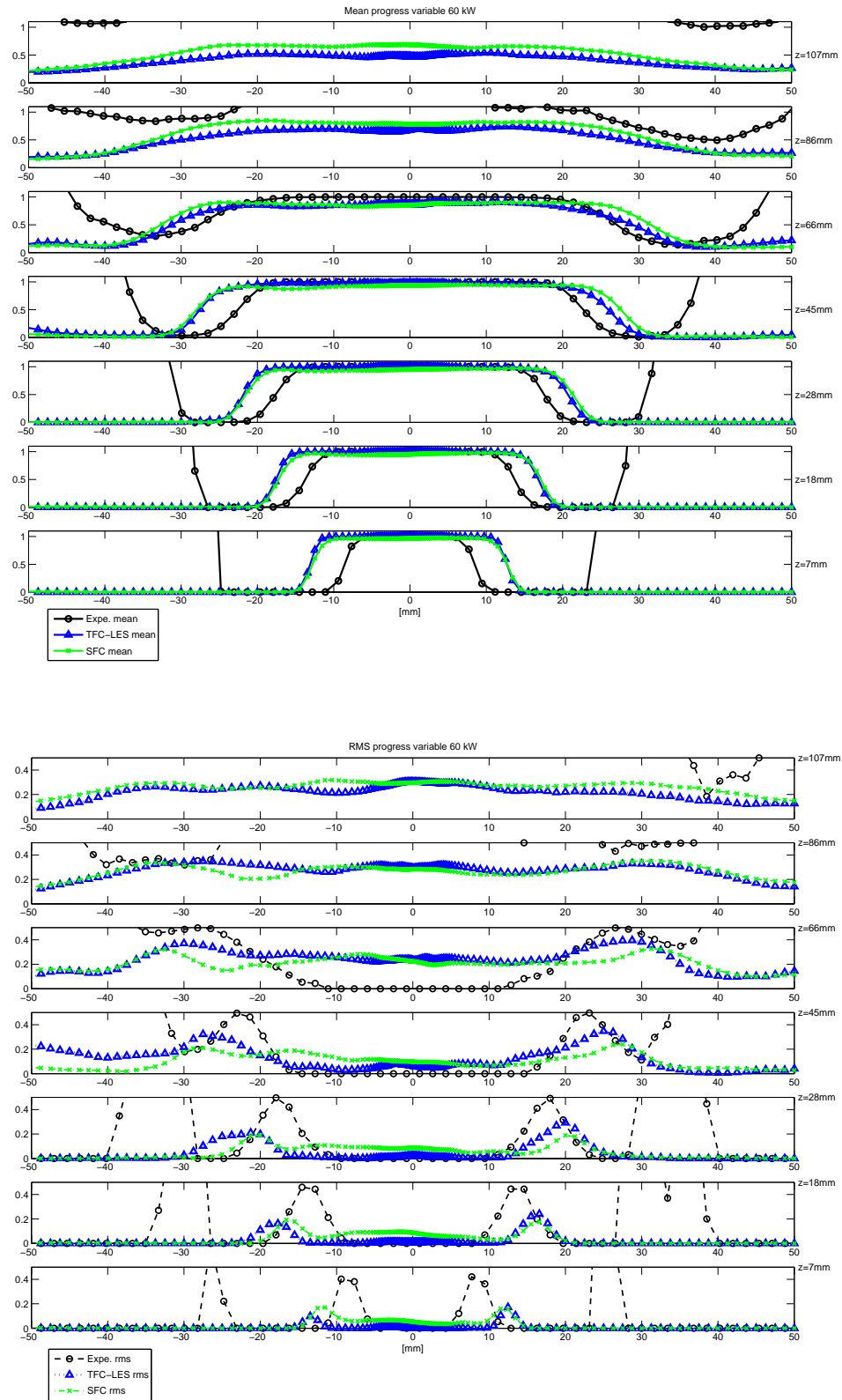


Fig. 8.31: Mean (top) and rms (bottom) progress variable for different vertical sections

## 8.4 Computer requirement

### 8.4.1 Mesh refinement

In this thesis, three models have been computed and compared on three different geometries, so that mesh refinement studies would have been too much time-consuming and CPU-demanding. Goal of mesh refinement studies is to define and select a mesh refinement for which the relative error is *reasonable*. It means that the error remains small compared to the precision improvement that a finer mesh would require, relative to its larger CPU-effort. In case of LES, and particularly with commercial solvers, it is mainly considered that the largest eddies should be resolved with five cells  $\Delta/l_t \leq 1/5$ . This must allow a direct computation of more than 70% of the turbulent kinetic energy, see section A.5 (p.222). For this reason, the three meshes have been designed in order to follow this pragmatical rule. Moreover, the meshes have been refined up to  $y^+ = 1$  at the walls, in order to compute explicitly the viscous sub-layer.

### 8.4.2 Modeling

The simulations have been achieved with *Fluent* 6.2, and different computer systems. As reference, a computational CPU-time is given in Table 8.8 (p.182) with a SUN Fire X4100 Block 4 Opteron-CPU's 2,4GHz for the PSI Burner. For this case, four transport equations for the flow have been solved. One additional transport equation has been solved for the turbulent kinetic energy with the SFC and TF' models. One additional scalar transport equation has been solved for the progress variable with the TFC-LES and SFC models, and two for the species with the TF' model. It appears that each additional scalar transport equation costs 10 % CPU-time, making the TF' and SFC models slightly slower than the TFC-LES model. The difference is particularly noticeable for the data-storage. A file for the TF' model is about 50 % larger than one of the TFC-LES model. Nevertheless, this last statement should be nuanced: More variables have been stored for both SFC and TF' models because of the development in the making. Some of them are not absolutely required to make usage of these two models, so that the effective additional memory requirement is probably 15 % for the SFC model, and 30-35 % for the TF' model.

As a conclusion, comparing both quality results and CPU-requirements, the SFC model justifies its 10-15 % larger CPU-requirement (time and storage) than the TFC-LES, since

model	TFC-LES	SFC	TF'
additional equations	1	2	3
time/iteration [s] (4 CPUs)	10.2	11.1	12.3
relative value [%]	100	109	121
.dat file [Mb]	247	278	367
relative Harddisk requirement [%]	100	125	148

**Tab. 8.8:** CPU-effort with the PSI burner and a 4-CPU cluster

it brings much better predictions. Especially, the SFC model does not require the adaptation of parameters, which makes it more usable for industrial applications. Similarly, the TF' model does not require such parameter adaptations, but costs more CPU-time and memory-capacities. This is due to its formulation based on species mass fractions. The CPU-requirement scales with the precision of the reaction mechanism.



## 9 Conclusion

In the scope of this thesis, LES modeling of inhomogeneously premixed turbulent combustion has been investigated. Chapters 2 and 3 respectively presented turbulent combustion theory and modeling. Chapters 4 to 7 focused on the detailed description of three LES combustion models. The last chapter consisted in validating these three models against experimental measurements for three different burners.

The following tasks have been completed:

- The Thickened Flame (TF) model, which has been largely used with the CFD-solver *AVBP* from *CERFACS*, has been implemented in a commercial solver. This implementation in commercial solvers, being difficult due to its formulation based on a high order derivative term, has only been possible for cartesian meshes.
- A slightly modified version (TF') of the Thickened Flame model, based on a finite volume approach, has been developed and implemented for any mesh structure. It has been validated against the original version TF and experimental results from the Volvo test-rig. Results obtained with the two formulations being similar, it confirms the validity of the TF' version. Numerical results are also comparable with experimental results, this validates the use of the TF/TF' model with a commercial solver.
- In parallel to the species mass fraction approach considered with the TF model, the progress variable approach has been studied. Its formulation for adiabatic perfectly premixed flames has been extended to non-adiabatic and inhomogeneously premixed flames. The non-adiabaticity has required the development of a submodel for thermal quenching, which is based on an enthalpy loss feedback into the progress variable transport equation. The inhomogeneously premixed mixture has been modeled with an additional transport equation for the mixture fraction, and a complemented progress variable transport equation.
- For the progress variable approach, the TFC-LES closure has been used. It has been developed by Zimont with RANS, and applied by Flohr and Pitsch with LES for adiabatic perfect premixed turbulent combustion in the thickened flame regime. It has presently been adapted, implemented and computed for non-adiabatic lean inhomogeneously premixed turbulent flames. Contrary to its RANS formulation, two model parameters have to be adapted, depending on the geometry, mesh and eventually LES turbulence models.
- This drawback of the TFC-LES model has motivated the development of a new model for the progress variable approach. A relevant Subgrid Flame Closure (SFC) has been derived using fractal theory and considering flamelet properties within cells,

for both corrugated and thickened flame regimes. Conjointly, a new submodel for the quenching and bending effect has been developed, according to the estimation of a turbulent chemical time. The dependence of gas mixture on stretch and dynamic perturbations is evaluated in terms of the Markstein number, in order to avoid any other parameter adaptations. However, the estimation of the Markstein number remains disputable in this context, and its use in this submodel may be further investigated.

The three models have been computed and compared to three different burners with mean and rms velocity profile, as well as temperature profile measurements. Comparison of numerical results have shown that:

- Inlet turbulent boundary conditions are difficult to reproduce precisely in commercial solvers. Turbulence introduced with the inlet parameters in the computational domain is often damped a few cells downstream. This has less consequences for the PSI burner and Volvo test-rig than for the TD1 burner. Indeed, for the two first mentioned burners, the flame stabilizes in the shear stress zone, where turbulence is produced. Best results have been obtained with the PSI burner, where the back-step produces intense turbulence, so that the solution is less sensitive to the inlet turbulent parameter.
- SFC and TF' models have given similar results and accurate predictions compared to experimental measurements for averaged profiles, as well as rms profiles. The TFC-LES model has given less accurate predictions. As already explained, it requires adaptation of its prefactor for the turbulent flame speed. Except for the Volvo test-rig, a default value has been used. Actually, a relevant value for the constant may be set, in order to reach the total burning rate in the domain. Nevertheless, the simultaneous adaptation of the parameter for the bending effect would make this task difficult.
- It is often expected that LES modeling have less impact than RANS modeling on results, because with LES only a part of turbulence is modeled. In this work, TFC-LES and SFC models have similar formulation and CPU-cost, but the prediction of the SFC model are much preciser. It demonstrates that the detailed development of this new model was worth, in order to exploit the specificity of LES.
- The comparisons between combustion models (TFC-LES, TF, TF' and SFC) with two different turbulence models (Smagorinsky and turbulent kinetic energy transport equation) have also demonstrated that the combustion model has more influence than the turbulence model. The TF/TF' model have namely given very similar results with both turbulence models. There are slightly more differences when comparing the SFC and TF' models, both computed with the tke transport equation turbulence model.
- The large influence of the combustion model on the flow dynamic is due to density change between burnt and unburnt gas. The position of the flame, and thus the density gradient interact with the velocity field. The prediction of the local heat release

---

distribution is thus very important. This has been stressed by comparing the intensity and location of the averaged and fluctuating heat release (or reaction rate) for the PSI burner. The SFC model has given a very precise prediction for the heat release, and in parallel the most accurate velocity profile and flame position results. Like the SFC model, the TF' model has given a fairly good shape for the reaction zone, but with smoother gradients due to its thickening formulation.

Purposes for future works may be the further validation of the TF' and SFC models. For example, the TD1 burner could be completely simulated with swirler. Indeed, the results with this burner have been strongly influenced with the inlet boundary conditions placed at the exit of the plenum. Nevertheless, this choice has permitted to limit the number of cells to approximately two million. The sub-model for bending-effect and quenching requires also validation on numerous configurations.



# Bibliography

- [AB89] R. G. Abdel-Gayed and D. Bradley. Combustion regimes and the straining of turbulent premixed flames. *Combustion and Flame*, 76:213–218, 1989.
- [ABL88] R. G. Abdel-Gayed, D. Bradley, and A. K. C. Lau. the straining of premixed turbulent flames. In *Symposium on Combustion, The Combustion Institute*, volume 22, pages 731–738, 1988.
- [Arb] Arbeitsgemeinschaft der Bayerischen Forschungsverbände. *abayfor*. <http://www.abayfor.de/>.
- [Bal05] S. Balibar. in *Sciences et Avenir*, Rubrique “Rencontre”. p. 38, Fevrier 2005. Physicien, auteur de “demain la physique”.
- [Bat53] G. K. Batchelor. *The Theory of Homogeneous Turbulence*. Cambridge University Press, 1953.
- [BAY] BAYERISCHER FORSCHUNGSVERBUND FÜR TURBULENTE VERBRENNUNG. *FortVer*. <http://www.abayfor.de/fortver/de/index.php>.
- [BDV05] K. Bray, P. Domingo, and L. Vervisch. Role of the progress variable in models for partially premixed turbulent combustion. *Combustion and Flame*, 2005.
- [BFR80] J. Bardina, J. H. Ferziger, and W.C. Reynolds. Improved Subgrid scale models for Large Eddy Simulation. In *AIAA Paper*, 1980. 80-1357.
- [BGG96] D. Bradley, P. H. Gaskell, and X. J. Gu. Burning Velocities, Markstein Lengths, and Flame Quenching for Spherical Methane-Air Flames: A Computational Study. *Combustion and Flame*, 104:176–198, 1996.
- [Bor85] R. Borghi. On the structure and morphology of turbulent premixed flames. *Recent advances in the aerospace sciences*, pages 117–138, 1985.
- [Bor88] R. Borghi. Turbulent combustion modelling. *Progress in Energy and Combustion Science*, 14:245–292, 1988.
- [Bra79] K. N. C. Bray. The interaction between turbulence and combustion. In *Colloquium on turbulence-combustion interactions*, pages 223–233, 1979.
- [Bra05] M. Brandt. *Beschreibung der Selbstzündung in turbulenter Strömung unter Einbeziehung ternärer Mischvorgänge*. PhD thesis, TU München, 2005.

- [BVBT98] M. Boger, D. Veynante, H. Boughanem, and A. Trouvé. Direct numerical simulation analysis of flame surface density concept for large eddy simulation of turbulent premixed combustion. In *Symposium on Combustion, The Combustion Institute*, volume 27, pages 917–925, 1998.
- [BZB02] T. Brutscher, N. Zarzalis, and H. Bockhorn. An experimentally based approach for the space-averaged laminar burning velocity used for modeling premixed turbulent combustion. In *Symposium on Combustion, The Combustion Institute*, volume 29, pages 1825–1832, 2002.
- [Cam] C. J. Campbell. Association for the Study of Peak Oil&Gas. <http://www.peakoil.net/>. Web resources.
- [CB88] R. S. Cant and K. N. C. Bray. strained laminar flamelet calculations of premixed turbulent combustion in a closed vessel. In *Symposium on Combustion, The Combustion Institute*, volume 22, pages 791–799, 1988.
- [CCO06] E.-S. Cho, S. H. Chung, and T. K. Oh. Local karlovitz numbers at extinction for various fuels in counterflow premixed flames. *Combustion Science and Technology*, 178(9):1559–1584, 2006.
- [CDVP00] O. Colin, F. Ducros, D. Veynante, and T. Poinso. A thickened flame model for large eddy simulation of turbulent premixed combustion. *Physics of Fluids*, 12(7):1843–1863, 2000.
- [CER] CERFACS. AVBP. <http://www.cerfacs.fr/cfd/>.
- [Cha00] P. Chassaing. *Mécanique des fluides, Éléments d'un premier parcours*. CÉPADUÉS-ÉDITIONS, 2nd edition, 2000.
- [Cla85] P. Clavin. Dynamic Behavior of Premixed Flame Fronts in Laminar and Turbulent Flows. *Progress in Energy and Combustion Science*, 11:1–59, 1985.
- [Col00] O. Colin. *Simulation aux Grandes Echelles de la Combustion Turbulente Prémélangée dans les Statoréacteurs*. PhD thesis, Institut National Polytechnique, 2000.
- [Coo97] A. W. Cook. Determination of the constant coefficient in scale similarity models of turbulence. *Physics of Fluids*, 9, 1997.
- [Cou99] J. M. Coulombeau. note de cours, Physique : Mécanique des fluides. lycée Janson de Sailly (mathématiques spéciales), 1999.
- [CP90] S. Candel and T. Poinso. Flame Stretch and the Balance Equation for the Flame Area. *Combustion Science and Technology*, 70:1–15, 1990.
- [CS03] A. Comte-Sponville. *Le Bonheur, désespérément*, volume Libro. Philosophie. J'ai Lu, 2003.

- [CW82] P. Clavin and F. A. Williams. Effects of molecular diffusion and of thermal expansion on the structure and dynamics of premixed flames in turbulent flows of large scale and low intensity. *Journal of Fluid Mechanics*, 116:251–282, 1982.
- [Dam40] G. Damköhler. Der Einfluß der Turbulenz auf die Flammengeschwindigkeit in Gasmischen. *Zeitschrift Elektrochemie*, 46:601–652., 1940.
- [DF04] C. Duwig and L. Fuchs. Study of A Gas Turbine Combustion Chamber: Influence Of The Mixing On The Flame Dynamics. In *Proceedings of ASME Turbo Expo 2004 Power for Land, Sea, and Air June 14-17, 2004, Vienna, Austria*, 2004. GT2004-53276.
- [DF05] C. Duwig and L. Fuchs. Study of flame stabilization in a swirling combustor using a new flamelet formulation. *Combustion Science and Technology*, 177:1485–1510, 2005.
- [DHP05] L. Durand, A. Huber, and W. Polifke. Implementation and validation of LES models for inhomogeneously premixed turbulent combustion. In *European Combustion Meeting*, 2005.
- [dKB97] N. Van der Kuyp and M. Bettelini. Implementation and Validation of a turbulent Combustion model based on a two-step kinetics. Technical report, ABB Corporate Research, Ltd., Baden, Switzerland, 1997.
- [DP00] L. Duchamp de Lageneste and H. Pitsch. A level-set approach to LES of premixed turbulent combustion. In *Summer Program 2000, Center for Turbulence Research*, pages 105–116, Stanford, USA, 2000.
- [DP01] L. Duchamp de Lageneste and H. Pitsch. Progress in large-eddy simulation of premixed and partially-premixed turbulent combustion. In *In Proceedings of the Summer Program 2001, Center for Turbulence Research*, pages 97–107, Stanford, USA, 2001.
- [DP02] L. Duchamp de Lageneste and H. Pitsch. Comparison of turbulent premixed flames at difference turbulence levels. In *In Proceedings of the Summer Program 2002, Center for Turbulence Research*, pages 91–101, Stanford, USA, 2002.
- [DP07] L. Durand and W. Polifke. Implementation of the Thickened Flame Model for Large Eddy Simulation of Turbulent Premixed Combustion in a Commercial Solver. In *ASME Turbo Expo 2007*. ASME Turbo Expo 2007, Montreal, Canada, 2007. GT2007-28188.
- [DPGS07] L. Durand, W. Polifke, P. Griebel, and P. Siewert. Development and validation of a LES model for turbulent premixed combustion. In *VDI-Flammentag*, Berlin, Germany, September 2007.

- [DPR<sup>+</sup>04] L. Durand, W. Polifke, D. Rieger, J. Yan, and J. Sesterhenn. Implementation and validation of models in a LES/DNS solver for premixed turbulent combustion. In *Workshop turbulent premixed combustion*, 2004. Heidelberg, Germany.
- [DSFT05] C. Duwig, R. Z. Szasz, L. Fuchs, and C. Troger. Large Eddy Simulation of a Swirling Flame Response to Swirl Modulation with Impact on Combustion Stability. In *43rd AIAA Aerospace Sciences Meeting and Exhibit 10 - 13 January 2005, Reno, Nevada*, 2005. AIAA 2005-1275.
- [DUF<sup>+</sup>06] C. Duwig, L. Urbina, L. Fuchs, P. Griebel, and P. Siewert. Large Eddy Simulation of a confined jet: influence of combustion on the velocity field. In *44th AIAA Aerospace Sciences Meeting and Exhibit*, number 2006-157 in AIAA, pages 1–12, 2006. 9 - 12 January 2006, Reno, Nevada.
- [DVB02] P. Domingo, L. Vervisch, and K. Bray. Partially premixed flamelets in LES of nonpremixed turbulent combustion. *Combustion Theory and Modelling*, 6:529–551, 2002.
- [DVR05] P. Domingo, L. Vervisch, and J. Réveillon. DNS analysis of partially premixed combustion in spray and gaseous turbulent flame-bases stabilized in hot air. *Combustion and Flame*, 141(3):431–437, 2005.
- [EF89] T. Echekki and J. Ferziger. A simplified reaction rate model and its application to the analysis of premixed flames. *Combustion Science and Technology*, pages 293–351, 1989.
- [Fav69] A. Favre. Statistical equations of turbulent gases. In SIAM, editor, *Problems of hydrodynamics and continuum mechanics*, pages 231–266, Philadelphia, 1969.
- [FJ00] H. Forkel and J. Janicka. Large-Eddy Simulation of a Turbulent Hydrogen Diffusion Flame. *Flow, Turbulence and Combustion*, 65:163–175, 2000.
- [FL94] C. Fureby and C. Löfström. Large-eddy simulations of bluff body stabilized flames. In *Symposium on Combustion, The Combustion Institute*, 25, pages 1257–1264, 1994.
- [FLU05] FLUENT Inc., Lebanon, New Hampshire. *FLUENT User's Guide Version 6.2*, 2005.
- [Fox03] R. O. Fox. *Computational Models for Turbulent Reacting Flows*. Cambridge University Press, 2003.
- [FP00] P. Flohr and H. Pitsch. A turbulent flame speed closure model for LES of industrial burner flows. In *Proceedings of the Summer Program 2000, Center for Turbulence Research*, pages 169–179, Stanford, USA, 2000.
- [FP02] J. H. Ferziger and M. Peric. *Computational Methods for Fluid Dynamics*. Springer, 2002.

- [Fri04] R. Friedrich. Grundlagen turbulenter Strömungen. TU München, 2004.
- [G90] O. L. Gülder. turbulent premixed combustion modelling using fractal geometry. In *Twenty-Third International Symposium on Combustion*, pages 743–750, Orléans, France, 1990. Symposium on Combustion, The Combustion Institute.
- [GGB04] E. Giacomazzi, V. Battaglia, and C. Bruno. The coupling of turbulence and chemistry in a premixed bluff-body flame as studied by LES. *Combustion and Flame*, 138:320–335, 2004.
- [GBF99] E. Giacomazzi, C. Bruno, and B. Favini. Fractal modelling of turbulent mixing. *Combustion Theory and Modelling*, 3(4):637–655, 1999.
- [GBF00] E. Giacomazzi, C. Bruno, and B. Favini. Fractal modelling of turbulent combustion. *Combustion Theory and Modelling*, 4(4):391–412, 2000.
- [GBI<sup>+</sup>05] P. Griebel, R. Bombach, A. Inauen, R. Schären, and P. Siewert. Flame characteristics and turbulent flame speeds of turbulent, high-pressure, lean-premixed methane-air flames. In *ASME Turbo Expo 2005*, 2005. GT2005-68565.
- [Ger92] M. Germano. Turbulence: the filtering approach. *Journal of Fluid Mechanics*, 238:325 – 336, May 1992.
- [Ger96] M. Germano. A statistical formulation of the dynamic model. *Physics of Fluids*, 8(2):565 – 570, February 1996.
- [GHL88] F. C. Gouldin, S. M. Hilton, and T. Lamb. experimental evaluation of the fractal geometry of flamelets. In *Symposium on Combustion, The Combustion Institute*, volume 22, pages 541–550, 1988.
- [GHLW00] X. J. Gu, M. Z. Haq, M. Lawes, and R. Wooley. Laminar Burning Velocity and Markstein Lengths of Methane-Air mixtures. *Combustion and Flame*, 121:41–58, 2000.
- [GHP05] E. Guyon, J.-P. Hulin, and L. Petit. *Ce que disent les fluides*. Belin - pour la science, 2005.
- [GOdG<sup>+</sup>02] G. R. A. Groot, J. A. Van Oijen, L. P. H. de Goey, K. Seshadri, and N. Peters. The effects of strain and curvature on the mass burning rate of premixed laminar flames. *Combustion Theory and Modelling*, 6:675–695, 2002.
- [GPMC91] M. Germano, U. Piomelli, P. Moin, and W. H. Cabot. A dynamic subgrid-scale eddy viscosity model. *Physics of Fluids*, A(3):1760–1765, 1991.
- [Gri05] P. Griebel. Private communication. Unpublished, 2005.
- [Gri06] P. Griebel. Private communication. Unpublished, email 28. Nov. 2006, 2006.
- [GS95] O. L. Gülder and G. J. Smallwood. Inner Cutoff Scale of Flame Surface Wrinkling in Turbulent Premixed Flames. *Combustion and Flame*, 103(1):107–114, 1995.

- [GSS<sup>+</sup>03] P. Griebel, R. Schären, P. Siewert, R. Bombach, A. Inauen, and W. Kreutner. Flow field and structure of turbulent high-pressure premixed methane-air flames. In *ASME Turbo Expo 2003*, 2003. GT2003-38398.
- [GSW<sup>+</sup>00] O. L. Gülder, G. J. Smallwood, R. Wong, D. R. Snelling, R. Smith B. M. Deschamps, and J.-C. Sautet. Flame Front Surface Characteristics in Turbulent Premixed Propane-Air Combustion. *Combustion and Flame*, 120(4):407–416, 2000.
- [HC01] E. R. Hawkes and R. S. Cant. Implications of a Flame Surface Density Approach to Large Eddy Simulation of Premixed Turbulent Combustion. *Combustion and Flame*, 126:1617–1629, 2001.
- [Hir02] C. Hirsch. Vorlesungsskriptum Technische Verbrennung. TU München (Thermodynamik), 2002.
- [Hof04] A. B. Hoffmann. *Modellierung turbulenter Vormischverbrennung*. PhD thesis, Fakultät für Chemieingenieurwesen der Universität Karlsruhe, 2004.
- [HSZ96] W. Hackbusch, H.R. Schwarz, and E. Zeidler. *Taschenbuch der Mathematik*. B.G. Teubner, 1996.
- [Kim04] S. E. Kim. Large Eddy Simulation using Unstructured meshes and dynamic subgrid-scale turbulence models. In *34th AIAA Fluid dynamics conference and exhibit*, 2004-2548, pages 1–18, 2004.
- [KJKW54] B. Karlovitz, D. W. Denniston Jr., D. H. Knapschaefer, and F. E. Wells. Studies on turbulent flames, A. Flame Propagation Across Velocity Gradients, B. Turbulence Measurements in Flames. , page 613, 1954.
- [KLW97] V. R. Karpov, A. N. Lipatnikov, and P. Wolanski. Finding the Markstein number using the measurements of expanding spherical laminar flames. *Combustion and Flame*, 109:436–448, 1997.
- [Kol41] A. N. Kolmogorov. Local structure of turbulence in an incompressible fluid at very high Reynolds numbers. *Dokl. Akad.Nauk SSSR*, 30:299–303, 1941.
- [Kol62] A. N. Kolmogorov. A refinement of previous hypotheses concerning the local structure of turbulence in a viscous incompressible fluid at high Reynolds number. *Journal of Fluid Mechanics*, 13:82–85, 1962.
- [Kon05] M. A. Konle. Simultane PIV LIF Mesungen zur Bestimmung der Flammenstreckungsrate. Diplomarbeit, Lehrstuhl für Thermodynamik der Technischen Universität München, 2005.
- [Krö03] M. Kröner. *Einfluss lokaler Löschvorgänge auf den Flammenrückschlag durch verbrennungsinduziertes Wirbelaufplatzen*. PhD thesis, Lehrstuhl für Thermodynamik der Technischen Universität München, 2003.

- [KRG98] J. M. Kech, J. Reissing, J. Gindele, and U. Spicher. Analysis of the Combustion Process in a Direct Injection Gasoline Engine. In *COMODIA 98, 4th Int. Symp. on Diagnostics and Modeling of Combustion in Internal Combustion Engines*, 1998. Kyoto, Japan.
- [Kum07] Aluri Naresh Kumar. *Numerical Modelling of Turbulent Premixed Combustion for Gas Turbine Conditions with Incorporation of Molecular Transport Effects*. PhD thesis, Lehrstuhl für Thermodynamik und Verbrennung der Universität Siegen, 2007.
- [Kuo86] K. K. Kuo. *Principles of Combustion*. Wiley-Interscience, 1986.
- [KVM02] R. Knikker, D. Veynante, and C. Meneveau. A priori testing of a similarity model for large eddy simulations of turbulent premixed combustion. In *International Symposium on Combustion*, 2002.
- [Law88] C. K. Law. dynamics of stretched flames. In *Symposium on Combustion, The Combustion Institute*, volume 22, pages 138–1402, 1988.
- [LC99] A. Lipatnikov and J. Chomiak. A Quasi-Fractal Subgrid Flame Speed Closure for Large Eddy Simulations of Premixed Flames, 1999.
- [LC02] A.N. Lipatnikov and J. Chomiak. Turbulent flame speed and thickness: phenomenology, evaluation, and application in multi-dimensionnal simulations. *Progress in Energy and Combustion Science*, 28:1–74, 2002.
- [LC04a] A. N. Lipatnikov and J. Chomiak. A study of the effects of pressure-driven transport on developing turbulent flame structure and propagation. *Combustion Theory and Modelling*, 8(2):211–225, 2004.
- [LC04b] A. N. Lipatnikov and J. Chomiak. Application of the Markstein number concept to curved turbulent flames. *Combustion Science and Technology*, 176:331–358, 2004.
- [LC04c] A.N. Lipatnikov and J. Chomiak. Molecular transport effects on turbulent flame propagation and structure. *Progress in Energy and Combustion Science*, 31:1–73, 2004.
- [Lec06] S. Lechner. LES-Simulation des TD1-Drallbrenners. Semesterarbeit, Lehrstuhl für Thermodynamik der Technischen Universität München, 2006.
- [Les87] M. Lesieur. *Turbulence in Fluids*. Martinus Nijhoff Publishers, 1987.
- [Lil92] D. K. Lilly. A proposed modification of the Germano& grid-scale closure method. *Physics of Fluids*, A 4(3):633–635, 1992.
- [Lol95] P. Lolos. Untersuchung der Struktur von mageren Vormischflammen und deren Einfluss auf die NO<sub>x</sub> Bildung. Diplomarbeit, RWTH Aachen (Institut für Technische Mechanik), 1995.

- [LPV00] J. P. Legier, T. Poinso, and D. Veynante. Dynamically thickened flame LES model for premixed and non-premixed turbulent combustion. In *Summer Program 2000, Center for Turbulence Research*, pages 157–168, Stanford, USA, 2000.
- [LS00] C. K. Law and C. J. Sung. Structure, aerodynamics, and geometry of premixed flamelets. *Progress in Energy and Combustion Science*, 26:459–505, 2000.
- [MADL05] S.P. R. Muppala, N. K. Aluri, F. Dinkelacker, and A. Leipertz. Development of an algebraic reaction rate closure for the numerical calculation of turbulent premixed methane, ethylene, and propane/air flames for pressures up to 1.0 MPa. *Combustion and Flame*, 140:257–266, 2005.
- [Mag81] B. F. Magnussen. On the structure of turbulence and a generalized eddy dissipation concept for chemical reaction in turbulent flow. In *AIAA, 19th Aerospace Sciences Meeting*, volume Fluid Mechanics and Heat Transfer, 1981. St. Louis, Mo., Jan. 12-15.
- [Man75] B. Mandelbrot. On the geometry of homogeneous turbulence, with stress on the fractal dimension of the iso-surfaces of scalars. *Journal of Fluid Mechanics*, 72(2):401–416, 1975.
- [Man82] B.B. Mandelbrot. *The Fractal Geometry of Nature*. W.H. Freeman and Company, 1982.
- [Man95] B. Mandelbrot. *Les objets fractals*. Champs Flammarion, 4th edition, 1995.
- [Mat73] J. Mathieu. *Mécanique des fluides*. Ecole Centrale de Lyon, 1973.
- [May06] M. Mayerhofer. Statistische Auswertung der LES Simulationen des TD1-Drallbrenners. Semesterarbeit, Lehrstuhl für Thermodynamik der Technischen Universität München, 2006.
- [MBAP04] V. Moureau, I.E. Barton, C. Angelberger, and T. Poinso. Towards large eddy simulation in internal combustion engines : simulation of a compressed tumble flow. In *SAE Spring Fuels and Lubricants Meeting*, pages SAE Paper 2004-01-1995, Centre de congrés P. Baudis, Toulouse - France, 2004.
- [MBP97] U. C. Mueller, M. Bollig, and N. Peters. Approximations for Burning Velocities and Markstein Numbers for Lean Hydrocarbon and Methanol Flames. *Combustion and Flame*, 108:349–356, 1997.
- [MC83] E. Mallard and H. L. Le Chatelier. *Annales des Mines*, 1883. 4, p. 379.
- [MFB89] J. Mantzaras, P. G. Felton, and F. V. Bracco. Fractals and turbulent premixed engine flames. *Combustion and Flame*, 77:295–310, 1989.
- [MGP64] G. H. Markstein, H. Guénoche, and A. A. Putnam. *Non-steady Flame Propagation*. Pergamon Press, 1964.

- [MK80] M. Metghalchi and J. C. Keck. Laminar burning velocity of propane-air mixtures at high temperature and pressure. *Combustion and Flame*, 38:143–154, 1980.
- [MP91] C. Meneveau and T. Poinso. Stretching and quenching of flamelets in premixed turbulent combustion. *Combustion and Flame*, 86(4):311–332, 1991.
- [MS87a] C. Meneveau and K. R. Sreenivasan. Simple Multifractal Cascade Model for Fully Developed Turbulence. *Physical Review Letters*, 59(13):1424–1427, 1987.
- [MS87b] C. Meneveau and K. R. Sreenivasan. The multifractal spectrum of the dissipation field in turbulent flows. *Nuclear Physics B - Proceedings Supplements*, 2:49–76, 1987.
- [MS89] C. Meneveau and K. R. Sreenivasan. Measurement of  $f(\alpha)$  from scaling of histograms, and applications to dynamical systems and fully developed turbulence. *Physics Letters A*, 137(3):103–112, 1989.
- [MS00] J. Mathieu and J. Scott. *An Introduction to Turbulent Flows*. Cambridge University Press, 2000.
- [MTS<sup>+</sup>02] Y. Mizobuchi, S. Tachibana, J. Shinjo, S. Ogawa, and T. Takeno. A numerical analysis of the structure of a turbulent hydrogen jet lifted flame. In *Symposium on Combustion, The Combustion Institute*, volume 29, pages 2009–2015. Symposium on Combustion, The Combustion Institute, 2002.
- [Nat] National Institute of Standards and Technology. *NIST Chemistry WebBook*. <http://webbook.nist.gov/chemistry/>.
- [NS90] G. L. North and D. A. Santavicca. The fractal Nature of Premixed Turbulent Flames. *Combustion Science and Technology*, 72:295–310, 1990.
- [OB01] E. S. Oran and J.P. Boris. *Numerical Simulation of Reactive Flow*. Cambridge University Press, 2nd edition, 2001.
- [PBP<sup>+</sup>03] J. Pieringer, M. Brandt, W. Polifke, P. Griebel, P. Siewert, R. Bombach, A. Inauen, and W. Kreutner. Anwendung von Modellen der turbulenten Flammgeschwindigkeit auf einen vorgemischten Strahlbrenner. VDI-Berichte Nr. 1750, pages 629–634, 2003.
- [PD02] H. Pitsch and L. Duchamp de Lageneste. Large-eddy simulation of premixed turbulent combustion using a level-set approach. In *Symposium on Combustion, The Combustion Institute*, volume 29, pages 2001–2008, 2002.
- [Pet86] N. Peters. Laminar flamelet concepts in turbulent combustion. In *Twenty-First International Symposium on Combustion*, pages 1231–1250. Symposium on Combustion, The Combustion Institute, 1986.
- [Pet94] N. Peters. Turbulente Brenngeschwindigkeit. Technical report, Abschlussbericht zum Forschungsvorhaben Pe 241/9-2, 1994.

- [Pet97] N. Peters. Four Lectures on Turbulent Combustion. Technical report, ERCOFTAC Summer School September 15-19, 1997 Aachen, Germany, 1997. Institut für Technische Mechanik RWTH Aachen.
- [Pet99] N. Peters. The turbulent burning velocity for large-scale and small-scale turbulence. *Journal of Fluid Mechanics*, 384:107–132, 1999.
- [Pet00] N. Peters. *Turbulent Combustion*. Cambridge University Press, 2000.
- [PFB00] W. Polifke, P. Flohr, and M. Brandt. Modeling of Inhomogeneously Premixed Combustion with an Extended TFC Model. In *ASME Turbo Expo 2000: Land, Sea and Air, ASME paper 2000-GT-0135*, Munich, Germany, 2000.
- [PGD98] W. Polifke, W. Geng, and K. Döbbeling. Optimization of Rate Coefficients for Simplified Reaction Mechanisms with Genetic Algorithms. *Combustion and Flame*, 113:119–134, 1998.
- [Pie02] J. Pieringer. Anwendung und Validierung von Modellen zur Berechnung der turbulenten Flammengeschwindigkeit. Diplomarbeit, Lehrstuhl für Thermodynamik der Technischen Universität München, 2002.
- [Piq99] J. Piquet. *Turbulent Flows*. Springer-Verlag, 1999.
- [Piq02] J. Piquet. La turbulence et sa modélisation. Ecole Centrale de Nantes, 2002.
- [Pit05] H. Pitsch. A consistent level set formulation for large-eddy simulation of premixed turbulent combustion. *Combustion and Flame*, 143(4):587–598, 2005.
- [Pit06] H. Pitsch. Large Eddy Simulation of Turbulent Combustion. *Annual Review of Fluid Mechanics*, 38:453–482, 2006.
- [PM98] C. D. Pierce and P. Moin. A dynamic model for subgrid-scale variance and dissipation rate of a conserved scalar. *Physics of Fluids*, 10(12):3041–3044, 1998.
- [Pol04] W. Polifke. Combustion Instabilities. Technical report, Brussels, BE, 2004.
- [Pop85] S. B. Pope. PDF Methods for turbulent reactive flows. *Progress in Energy and Combustion Science*, 11:119–192, 1985.
- [Pop90] S. B. Pope. computations of turbulent combustion: progress and challenges. In *Twenty-Third International Symposium on Combustion*, pages 591–612, Orléans, France, 1990. Symposium on Combustion, The Combustion Institute.
- [Pop00] S. Pope. *Turbulent Flows*. Cambridge, 1st edition, 2000.
- [PS94] B. Peck and L. W. Sigurdson. The 3 dimensional vortex structure of an impacting water drop. *Physics of Fluids*, 6:564 – 578, 1994.
- [PV01] T. Poinso and D. Veynante. *Theoretical and Numerical Combustion*. Edwards, 1st edition, 2001.

- [PV05] T. Poinso and D. Veynante. *Theoretical and Numerical Combustion*. Edwards, 2nd edition, 2005.
- [PVC90] T. J. Poinso, D. Veynante, and S. Candel. Diagrams of premixed turbulent combustion based on direct simulations. In *Twenty-Third International Symposium on Combustion*, pages 613–619, Orléans, France, 1990. Symposium on Combustion, The Combustion Institute.
- [REO93] R. Rydén, L. E. Eriksson, and S. Olovsson. Large Eddy Simulation Of Bluff Body Stabilised Turbulent Premixed Flames. In *ASME Turbo Expo 1993, Cincinnati, Ohio*, pages 1–12, 1993. 93-GT-157.
- [Rey83] O. Reynolds. An experimental investigation of the circumstances which determine whether the motion of water shall be direct or sinuous and of the law of resistance in parallel channels. *Transactions of the Royal Society of London*, 174:935–984, 1883.
- [Rog88] B. Rogg. Response and Flamelet Structure of Stretched Premixed Methane-Air Flames. *Combustion and Flame*, 73:45–65, 1988.
- [RP90] B. Rogg and N. Peters. The Asymptotic Structure of Weakly Strained Stoichiometric Methane-Air Flames. *Combustion and Flame*, 79:402–420, 1990.
- [Sag01] P. Sagaut. *Large Eddy Simulation for incompressible flows*. Springer Verlag, 2001.
- [Sen05] J.M. Senoner. Weiterentwicklung des Thickened Flame Modells in turbulenten Verbrennungssimulationen. Semesterarbeit, Lehrstuhl für Thermodynamik der Technischen Universität München, 2005.
- [SGS<sup>+</sup>95] G. J. Smallwood, O. L. Gülder, D. R. Snelling, B. M. Deschamps, and I. Gokalp. Characterization of Flame Front Surfaces in Turbulent Premixed Methane-Air Combustion. *Combustion and Flame*, 101(4):461–470, 1995.
- [SHL92] A. Sjunnesson, P. Henrikson, and C. Lofstrom. CARS measurements and visualization of reacting flows in a bluff body stabilized flame. In *SAE, ASME, and ASEE, Joint Propulsion Conference and Exhibit*, number 3650 in AIAA-1992, 1992. 28th, Nashville, TN, July 6-8, 1992.
- [Sie06] P. Siewert. *Flame front characteristics of turbulent premixed lean methane / air flames at high-pressure and high-temperature*. PhD thesis, Paul Scherrer Institut, 2006.
- [Sig97] L. W. Sigurdson. Flow visualization in turbulent large scale structure research, atlas of visualization. *Flow Visualization Society of Japan*, 3:99 – 113, 1997.
- [Sin00] J. F. Sini. *Mécanique des Fluides*. Ecole Centrale de Nantes, 2000.
- [Siv77] G. I. Sivashinsky. Nonlinear analysis of hydrodynamic instability in laminar flames - I. Derivation of basic equations. *Acta Astronautica*, 4(11-12):1177–1206, 1977.

- [SLP<sup>+</sup>02] L. Selle, G. Lartiguey, T. Poinsoz, P. Kaufmann, W. Krebs, and D. Veynante. Large-eddy simulation of turbulent combustion for gas turbines with reduced chemistry. In *Proceedings of the 2002 Summer Program*. Center for Turbulent Research, 2002.
- [SLP<sup>+</sup>04] L. Selle, G. Lartigue, T. Poinsoz, R. Koch, K.-U. Schildmacher, W. Krebs, B. Prade, P. Kaufmann, and D. Veynante. Compressible Large-Eddy Simulation of turbulent combustion in complex geometry on unstructured meshes. *Combustion and Flame*, 137(4):489–505, 2004.
- [SM86] K. Sreenivasan and C. Meneveau. The fractal facets of turbulence. *Journal of Fluid Mechanics*, 173:357–386, 1986.
- [Sma63] J. Smagorinsky. General circulation experiments with the primitive equations. *Monthly Weather Review*, 91(3):99–164, 1963.
- [SNM91] A. Sjunnesson, C. Nelsson, and E. Max. LDA Measurements of Velocity and Turbulence in a Bluff Body Stabilized Flame. In *4th International Conference on Laser Anemometry Advances and Applications*, ASME, volume 3, pages 83–90, Cleveland, USA, 1991.
- [Soh05] S.A. Sohoni. Large Eddy Simulation of Turbulent Premixed Methane-Air Combustion. Master thesis, TU München (Thermodynamik) - IIT Madras, 2005.
- [Sou03] T. Soulères. *Simulations des grandes échelles d'écoulements dans des géométries fixes et mobiles : Application aux moteurs à pistons*. PhD thesis, Institut National Polytechnique de Toulouse, 2003. TH/CFD/03/17.
- [Sre91] K. R. Sreenivasan. Fractals and Multifractals in Fluid Turbulence. *Annual Review of Fluid Mechanics*, 23:539–600, 1991.
- [SSO94] M. Sussman, P. Smereka, and S. Osher. A Level Set Approach For Computing Solutions To Incompressible Two-Phase Flow. *Journal of Computational Physics*, 114(1):146–159, 1994.
- [Tay35] G. I. Taylor. Statistical theory of turbulence: Parts I-II. *Proceedings of the Royal Society of London A*, pages 421–464, 1935.
- [TL87] H. Tennekes and J. L. Lumley. *First Courses in Turbulence*. MIT Press, 11th edition, 1987.
- [TRS<sup>+</sup>05] L. Thobois, G. Rymer, T. Soulères, T. Poinsoz, and B. Van den Heuvel. Large-eddy simulation for the prediction of aerodynamics in IC engines. *International Journal for Vehicle Design*, 39(4):368–382, 2005.
- [Tru01] K. Truffin. Modélisation de flammes prémélangées de méthane/air à l'aide de schémas cinétiques détaillés et réduits. rapport DEA WN/CFD/01/14, CER-FACS, June 2001.

- [Tru06] K. Truffin. Private communication. Unpublished, 2006.
- [Tur00] S. R. Turns. *An Introduction to Combustion, Concepts and Applications*. McGraw Hill, 2nd edition, 2000.
- [TVP03] K. Truffin, B. Varoquié, and T. Poinso. Measurements of transfer functions in reacting flows using Large Eddy Simulations. In *10th International Congress On Sound And Vibration*, pages 785–793, Stockholm, Sweden, 2003.
- [TVV<sup>+</sup>04] K. Truffin, B. Varoquié, D. Veynante, T. Poinso, and F. Lacas. Large Eddy Simulations and experimental characterization of the unsteady response of partially premixed flames. Technical Report TR/CFD/04/36, CERFACS, January 2004.
- [TW04] G. Tabor and H.G. Weller. Large Eddy Simulation of Premixed Turbulent Combustion Using a Flame Surface Wrinkling Model. *Flow, Turbulence and Combustion*, 72:1–28, 2004.
- [TYUM06] K. Takita, H. Yamazaki, T. Uchida, and G. Masuya. Extinction karlovitz numbers of premixed counterflow flames under various pressures. *Combustion Science and Technology*, 178(9):1649–1668, 2006.
- [VBGD05] J.A. Van Oijen, R.J.M. Bastiaans, G.R.A. Groot, and L.P.H. De Goey. Direct Numerical Simulations of Premixed Turbulent Flames with Reduced Chemistry: Validation and Flamelet Analysis. *Flow, Turbulence and Combustion*, 75:67–84, 2005.
- [Ver04] L. Vervisch. Quelques problèmes rencontrés en chimie numérique : Hydrologie - Combustion - Atmosphère Turbulent Combustion Modeling, 2004. lecture.
- [VLED02] D. Veynante, F. Lacas, E. Esposito, and N. Dabiha. Combustion. Ecole Centrale de Nantes, 2002.
- [VTBM97] D. Veynante, A. Trouvé, K. N. C. Bray, and T. Mantel. Gradient and counter-gradient scalar transport in turbulent premixed flames. *Journal of Fluid Mechanics*, 332:263–293, 1997.
- [WD81] C.K. Westbrook and F.L. Dryer. Simplified Reaction Mechanisms for the Oxidation of Hydrocarbon Fuels in Flames. *Combustion Science and Technology*, 27:31–43, 1981.
- [WD84] C. K. Westbrook and F. L. Dryer. Chemical Kinetic Modeling of hydrocarbon Combustion. *Progress in Energy and Combustion Science*, 10:1–57, 1984.
- [Wei06] S. Weiß. Experimentelle Untersuchungen zum Einfluss der Flammenfrontstreckung auf die turbulente Brenngeschwindigkeit. Unpublished, Vortrag 7. Juli 2006, Lehrstuhl für Thermodynamik, TU München, 2006.

- [WHZ06] F. Wetzel, P. Habisreuther, and N. Zarzalis. Numerical investigation of lean blow out of a model gas turbine combustion chamber using a presumed jpdf-reaction model by taking heat loss processes into account. In *Proceedings of GT2006, ASME Turbo Expo 2006: Power for Land, Sea and Air*, Barcelona, Spain, May 8-11, 2006 2006. GT2006-90064.
- [Wik06] Wikipedia. *Wikipedia*, Aug. 2006. <http://en.wikipedia.org/wiki>.
- [Wil84] F. A. Williams. *Combustion Theory*. The Benjamin/Cummings Publishing Company, Inc., 1984.
- [Wil00] F. A. Williams. Progress in knowledge of flamelet structure and extinction. *Progress in Energy and Combustion Science*, 26:657–682, 2000.
- [WWS04] A. Winkler, J. Wäsle, and T. Sattelmayer. Investigation of Combustion Noise by Real Time Laser Measurement Techniques. In *CFA/DAGA Joint Congress*, Strasbourg, France, 2004.
- [WWS05a] A. Winkler, J. Wäsle, and T. Sattelmayer. Experimental Investigations on the Acoustic Efficiency of Premixed Swirl Stabilized Flames. In *11th AIAA/CEAS Aeroacoustics Conference*, page 19, Monterey, USA, 2005. AIAA-2005-2908.
- [WWS05b] J. Wäsle, A. Winkler, and T. Sattelmayer. Influence of the Combustion Mode on Acoustic Spectra of Open Turbulent Swirl Flames. In *12th International Congress on Sound and Vibration*, volume 12, page 100, Lisbon, Portugal, 2005.
- [WWS05c] J. Wäsle, A. Winkler, and T. Sattelmayer. Spatial Coherence of the Heat Release Fluctuations in Turbulent Jet and Swirl Flames. *Flow, Turbulence and Combustion*, 75(4):29–50, 2005.
- [WWS05d] J. Wäsle, A. Winkler, and T. Sattelmayer. TD1: Experimental investigation of the TD1 swirl burner. Technical report, TU München (Thermodynamik), 2005.
- [WWS06] J. Wäsle, A. Winkler, and T. Sattelmayer. Development of an Annular Porous Burner for the Investigation of Adiabatic Unconfined Flames. In *13th International Symposium on Applications of Laser Techniques to Fluid Mechanics*, volume 13, pages 1–12, Lisbon, Portugal, 2006.
- [YST96] H. Yamashita, M. Shimada, and T. Takeno. A numerical study on flame stability at the transition point of jet diffusion flames. In *Symposium on Combustion, The Combustion Institute*, volume 26, pages 27–34. Symposium on Combustion, The Combustion Institute, 1996.
- [ZB02] V. L. Zimont and F. Biagioli. Gradient, counter-gradient transport and their transition in turbulent premixed flames. *Combustion Theory and Modelling*, 6:79–101, 2002.

- [ZB06] V. L. Zimont and V. Battaglia. Joint RANS/LES approach to premixed flame modelling in the context of the TFC combustion model. 2006. draft 2006.
- [ZBLM85] Y. B. Zeldovitch, G. I. Barenblatt, V. B. Librovich, and G. M. Makhviladze. *The mathematical theory of combustion and explosions*. Plenum Publishing Corporation, 1985.
- [Zim79] V. L. Zimont. Theory of turbulent combustion of homogeneous fuel mixture at high Reynolds numbers. *Combustion Explosion and Shock Waves*, pages 305–311, 1979.
- [ZL95] V. L. Zimont and A. N. Lipatnikov. A numerical model of premixed turbulent combustion of gases. *Chemical and Physical Report*, 14(7):993–1025, 1995.
- [ZPBW97] V. L. Zimont, W. Polifke, M. Bettelini, and W. Weisenstein. An efficient computational model for premixed turbulent combustion at high Reynolds numbers based on a turbulent flame speed closure. In *Transactions of the ASME*, 1997. 97-GT-395.



# A Annexes

## A.1 Fractal theory

The Fractal theory is typically employed to evaluate the ratio between the turbulent flame speed and the laminar flame speed  $S_t/S_l$ . The estimation of this ratio is achieved knowing the surface ratio  $A_t/A$ . Several combustion LES models have been developed considering that the turbulent flame front behaves like a fractal surface. In the following, notion of fractal and definitions required for this thesis (the fractal theory is required for the derivation of the SFC model in section 7 (p.99)) are summarized.

Fractal theory has become well known due to numerous (and for several applications) publications of Mandelbrot [Man75, Man82, Man95]. His classical example to illustrate the fractal theory is the length of shores. Measure of their length depends on the distance from which the measure is carried out. From an airplane, fifty meter details can be measured. Going along the shore, fifty centimeter details can be measured, and more details revealed. As the total measured length is the sum of all pieces length, measure achieved at the ground level is the largest one. This illustrates that fractal edges have a length depending on the precision of measure, or on the *observation scale*.

For the combustion modeling this property is expressed mostly in term of surfaces (rather than with length), since the flame front surface scales with the reaction rate. The surface scales with the precision of observation according to the *fractal dimension*  $\mathcal{D} \in [2; 3]$ :

$$A(\xi) \sim \xi^{2-\mathcal{D}}. \quad (\text{A.1})$$

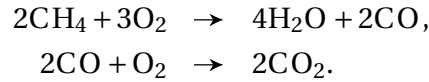
In this expression  $A(\xi)$  is a measure of the surface  $A$  at the observation scale  $\xi$ . As the exponent  $2 - \mathcal{D}$  is negative, the surface (or better said its measure) increases with a smaller observation scale. The relation Eq. (A.1) is only valid in a range of scales  $[\xi_i; \xi_o]$ , where  $\xi_i$  and  $\xi_o$  are respectively defined as the *inner and outer cut-off scales* as depicted in Figure A.1 (p.206). This property of fractals is largely used for the derivation of the SFC model in section 7 (p.99), and for two models presented in the review section 3.4 (p.50).

For the specific case of turbulent combustion, it has been demonstrated by Sreenivasan [Sre91], and measured by Gouldin et al., Gülder and Smallwood [GHL88, GSW<sup>+</sup>00, SGS<sup>+</sup>95], that the fractal dimension varies between  $\mathcal{D} = 2$  for low turbulence intensity, and the value  $\mathcal{D} \approx 2.37$  for high turbulence intensity. In the early nineties, reviews for the value of  $\mathcal{D}$  were made by Gülder [G90](p. 12) and Sreenivasan [Sre91](p. 567).

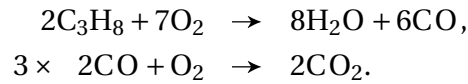
## A.2 TF and TF' models: Thermo-chemical properties

### A.2.1 Reduced reaction mechanisms

The TF-LES model is formulated with species mass fraction transport equations, it can therefore be used for the description of complex reaction mechanisms. Unfortunately, taking several reactions rapidly increases the number of species and therefore of transport equations. This leads to high CPU-costs, especially with LES modeling. A classical two-step mechanism with 6 species is selected to describe the combustion process of the methane:



The similar mechanism can be written for the propane oxidation:



For both fuels, the first reaction step can be defined with water  $\text{H}_2\text{O}$  as catalyst. In that case water does not alter the reaction mechanism itself, but the mass fraction of water appears in the evaluation of the reaction rate. The second step can also be refined by taking into account the backward reaction, modifying the reaction rate for this step with  $y_{\text{CO}_2}$ .

Only three extra transport equations are solved: two for the mass fractions of fuel  $y_F$  and carbon monoxide  $y_{\text{CO}}$ , and one for the mixture fraction  $Z$ . The latter allows the simulation of inhomogeneously premixed turbulent combustion.  $y_{\text{CH}_4}$ ,  $y_{\text{CO}}$  and  $Z$  are computed by solving their respective transport equations. The mass fractions of the other species  $y_{\text{O}_2}$ ,  $y_{\text{CO}_2}$  and  $y_{\text{H}_2\text{O}}$  are required to calculate the reaction rates. They can be evaluated from the algebraic relation (adapted from Van der Kuyp and Bettelini [dKB97](p. 19)) derived from C,

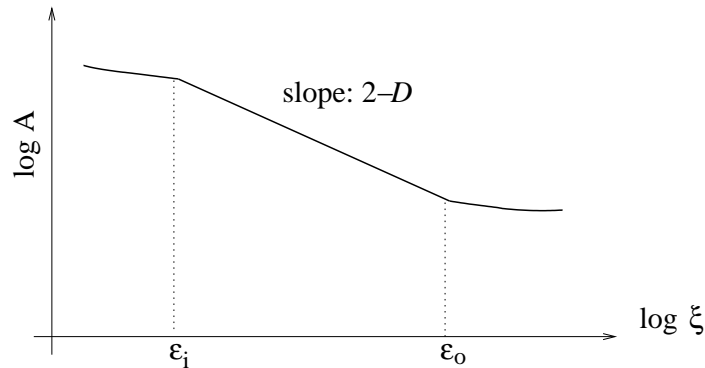


**Fig. A.1:** Inner and outer cut-off scales

	$f_o$	$i_1$	$i_2$
Methane	0.2330	12.84	2.451
Propane	0.2330	10.90	2.469

**Tab. B.1:** Air-fuel mass parameters

H and O element conservation:

$$y_{O_2} = f_0 \left[ 1 + y_{CH_4} \left( i_1 + i_2 \frac{M_{CO}}{M_F} \right) + i_2 y_{CO} - Z \left( 1 + i_1 + i_2 \frac{M_{CO}}{M_F} \right) \right], \quad (B.2)$$

$$y_{CO_2} = \frac{M_{CO_2}}{M_F} (Z - y_F) - \frac{M_{CO_2}}{M_{CO}} y_{CO}, \quad (B.3)$$

$$y_{H_2O} = \frac{M_{H_2O}}{M_F} (Z - y_F). \quad (B.4)$$

In the previous equations,  $f_o$  is the mass of oxygen contained in air,  $i_1$  is the mass of air needed to burn 1 kg of fuel and  $i_2$  the mass of air needed to burn 1 kg of carbon monoxide.

Either the combination  $(y_F, y_{CO})$ , or the combination  $(y_F, y_{CO_2})$  can be computed. The mathematical formalism is easier when employing  $y_{CO_2}$ , because this species appears only in one reaction step, as well as the fuel. This mass fraction is thus a simple indicator of the chemical advancement of the second reaction step. Nevertheless, computing with  $y_{CO}$  enables a direct and more precise evaluation of this gas, taking explicitly into account the effect of diffusion and convection between the cells. Finally, the combination  $(y_F, y_{CO})$  has been selected, because CO has a large influence on the reaction equilibrium.

### A.2.2 Reaction rates

The reaction rates for the two-step reduced mechanism are based on the Arrhenius formulation. They can include the influence of water in the first reaction of oxidation of the fuel ( $F=CH_4$  or  $C_3H_8$ ), and a second backward reaction:

$$\begin{aligned} \omega_1 &= [F]^{\alpha_1} [O_2]^{\beta_1} [H_2O]^{\gamma_1} A_1 \exp\left(-\frac{Ea_1}{\mathcal{R}T}\right), \\ \omega_{2f} &= [CO]^{\alpha_2} [O_2]^{\beta_2} A_{2f} \exp\left(-\frac{Ea_2}{\mathcal{R}T}\right), \\ \omega_{2b} &= [CO_2]^{\gamma_2} A_{2b} \exp\left(-\frac{Ea_2}{\mathcal{R}T}\right). \end{aligned} \quad (B.5)$$

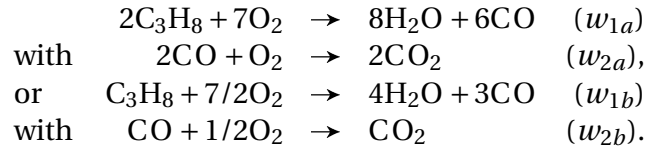
The choice of these parameters is important since the precision of the models, as well as the numerical convergence, rely on them. Getting convergence with CFD solvers is namely more difficult with stiffer mechanisms, which lead to large variations for small changes of

fuel	$w_i$	$A_i$	$Ea_i$	$\alpha_i$	$\beta_i$	$\gamma_i$
methane	$w_1$	$5.012 \times 10^{11}$	$2.0 \times 10^8$	0.7	0.8	
	$w_{2f}$	$2.239 \times 10^{12}$	$1.7 \times 10^8$	1.0	0.25	0.5 (H <sub>2</sub> O)
	$w_{2b}$	$5.0 \times 10^8$	$1.7 \times 10^8$			1.0 (CO <sub>2</sub> )
propane	$w_1$	$5.62 \times 10^9$	$1.256 \times 10^8$	0.1	1.65	
	$w_{2f}$	$2.239 \times 10^{12}$	$1.7 \times 10^8$	1.0	0.25	0.5 (H <sub>2</sub> O)
	$w_{2b}$	$5.0 \times 10^8$	$1.7 \times 10^5$			1.0 (CO <sub>2</sub> )

**Tab. B.2:** Arrhenius coefficients taken from *Fluent*[SI-J-kmol]

mass fractions or temperature. Different sources have been consulted to choose the most practical set of pre-exponential factor, activation energy and concentration exponent values. The coefficients obtained by Westbrook and Dryer [WD81], which are used for the database in *Fluent* [FLU05], are calculated according to experimental investigations, and aim to estimate the laminar flame velocity for a wide range of conditions: AFR, unburnt temperature and pressure. In our chair, a numerical optimization method has been developed by Polifke et al., and Brandt [PGD98, Bra05] to obtain reduced mechanisms from detailed mechanism. This application is more specific, and the algorithm must be computed for each case. Similarly, coefficients from *CERFACS* and *ECP-EM2C*, obtained from laminar flame calculation with detailed mechanisms, used by Truffin et al. [TVP03] for combustion of propane at  $\phi \approx 0.8$ , have been consulted.

Some reaction mechanisms are written with integer stoichiometric coefficients, and some others with a unity factor for the fuel, for example:



This does not naturally change the stoichiometry of the reaction, but the species reaction rates must be written accordingly:

$$\begin{aligned}
 w_{\text{C}_3\text{H}_8} &= -2w_{2a} = -w_{2b}, \\
 w_{\text{CO}} &= 6w_{1a} - 2w_{2a} = 3w_{1b} - w_{2b}
 \end{aligned}$$

The Arrhenius coefficients and associated reaction rates evidently only make sense, if the absolute stoichiometry of the reaction is conjointly written.

The set of values by Westbrook and Dryer [WD81](p. 38) [WD84] has been slightly modified and used in *Fluent* [FLU05]. It delivers higher values of the activation energy, and a very low exponent argument for the species, especially for propane (see Table B.2 (p.208)). This tends to rise to numerical difficulties, since the gradient of the reaction rate with temperature is steeper. Besides, the original set of values from Westbrook and Dryer for methane included negative exponent parameter for the methane [WD81](p. 38) [WD84](p. 28). This leads to a numerical difficulty when  $y_F$  locally decreases to zero, and therefore in case of the lean premixed combustion.

AFR	$w_i$	$A_i$	$Ea_i$	$\alpha_i$	$\beta_i$
$\phi = 1$	$w_1$	$2.637 \times 10^{10}$	$1.165 \times 10^7$	0.347	0.892
	$w_2$	$5.114 \times 10^{10}$	$9.665 \times 10^6$	0.946	0.613
$\phi = 0.7$	$w_1$	$5.543 \times 10^{14}$	$1.602 \times 10^7$	0.803	1.099
	$w_2$	$6.454 \times 10^{13}$	$1.046 \times 10^7$	1.243	1.091
$\phi = 0.58$	$w_1$	$9.802 \times 10^{14}$	$1.704 \times 10^7$	0.772	1.207
	$w_2$	$1.201 \times 10^{14}$	$1.255 \times 10^7$	1.069	1.254

**Tab. B.3:** Arrhenius coefficients for the methane obtained from genetic algorithm [SI-J-kmol]

fuel	$w_i$	$A_i$	$Ea_i$	$\alpha_i$	$\beta_i$	$\gamma_i$
methane (2S_CM2)	$w_1$	$2.0 \times 10^{15}$	$34.5 \times 10^3$	0.9	1.1	
	$w_{2f}$	$2.0 \times 10^9$	$12.0 \times 10^3$	1.0	0.5	
	$w_{2b}$	$2.0 \times 10^9$	$12.0 \times 10^3$			1.0 (CO <sub>2</sub> )
propane (2S_KT1)	$w_1$	$1.5 \times 10^{10}$	$20.812 \times 10^3$	0.77	0.7044	
	$w_{2f}$	$1.0 \times 10^{10}$	$19.9 \times 10^3$	0.5	1.0	
	$w_{2b}$	$1.0 \times 10^{10}$	$19.9 \times 10^3$			1.0 (CO <sub>2</sub> )

**Tab. B.4:** Arrhenius coefficients taken from CERFACS sources [cgs-cal-mol]

The set of values obtained from genetic algorithm after a reduction of a complete mechanism by Polifke et al. and Brandt [PGD98, Bra05] are optimized to obtain the best fitting of the heat release  $w_H$  and carbon monoxide reaction rate  $w_{CO}$ . They have been computed for the combustion of methane at  $T = 300$  K at atmospheric pressure and for different air fuel ratios  $\phi = 0.58, 0.7$  and  $1.0$ . Unfortunately, equivalent parameter sets for propane have not been computed.

Finally, simulations have been achieved with the set of values used with the previous publication of the TF model for propane according to Truffin et al. [TVP03, TVV<sup>+</sup>04], and methane according to Selle et al. [SLP<sup>+</sup>02, SLP<sup>+</sup>04, Tru01] listed in Table B.4 (p.209).

## Units

In publications, different unit systems for the activation energies  $E_a$  and pre-exponential  $A$  constants for the Arrhenius formulation appear. It can be the *cgs* (centimeter-gramme-second) unit system associated with calories for the energy, or the international system *SI*: Meter [m], kilogram [kg], second [s], Joule [J] and mole [mol]. [kilo-mol] is sometimes employed to quantify the number of chemical species. One can write for both systems:

$$k_{cgs} = A_{cgs} [F]_{cgs}^{\alpha} [Ox]_{cgs}^{\beta} \exp\left(-\frac{E_{acgs}}{R_{cgs} T}\right) \quad (\text{B.6})$$

$$k_{SI} = A_{SI} [F]_{SI}^{\alpha} [Ox]_{SI}^{\beta} \exp\left(-\frac{E_{aSI}}{R_{SI} T}\right) \quad (\text{B.7})$$

	$k$	$A$	[.]	$E_a$	$\mathcal{R}$
cgs-cal-mol (CERFACS)	mol/(cm <sup>3</sup> s)	mol/(cm <sup>3</sup> s)	mol/cm <sup>3</sup>	cal/mol	1.9859 cal/(mol K)
SI-J-kmol (FLUENT)	kmol/(m <sup>3</sup> s)	kmol/(m <sup>3</sup> s)	kmol/m <sup>3</sup>	J/kmol	8314.5 J/(kmol K)
SI	mol/(m <sup>3</sup> s)	mol/(m <sup>3</sup> s)	mol/m <sup>3</sup>	J/mol	8.3145 J/(mol K)

**Tab. B.5:** Reaction rates: unit conversion

	$w_i$	factor $A_i$	Act. energy $Ea_i$	$\alpha_i$	$\beta_i$	$\gamma_i$
<i>Fluent</i>	$w_1$	(1/2×)1.585×10 <sup>10</sup>	2.0×10 <sup>5</sup>	0.7	0.8	
	$w_{2f}$	(1/2×)1.259×10 <sup>10</sup>	1.7×10 <sup>5</sup>	1.0	0.25	0.5 (H <sub>2</sub> O)
	$w_{2b}$	(1/2×)5.0×10 <sup>8</sup>	1.7×10 <sup>5</sup>			1.0 (CO <sub>2</sub> )
<i>CERFACS "2S_CM2"</i>	$w_1$	2.×10 <sup>9</sup>	1.444×10 <sup>5</sup>	0.9	1.1	
	$w_{2f}$	2.×10 <sup>6</sup>	5.024×10 <sup>4</sup>	1.0	0.5	
	$w_{2b}$	2.×10 <sup>6</sup>	5.024×10 <sup>4</sup>			1.0 (CO <sub>2</sub> )
gen. alg. $\phi = 1$	$w_1$	5.06×10 <sup>9</sup>	1.165×10 <sup>4</sup>	0.347	0.892	
	$w_2$	1.08×10 <sup>9</sup>	9.665×10 <sup>3</sup>	0.946	0.613	

**Tab. B.6:** Implemented Arrhenius coefficients for methane [SI]

Considering the unit conversion rules (see Table B.5 (p.210)), one should modify the numeric values so that:

$$\begin{cases} A_{SI} = 10^{-6(-1+\alpha+\beta)} A_{cgs} \\ Ea_{SI} = 4.1868Ea_{cgs} \end{cases}$$

and:

$$\begin{cases} A_{SI} = 10^{-3(-1+\alpha+\beta)} A_{SI-J-kmol} \\ Ea_{SI} = 10^{-3} Ea_{SI-J-kmol} \end{cases}$$

This makes the compilation of the different sources in one table for methane (see Table B.6 (p.210)) and propane (see Table B.7 (p.211)) possible, and yields an easier comparison. One should notice that:

- The coefficients  $\alpha_2$  and  $\beta_2$  taken from *CERFACS* for the second methane reaction step ( $w_{2f}$  in Table B.4 (p.209) and Table B.7 (p.211)) have been swapped to be rectified after discussion with K. Truffin [Tru06].
- The coefficients from *Fluent* are written for reactions with stoichiometry based on one mol of fuel. The factor value  $A_i$  predicted for the fuel consumption should thus be divided by two to be compared with the other sets. This is stressed in tables Table B.6 (p.210) and Table B.7 (p.211) with "(1/2×)" in the column  $A_i$ .

### A.2.3 DTF-LES Model

The major drawback of the thickened flame model (except its challenging implementation in a commercial solver) is the modification of the diffusion throughout the computation

	$w_i$	factor $A_i$	Act. energy $Ea_i$	$\alpha_i$	$\beta_i$	$\gamma_i$
<i>Fluent</i>	$w_1$	$(1/2 \times) 3.160 \times 10^7$	$1.256 \times 10^5$	0.1	1.65	
	$w_{2f}$	$(1/2 \times) 1.259 \times 10^{10}$	$1.7 \times 10^5$	1.0	0.25	0.5 (H <sub>2</sub> O)
	$w_{2b}$	$(1/2 \times) 5.0 \times 10^8$	$1.7 \times 10^5$			1.0 (CO <sub>2</sub> )
<i>CERFACS "2S_KT1"</i>	$w_1$	$2.148 \times 10^7$	$8.714 \times 10^4$	0.77	0.7044	
	$w_{2f}$	$1.0 \times 10^7$	$8.332 \times 10^4$	1.0	0.5	
	$w_{2b}$	$1.0 \times 10^7$	$8.332 \times 10^4$			1.0 (CO <sub>2</sub> )

**Tab. B.7:** Implemented Arrhenius coefficients for propane [SI]

domain. The diffusivity is indeed multiplied with the thickening factor  $F$  also far away from the flame. This can lead to a false prediction of species mass fractions in regions where the diffusion is very important (near walls for example). Actually this could lead to false predictions in the whole domain, since the reciprocal action of the diffusion and of the convection in the balance equation is distorted particularly for inhomogeneously premixed combustion, but also for perfectly premixed combustion. To correct this disadvantage a *dynamically thickened flame* model has been developed at the *CERFACS* by Legier et al. [LPV00, TVP03], and has also been included within our present implementation by Senoner [Sen05].

### Sensor

A sensor  $\Omega$  is detecting the presence of the flame (progress variable  $c$ ), so that the thickening factor becomes a local factor and acts only in vicinity of the flame:

$$F = 1 + (F_{max} - 1)\Omega(c) \quad (\text{B.8})$$

$$\Omega(c) = 16[c(1-c)]^2 \quad (\text{B.9})$$

$$c = 1 - \frac{Y_f}{Y_f^{st}} \quad (\text{B.10})$$

Legier et al. [LPV00](p. 159) have used a sensor based on the Arrhenius expression which allows a smoother distinction between the flame front and the zone close to it.

The diffusion coefficients are evaluated with a blend function of the laminar viscosity  $\nu(T)$  and turbulent viscosity  $\nu_t(T)$  and with the help of the respective Schmidt numbers:

$$D = \frac{\nu}{Sc} E \underbrace{(1 + (F_{max} - 1)\Omega)}_{F_{loc}} + (1 - \Omega) \frac{\nu_t}{Sc_t} \quad (\text{B.11})$$

Similarly, the thermal conductivity is estimated employing Prandtl numbers for the enthalpic transport equation:

$$\lambda = \rho c_p \left[ \frac{\nu}{Pr} E \underbrace{(1 + (F_{max} - 1)\Omega)}_{F_{loc}} + (1 - \Omega) \frac{\nu_t}{Pr_t} \right]. \quad (\text{B.12})$$

### Transport equations for the thickened variables

The transport equations for the Favre-filtered species mass fraction  $Y_f$ ,  $Y_{CO}$ , the mixture fraction  $Z$  and for the energy equation are modified by the local thickening factor  $F$  and the efficiency function  $E$  to use the filter especially developed for the TF/TF' model:

$$\begin{aligned}\frac{\partial \overline{\rho} \widetilde{y}_\alpha}{\partial t} + \frac{\partial \overline{\rho} \widetilde{u}_i \widetilde{y}_\alpha}{\partial x_i} &= \frac{\partial}{\partial x_k} \left( E F D_\alpha \frac{\partial \widetilde{y}_\alpha}{\partial u_k} \right) + \frac{E}{F} \widetilde{\omega}_\alpha \\ \frac{\partial \overline{\rho} \widetilde{Z}}{\partial t} + \frac{\partial \overline{\rho} \widetilde{u}_i \widetilde{Z}}{\partial x_i} &= \frac{\partial}{\partial x_k} \left( E F D_Z \frac{\partial \widetilde{Z}}{\partial u_k} \right) \\ \frac{\partial \overline{\rho} \widetilde{h}}{\partial t} + \frac{\partial \overline{\rho} \widetilde{u}_i \widetilde{h}}{\partial x_i} &= \frac{\partial}{\partial x_k} \left( E F \frac{\lambda}{c_p} \frac{\partial \widetilde{h}}{\partial x_k} \right) + \frac{E}{F} \widetilde{w}_h\end{aligned}$$

### A.3 TF and TF' models: Implementation in *Fluent*

In this section, strategies for the implementation of the TF and TF' versions in *Fluent* are described. The version TF' based on a finite volume approach and suitable for unstructured meshes should be adaptable for any other commercial solvers. There are indeed discrepancies between the apparently simple formulation of the original TF model and its practical implementation which is very dependent on the solver. The first section details the algorithm for the original TF implementation in *Fluent* through UDFs. The next appendix A.3.2 (p.215) describes the TF' implementation.

#### A.3.1 Cartesian mesh: original TF Model

As proposed in section 4.1.2 (p.63), the velocity fluctuation at the filter scale  $u'_{\Delta_e}$  in the TF model is defined by a combination of spatial operators: the rotational and Laplacian operators applied to the mean velocity vector (see Eq. (4.19)). An interchange of the order of the terms:

$$\begin{aligned}OP(\tilde{\mathbf{u}}) &\sim \Delta_x \Delta_e^2 \nabla \times [\nabla^2(\tilde{u}), \nabla^2(\tilde{v}), \nabla^2(\tilde{w})] \\ OP(\tilde{\mathbf{u}}) &\sim \Delta_x \Delta_e^2 \nabla^2(\overrightarrow{\text{rot}} \tilde{\mathbf{u}}) \sim \Delta_x \Delta_e^2 \nabla^2(\nabla \times \tilde{\mathbf{u}})\end{aligned}\tag{C.13}$$

is very useful for the implementation in *Fluent*. The third derivative of velocity has to be calculated, but in *Fluent* neither third nor second derivative of the velocity are accesible. Nevertheless the gradient of the velocity is available in *Fluent*. The vorticity vector can be written as a function of the different components of the gradient. Consequently, the calculation of the Laplacian operator has to be implemented in a *user defined file (UDF)* and then to be applied to the vorticity  $\nabla \times \mathbf{u}$ .

Another possibility would be the definition of each component of the velocity gradient as a *user defined scalar (UDS)*. Doing this, it is possible to obtain the gradient of this scalar. But as the third derivative of velocity is needed, this procedure should be used reciprocally

for each new gradient component and  $3^2 = 9$  UDSs should be declared, leading to large memory allocation and RAM requirements. An additional drawback of this method is that the the transport equations for the UDSs must be solved by *Fluent* to obtain the gradients. During this iterative process the scalar values are likely to be modified. To resume the retained strategy, it is advantageous to calculate the Laplacian operator by programming a UDF, and then to apply it to the components of the vorticity.

### Discretization implementation

Coming back to the first strategy the vorticity can be evaluated with the help of *Fluent* by arranging the components of the gradient

$$\nabla \times \tilde{\mathbf{u}} = \overrightarrow{\text{rot}} \tilde{\mathbf{u}} = \begin{pmatrix} \frac{\partial \tilde{w}}{\partial y} - \frac{\partial \tilde{v}}{\partial z} \\ \frac{\partial \tilde{u}}{\partial z} - \frac{\partial \tilde{w}}{\partial x} \\ \frac{\partial \tilde{v}}{\partial x} - \frac{\partial \tilde{u}}{\partial y} \end{pmatrix} = \begin{pmatrix} \tilde{w}_{,y} - \tilde{v}_{,z} \\ \tilde{u}_{,z} - \tilde{w}_{,x} \\ \tilde{v}_{,x} - \tilde{u}_{,y} \end{pmatrix} \quad (\text{C.14})$$

By this way the complete operator can be developed to:

$$OP(\tilde{\mathbf{u}}) = c\Delta_x^3 \nabla^2 (\nabla \times \tilde{\mathbf{u}}) = c\Delta_x^3 * \begin{pmatrix} (\tilde{w}_{,y} - \tilde{v}_{,z})_{,xx} + (\tilde{w}_{,y} - \tilde{v}_{,z})_{,yy} + (\tilde{w}_{,y} - \tilde{v}_{,z})_{,zz} \\ (\tilde{u}_{,z} - \tilde{w}_{,x})_{,xx} + (\tilde{u}_{,z} - \tilde{w}_{,x})_{,yy} + (\tilde{u}_{,z} - \tilde{w}_{,x})_{,zz} \\ (\tilde{v}_{,x} - \tilde{u}_{,y})_{,xx} + (\tilde{v}_{,x} - \tilde{u}_{,y})_{,yy} + (\tilde{v}_{,x} - \tilde{u}_{,y})_{,zz} \end{pmatrix} \quad (\text{C.15})$$

A discretization of the second derivative has to be implemented for each direction. The original discretization by Colin et al. [CDVP00](p. 1854) has the particularity to be expressed on a  $(2\Delta_x)$  mesh step (i.e. a  $(4\Delta_x)$  stencil), which reduces the cut-off wavenumber. This feature is also employed here.

*In the following, the discretization is formulated with the finite difference approximation, and a structured grid is presumed.* For the present implementation, cartesian grids are used with a non-uniform size of cells. The faces must be orthogonal to one of the main axis  $\tilde{x}, \tilde{y}, \tilde{z}$ . A classic second order finite difference approximation has to be adapted for cells with various size and for the  $(2\Delta_x)$  mesh step:

$$\frac{\partial^2 \tilde{f}}{\partial^2 x} = \frac{\tilde{f}(x_{i+2}) \cdot (x_{i-2} - x_i)}{\kappa} + \frac{\tilde{f}(x_i) \cdot (x_{i+2} - x_{i-2})}{\kappa} + \frac{\tilde{f}(x_{i-2}) \cdot (x_i - x_{i+2})}{\kappa} + O(\Delta_x),$$

$$\text{within } \kappa = \frac{2}{(x_{i-2} - x_i)(x_{i+2} - x_i)(x_{i+2} - x_{i-2})}.$$

where  $\tilde{f}$  stands for one of the components of the vorticity.

### Finding the neighbor cells

To calculate this derivative at the cell  $i$ , values of the variable  $f_j$  and the coordinates from the cells  $j = (i + 2)$  and  $j = (i - 2)$  have to be known. As *Fluent* even treats structured grids

as if they were unstructured, a prerequisite is to find out and identify the *neighbor cells* ( $i + 2$ ) and ( $i - 2$ ) of each cell in the three directions (see Figure C.2 (p.214)). The most efficient algorithm to achieve this is to loop over all faces of the mesh.

First the orientation of a face has to be determined. This is achieved by testing the scalar product of the normal vector to the face with the different cartesian directions  $\vec{x}$ ,  $\vec{y}$ ,  $\vec{z}$ . Then the two cells, to which the face belongs to, are defined as neighbor cells for the current direction. As this procedure gives only the direct neighbor cells ( $i + 1$ ) and ( $i - 1$ ), a further operation is carried out to find out the cells ( $i + 2$ ) and ( $i - 2$ ). This is simply achieved by looping over cells. The direct neighbor cell of the direct neighbor cell is attributed as the undirect neighbor cell in the direction considered (see Figure C.2 (p.214)).

In the same time, the coordinates of the cells ( $i + 2$ ) and ( $i - 2$ ) are saved in their respective UDM memories. For the 3D calculations twelve UDM memories have to be declared: six UDMs are used for the coordinates and six for the identity of the cells ( $i \pm 2$ ). The informations concerning the direct neighbor cells are deleted since not employed.

To avoid running this algorithm at each iteration step, the procedure is implemented in such a way that the address of the neighbor cells ( $i + 2$ ) and ( $i - 2$ ) and the values of their coordinates are saved in the *user defined memories (UDMs)*. This global procedure has to be called just once before starting a new calculation as a *pre-processing*. This ensures a low time-consumption, since it does not proceed during a simulation.

### Implementation of a 4th-order discretization

The information about the direct neighbor cells may be also saved (in this case 24 UDMs are required). A 4th-order discretization operator can be programmed, since five cells are available in each direction. This operator has not been actually employed for two reasons:

- It imposes the allocations of 12 additional UDMs. The cost in terms of RAM requirement or data storage capacities by saving the data files is too high for fine meshes
- It is not delivering a 4th-order discretization of the velocity  $u'_{\Delta_e}$ . The gradients of the velocity are namely obtained by *Fluent* to the 2nd-order. The improvement for the precision is restricted to the Laplacian operator.

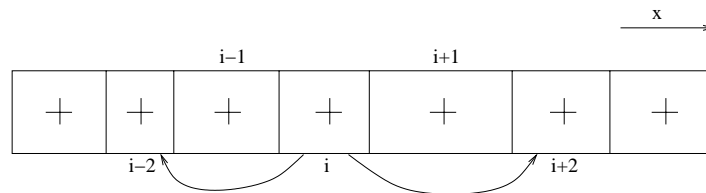


**Fig. C.2:** Indirect neighbor cells in the horizontal direction

**During the computation**

The velocity fluctuation  $u'_{\Delta_e}$  is evaluated at the beginning of each new *iteration* in a *DEFINE\_ADJUST*-function. The value is saved in a UDM, and then recalled for the evaluation of the wrinkling factor  $\Xi$  and of the efficiency function  $E$  in a *DEFINE\_SOURCE*-function. This evaluation is actually achieved in the routine evaluating the energy source term, since this is the first one executed. The source terms for the scalars are also evaluated in this routine, and only recalled when required in the iterative process. The efficiency function  $E$  and the local thickening factor  $F$  are also saved in UDMs, and recalled for the evaluation of the local diffusion coefficients for the scalars in (*DEFINE\_DIFFUSIVITY*), as well as for the thermal conductivity in (*DEFINE\_PROPERTY*) for the enthalpy equation:

1. *DEFINE\_ADJUST*:  $u'_{\Delta_e}$  evaluated and saved in UDM
2. *DEFINE\_SOURCE* for Energy Equation:  $\Xi$ ,  $F$ ,  $E$  and scalar source terms (reaction rates) evaluated and saved in UDMs
3. *DEFINE\_PROPERTY* for Energy Equation:  $F$ ,  $E$ , reaction rates recalled and used
4. *DEFINE\_SOURCE* for Scalar Equations:  $F$ ,  $E$  and scalar source terms (reaction rates) recalled and used
5. *DEFINE\_PROPERTY* for Scalar Equations:  $F$ ,  $E$  recalled and used.

**A.3.2 Modification for unstructured meshes: TF' version**

The TF model is very complex (even quite impossible) to implement for any mesh without use of intern discretization routines because of the velocity  $u'_{\Delta_e}$ . Another formulation of the operator close to the original one has been developed (see section 4.2 (p.66)) and implemented. This is a finite volume instead of a finite difference approach for the operator discretization.

**Specific parameters**

The routine for the TF' version is implemented, so that for several gases (propane and methane), their respective chemical mechanism as well as different turbulence models (Smagorinsky, the transport equation and MSM) can be employed only by changing respectively one parameter:

- CHOICE\_FUEL
- CHEMIE\_COEFF
- TURB\_MODEL.

The choice of the turbulence model in the routine is only informative, so that the routine calls the relevant variable according to the employed model.

### Pre-processing

Like for the TF routine, a pre-processing is required (*DEFINE\_ON\_DEMAND*). For the TF', three steps for each cell are executed:

- Find the surrounding cells
- Evaluate the three cell volume gradients:  $\partial\text{vol}_k/\partial x$ ,  $\partial\text{vol}_k/\partial y$  and  $\partial\text{vol}_k/\partial z$
- Evaluate the three test filter volume gradients:  $\sum_k \partial\text{vol}_k/\partial x$ ,  $\sum_k \partial\text{vol}_k/\partial y$  and  $\sum_k \partial\text{vol}_k/\partial z$ .

A loop over the cells including a loop over the faces (four or six) for each of them is carried out in order to find the neighbor cells. For each cell the identity number of the neighbor cells is saved in six UDMs. If the cell counts less than six surrounding cells, the other UDMs are set to zero. The count of non-zero UDMs allows to recognize, whether the mesh is locally tetrahedral or hexahedral or near a boundary. Another UDM is used to save the volume of the test filter volume:  $\sum_k \text{vol}_k$ . This makes the computation faster, since this variable is required.

The cell volume gradients  $\partial\text{vol}_k/\partial x$ ,  $\partial\text{vol}_k/\partial y$  and  $\partial\text{vol}_k/\partial z$  are obtained using *Fluent*. A UDS is allocated for this purpose. This scalar is defined as the cell volume. Computing one iteration only for this scalar, *Fluent* evaluates the three components of the gradient. After that this scalar and its gradients remain allocated, but they are no more solved. By this way, the gradient of the cell volume remains accessible during the simulation.

The test filter volume gradients  $\sum_k \partial\text{vol}_k/\partial x$ ,  $\sum_k \partial\text{vol}_k/\partial y$  and  $\sum_k \partial\text{vol}_k/\partial z$  are calculated as sum for each cell of the surrounding cell volume gradient. These three variables are saved in UDMs.

A macro has been written to assure the pre-processing, since the procedure with the volume gradient is quite particular.

### During the computation

Compared to the implementation of the TF version, only the evaluation of the velocity fluctuation  $u'_{\Delta_e}$  is modified. The finite volume approach with the test filter is executed in the *DEFINE\_ADJUST*-function, instead of the finite difference discretization. The different variables required are saved in UDMs and called in the respective UDFs during the iteration. When using the MSM turbulence model, a complementary loop is achieved in the *DEFINE\_ADJUST*-function to evaluate the turbulent kinetic energy  $k_{sgs}$  and the turbulent viscosity  $\nu_t$ . This one is then called for the solver with a *DEFINE\_TURBULENT\_VISCOSITY*-function.

### A.3.3 TF' model with MSM turbulence model

In this thesis, the three LES combustion models have been computed conjointly with the Smagorinsky model and the turbulent kinetic energy transport equation. Since an explicit filter has been developed in order to achieve the integration of the TF' model in *Fluent*, an *alternative LES turbulent model, which exploits the same explicit filter*, should be used.

#### Choice of an alternative LES model

Concretely, it is not judicious to use the Smagorinsky model with our implementation of the TF' model. Namely, this turbulence model does not take advantage of the test filter which is employed for the combustion model.

Similarly, the use of the turbulent kinetic energy transport equation, which has been used in this work, is not optimal when considering the CPU-effort. A redundant procedure with the developed TF' implementation for the evaluation of the test filter is imposed. The explicit filter for the TF' model has to be developed within a UDF, because particular informations are required. It is thus impossible to couple or more simplify the TF' implementation using the tke transport equation model implemented in *Fluent* by Kim [FLU05] [Kim04](p. 6).

In *Fluent*, a third LES turbulence model is available and has not been used: The *Germano's model* or *dynamic Smagorinsky model* [GPMC91, Ger92, Lil92] [Kim04](p. 4). The drawback is analogous with the tke transport equation model: Enabling this turbulence model in *Fluent* would imply that explicit filtering is carried out twice, and it would not bring more accurate results than the tke transport equation model. Programming the dynamic Smagorinsky model in the UDF could be a possible solution. But this model, like the normal Smagorinsky model, remains based on the turbulent viscosity prediction as stressed by Sagaut [Sag01](p. 95). Since the TF' model requires an accurate prediction of the velocity fluctuation rather than of the turbulent viscosity, one should focus on models based on the subgrid kinetic energy prediction rather on viscosity models.

So that, the possibility to implement a LES model based on the prediction of the sugrid kinetic energy, and based on a test filter, such as the *mixed scale model (MSM)* presented by Sagaut [Sag01](p. 100), is investigated in the following.

#### Presentation of the MSM model

If the MSM model replaces one of the turbulence model available in *Fluent*, it must also deliver a value for the subgrid turbulent viscosity  $\nu_t$  in order to ensure the complete model closure for the momentum transport equations. Sagaut [Sag01](p. 99) proposes a formulation based both on large and small scales:

$$\nu_{t\alpha} = C_m \tilde{S}^\alpha (q_c^2)^{\frac{1-\alpha}{2}} \Delta^{1+\alpha}, \quad (\text{C.16})$$

$$\text{with } C_m = 0.18^{1-\alpha} 0.20^{2\alpha}. \quad (\text{C.17})$$

The coefficient  $\alpha \in [0, 1]$  enables to weigh the relative influence of the large scales ( $\tilde{S}$ ) and the small scales ( $q_c^2$ ). Taking  $\alpha = 1$ , the formulation is namely equivalent to the Smagorinsky model.

A prerequisite for the MSM model is thus the evaluation of the band of turbulent kinetic energy  $q_c^2$  *included between* the implicit filter scale  $\Delta$  (the subgrid scale) and the test filter scale  $\hat{\Delta}$  (see Figure C.3 (p.218)):

$$q_c = |\tilde{\mathbf{u}} - \hat{\mathbf{u}}| \quad (\text{C.18})$$

$$q_c^2 = \frac{1}{2}(\tilde{u}_i - \hat{u}_i). \quad (\text{C.19})$$

$q_c^2$  is perfectly defined with the help of the grid filtered  $\tilde{u}$  and test filtered  $\hat{u}$  velocity fields already used with the TF' model.  $q_c^2$  can also be expressed using the turbulent energy spectrum assuming that the two cut-off scales belong to the inertial range:

$$q_c^2 = \int_{\kappa'_c}^{\kappa_c} E(\kappa) d\kappa = E_0 \left( \kappa_c'^{-2/3} - \kappa_c^{-2/3} \right) \quad (\text{C.20})$$

where  $\kappa'_c = \pi/\hat{\Delta}$  and  $\kappa_c = \pi/\Delta$  are the wave numbers respectively associated to the test filter and the grid scale. Writing the equivalent relation for the subgrid kinetic energy:

$$k_{sgs} = \int_{\kappa_c}^{\infty} E(\kappa) d\kappa \approx E_0 \kappa_c^{-2/3} \quad (\text{C.21})$$

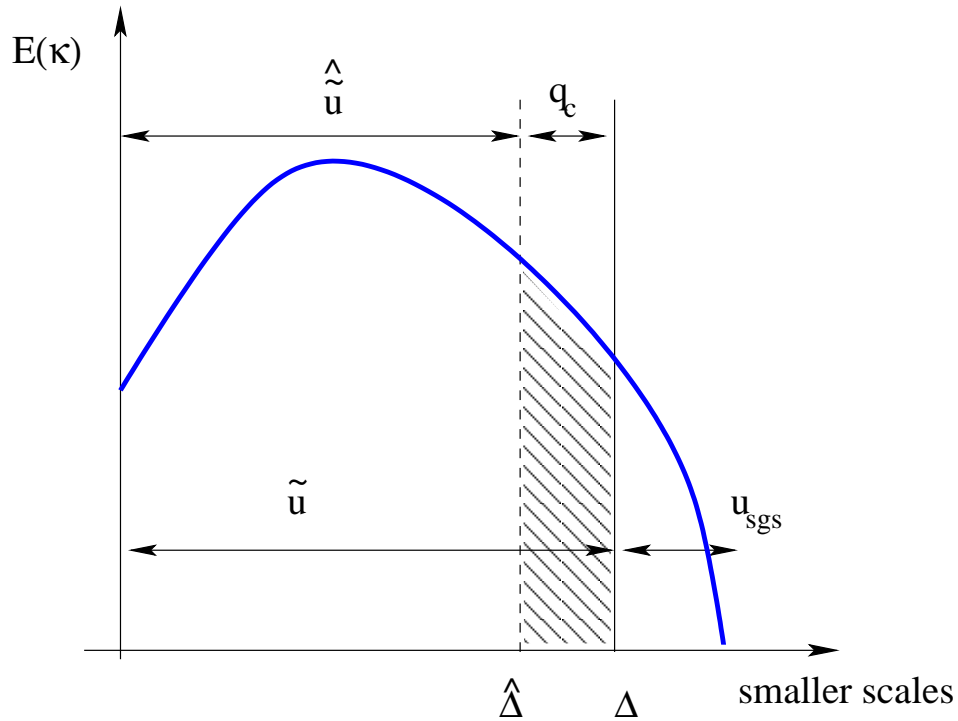


**Fig. C.3:** Scales and MSM model

so that:

$$k_{sgs} \approx q_c^2 \left[ \left( \frac{\kappa_c'}{\kappa_c^{-2/3}} \right) - 1 \right]^{-1}. \quad (\text{C.22})$$

With this relation, the MSM model enables a precise evaluation of the subgrid kinetic energy  $k_{sgs}$  using a test filter, and without additional transport equation. Moreover, in the specific application constituted by the TF' model and the evaluation of the filtered velocity  $u'_{\Delta_e}$ , the MSM model is fairly practical to evaluate the similarity constant  $c$ , as detailed in the next paragraph.

#### A.3.4 Evaluation of the similarity constant for TF'-MSM

The MSM model may offer the possibility to evaluate the similarity constant  $c$ , required for the estimation of the fluctuation velocity in the TF' model:

$$u'_{\Delta_e} \sim c |\tilde{\mathbf{u}} - \hat{\mathbf{u}}| \sim c \sqrt{q_c^2}. \quad (\text{C.23})$$

The magnitude of the fluctuation velocity  $q_c^2$  between the scales  $\kappa_c$  and  $\kappa_c'$  can be correctly evaluated as detailed in appendix A.3.3 (p.217) and exploited for this aim.

Analogous to the relation between  $q_c^2$  and  $q_{sgs}^2$  in Eq. (C.22), the band of kinetic energy  $q_{\Delta_e}^2$  between the scales  $\kappa_e = \pi/\Delta_e$  and  $\kappa_c' = 2\pi/\hat{\Delta}$  fulfills (see the hatching zone in Figure C.5 (p.221)):

$$q_{\Delta_e}^2 = \beta' (q_c^2 + q_{sgs}^2) \quad (\text{C.24})$$

$$\beta' = \left( \frac{\kappa_e}{\kappa_c'} \right)^{-2/3} - 1. \quad (\text{C.25})$$

Since the filtered velocity  $u'_{\Delta_e}$  is the measure of the turbulent kinetic energy from the smallest scales up to the filter scale  $\Delta_e$ , it is obtained from the previous results Eqs. (C.18) and (C.24):

$$\begin{aligned} \frac{3}{2} u'_{\Delta_e}{}^2 &= q_{\Delta_e}^2 + (q_c^2 + q_{sgs}^2) = q_c^2 \frac{\kappa_e}{\kappa_c'} (1 + \beta^{-1}), \\ \frac{3}{2} u'_{\Delta_e}{}^2 &= \frac{(\kappa_e/\kappa_c)^{-2/3}}{(\kappa_c'/\kappa_c)^{-2/3} - 1} q_c^2. \end{aligned} \quad (\text{C.26})$$

The last expression emphasizes the influences due to:

- The thickening factor  $F = \Delta_e/\Delta = \kappa_c/\kappa_e$
- The size ratio between the grid filter  $\kappa_c$  and the test filter  $\kappa_c'$ ,

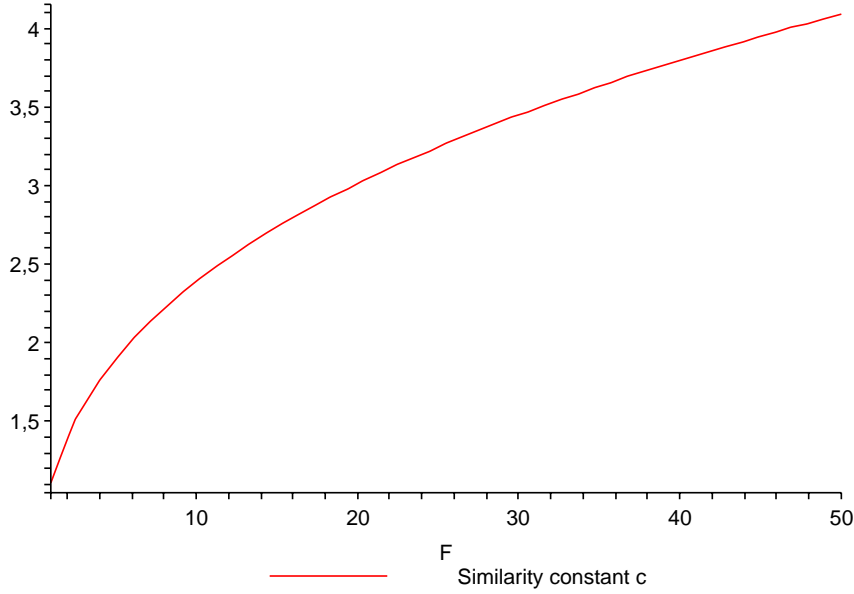


**Fig. C.4:** Influence of the thickening factor  $F$  on the similarity constant  $c$

on the prediction of the filtered velocity  $u'_{\Delta_e}$ . The value of the similarity constant  $u'_{\Delta_e} \sim c |\tilde{\mathbf{u}} - \hat{\mathbf{u}}|$  can be locally evaluated (see Figure C.4 (p.220)):

$$u'_{\Delta_e} = \underbrace{\sqrt{\frac{2}{3} \frac{F^{2/3}}{(\kappa'_c/\kappa_c)^{-2/3} - 1}}}_c \sqrt{q_c^2}. \quad (\text{C.27})$$

Numerically, taking a homogeneous  $\kappa'_c/\kappa_c = 7^{-1/3}$ , and a thickening factor equal to  $F = 10$  or  $F = 20$ :

$$F = 10 \Rightarrow c \approx 2.39, \quad (\text{C.28})$$

$$F = 20 \Rightarrow c \approx 3.00. \quad (\text{C.29})$$

It has been implicitly supposed that the thickening factor is large enough for the scale  $\Delta_e$  to contain the explicit filter scale  $\hat{\Delta}$ . The minimal value for the thickening factor should be:

$$F > \frac{\hat{\Delta}}{\Delta} \approx 7^{-1/3} \approx 1.91. \quad (\text{C.30})$$

Therefore, using the dynamic thickening factor with a local value of  $F$ , in the case  $1 < F < 2$  one should use the minimal value for the constant  $c \approx 1.40$ . Comparing to the work achieved by Colin to evaluate this similarity constant  $c$  Colin et al. [CDVP00] have selected an approximate value  $c \approx 2$  where the filtered scale has been taken constant  $\Delta_e = 10\Delta_x$ .

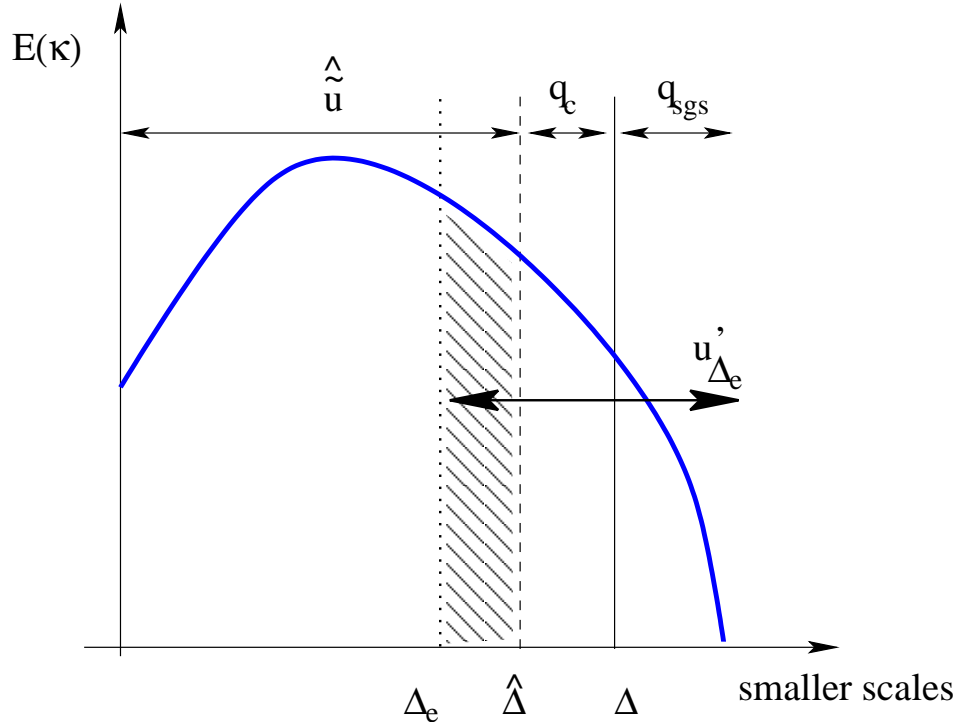


**Fig. C.5:** Filter velocity  $u'_{\Delta_e}$

The MSM model has been implemented in *Fluent* with the TF' model, but unfortunately not enough simulations have been carried out to propose a complete validation in this thesis.

#### A.4 Progress variable approach: Evaluation of $\bar{S}_l(\tilde{Z}, \widetilde{Z''^2})$

This part details how the laminar flame speed  $\bar{S}_l(\tilde{Z}, \widetilde{Z''^2})$ , presented in section 5.2.3 (p.78), can be numerically estimated.

The third product  $\frac{\Gamma(\gamma)}{\Gamma(\alpha)\Gamma(\beta)}$  in Eq. (5.25) is the Beta-function  $B(\alpha, \beta)$ , since  $\gamma = \alpha + \beta$  (see again Hackbusch et al. [HSZ96](p. 125)). In Eq. (5.24), a continuous function  $S_l$  of  $Z$  is required to achieve the integration. The polynomial Eq. (5.23) has been derived for this purpose.  $\tilde{Z}$  and  $\widetilde{Z''^2}$  are parameters in the integral so that the mean laminar flame speed  $\bar{S}_l$  can be evaluated for different couples of values  $(\tilde{Z}, \widetilde{Z''^2})$  in a discrete way. Practically this evaluation of the mean laminar flame speed  $\bar{S}_l(\tilde{Z}, \widetilde{Z''^2})$  raises two difficulties:

- Numerical problems occur for small values of  $\widetilde{Z''^2}$
- The calculation effort is non negligible as already pointed out by Kech et al. [KRGS98](p. 299)

Concerning the first issue, the Gamma-function  $\Gamma$  is increasing very fast because of its mathematical definition. With typical values  $\tilde{Z} = 0.05$  and  $\widetilde{Z''^2} = 10^{-4}$ ,  $\gamma$  is an integer and equals 474, so that  $\Gamma(\gamma) = 474! \equiv 474 \times 473 \times \dots \times 2 \times 1$ . This result exceeds capacity of computers or leads to round-off errors. Working directly with the Beta-function:

$$Beta(\alpha, \beta) = \frac{\Gamma(\gamma)}{\Gamma(\alpha)\Gamma(\beta)}$$

ameliorates the numerical solution and enables to treat larger values. With *Matlab*<sup>1</sup> and by restating the definition results have been obtained up to  $\widetilde{Z''^2} = 2 \times 10^{-5}$ .

For the second issue, Keich et al. proposed a simplified function to replace the expression Eq. (5.24):

$$\bar{S}_l(\tilde{Z}, \widetilde{Z''^2}) = S_l(Z_{st}) \left( P_Z(\tilde{Z}, \widetilde{Z''^2}) \right)^{2/3} C_{Z_{st}} \quad (D.31)$$

(where  $Z_{st}$  is the mixture fraction value at the stoichiometric conditions and  $C_{Z_{st}}$  was found to be 0.9) and compared the result of this function with the original one for Iso-Octan at ( $p = 8$  bar,  $T_u = 700$  K). This function Eq. (D.31) has the advantage of avoiding the numerical effort due to the integral, and also to enable an implementation in a routine of a CFD program. Nevertheless it does not resolve the numerical problem due to the Gamma-function. Kech et al. did not display smaller fluctuation values  $\widetilde{Z''^2}$  than  $3 \times 10^{-4}$  (smaller values are required for the LES modeling within fluctuation scales are still reduced), and its derivation was not justified.

## A.5 SFC model: Mesh refinement and resolved turbulent energy

In section 7.1.2 (p.101), two dimensionless numbers MR and RTE have been introduced to evaluate respectively the *mesh refinement* MR and the *resolved turbulent energy* RTE. These two numbers are required to express a relation between subgrid and integral length scales, since the ratios  $\Delta/l_t$  and  $u_{sgs}^2/u'^2$  appear as parameters in the closure models. Even if the resolved turbulent energy RTE does not only depend on the mesh refinement MR, it is possible to derive a relation between these two numbers by making some assumptions or setting some extra conditions. Pope has derived such a relation with the Gauss and sharp spectral filters [Pop00] (p. 577). The relation is here derived for a *box filter*, since *Fluent* is based on such a filter through the discretization with the finite volume method [FLU05]. The subgrid turbulent energy can be evaluated in this case as function of the energy spectrum  $E(\kappa)$  and of the transfer function of the filter  $\hat{G}(\kappa)$ :

$$\hat{G}(\kappa) = \frac{\sin(1/2\kappa\Delta)}{1/2\kappa\Delta}. \quad (E.32)$$

<sup>1</sup>R14.3 under Linux with Intel P4 computer

The unresolved or subgrid turbulent energy  $k_{sgs}$  is then expressed supposing an homogeneous isotropic turbulence and an isotropic filter i.e. mesh of length scale  $\Delta = \pi/\kappa_c$ :

$$k_{sgs} = \int_0^\infty [1 - \hat{G}(\kappa)^2] E(\kappa) d\kappa, \quad (\text{E.33})$$

$$k_{sgs} = \int_0^{\kappa_{EI}} \left[ 1 - \left( \frac{\sin(1/2\kappa\Delta)}{1/2\kappa\Delta} \right)^2 \right] E(\kappa) d\kappa + \int_{\kappa_{EI}}^{\kappa_{DI}} \left[ 1 - \left( \frac{\sin(1/2\kappa\Delta)}{1/2\kappa\Delta} \right)^2 \right] E(\kappa) d\kappa + \int_{\kappa_{DI}}^\infty \left[ 1 - \left( \frac{\sin(1/2\kappa\Delta)}{1/2\kappa\Delta} \right)^2 \right] E(\kappa) d\kappa. \quad (\text{E.34})$$

The first integral corresponds to the *energy-containing range*, the second to the *inertial range* and the last one to the *dissipation range* as described by Pope [Pop00](p. 231).  $\kappa_{EI}$  is the cutoff scale between the energy-containing range of eddies and the small eddies.  $\kappa_{DI}$  is the cutoff scale between the dissipation range and the inertial subrange. Considering the contribution of each term:

- Energy-containing range:  
in a first approximation the part relative to the energy-containing range can be neglected supposing that the mesh is designed in order to obtain  $1 - \hat{G}(\kappa)^2 \approx 0$ .
- Dissipation range:  
similarly the part relative to the dissipation range is neglected since both the energy spectrum  $E(\kappa)$  and the function  $1 - \hat{G}(\kappa)^2$  tend to zero.
- Inertial range:  
in the case of the box filter the result of:

$$k_{sgs_{IR}} \equiv \int_{\kappa_{EI}}^{\kappa_{DI}} \left[ 1 - \left( \frac{\sin(1/2k\Delta)}{1/2k\Delta} \right)^2 \right] k^{-5/3} dk \quad (\text{E.35})$$

is difficult to estimate. It is almost impossible to express the formal solution and requires some approximations to calculate the numerical value. With the help of *Maple* the evaluation of:

$$\int_0^\infty \left[ 1 - \left( \frac{\sin(1/2k\Delta)}{1/2k\Delta} \right)^2 \right] k^{-5/3} dk \approx 1.94 k_c^{-2/3} \quad (\text{E.36})$$

can be achieved. Compared to the desired function, a part with low wave number and a part with high wave number have been added. The discrepancy due to the contribution of the former part  $\int_0^{\kappa_{EI}} \left[ 1 - ((\sin(1/2k\Delta))/(1/2k\Delta))^2 \right] k^{-5/3} dk$  can be reduced by the choice of the mesh. Indeed the function  $1 - \hat{G}^2(\kappa)$  is smaller than 0.05% for  $\kappa/\kappa_c < 0.5$  as evaluated by Pope [Pop00](p. 569). A choice of  $\kappa_{EI}/\kappa_c = 6\Delta/l_t < 0.5$  (see Eq. (E.39)), i.e. a mesh with  $\Delta < l_t/10$  would completely cancel out the discrepancy.

The contribution of the latter part  $\int_{\kappa_{DI}}^\infty \left[ 1 - ((\sin(1/2k\Delta))/(1/2k\Delta))^2 \right] k^{-5/3} dk$  could be neglected if the bound  $\kappa_{DI}$  is pushed toward the higher values of the wave number  $\kappa$ . This corresponds to a high turbulence intensity, since  $\kappa_{DI}$  scales with the turbulent Reynolds number  $\text{Re}_t^{3/4}$  in Eq. (E.40).

In the following formulation the exact result of the integration Eq. (E.35) is noted  $I_0 k_c^{-2/3}$  and the value  $I_0 \approx 1.94$  is employed for numerical applications:

$$k_{sgsIR} \sim C_K \varepsilon^{2/3} \int_{k_{EI}}^{k_{DI}} \left[ 1 - \left( \frac{\sin(1/2k\Delta)}{1/2k\Delta} \right)^2 \right] k^{-5/3} dk \sim C_K \varepsilon^{2/3} I_0 \kappa_c^{-2/3},$$

$$k_{sgsIR} \sim C_K I_0 k^2 (L \kappa_c)^{-2/3} \sim C_K I_0 k^2 \left( \frac{0.43}{\pi} \right)^{2/3} \left( \frac{\Delta}{l_t} \right)^{2/3}, \quad (\text{E.37})$$

where the coefficients

$$C_K \approx 1.507 \text{ the universal Kolmogorov constant}, \quad (\text{E.38})$$

$$l_{EI} = \frac{\pi}{\kappa_{EI}} = \frac{1}{6} L_{11}, \quad (\text{E.39})$$

$$l_{DI} = \frac{\pi}{\kappa_{DI}} = 60\eta, \quad (\text{E.40})$$

$$l_t = L_{11} = 0.43L \equiv 0.43 \frac{k^{3/2}}{\varepsilon}, \quad (\text{E.41})$$

have been successively used by Pope [Pop00](p. 231, 237).

According to the definition of the two numbers MR and RTE, the relation is written ( $I_0$  is defined in the following):

$$k_{sgs} \approx k_{sgsIR} \approx 1 - \text{RTE} \sim 0.4 I_0 \text{MR}^{2/3}$$

$$\Leftrightarrow \text{RTE} \approx 1 - 0.4 I_0 \text{MR}^{2/3}. \quad (\text{E.42})$$

As a consequence, computing 80% of the turbulent kinetic energy requires a mesh with  $\Delta < 1/8 l_t$ . Reciprocally a mesh with  $\Delta \approx 1/5 l_t$  enables to compute 73% of the turbulent kinetic energy, and one with  $\Delta \approx 1/3 l_t$  nearly 63%. This emphasizes the cost in terms of cell numbers to resolve explicitly more than 80% of the turbulent kinetic energy. For comparison, the sharp spectral and the Gaussian filters respectively require  $\Delta/l_t \approx 1/5.2$  and  $\Delta/l_t \approx 1/7.5$ . The sharp spectral filter is the most effective thanks its Heaviside-like transfer function.

Again this relation is only valid for the following conditions:

- High Reynolds number homogeneous isotropic turbulence
- Box filter i.e. perfect hexaedral structured cells
- Isotropic filter i.e. mesh such as  $\Delta = \Delta_x = \Delta_y = \Delta_z$
- The value  $I_0 \approx 1.94$  is an “optimistic” numerical value since a more precise evaluation would give a smaller value, which would lead to a less favorable (in term of required cell number) ratio of  $\Delta/l_t$  to obtain a certain value of the resolved turbulent energy RTE.

## A.6 Post-processing achieved with *Tecplot* and *Matlab*

Since LES simulations delivers transient results, a procedure must be employed to obtain mean and rms values for the variables of interest. Parallel to the option of *Fluent*, which offers this possibility for the flow variable (velocity components, pressure, density, enthalpy), a procedure has been developed to achieve this statistical treatment for any variables (flow variable as well as UDSs and UDMs).

Calculating the mean and rms values for any variables can be achieved *on-line* in *Fluent*. Nevertheless, this additional procedure requires the allocation of two new UDMs for each variable of interest. Some difficulties can also appear if computations have crashed. For these reasons the procedure to obtain mean and rms values has been developed as a post-processing. This post-processing is requiring three steps: computation in *Fluent*, exportation in a *Tecplot*-format and mathematical treatment in *Matlab*.

### A.6.1 Computation

The complete simulation is carried out:  $N$  data files are exported every  $n$  time-steps. The value of  $N$  must be large enough to permit a relevant evaluation of the mean and rms values in terms of statistics. According to Siewert [Sie06](p.),  $N \approx 400$  in this work. Larger values like  $N = 800$  bring only a reduced precision compared to the double cost in terms of both CPU-effort and storage requirement. The frequency of exportation  $n$  must be selected so that the total time of computation  $\Delta T$ :

$$\Delta T = N \cdot n \cdot \Delta t \quad (\text{E.43})$$

exceeds a convective time of the burner. This criterion assures that the averaging operation is relevant according to the physical phenomena. Increasing  $n$  is reducing the maximum frequency available with this method. The actual frequency  $f'$  available after exporting the data files is namely:

$$f' = \frac{1}{\Delta t'} = \frac{1}{n \Delta t}. \quad (\text{E.44})$$

This is the main drawback of this procedure. Nevertheless with typical values of  $\Delta t = 5 \cdot 10^{-6}$  s and  $n = 20$ , the actual frequency is  $f' = 10$  kHz which is still one order higher than the measurement frequency used by Wäsle et al. [WWS05d]. In other words, time resolution information is lost with this procedure, but it still remains more precise than the experimental one.

### A.6.2 Exporting to *Tecplot*

The exported  $N$  data files contain all three-dimensional informations of the flow field. After the simulation, each data file is read and variables of interest are exported in a plane (or in several planes) with a *Tecplot*-format. This operation of reading/exporting is activated with a journal file which is automatically generated from a script file. *Tecplot*-files

have a structure composed of three parts. A short header gives the number of cells and nodes and the list of variables. The second part is the succession of five-column blocks. Each block contains all the values of one variable for the whole exported plane. The variables are ordered according to the header-list. The last part is a four-column block which gives the topology of the plane, i.e. how the points are connected.

### A.6.3 Treatment in *Matlab*

*Matlab*-routines have been written to read and convert the *tecplot* files into matrix. After this operation all the information contained in the  $N$  *Tecplot* files is transferred in the workspace. A matrix is defined for each variable. A dimension corresponds to the list of points, and the second to the different  $N$  time-steps. By this way the commands of *Matlab* can be easily employed to obtain mean and rms values for each variables and points. A last step consists in writing the mean and rms results again in two *tecplot* files in order to visualize them.

## A.7 SFC model: Synopsis

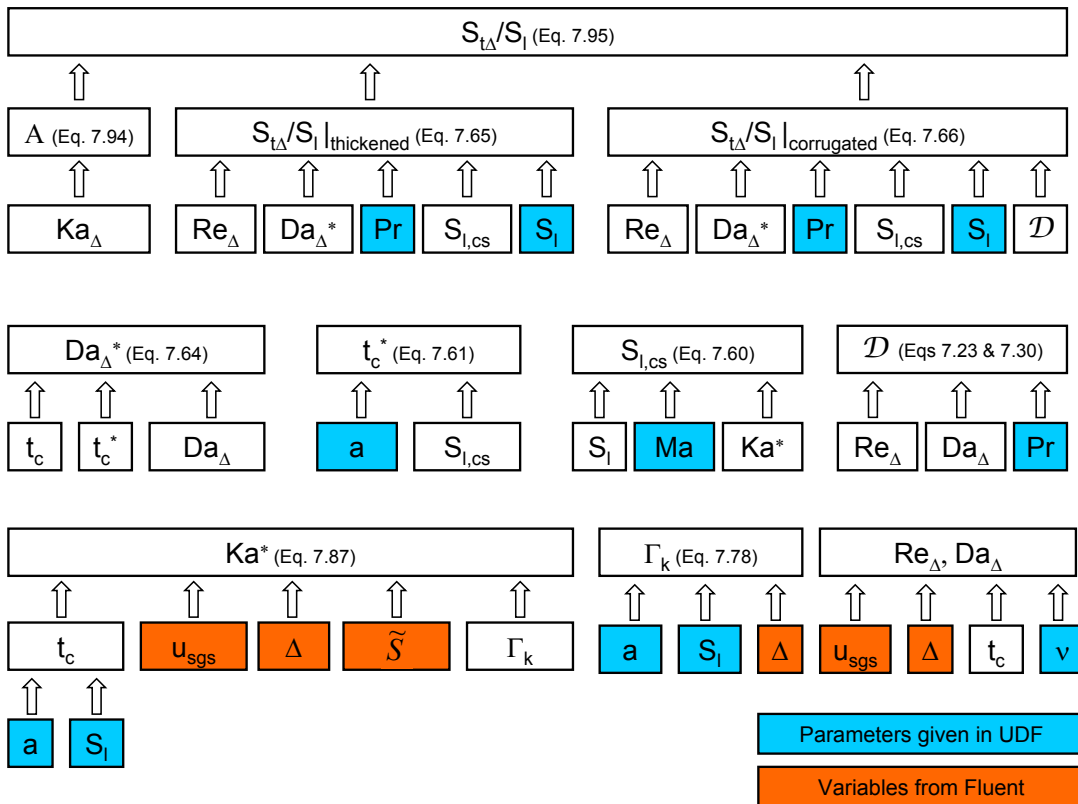


Fig. G.6: SFC model synopsis

# Lebenslauf

## Persönliche Daten

Name: Ludovic Durand  
Geburtsdatum: 01.04.1978  
Geburtsort: Sens, Yonne (Frankreich)  
Eltern: Marylise und Jean-Claude Durand  
Staatsangehörigkeit: französisch

## Schulbildung

1984 - 1989: Grundschule *Theil-sur-Vannes; Fontaine-la-Gaillarde*; Lucien Cornet (*Sens*)  
1989 - 1993: Collège Stéphane Mallarmé (*Sens*), Hauptschule  
1993 - 1996: Lycée Polyvalent Régional (*Sens*), Gymnasium  
Abschluss: Wissenschaftliches Abitur

## Studium

1996 - 1999: Lycée Janson de Sailly (*Paris*)  
Vorbereitungsklassen für die Aufnahmeprüfung im Ausleseverfahren  
1999 - 2002: Ecole Centrale de Nantes, Technische Hochschule  
Studiengang "numerische Strömungsmechanik"  
Abschluss: Diplom-Ingenieur

## Beruflicher Weg

2002 - 2006: Technische Universität München  
Lehrstuhl für Thermodynamik  
Wissenschaftlicher Mitarbeiter  
seit 2007 Mitarbeiter der BMW Group